Behrmann, J.H., Lewis, S.D., Musgrave, R.J., et al., 1992
Proceedings of the Ocean Drilling Program, Initial Reports, Vol. 141

10. SITE 863[1]

Shipboard Scientific Party[2]

HOLE 863A

Date occupied: 29 December 1991, 0245[3]

Date departed: 1 January 1992, 1430

Time on hole: 3 days 11 hr 45 min

Position: 46°14.210'S, 75°46.371'W.

Bottom felt (rig floor; m, drill-pipe measurement): 2575.9

Distance between rig floor and sea level (m): 11.65

Water depth (drill-pipe measurement from sea level; m): 2564.2

Total depth (rig floor; m): 2873.2

Penetration (m): 297.3

Number of cores (including cores with no recovery): 31

Total length of cored section (m): 297.3

Total core recovered (m): 75.39

Core recovery (%): 25.4

Deepest sediment cored:

Depth (mbsf): 297.3
Nature: Silty sandstone to sandy siltstone
Age: early Pleistocene
Measured velocity (km/s): Approximately 1.9

HOLE 863B

Date occupied: 1 January 1992, 1430

Date departed: 9 January 1992, 1100

Time on hole: 7 days, 20 hr, 30 min

Position: 46°14.210'S, 75°46.371'W.

Bottom felt (rig floor; m, drill-pipe measurement): 2575.9

Distance between rig floor and sea level (m): 11.65

Water depth (drill-pipe measurement from sea level; m): 2564.2

Total depth (rig floor; m): 3318.8

Penetration (m): 742.9

Number of cores (including cores with no recovery): 49

Total length of cored section (m): 445.6

Total core recovered (m): 192.91

Core recovery (%): 43.3

Deepest sediment cored:

Depth (mbsf): 742.9
Nature: Siltstone and well-cemented sandstone
Age: late Pleistocene (note this underlies early Pleistocene)
Measured velocity (km/s): approximately 3.2

Principal results: Site 863 is located at the base of the trench slope of the Chile Trench at the point where the Chile Ridge is being subducted. The purposes of drilling at Site 863 were (1) to determine the lithologies and depositional environments of the sediment sequences at the base of the trench slope that have been modified by hydrothermal circulation and near-trench volcanism and (2) to identify the structural fabrics and deformation caused by rift subduction.

Two lithologic units were defined at Site 863: Unit I is composed of silt- and clay-sized sediment, both lithified and unlithified, to a depth of 104.4 mbsf. Unit I is further divided into two subunits: Subunit IA, defined between the seafloor and 46.6 mbsf, is composed of about 4 m of Quaternary(?) unlithified, undeformed silty clay to clayey silt overlying lower(?) Pleistocene sulfide/organic-rich silty clay to clayey silt, with minor sand. The lower(?) Pleistocene section is completely faulted and deformed. Lithologic Subunit IB, defined between 46.6 and 104.4 mbsf, is upper(?) Pleistocene silty claystone to clayey siltstone, with minor sandstone.

Lithologic Unit II extends from 104.4 to 742.9 mbsf and is composed of lower and upper Pleistocene sandstone and bioturbated siltstone, with sandy silty claystone. Bedding in Unit II is predominantly steep to vertical, with intervals of broken formation that mark fault zones. Biostratigraphic order is inverted; lower Pleistocene lies above upper Pleistocene, with the break occurring between 290 and 325 mbsf.

Diatoms and radiolarians are poorly preserved at Site 863, except in APC cores. Only the most robust foraminifer forms are preserved, but these often have been completely replaced by silica during diagenesis. Pyritized shelf benthic species were recovered. The entire drilled section at Site 863 is Pleistocene in age.

A steeply inclined, normally polarized overprint dominates the natural remanent magnetization (NRM) through most of the sequence, and this still persists after 15-mT demagnetization. Between 350 and 500 mbsf, however, the steeply inclined overprint is greatly reduced and a low-inclination component is revealed, which probably represents the primary magnetization in this near-vertically bedded part of the sequence. This interval has been a zone of enhanced fluid chemical activity (see below), and it may be that the carrier of the overprint has been leached out.

From the seafloor to 60 mbsf is a zone of sulfate diagenesis that is typical of microbial hemipelagic diagenesis. A methanogenic layer exists between about 60 and 147 mbsf, where the calcium content drops to 20% of seawater. In the zone between 147 and 400 mbsf, interstitial fluid compositions are near those of seawater, but between 400 and 500 mbsf sharp chemical gradients occur that likely reflect intense diagenetic reactions in this interval, or possibly lateral fluid flow.

Below 490 mbsf, fluids comprise a strongly alkaline $CaCl_2$ brine. Na^- and Cl^- contents are up to 15% above seawater, pH is 10.5 in the lower 150 m of the hole, and calcium reaches concentrations up to 150 mM, while Mg and K are completely depleted. This fluid has a composition that might be expected from retrograde alteration of serpentinized ultramafics by a Mg-free hydrothermal solution.

Organic geochemical data define zones dominated by either biogenic gas or thermogenic gas likely to have migrated into the region of Site 863. The depth interval between 0 and 60 mbsf contains little methane or other hydrocarbon gases. Some biogenic gas is present between 60 and 125 mbsf, with C_1/C_2 ratios of about 800. Starting at about 350 mbsf, there is an increase in ethane, and the C_1/C_2 ratio decreases to about 5. Propane and higher hydrocarbons up to and beyond C_7 appear in the interval between 460 mbsf and total depth (TD). The organic matter content of the drilled section between 0 and 350 mbsf is made up of both terrestrial and marine components. Bitumen is generally immature.

Porosity decreases from approximately 60% to 35% between the seafloor and 150 mbsf, reflecting cementation with carbonate (micritic) cement. Compressional-wave velocities are 1600 m/s at the seafloor and

[1]Behrmann, J.H., Lewis, S.D., Musgrave, R.J., et al., 1992. *Proc. ODP, Init. Repts.,* 141: College Station, TX (Ocean Drilling Program).

[2]Shipboard Scientific Party is as given in the list of participants preceding the contents.

[3]All times are local time, UTC – 3 hr.

increase linearly from 1750 to 3200 m/s between 250 mbsf and TD. Some calcareous units have velocities up to 4500 m/s.

The minimum temperature gradient of the top 250 m of Site 863 is 73°C/km. Higher-temperature intervals at 30, 60, and 230–250 mbsf are imposed on this. Wireline measurements of the borehole temperature at the bottom of Hole 863B indicate a minimum temperature of 65°C and a minimum overall temperature gradient of 85°C/km. Equilibrium temperature had probably not been reached, however.

Despite a stuck pipe during logging, four successful logging runs were completed. Six log units were defined, primarily based on the resistivity, gamma ray, and density logs.

BACKGROUND AND OBJECTIVES

The Chile Triple Junction (Fig. 1) represents the only zone of spreading-ridge subduction where the overriding plate is composed of continental lithosphere. Here, the Nazca and Antarctic plates and the oceanic spreading ridge separating them (the Chile Ridge) are underthrusted in a shallowly dipping subduction zone. The Chile Ridge first collided with the South American continent at 14 Ma in the region of Tierra del Fuego, and other ridge segments were subducted between there and the Taitao Peninsula later. Prior to ridge collision, the Nazca Plate was subducted at a rapid rate in a direction slightly north of east. Subduction rates were roughly 80 mm/yr for the past 3 Ma and were as fast as 130 mm/yr during the late Miocene (Chase, 1978). South of the triple junction, the Antarctic Plate is being subducted at a much slower rate, roughly 20 mm/yr for the past 15 Ma in a direction slightly south of east (Chase, 1978). Currently, the section of the Chile Ridge between the Darwin and the Taitao fracture zones is gradually being subducted beneath the landward trench slope (Fig. 2). SeaBeam bathymetric data acquired during *Conrad* cruise C-2901 show that the southern part of the ridge segment is already partly covered by the leading edge of the advancing South American forearc.

Site 863 is located in the toe region of the accretionary wedge overriding the axial zone of the Chile Ridge about 20 km north of the ridge-transform intersection with the Taitao Fracture Zone. The frontal thrust of the accretionary wedge is approximately 2 km west-southwest of the drill site (Fig. 3). The top of the oceanic crust is imaged by a band of strong reflections, and a subsurface high of this band immediately below Site 863 is interpreted to image the subducted rift axis. Reflectors within the toe of the accretionary wedge have an eastward dip and may correspond to thrusts or landward-dipping surfaces of lithologic contrast. Approximately 5 km east-northeastward from Site 863 on the landward trench slope lies a steep, west-facing scarp almost 1000 m high that may have been created by slip on a steeply west-dipping normal fault (Fig. 3) of Holocene age. The normal faulting is probably in response to the wedge-toe moving over the rugged topography of the eastern flank of the subducting spreading ridge. If such a process has occurred at Site 863, it would be recorded by the overprinting of early reverse faults formed during initial accretion by later normal faults. With the toe of the accretionary wedge emplaced over the rift zone, hydrothermal effluents from the ridge may penetrate into the accreted sediments and modify the fluid discharge system both thermally and chemically. To study downhole in-situ conditions at Site 863, temperature measurements using the ADARA, WSTP, and Uyeda probes were undertaken, along with a sampling program for interstitial fluids and gases. Most of the scientific objectives for Site 863 are similar to those enumerated for Site 859 (see Site 859 chapter, this volume), and the interpretation of results is closely linked to the findings there. In detail, the scientific objectives for Site 863 are as follows:

1. To define the lithology, depositional environment, and age of the accreted sediment sequences. In addition, lithologic units that have been modified by hydrothermal circulation and near-trench volcanism are sampled.
2. To analyze the deformation and structural fabrics of the sediments at the toe of the accretionary wedge. This is to investigate the relation of these fabrics to the plate kinematic framework, and the geometrical modifications the accretionary wedge has to undergo in the process of emplacement onto the active Chile spreading ridge.
3. To determine the chemical composition of rocks, interstitial fluids, and gases. This is to identify patterns of fluid and gas flow within the accretionary wedge and between the subducting spreading ridge and the wedge.

OPERATIONS

Site 863

After leaving Site 862, the ship proceeded up the Chilean coast for 240 nmi to Puerto Quellon and transferred an injured crane operator to the Chilean agent and medical authorities. The 200-nmi trip back south to the start of the presite survey for Site 863 took 18 hr. The survey was routine, and a 14-kHz Datasonics commandable/releasable beacon was dropped at 0245 hr (local time is used throughout, local = UTC − 3 hr) on 29 December 1991.

The seismic gear was retrieved, and the ship returned to the beacon location but found the beacon to be too erratic for reliable positioning. A second commandable/releasable beacon was dropped and used for dynamic positioning for the remainder of the time on site. The malfunctioning beacon was recovered two days later while routine coring operations continued.

Hole 863A

An advanced piston corer/extended core barrel (APC/XCB) bottom-hole assembly (BHA) was made up and auxiliary subs were required to permit deployment of the motor-driven core barrel (MDCB). As clay-rich sediments similar to those encountered at Sites 859 and 860 were expected, a new RBI large cutter PDC bit was used. An identical bit had provided a good rate of progress and apparent freedom from balling at Site 860.

While the BHA and drill pipe were run to bottom, a precision depth recorder (PDR) reading was taken. We determined the seafloor to be at a depth of 2487 m below sea level (mbsl). As previous PDR readings in the vicinity had been unreliable, the driller felt for bottom before the first APC core was attempted. A tenuous bottom tag, presumed to be very soft upper sediments, was felt at 2498 mbsl, and the first APC core was attempted from 7 m above that point in an effort to establish a mudline without getting an overfilled core barrel. The effort was in vain as five water cores, each 9.5 m deeper than the one before, failed to contact the seafloor. Again, the driller felt for bottom and on the next APC core the mudline was captured and determined to be at 2564.2 mbsl, some 77.2 m deeper than the PDR estimate (Table 1).

Six piston cores were attempted, but it was obvious that the sediment would be too stiff for effective deep APC work when Core 141-863A-2H needed an overpull of 50,000 lb (kips) to be extracted. Piston Cores 141-863A-2H through -6H failed to stroke completely and suffered an overpull of 40–55 kips. The Tensor electronic orientation tool was used to orient Core 141-863A-3H, but failed because of erratic battery behavior. The old Eastman-Christensen multishot tool was used to orient Cores 141-863A-4H through -6H magnetically.

After repeated partial strokes and declining recovery through six cores, the point of APC refusal was reached and the coring mode was changed to XCB. Coring with the XCB continued from Core 141-863A-7X at 56.1 mbsf to Core 141-863A-31X at 297.3

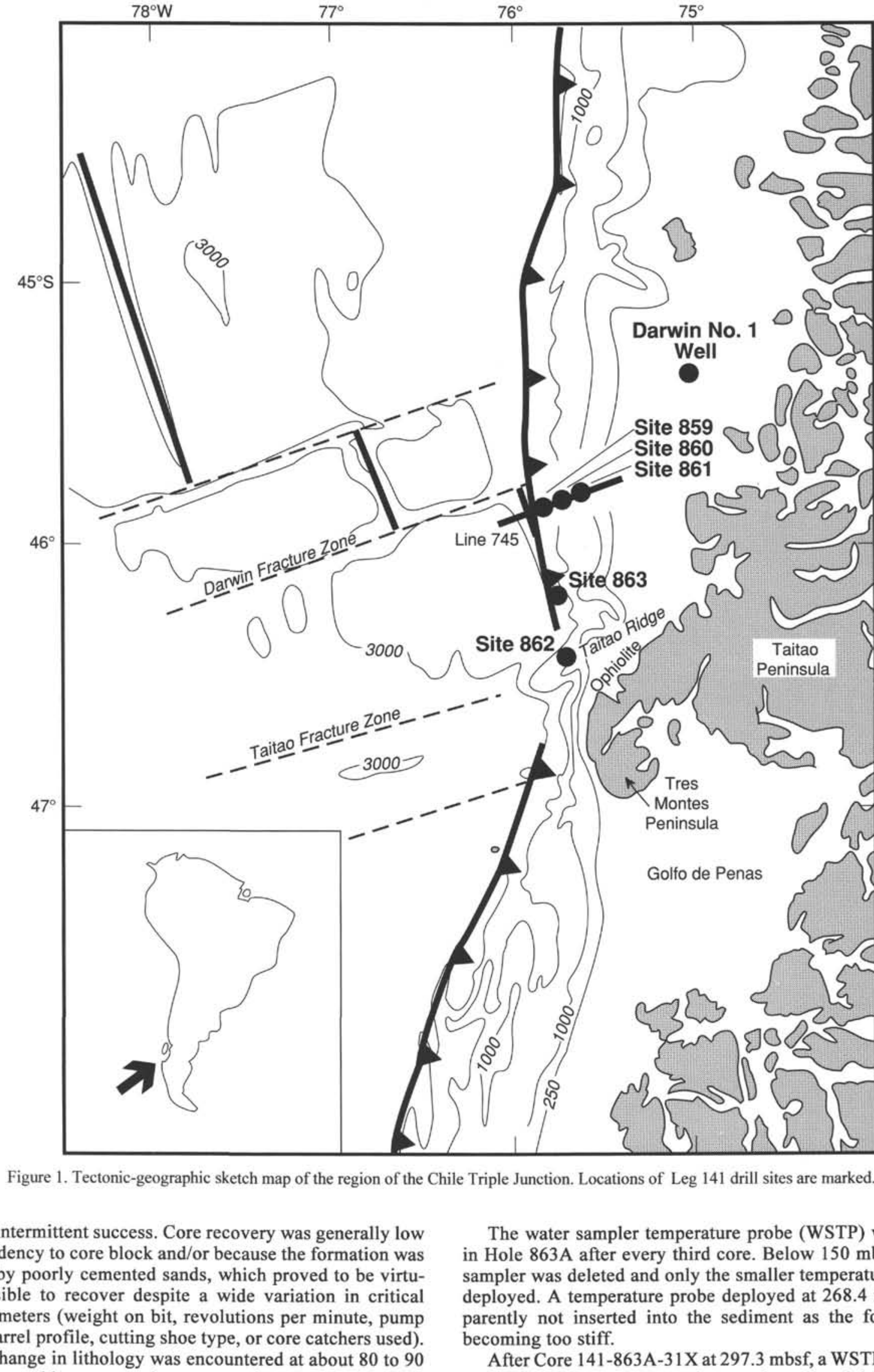

Figure 1. Tectonic-geographic sketch map of the region of the Chile Triple Junction. Locations of Leg 141 drill sites are marked.

mbsf, with intermittent success. Core recovery was generally low due to a tendency to core block and/or because the formation was dominated by poorly cemented sands, which proved to be virtually impossible to recover despite a wide variation in critical coring parameters (weight on bit, revolutions per minute, pump rate, core barrel profile, cutting shoe type, or core catchers used). A distinct change in lithology was encountered at about 80 to 90 mbsf, where sand became much more prominent.

The water sampler temperature probe (WSTP) was deployed in Hole 863A after every third core. Below 150 mbsf, the water sampler was deleted and only the smaller temperature probe was deployed. A temperature probe deployed at 268.4 mbsf was apparently not inserted into the sediment as the formation was becoming too stiff.

After Core 141-863A-31X at 297.3 mbsf, a WSTP temperature probe was lost when a stop-piece on the colleted delivery system

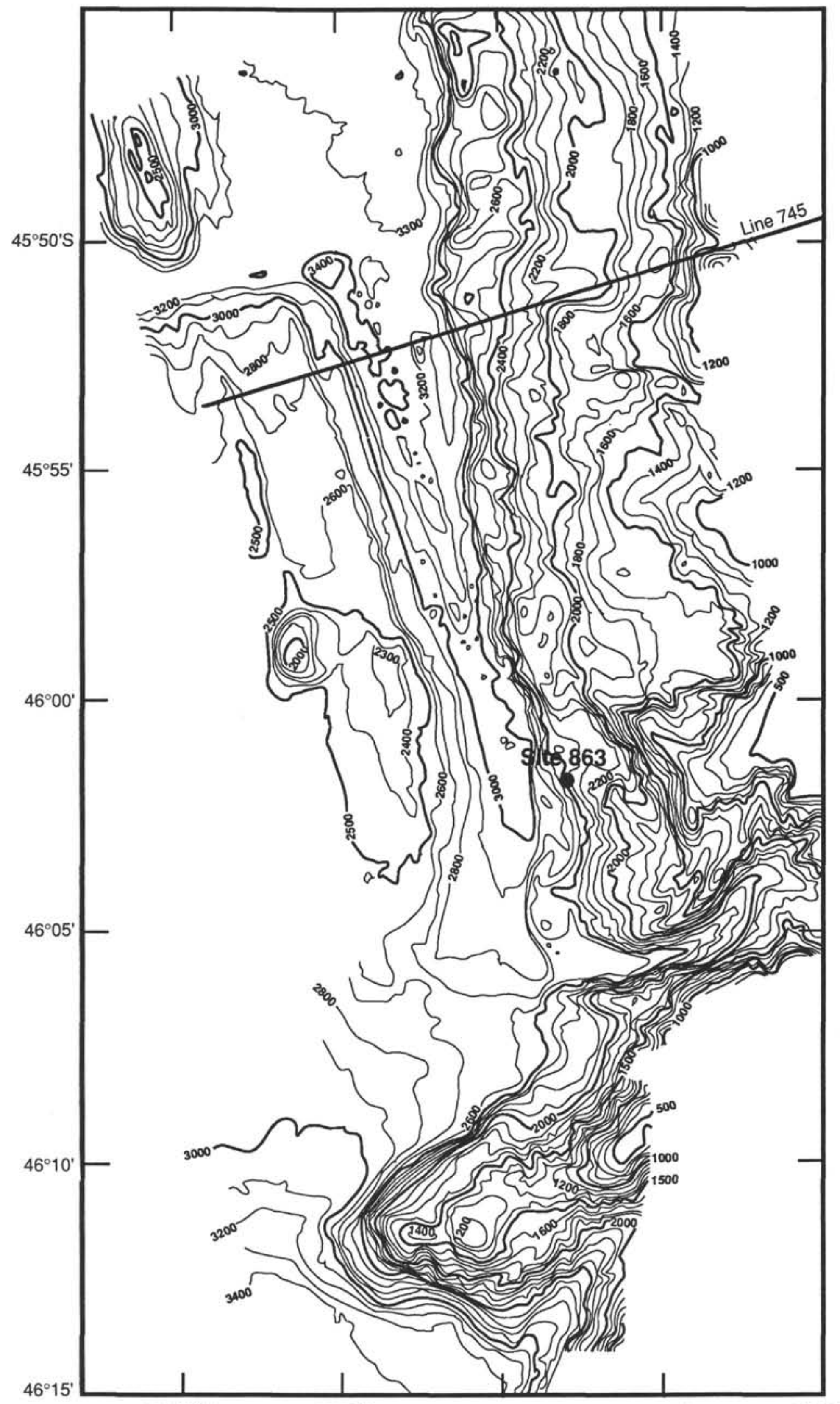

Figure 2. Detailed SeaBeam bathymetric map of the collision zone of the Chile Ridge and Chile Trench. Locations of seismic line 751 and Site 863 are marked. Contour intervals are 50 m.

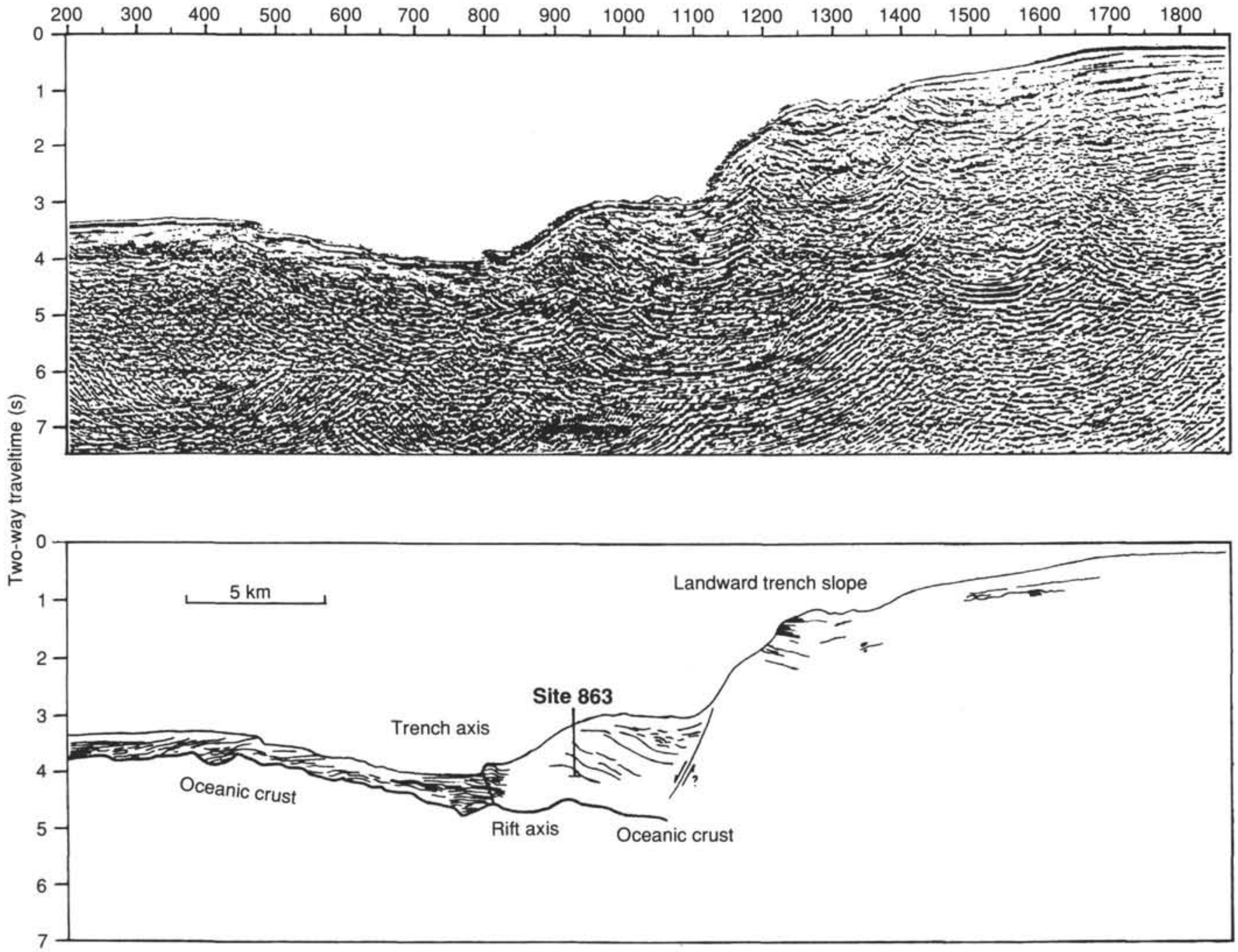

Figure 3. Reflection seismic line 751, and interpretative cross section. Location of Site 863 is marked.

backed off leaving the probe and about the lower one-third of the delivery system in the hole. The fish was 11.7 m long, dangerously close to the distance the driller had picked up the bit off bottom (about 10.5 m) to hang off the string for recovering the sinker bars and probe. When the probe was discovered to be missing, the string was gingerly lowered 5 m to keep from heaving up over the fish. The first inside-the-pipe fishing attempt used a small spiral grapple spear to stab for the inside of the collet. The fish was tagged about 6 m up inside the BHA, but the spear could not get a grab on the collet. The spear was recovered and inspected, but showed no signs of engagement with the fish. The same spear was tried again with more violent hammering via the sinker bar spang jars, but again no engagement was achieved. During the second fishing run, the bit could not get over the fish, but the fish was tagged at the same wireline depth, very near the depth of the bit.

A different spear grapple was deployed for a third fishing attempt, and again, the fish was tagged near the bit, but no engagement was achieved. While a special, rig-modified grapple spear was being prepared in the mechanic shop, the pipe was lowered and rotated gently in an attempt to get down over the top of the fish again. The bit could not be lowered without taking weight and it was assumed that the fish had escaped out the end of the pipe beyond the bit. This was confirmed when the fourth fishing run could not tag the top of the fish, even when the sandline was lowered to a depth below the bit depth.

With the hole junked by an 11.7-m-long fish, the pipe was pulled to the seafloor, ending Hole 863A at 1430 hr, 1 January 1992.

Hole 863B

The vessel was offset 10 m east to start Hole 863B so that coring could be continued to the target depth of at least 700 mbsf. A center bit was pumped in place, and the hole was drilled without coring to 297.3 mbsf, the termination depth of Hole 863A. Penetration rates and torque response of the bit during drilling were normal, so it was assumed at the time that the bit had not suffered any significant damage while attempting to wash over the fish in Hole 863A.

Coring was resumed using the XCB, but problems ensued immediately. The first three XCB cores were recovered completely empty and showed no signs of even making contact with the formation, much less sampling it. It was assumed that the core barrels were not landing and latching in the BHA for reasons unknown, although it was clear that the center bit used to drill the upper portion of the hole had latched in normally. A bit deplugger

Table 1. Summary of coring operations at Site 863.

Core	Date (Dec 1991)	Time (UTC)	Depth (mbsf)	Length cored (m)	Length recovered (m)	Recovery (%)	Age
141-863A-							
1H	29	2000	0.0–8.6	8.6	8.67	101.0	L.?Pleistocene
2H	29	2030	8.6–18.1	9.5	10.20	107.3	L.?Pleistocene
3H	29	2230	18.1–27.6	9.5	8.65	91.0	Pleistocene
4H	30	0140	27.6–37.1	9.5	4.13	43.5	Pleistocene
5H	30	0300	37.1–46.6	9.5	3.66	38.5	Pleistocene
6H	30	0545	46.6–56.1	9.5	3.45	36.3	Pleistocene
7X	30	0910	56.1–65.5	9.4	8.15	86.7	Pleistocene
8X	30	1030	65.5–75.4	9.9	6.28	63.4	Pleistocene
9X	30	1145	75.4–85.1	9.7	1.09	11.2	Pleistocene
10X	30	1445	85.1–94.7	9.6	0.30	3.1	Pleistocene
11X	30	1600	94.7–104.4	9.7	0.14	1.4	Pleistocene
12X	30	1815	104.4–114.0	9.6	0.00	0.0	Pleistocene
13X	30	2150	114.0–123.7	9.7	0.00	0.0	Pleistocene
14X	30	2315	123.7–133.4	9.7	2.05	21.1	Pleistocene
15X	31	0050	133.4–143.0	9.6	0.30	3.1	Pleistocene
16X	31	0400	143.0–152.7	9.7	0.39	4.0	Pleistocene
17X	31	0505	152.7–162.4	9.7	0.86	8.9	Pleistocene
18X	31	0620	162.4–172.0	9.6	0.41	4.3	Pleistocene
19X	31	0915	172.0–181.6	9.6	1.04	10.8	Pleistocene
20X	31	1015	181.6–191.3	9.7	0.35	3.6	Pleistocene
21X	31	1200	191.3–200.9	9.6	1.00	10.4	Pleistocene
22X	31	1545	200.9–210.6	9.7	0.43	4.4	Pleistocene
23X	31	1810	210.6–220.3	9.7	0.43	4.4	Pleistocene
24X	31	1930	220.3–229.8	9.5	1.16	12.2	L. Pleistocene
25X	31	2235	229.8–239.5	9.7	1.56	16.1	L. Pleistocene
	(Jan 1992)						
141-863A-							
26X	01	0150	239.5–249.2	9.7	1.46	15.0	L. Pleistocene
27X	01	0310	249.2–258.8	9.6	1.45	15.1	L. Pleistocene
28X	01	0440	258.8–268.4	9.6	1.74	18.1	L. Pleistocene
29X	01	0750	268.4–278.1	9.7	1.93	19.9	L. Pleistocene
30X	01	0930	278.1–287.6	9.5	2.93	30.8	L. Pleistocene
31X	01	1100	287.6–297.3	9.7	1.18	12.1	L. Pleistocene
Coring totals				297.3	75.39	25.4	
			Washed from 0–297.3 mbsf				
141-863B-							
1X	02	0915	297.3–306.6	9.3	0.00	0.0	U. Pleistocene
2X	02	1145	306.6–316.2	9.6	0.00	0.0	U. Pleistocene
3X	02	1330	316.2–325.9	9.7	0.00	0.0	U. Pleistocene
4X	02	1700	325.9–335.6	9.7	7.16	73.8	U. Pleistocene
5X	02	1945	335.6–345.2	9.6	0.27	2.8	U. Pleistocene
6X	02	2130	345.2–354.9	9.7	0.46	4.7	U. Pleistocene
7N	03	0005	354.9–357.4	2.5	2.51	100.0	U. Pleistocene
8N	03	0240	357.4–361.4	4.0	1.37	34.2	U. Pleistocene
9X	03	0525	361.4–371.0	9.6	0.52	5.4	U. Pleistocene
0R	04	0300	371.0–376.6	5.6	1.18	21.1	U. Pleistocene
11R	04	0430	376.6–386.3	9.7	0.88	9.1	U. Pleistocene
12R	04	0550	386.3–395.8	9.5	1.44	15.1	U. Pleistocene
13R	04	0725	395.8–405.5	9.7	0.87	9.0	U. Pleistocene
14R	04	0915	405.5–415.2	9.7	3.10	31.9	U. Pleistocene
15R	04	1100	415.2–424.7	9.5	3.21	33.8	U. Pleistocene
16R	04	1230	424.7–434.4	9.7	6.95	71.6	U. Pleistocene
17R	04	1415	434.4–444.0	9.6	9.28	96.6	U. Pleistocene
18R	04	1545	444.0–453.7	9.7	5.23	53.9	U. Pleistocene
19R	04	1730	453.7–463.4	9.7	6.40	66.0	U. Pleistocene
20R	04	1915	463.4–473.0	9.6	3.39	35.3	U. Pleistocene
21R	04	2100	473.0–482.7	9.7	2.47	25.4	U. Pleistocene
22R	04	2255	482.7–492.4	9.7	4.75	48.9	U. Pleistocene
23R	05	0055	492.4–502.0	9.6	6.92	72.1	U. Pleistocene
24R	05	0250	502.0–511.7	9.7	6.57	67.7	U. Pleistocene
25R	05	0440	511.7–521.4	9.7	5.56	57.3	U. Pleistocene
26R	05	0620	521.4–530.6	9.2	2.27	24.7	U. Pleistocene
27R	05	0755	530.6–540.2	9.6	7.33	76.3	U. Pleistocene
28R	05	0930	540.2–549.7	9.5	2.07	21.8	U. Pleistocene
29R	05	0830	549.7–559.4	9.7	0.28	2.9	U. Pleistocene
30R	05	1400	559.4–569.1	9.7	0.13	1.3	U. Pleistocene
31R	05	1910	569.1–578.8	9.7	6.69	68.9	U. Pleistocene
32R	05	2025	578.8–588.4	9.6	9.21	95.9	U. Pleistocene
33R	05	2200	588.4–598.1	9.7	4.59	47.3	U. Pleistocene
34R	05	2340	598.1–607.7	9.6	8.40	87.5	U. Pleistocene
35R	06	0015	607.7–617.4	9.7	8.44	87.0	U. Pleistocene
36R	06	0305	617.4–627.0	9.6	5.36	55.8	U. Pleistocene
37R	06	0455	627.0–636.6	9.6	7.81	81.3	U. Pleistocene
38R	06	0645	636.6–646.3	9.7	4.58	47.2	U. Pleistocene
39R	06	0900	646.3–655.9	9.6	4.37	45.5	U. Pleistocene
40R	06	1130	655.9–665.5	9.6	4.06	42.3	U. Pleistocene
41R	06	1415	665.5–675.2	9.7	5.51	56.8	U. Pleistocene
42R	06	1615	675.2–684.8	9.6	4.05	42.2	U. Pleistocene
43R	06	1830	684.8–694.5	9.7	3.48	35.9	U. Pleistocene
44R	06	2040	694.5–704.2	9.7	6.65	68.5	U. Pleistocene
45R	06	2240	704.2–706.8	2.6	1.97	75.7	U. Pleistocene
46R	07	0030	706.8–713.8	7.0	2.70	38.6	U. Pleistocene
47R	07	0230	713.8–723.5	9.7	4.06	41.8	U. Pleistocene
48R	07	0505	723.5–733.2	9.7	2.27	23.4	U. Pleistocene
49R	07	0725	733.2–742.9	9.7	6.14	63.3	U. Pleistocene
Coring totals				445.6	192.91	43.3	

was dropped and recovered and showed indications of proper landing and latch-in. An ADARA temperature shoe was made up to a modified XCB barrel and lowered into the sediment in an attempt to get both a final in-situ temperature measurement and a push-core sample. Neither effort was successful as the ADARA shoe programming faltered, causing the tool to stop sampling prematurely. The push-core was not present, and again, the tools did not show signs of having come into contact with the formation.

Core 141-863B-4X was cut with an extended XCB cutting shoe and recovered 7.16 m of well-trimmed core. Two more XCB cores were attempted, but recovery was low because of core jamming after a partial core had been acquired. The explanation for the failure to recover core during the first three XCB attempts was never found. More importantly, the formation was becoming tough enough to cause significant damage to the tungsten-carbide insert cutting shoes in use.

To attempt to achieve higher quality cores as well as to discharge a JOIDES Planning Committee (PCOM) testing mandate, the MDCB coring system was used for the next two cores. Both deployments were mildly successful in terms of core recovery and almost completely successful in terms of testing the latest version of the MDCB. Despite recovering good cores with the MDCB, it was clear that the scientific objectives of the hole could not be achieved in the time available at the speed of net penetration possible with the short (4.5 m) MDCB system. Thus, the MDCB was retired and one further XCB core was cut before the drillers opted to terminate coring in the hole and trip the pipe for the rotary core barrel (RCB) system.

The decision to change coring systems was fully justified when the large cutter PDC bit was recovered and found to be almost completely destroyed from either junk damage in Hole 863A or lost-cutter damage later.

Before tripping out of the hole, a minicone (free-fall funnel, FFF) was dropped around the pipe and into the hole. The pipe was tripped to the deck and a 12-drill-collar BHA was assembled with a standard 9-7/8-in. roller-cone bit plus a mechanical bit release and Hydrolex drilling jars. The pipe was tripped back to bottom and the Colmek TV was run in on the VIT frame.

The search to find the FFF and re-enter the hole was a difficult one. Despite having a mini-mudskirt and three flotation balls on tethers, all designed to make finding the cone easier, the FFF proved difficult to identify. The cone and hole were actually spotted at least three times before the first re-entry stab, but the cone was so obscured that it was thought to be the top of Hole 863A and not an FFF at all. No flotation balls were ever spotted. After 5 hr of frustration, the only target available was stabbed and re-entered and was proven to be the correct hole only when the pipe was advanced without obstruction to a point deeper than Hole 863A.

Coring in Hole 863B was resumed using the RCB. After four cores with lackluster recovery similar to the disappointing earlier XCB results, a formation change wrought a dramatic improvement in core recovery, which stayed high through the remainder of the hole in fine-grained siltstone and sandstone with near-vertical bedding planes. Thirty-six more RCB cores were taken with excellent core recovery and only minor problems when the bit plugged at one point. A drift survey at 100-m intervals was taken and revealed a dogleg with drift angles that increased from 2° off vertical at 75 mbsf to at least 9° at 175 mbsf, and then going back to 3°–5° deeper in the hole. A keyseat at the dogleg seemed possible but was thought not to exist because there had been no drag or overpull while pulling up pipe between connections. Later evidence refuted this assumption.

Coring was terminated with Core 141-863B-49R at 742.9 mbsf when time for drilling operations expired and the original depth target for the site had been surpassed. A short wiper trip was performed over the lower half of the hole only, as the upper half had been in good shape when re-entered three days earlier. The hole was circulated clear, and the bit was released 10 m off bottom with a routine activation of the mechanical bit release (MBR).

The pipe was pulled to logging depth while displacing the hole with bentonite mud treated with 1% KCl. Before reaching the intended logging depth of 65 mbsf, the pipe began to drag and then became thoroughly stuck, with the end of pipe at 2795.3 mbsl (231.1 mbsf). This would have placed the uppermost 8-1/4-in. drill collar in the approximate center of the dogleg. The string could not be made to go up, down, or rotate. Full circulation was available with uninhibited back pressure. These conditions strongly suggested that the BHA was tightly wedged in a keyseat. After trying to free the pipe with no success, we hung off the string with about 30 kips download and logging operations were commenced. The drillers hoped that heave cycles pushing down the pipe during two days of logging would free the BHA from the keyseat.

The heave compensator was used on all logging runs and was turned on and off at 290 mbsf. Four runs were made (Table 2). The first run was with the geophysical tool string (spectral gamma-ray, sonic, caliper, resistivity, and LDGO temperature tools). The tool string hit a constriction in the pipe at approximately the seafloor (2564.6 m), but was able to pass through when the drill pipe was pulled up enough to remove the bow in the pipe. Downgoing logs were recorded from 232.0 to 734.8 mbsf, less than 10 m above terminal depth (TD) of 742.9 mbsf. The sonic tool malfunctioned at the bottom of the hole and had to be turned off for the uphole logging run. Gamma-ray and resistivity logs were recorded uphole from 742.9 to 232.0 mbsf.

The second logging run was with the geochemical tool string. On the first pass, the hole was logged from near bottom (734.0 mbsf) to base of pipe (232.0 mbsf) in the open hole and from 232.0 to 0.0 mbsf through pipe. The second pass was recorded in the open hole from 549.1 to 232.0 mbsf.

The formation microscanner sonde (FMS) tool string was rigged up and lowered to maximum logging depth (738.1 mbsf). During the first upward pass, the Schlumberger computer malfunctioned when the tool string was at 290.0 mbsf. The tool string was lowered back 50 m and data recorded to pipe (232.0 mbsf). A second pass was made with the FMS tool string over the entire open hole.

The fourth run was made with the lithoporosity tool string (spectral gamma-ray, neutron porosity, lithodensity, and LDGO temperature tools) from 732 mbsf to the base of pipe. Six 10-min stations (three in pipe; three in open hole) were also occupied to obtain temperature measurements. This last tool string was run up

Table 2. Hole 863B well log data.

Log Type	Depth (mbsf)
Resistivity	232.0–730.6
Bulk density	232.0–731.9
Neutron porosity	232.0–728.2
Sonic velocity	232.0–719.8
Gamma ray/U-Th-K[a]	0.0–718.7
Aluminum[a]	0.0–721.9
Geochemistry[a]	0.0–732.7
Caliper	232.0–718.0
Formation microscanner	232.0–736.8
LDGO temperature[a]	0.0–734.8

Note: Values assume seafloor at 2564.6 mbsl and with all logs correlated and depth shifted to the gamma-ray log from the geophysical tool string.
[a]These logs were recorded in pipe from seafloor to 232.0 mbsf.

to the rig floor and rigged down at 2200 hr, 8 January 1992, ending logging operations in Hole 863B.

At the end of logging operations, the pipe was still firmly stuck in the keyseat and could not be induced to budge even after 3 hr of working the string with 1200 gpm flow and maximum allowable overpull. With all other options exhausted, a Schlumberger severing charge was assembled and run into the transition joints immediately above the BHA. The pipe was severed cleanly. The string was immediately free and was pulled up 28 m, where a 31-bbl plug of 15.5-ppg cement was spotted to plug the hole in accordance with standard Pollution Prevention and Safety Panel (PPSP) policy for continental margin sites having no hydrates.

The pipe was pulled clear of the seafloor and tripped to the deck passing through the rotary at 1100 hr, 9 January 1992, officially ending site operations for the leg. As the pipe was pulled, the beacon was released and recovered routinely in fair daylight conditions.

With extra time in hand for the return voyage to Valparaiso, the ship proceeded 17 nmi south to the location of Site 862 to collect the beacon that had been abandoned there. Release and recovery were straightforward and at 1505 hr, 9 January, the vessel got underway for Valparaiso.

Final Transit to Valparaiso

The final downhole and beacon recovery operations had proceeded ahead of schedule, leaving more than adequate time to steam to Valparaiso to meet the scheduled arrival time of 0600 hr, 13 January. Although the original intention was to proceed at a modest speed for the purpose of fuel savings, this plan was dropped in lieu of proceeding at full speed to achieve an early arrival. This would allow for extra time either at anchor or at a dockside berth to move the drilling and re-entry equipment from the forward drill-collar racks to the riser hold in preparation for the massive amount of equipment to be loaded aboard for the diamond coring system (DCS) leg about to begin. Leg 141 officially ended with the first mooring line in the port of Valparaiso at 1750 hr, 12 January 1992.

LITHOSTRATIGRAPHY

Summary

Hole 863A was cored by the APC to 56.1 mbsf (Cores 141-863A-1H to -6H), and coring was continued by the XCB to a total depth of 297.3 mbsf (Cores 141-863A-7X to -31X). Recovery was 100% only in the first 25.2 mbsf; most of the rest of Hole 863A had recovery less than 20%, making it difficult to define lithostratigraphic units. Hole 863B was offset 10 m and was washed down to 297.3 mbsf, then drilled by the XCB. The first three cores had no recovery, thus Hole 863B stratigraphy does not overlap with Hole 863A stratigraphy. The stratigraphic record for Hole 863B begins at 325.9 mbsf; recovery varied from less than 20% for much of the upper 100 m to over 50% for the lower 300 m. Hole 863B was drilled to a total depth of 742.9 mbsf (XCB, MDCB, RCB). Two lithologic units have been recognized at Site 863 (Table 3, Figs. 4 and 5), on the basis of composition, lithification, and sedimentary structures. Subunit boundaries are defined by downhole changes in structure (Subunits IA and IB), composition (Subunits IIA and IIB), and diagenesis (Subunits IA and IB, and IIB and IIC). These boundaries are transitional in character.

Lithologic Unit I (Cores 141-863A-1H through -11X; age: Quaternary; depth: 0–104.4 mbsf)

Lithologic Unit I is restricted to Hole 863A and consists of unlithified to lithified sediments and sedimentary rocks recovered

Table 3. Lithostratigraphy for Site 863.

Units	Age	Interval and depth	Lithology
Subunit IA	late Pleistocene	Cores 141-863A-1H through -5H (0–46.6 mbsf)	Silty clay and clayey silt with intervals of disseminated sand; locally high sulfide/organic content and intense structural deformation
Subunit IB	late Pleistocene	Cores 141-863A-6H through -11X (46.6–104.4 mbsf)	Silty clay and clayey silt with thin sand beds
Subunit IIA	early to late Pleistocene	Cores 141-863A-12X to -24X (104.4–220.3 mbsf)	Sandstone, sandy siltstone and sandy silty claystone
Subunit IIB	early to late Pleistocene	Cores 141-863A-24X to -31X and 141-863B-1X to -13R (220.3–405.5 mbsf)	Sandstone, sandy siltstone and sandy silty claystone
Subunit IIC	late Pleistocene	Cores 141-863B-14R to -49R (405.5–742.9 mbsf)	Claystone, silty claystone, sandy silty claystone, and sandstone; common diagenetic phases include smectite, carbonate and zeolites(?)

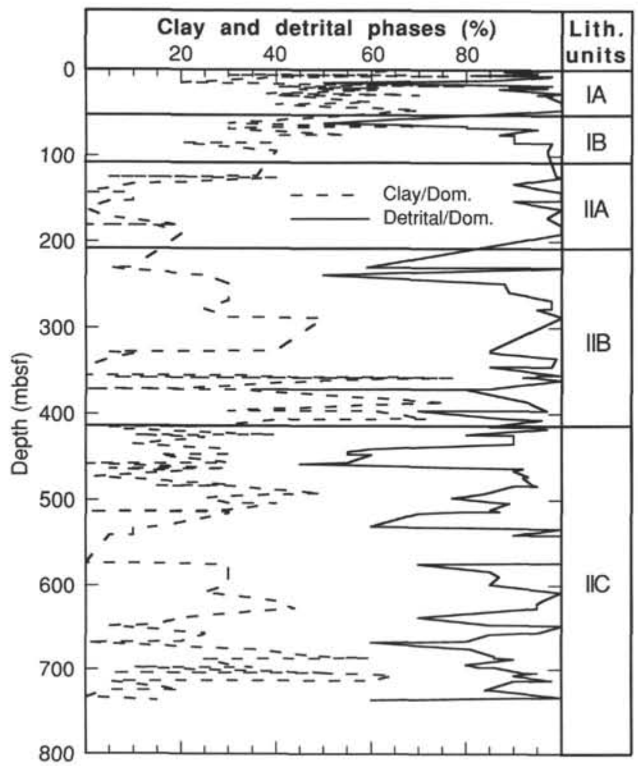

Figure 4. Lithologic units for Site 863, shown with respect to the percent clay and total detrital (clay, silt, and sand) minerals in the dominant lithologies. Unit I is much more clay-rich than most of Unit II, although a clay-rich interval marks the lower 50 m of Subunit IIB. Fluctuations in clay content within Subunit IIC illustrate the cyclic recurrence of fining-upward sequences.

within the top 104.4 mbsf. It includes two subunits: Subunit IA (0–46.6 mbsf), about 4 m of grayish green silty clay to clayey silt overlying intensely deformed black to grayish black firm clay, rich in organic material and sulfides; and Subunit IB (46.6–114.0 mbsf), mildly deformed grayish green clay and silt with nannofossils, containing grayish black pyrite concentrations and minor sand layers. The base of Subunit IA must be tectonic because of the change in structural style (see Structural Geology section, this chapter). No microfossils of post-upper Pleistocene age have been observed (see Biostratigraphy section, this chapter).

Subunit IA (Cores 141-863A-1H through -5H; age: Quaternary; early (?) Pleistocene indicated in Cores 141-863A-1H and -2H; depth: 0–46.6 mbsf)

The upper 4 m of Subunit IA is a soft, unlithified grayish green (5Y 3/2) silty claystone to clayey siltstone with minor intervals of disseminated sand (Fig. 6) and rare laminae of silty sand. The sediment contains sparse concentrations of black organic material, rare framboidal pyrite, and scattered pyrite nodules. It is largely structureless except for slight to moderate bioturbation.

At about 4 mbsf the sediment changes to firm, partially lithified, olive gray to greenish gray (5Y 2/1 to 3/2) silty clay and clayey silt with olive black to black (5Y 2/1 to N5) organic-rich pods and laminae (Fig. 7). Coincident with the color and composition change is an increase in the degree of structural deformation: contorted laminae are offset along numerous deformation bands and faults (see Structural Geology section, this chapter). The lithology in this interval consists of very firm sediment interbedded with very soft rock. In spite of tectonic disruption, the original bedding style can be inferred from gross variations in composition from pyrite/organic-rich silt and clay, to dark greenish gray nannofossil-rich silt and clay (Fig. 8), to massive clayey silt to silty clay. Local intervals of dispersed sand occur within the muddy material, as well as thin interbeds (0.5–1.0 cm) of dark-gray to black pyrite-bearing sand. Sand interbeds are typically laminated and exhibit small-scale basal scours (Fig. 9). Some of the coarser sand laminae appear to be inversely graded.

The black sulfide/organic-rich zones are dominated by opaque minerals. Rare framboidal pyrite is observed. Certain intervals of the cores oxidized quickly after being opened, resulting in a color change from black (N1) to dark grayish green (5G 4/2). In some cases, the black concentrations are localized around and within burrows; in other cases, they form laminations (possibly of diagenetic origin) or are concentrated along faults. Pyrite nodules are common within Subunit IA both as isolated small concretions 2–5 mm in diameter and as concentrations of nodules within beds of fine sand (Fig. 10). The entire unit contains fine disseminated pyrite.

Sand- and silt-sized components in Subunit IA include quartz, feldspar (altered and fresh), chert, schist fragments, muscovite,

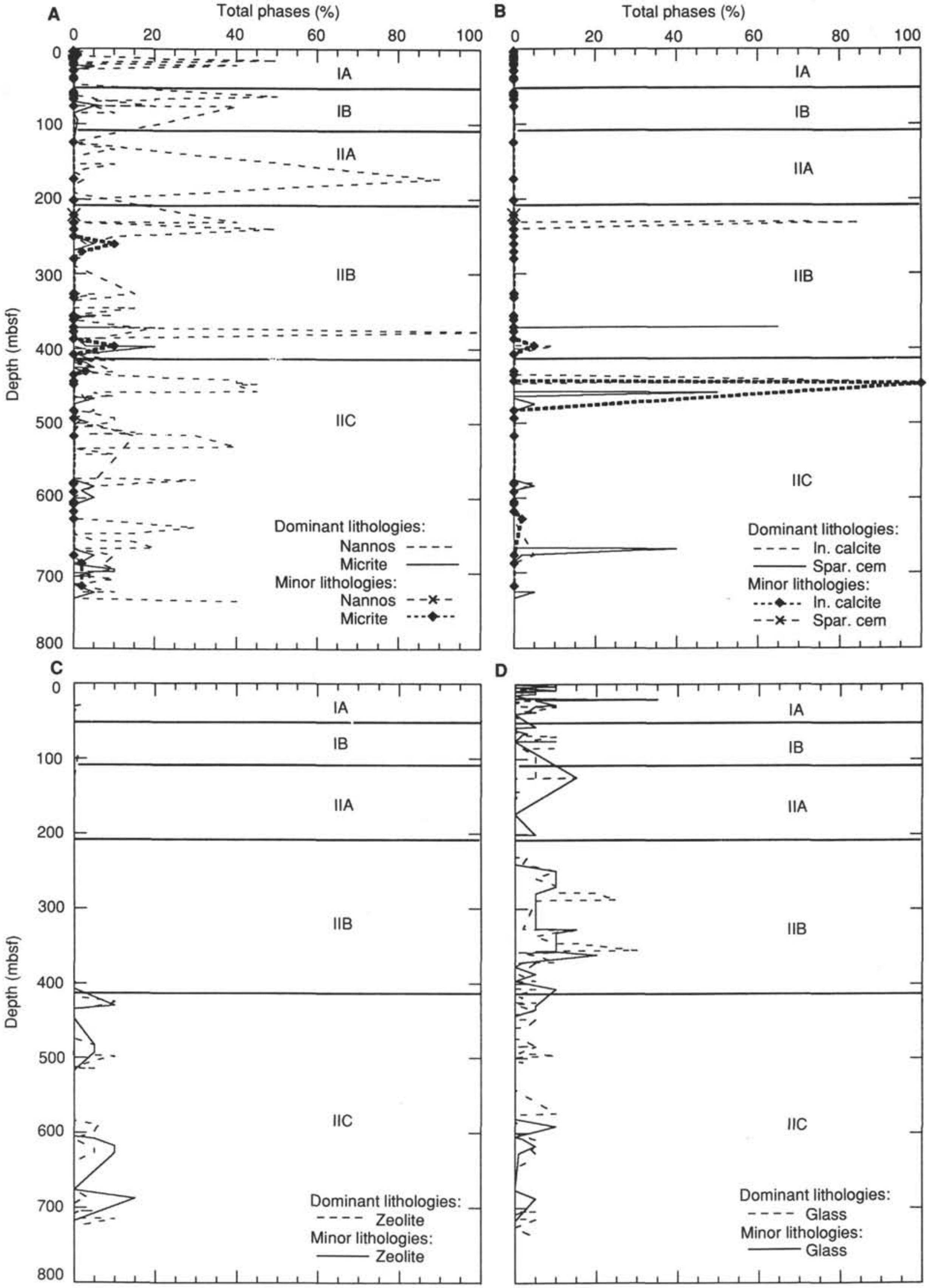

Figure 5. Variation in selected sedimentary and authigenic components at Site 863. **A.** Nannofossils and micrite. **B.** Inorganic calcite and sparry calcite cement. **C.** Zeolites. **D.** Glass.

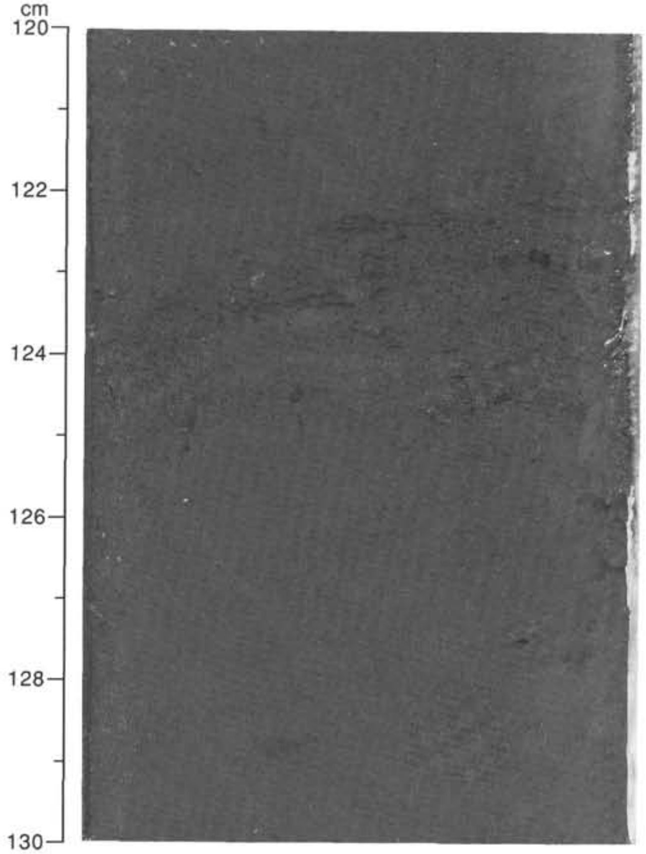

Figure 6. Core photograph, sandy interval in clayey siltstone of Subunit IA; sand was probably disseminated by bioturbation. Light and dark burrows and isolated small black organic concentrations occur above and below the sandy interval (Section 141-863A-1H-2, 120–130 cm).

and biotite, as well as colorless, tan and black, tachylitic glassy volcanic fragments that exhibit vesicular to pumiceous and microlitic textures. These sediments contain a diverse suite of heavy minerals including pyroxene, amphibole, opaques (including framboidal pyrite), sphene, garnet, epidote, and zircon. Microfauna include foraminifers, nannofossils, diatoms, radiolarians, silicoflagellates, and sponge spicules. Organic matter includes some spores and plant debris.

An angular fragment of diorite (2×3 cm across) occurs at 12.8 mbsf (Section 141-863A-2H-3, 118–130 cm); it is interpreted as a dropstone because it is firmly embedded within sediment in the center of the hydraulic piston core (Fig. 11).

Subunit IB (Cores 141-863A-6H through -11X; age: late(?) Pleistocene; depth: 46.6–104.4 mbsf)

Subunit IB is characterized by a decrease in both the black pyrite/organic-rich concentrations and the degree of deformation. Its contact with the overlying Subunit IA is assumed to be tectonic because of the abrupt change in structural style and a likely age inversion between early Pleistocene in Cores 141-863A-1H and 2H, and late Pleistocene in Core 141-863A-8X (see Structural Geology and Biostratigraphy sections, this chapter). The degree of lithification also appears to decrease slightly.

This subunit consists of dark greenish gray (5Y 4/1 to 3/2) and gray to black (N3 to 5Y 2/1) silty clay and clayey silt (Fig. 12). It is moderately bedded, with alternating intervals of laminated organic-rich clay/silt and massive bioturbated calcareous clay/silt. Black laminations and dispersed clots of sulfide/organic-rich sediment are present throughout, but are much less

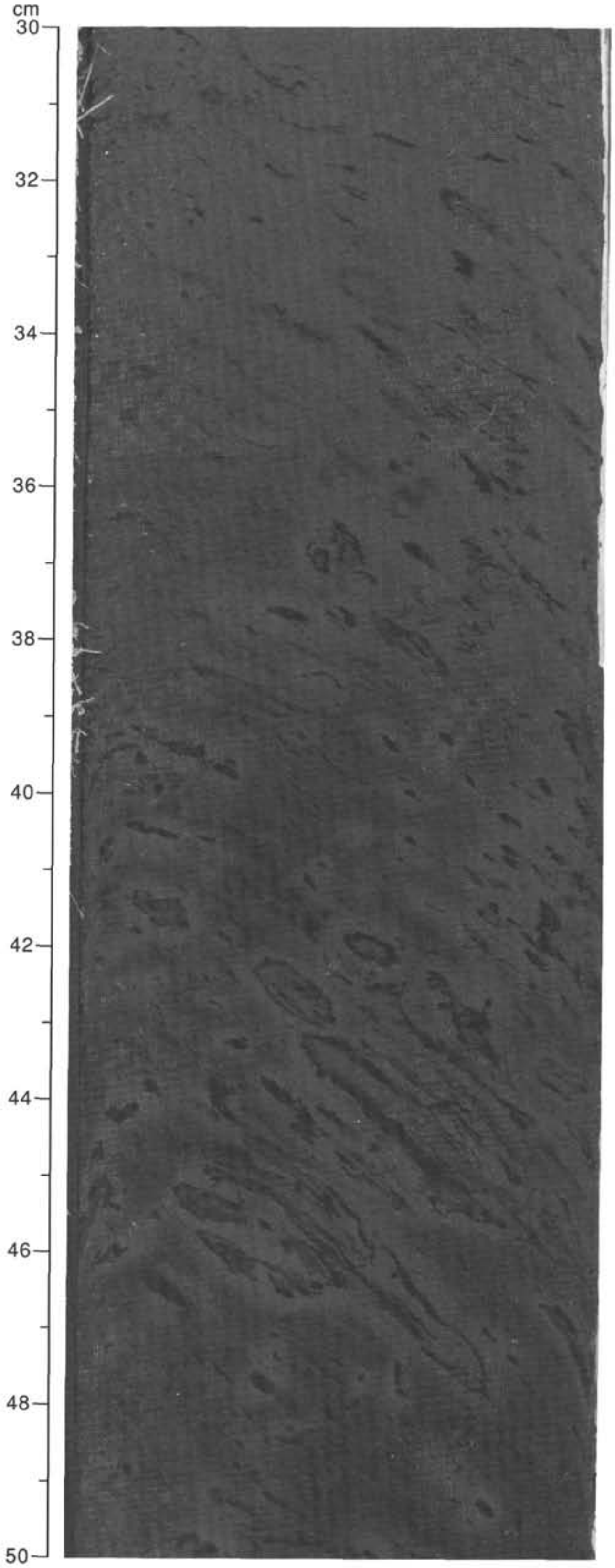

Figure 7. Core photograph, marblelike appearance of Subunit IA, caused by deformed thin laminations and clots of black organic- and sulfide-rich material in gray silty clay to clayey silt. The bull's-eye structure of the clots suggests that they may be deformed burrows, and lighter halos suggest that they are, in part, diagenetic features. Drawdown along sides of core is drilling disturbance (Core 141-863A-4H-1, 30–50 cm).

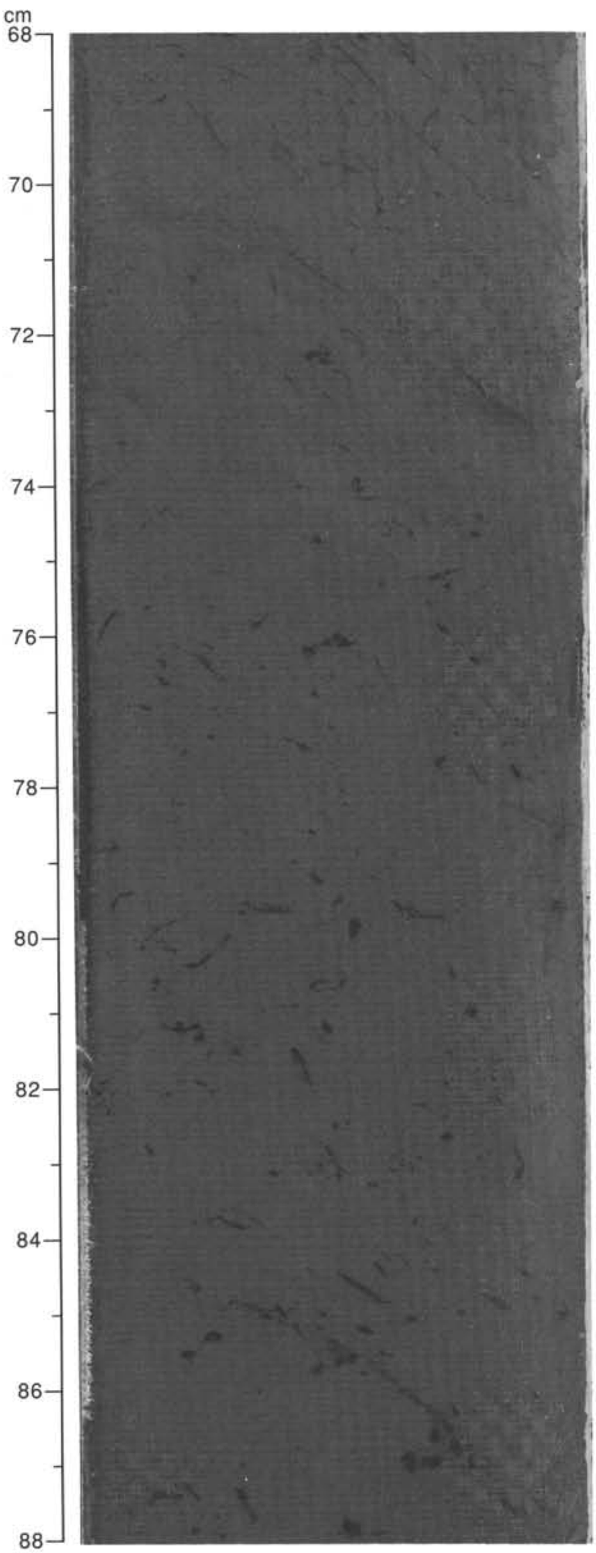

Figure 8. Core photograph, lighter gray nannofossil clayey silt (interval at 66–74 cm) interbedded with darker gray silty clay containing concentrations of black sulfide-rich organic material. Bedding is dipping to the right in this view (Section 141-863A-5H-2, 68–88 cm).

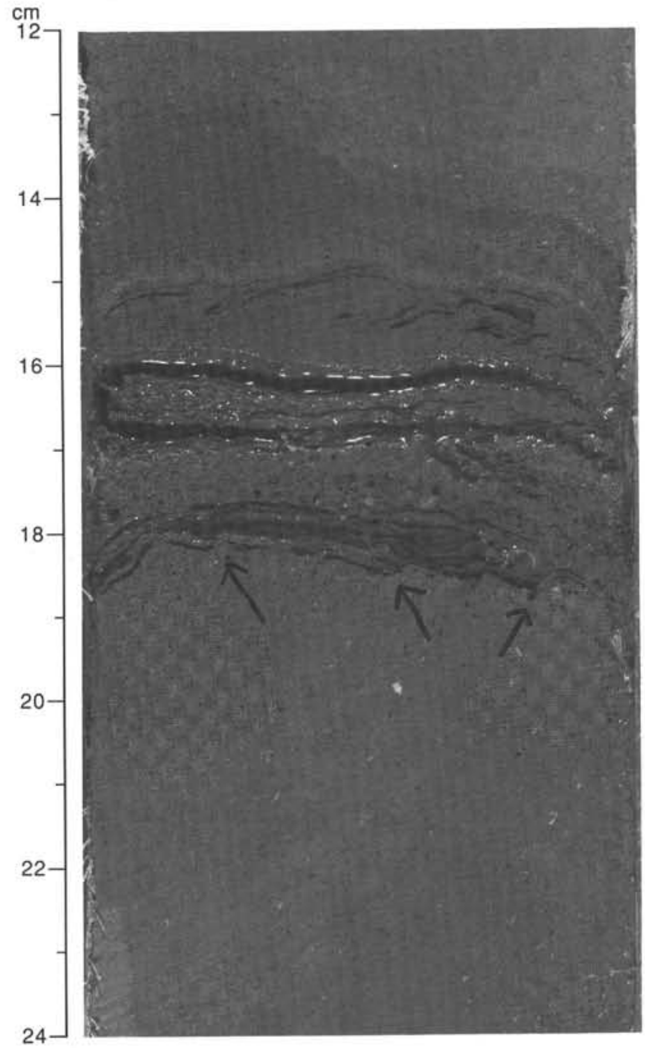

Figure 9. Core photograph, sand and sandy silt interbeds within Subunit IA, with thin internal laminations, crossbeds, and scoured bases. The base of the lower sand is offset by normal growth faults that die out upward (arrows; Section 141-863A-2H-2, 12–24 cm).

concentrated than in Subunit IA. Pyrite occurs throughout Subunit IB as fine disseminated grains and small nodules (1–4 mm in diameter). Thin sand beds (<0.5 cm) at widely spaced intervals exhibit laminations and basal scours (Fig. 13). Section 141-863A-8X-3, 60–100 cm, shows a slight coarsening-upward trend from clayey silt to clayey sand with relatively gradational lower and upper contacts to silty clay. The lower part of Subunit IB, below 85.1 mbsf (Cores 141-863A-10X and -11X) is only partially consolidated, consisting of silty clay to sandy silty claystone and minor silty sandstone.

Sand and silt-sized components include quartz, feldspar, rock fragments, biotite, as well as variably vesicular and microlitic colorless, brown/tan, and black tachylitic volcanic glassy fragments. A diverse suite of heavy minerals includes opaques, amphibole, pyroxene, and epidote. Microfauna include nannofossils, foraminifers, diatoms, radiolarians, sponge spicules, and silicoflagellates. Nannofossils are locally recrystallized to micrite.

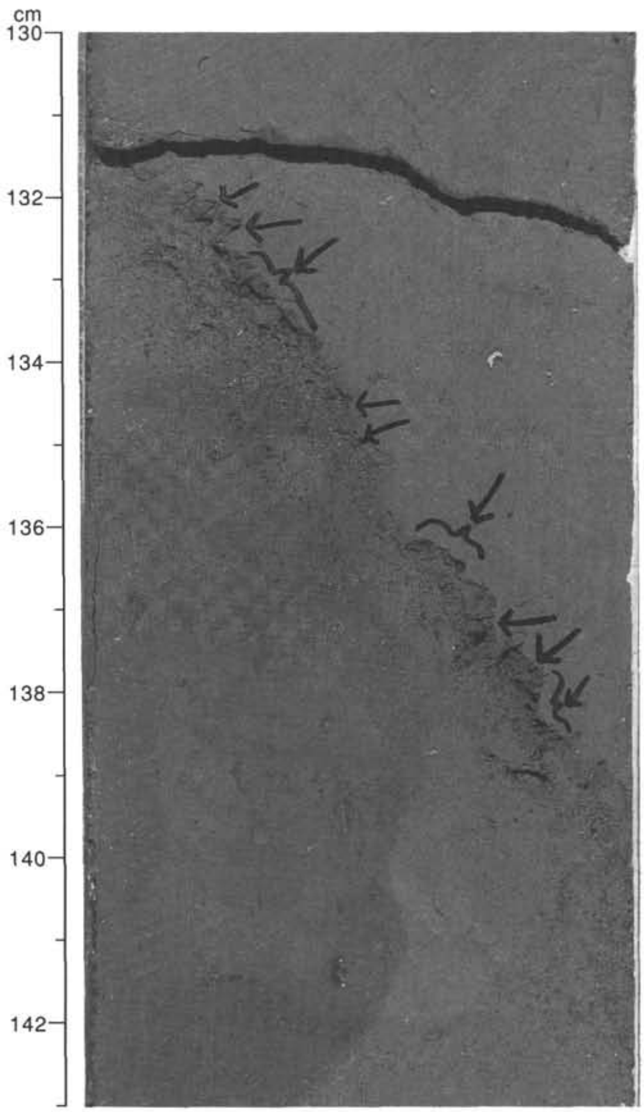

Figure 10. Core photograph, layer of sand within Subunit IA containing nodules (1–3 mm diameter) of pyrite (arrows). Sand bed is overlain by light gray silty clay; below the sand is a 2-cm-thick interval of sandy silty clay that fines downward into clayey silt. Mottled color of silt and the dispersion of sand below the interbed are probably due to bioturbation (Section 141-863A-2H-1, 130–143 cm).

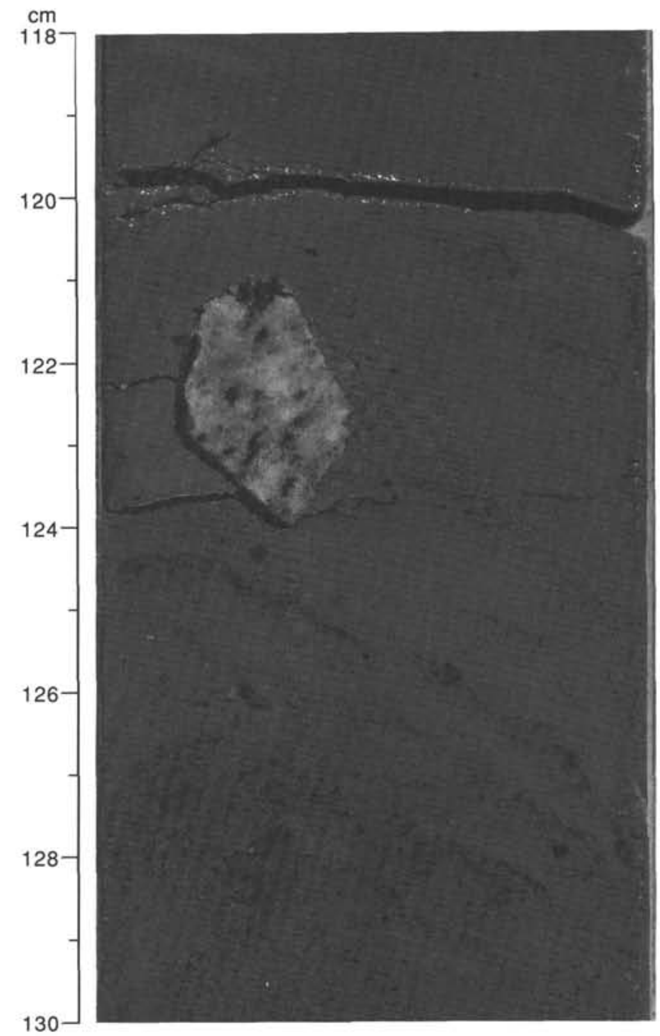

Figure 11. Core photograph, diorite dropstone within sandy clayey silt of Subunit IA. The interval below the dropstone consists of somewhat dispersed sand within clayey silt, and contains numerous pyrite concretions 1–3 mm in diameter (Section 141-863A-2H-3, 118–130 cm).

Lithologic Unit II (Cores 141-863A-12X through -31X and 141-863B-1X through -49R; age: early and late Pleistocene; stratigraphic order inverted, with early Pleistocene lying above late Pleistocene, the boundary occurring between 290 and 325 mbsf; depth: 104.4–742.9 mbsf)

The top of Unit II is marked by a zone of no recovery at 104.4–123.2 mbsf. Below 123 mbsf, over a vertical distance of about 15 m, the cores change from partially lithified to well-lithified sandstone with an overall decrease in clay content (Fig. 4). Bedding attitude is dominantly steep to vertical where observed, although some intervals of gently to moderately inclined bedding are present (see Structural Geology section, this chapter). Because of the steepness of bedding throughout much of Unit II, it is likely that the stratigraphic thickness penetrated is actually much less than the 638.5 m drilled. Various estimates of minimum stratigraphic thickness for Unit II range from 60 to 200 m, calculated from multiple sand layers within single cores.

Unit II consists almost entirely of slightly- to moderately-bioturbated sandy silty claystone, siltstone, and relatively thin beds of fine- to medium-grained sandstone. Unit II is divided into three subunits on the basis of subtle compositional changes. Subunit IIA is much less clay-rich than the overlying Unit I, and shows a general trend of decreasing clay downward (Fig. 4); it is more massive and less cemented than the rest of Unit II. Subunit IIB has more nannofossil-rich interbeds and exhibits an increase in clay downward (Figs. 4 and 5A); Subunit IIC contains much less clay than the base of IIB (Fig. 4) and has more carbonate cement as well as a significant increase in smectite and zeolites (Figs. 5B and 5C). Volcanic glass, ubiquitous throughout Holes 863A and 863B, decreases in Subunit IIC (Fig. 5D).

Subunit IIA (Cores 141-863A-12X to -24X; age: late(?) to early Pleistocene; depth: 104.4–220.3 mbsf)

Subunit IIA consists mainly of olive-gray (5Y 3/2) fine-grained sandstone to sandy siltstone and sandy silty claystone, with rare interbeds of yellowish brown (10YR 4/2) nannofossil

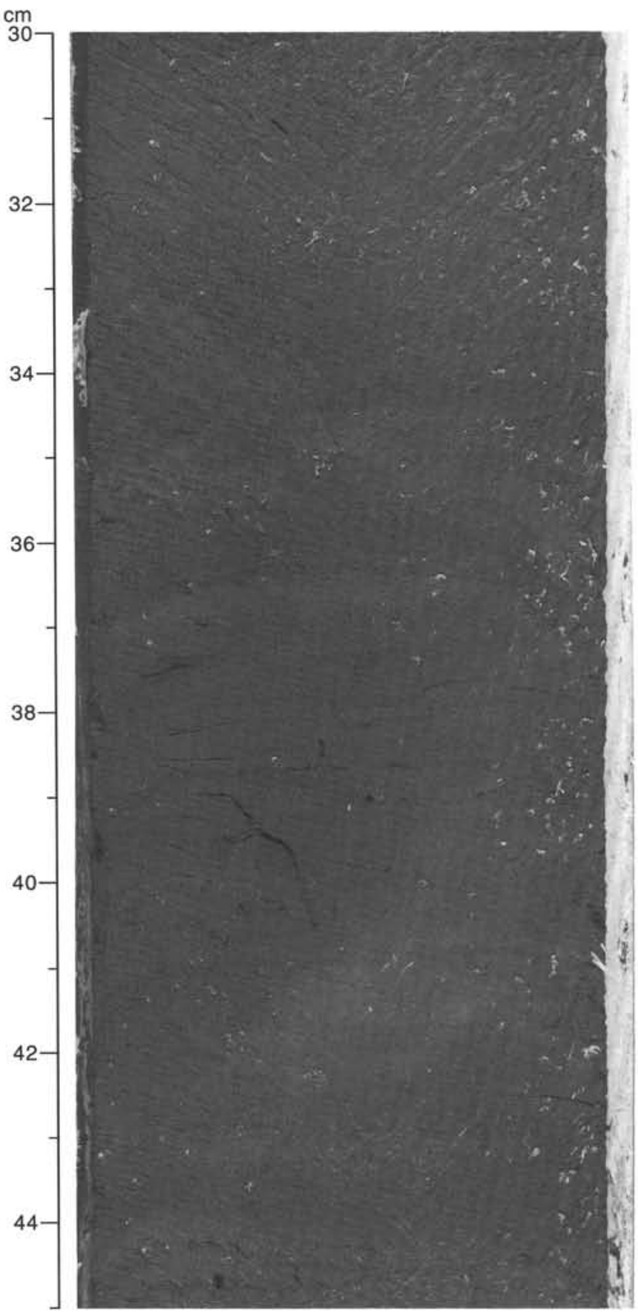

Figure 12. Core photograph, clayey silt and silty clay of Subunit IB. The light gray clayey silt bed at 32–39 cm is internally laminated, has a sharp base, and coarsens slightly upward at its top. The dark laminae within this bed are sulfide/organic-rich concentrations. The silt is interbedded with mottled, slightly bioturbated laminated to thinly bedded silty clay. A number of normal faults with small separations cut the sediment (Section 141-863A-7X-2, 30–45 cm).

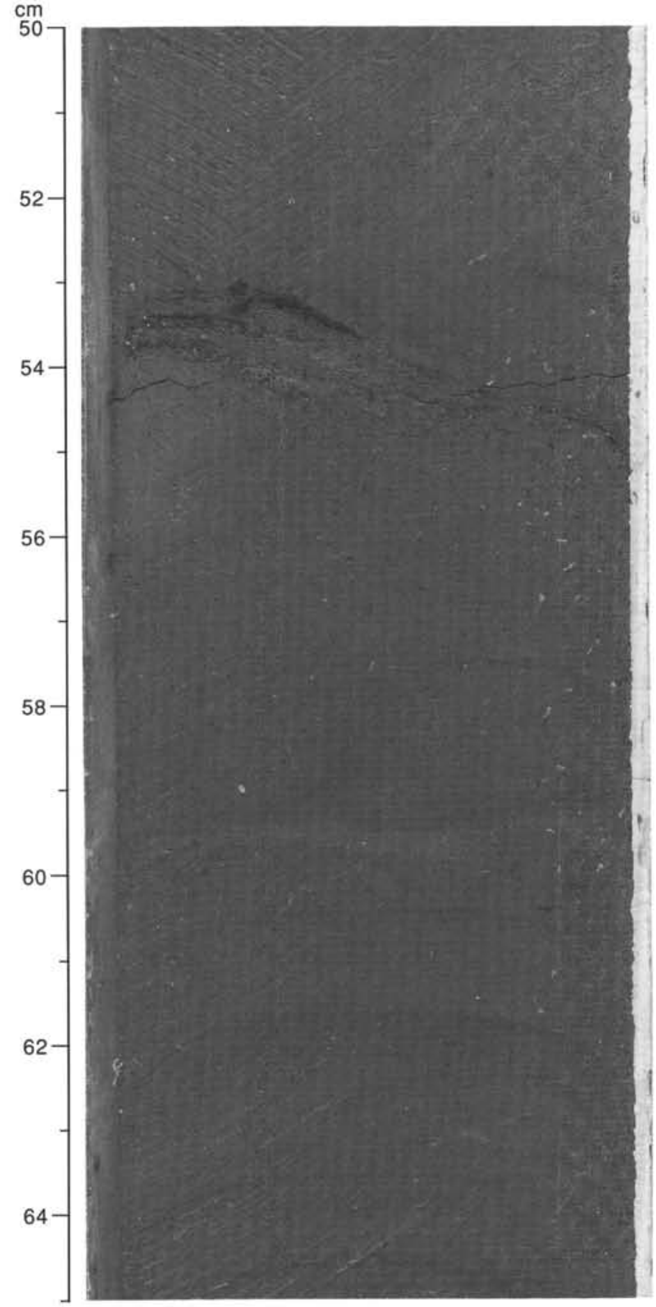

Figure 13. Core photograph, thin sand interbed within clayey silt/silty clay of Subunit IB. The thin dark lines bowed downward at core margins are boundaries of drilling biscuits (Section 141-863A-7X-1, 50–65 cm).

chalk. Sandstone grains are angular to rounded, and some sandstone beds are thinly laminated (Fig. 14) to cross-laminated. In Cores 141-863A-20X and -21X, thin (5–10 cm) layers of granule to pebbly conglomerate and pebbly sandstone are interbedded with medium to fine sandstone and sandy siltstone. The angular clasts were probably formed by in-situ brecciation. Textural grading and fining-upward sequences are preserved in some of the less drilling-disturbed intervals. The subunit is sparsely bioturbated and contains rind burrows lined with sponge spicules recognizable as white rings and ovals that contrast with the darker rock around them.

Compared to the rest of Unit II, Subunit IIA is rather massive. It is less cemented than the rest of Unit II and contains less authigenic pyrite. Sand and silt-sized components include quartz, feldspar, rock fragments, biotite, as well as colorless, brown/tan and black, tachylitic volcanic glassy fragments. A diverse suite of heavy minerals includes opaques, garnet, amphibole, pyroxene, and epidote. Microfauna include nannofossils, foraminifers, and sponge spicules. The sandstone interval in Section 141-863B-14X-1 is pervasively cemented by carbonate.

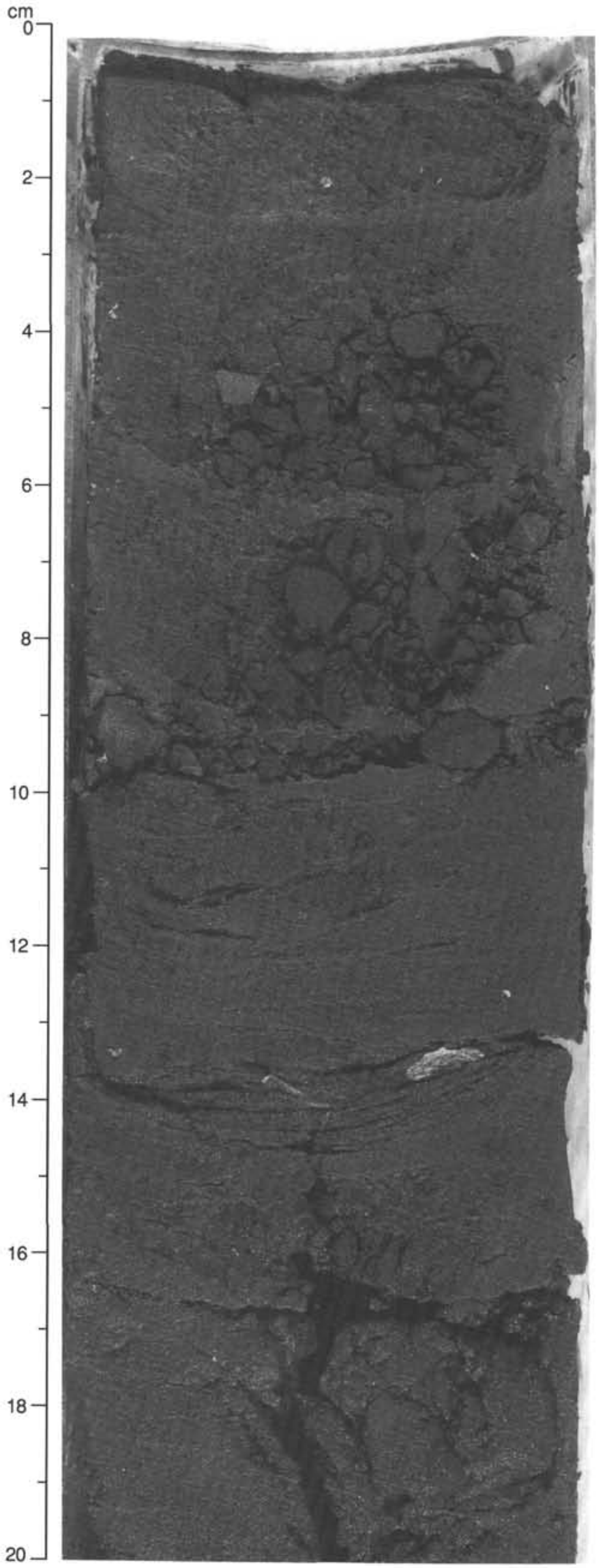

Figure 14. Core photograph, thinly laminated to cross-laminated sandstone of Subunit IIA, crossed by drilling biscuit boundaries at 3- to 5-cm intervals. The better cemented sandstone has broken into semicoherent drilling breccia between 3.5 and 9.5 cm (Section 141-863A-18X-CC, 0–20 cm).

Subunit IIB (Cores 141-863A-24X to -31X and 141-863B-1X to -13R; age: early to late Pleistocene [stratigraphy inverted]; depth: 220.3–405.5 mbsf)

Subunit IIB differs from Subunit IIA mainly in having interbeds with 10%–20% nannofossils, and in having well-developed sedimentary structures. Overall, Subunit IIB consists of olive gray (5Y 3/2 to 4/1) interbeds of fine- to medium-grained sandstone to sandy siltstone and sandy silty claystone with nannofossils. With increasing sub-bottom depth, the sandstone becomes more carbonate-cemented. Below 335 mbsf the calcareous microfossils are recrystallized. A concretion of pyrite occurs in Section 141-863A-26X-1 at 45 cm.

Steeply inclined bedding occurs in Cores 141-863A-29X to -31X, and throughout Subunit IIB the bedding is generally steeply inclined to vertical. The sedimentary structures that characterize this subunit take the form of sandstone and siltstone beds 15–20 cm thick in fining-upward sequences or thin (1–2 cm), medium- to fine-grained, graded sandstones with sharp bases and bioturbated tops (Fig. 15). Typically, these consist of olive gray to olive black (5Y 3/2 to 2/1) sandstone or sandy siltstone with sharp, scoured bases. Fine laminae and cross-laminae are preserved within the sandstone or sandy siltstone (Fig. 16). The intervals of well-preserved sedimentary structures are interbedded with intervals of bioturbated sandy silty claystone. In Core 141-863B-4X, laminated sandstone grades to siltstone and to clayey siltstone within the core diameter. A typical sequence of laminated to cross-laminated fine-grained sandstone that fines to silty claystone and then to claystone is seen in Core 141-863B-8N.

Bioturbation also increases within Subunit IIB, as do clots of spicules and rind burrows 0.2–1.0 cm in diameter (Fig. 17). The rind burrows are lined with light gray sponge spicules and filled with olive gray mud. *Chondrites* burrows are filled with dark gray to olive gray sand or mud (Fig. 18). Shell fragments are present in Cores 141-863B-4X, -11R, and -12R.

Sand and silt-sized components of Subunit IIB include quartz, feldspar (fresh to very altered), a wide variety of rock fragments including sedimentary, chert, and schist fragments, biotite, and colorless, brown and black, tachylitic volcanic glassy fragments, most of which are microlitic and/or variably vesicular. A diverse suite of heavy minerals is also present that comprises opaques (including framboidal pyrite), amphibole, garnet, sphene, epidote, zircon, and pyroxene. Microfauna include foraminifers, nannofossils, radiolarians, and sponge spicules. Some micrite (recrystallized nannofossils?) and rare bioclasts are also present. Well-rounded quartz grains present in one slide suggest an element of sedimentary recycling.

Deformation increases below 325 mbsf with bedding becoming steeply inclined or vertical; in some cases the same stratigraphic interval persists along the length of the core for 25 cm.

Subunit IIC (Cores 141-863B-14R to -49R; age: late Pleistocene; depth: 405.5–742.9 mbsf)

Subunit IIC consists of bioturbated, olive black to olive gray (5Y 2/1 to 3/2) claystone, silty claystone, and sandy silty claystone with interbeds of fine- to medium-sized sandstone (Figs. 19 through 21). Nannofossils are common, especially in the finer-grained rocks (Fig. 5A). Burrows are filled with gray (N4 to N7), calcareous-cemented silt and sand containing pyrite (Fig. 19), and include *Chondrites* and rind burrows. The siltstone and claystone contain foraminifers and nannofossils that have been recrystallized to micrite. Concentrations of sponge spicules are commonly associated with the bioturbated intervals (Fig. 19). Shell fragments occur in Core 141-863B-21R. Veins filled with calcite and other authigenic minerals are common throughout the

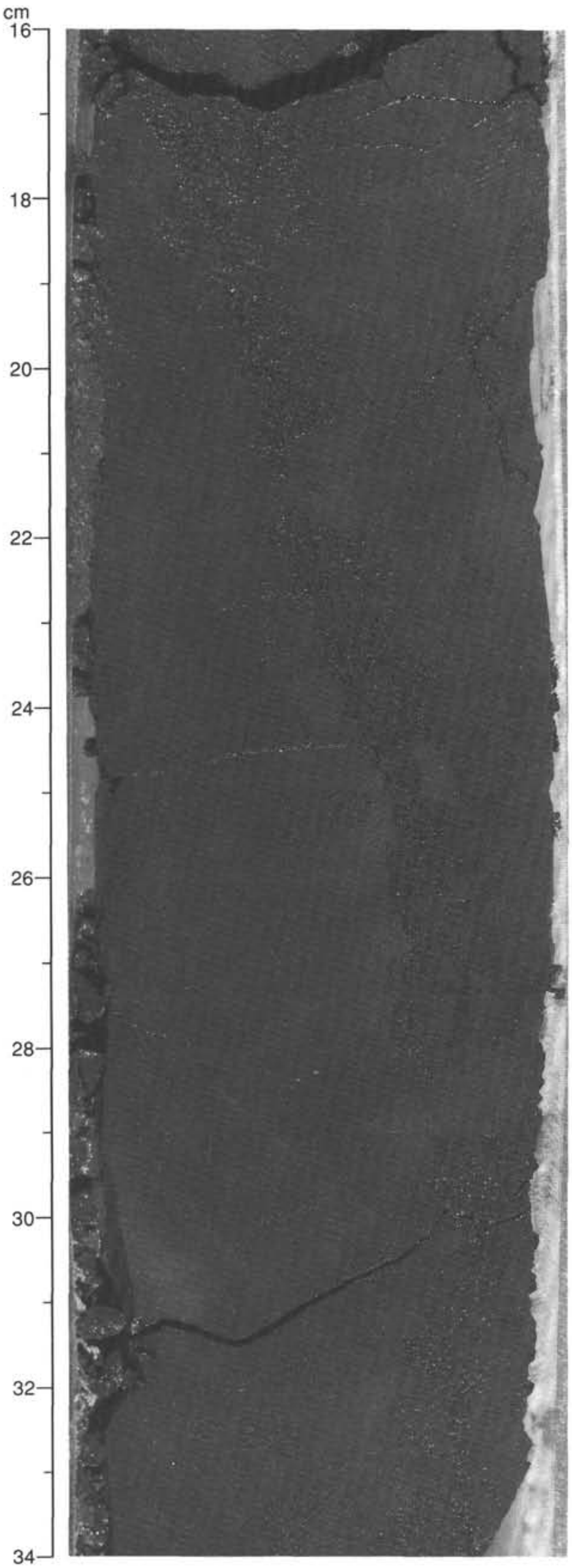

Figure 15. Core photograph, bioturbated medium- to fine-grained sandstone bed of Subunit IIB with a sharp scoured base and textural fining (to the right). Irregular bed contact is due to bioturbation. The bed is steeply inclined and extends continuously for more than 25 cm of the core length (Section 141-863B-7N-2, 16–34 cm).

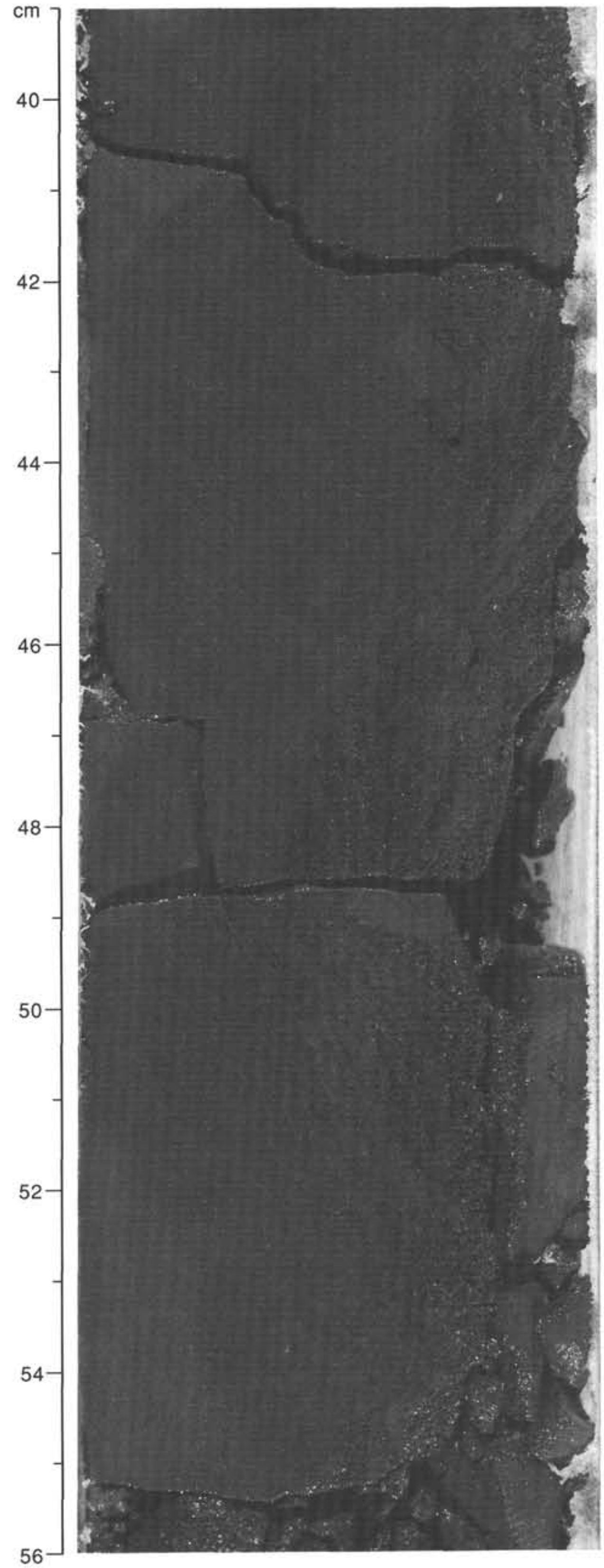

Figure 16. Core photograph, cross-laminated medium- to fine-grained sandstone bed of Subunit IIB. The sandstone grades upward (to the left) into sandy siltstone with mud-filled burrows (50–55 cm); a small fault at 42–47 cm exhibits reverse separation (Section 141-863B-8N-1, 39–56 cm).

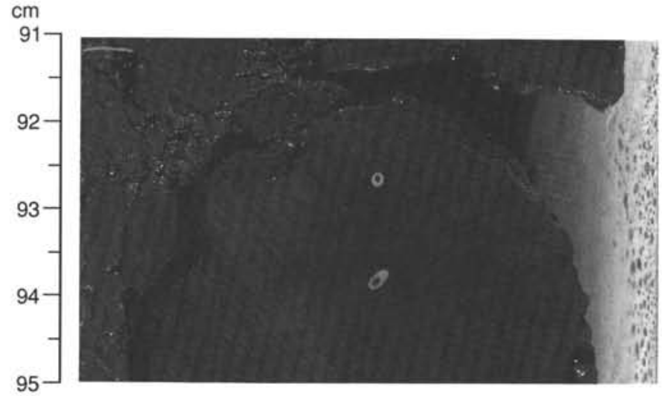

Figure 17. Core photograph, sponge-spicule-lined rind burrows in Subunit IIB. Similar features are observed throughout Subunit IIC (Section 141-863A-30X-1, 91–95 cm).

subunit. Disseminated pyrite occurs in trace amounts throughout the subunit, and pyrite concretions are common.

Generally, the sandstone interbeds range from 2 to 10 cm in total thickness. They are massive to laminated or cross-laminated and grade upward into fine silt and claystone. The bases of sandstone beds exhibit shallow to relatively deep scour structures and some load structures (e.g., Cores 141-863B-32R, -39R and -44R, see Figs. 20 and 21). Sandstone interbeds can be locally carbonate cemented (Core 141-863B-36R), especially in the coarsest portions above the scoured contacts (Core 141-863B-44R, see Fig. 20). In Core 141-863B-32R, the 2- to 5-cm-thick sandstone intervals are arranged into five distinct beds interbedded with 20-cm-thick intervals of fine-grained sediments that probably represent a typical succession of layers in Subunit IIC. Wavy-laminated sandstone occurs in Sections 141-863B-20R-3 and -32R-5. Sandstone in Section 141-863B-21R-1 shows trends from horizontally laminated medium-grained sandstone to wavy-laminated and cross-laminated fine-grained sandstone. The sandstone is fine- to coarse-grained, and occurs as beds 2 to 3 cm thick with sharp scoured bases, that grade upward into intensely bioturbated sandy siltstone. Some sandstone beds also have isolated burrows starting at their bases, suggesting they may be "escape burrows" formed after rapid deposition of the layer (Fig. 21).

Section 141-863B-48R-3, 15–70 cm, shows in detail a typical fining-upward sequence of Subunit IIC, about 13 cm in total thickness (Fig. 22). It begins with cross-laminated fine-grained sandstone, 3 cm thick. The lower contact with silty claystone is slightly scoured and some massive sandstone occurs above the contact. The succeeding very fine-grained sandstone/siltstone interval is convolute to horizontally laminated. The uppermost 7 cm in this sequence is massive silty claystone.

In some cores, bedding is vertical, with individual layers continuing lengthwise for over 200 cm. Some of the sandstone beds can be shown to be overturned because of the excellent preservation of top-specific sedimentary structures within the sandstone beds. Although the rocks are not greatly deformed, some bedding surfaces are tectonically modified (see Structural Geology section, this chapter).

XRD Results

Forty-three samples were selected from Site 863 cores for X-ray diffraction analysis. Bulk powders (25 samples) and clay-size separates (18 samples) were prepared and analyzed on board with the *JOIDES Resolution's* Phillips ADP 3520 X-ray diffractometer.

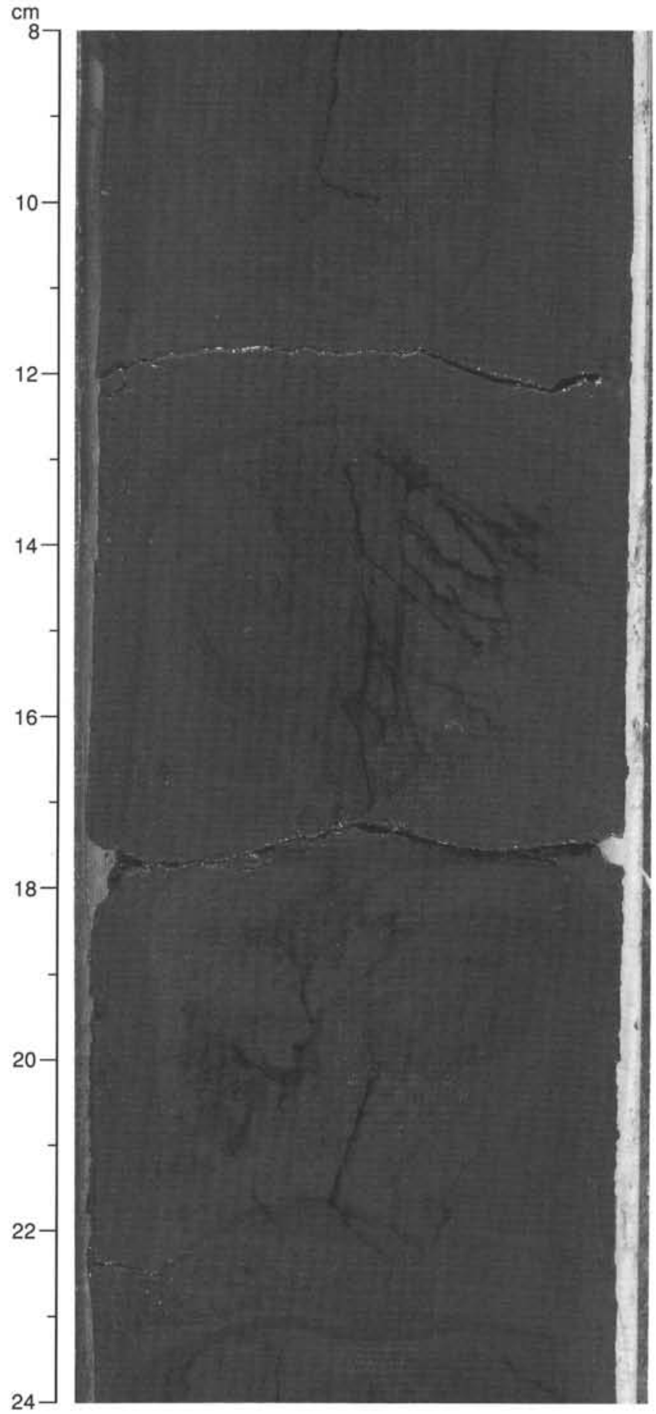

Figure 18. Core photograph, large burrows filled with dark olive-gray fine- to medium-grained sandy material are a characteristic feature of Subunit IIB. Drilling biscuit boundaries are at 13, 18, and 23 cm (Section 141-863A-30X-2, 8–24 cm).

In sediments from Holes 863A and 863B, the dominant phases present in all of the bulk samples are quartz and feldspar with only small fluctuations in their abundance (Table 4). All samples have a minor to trace amount of hornblende. Calcite is rare overall, being present only in trace to minor amounts in cores below Core 141-863A-20X (182 mbsf). However, calcareous material is locally concentrated in burrow fillings and veins, as well as in

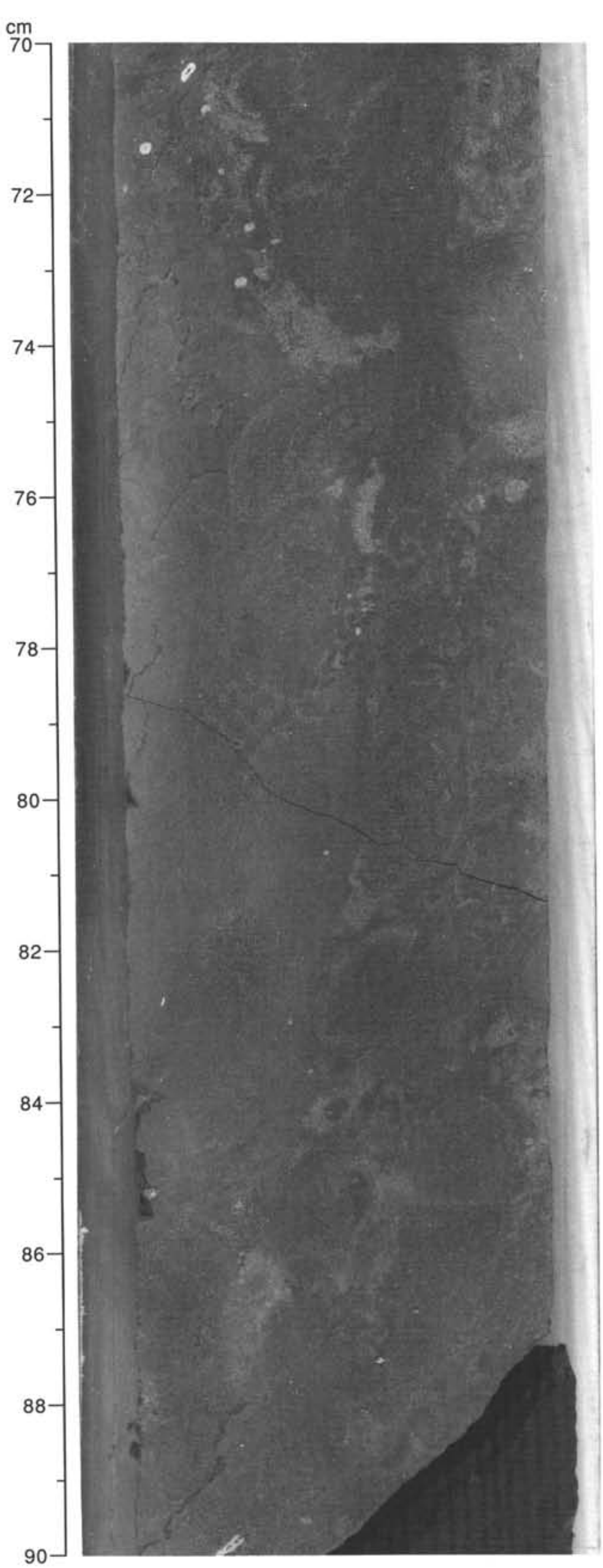

Figure 19. Core photograph, intensely bioturbated sandy siltstone of Subunit IIC; burrows are filled with gray, carbonate-cemented, pyrite-bearing sandstone. Bedding orientation is vertical (Section 141-863B-18R-1, 70–90 cm).

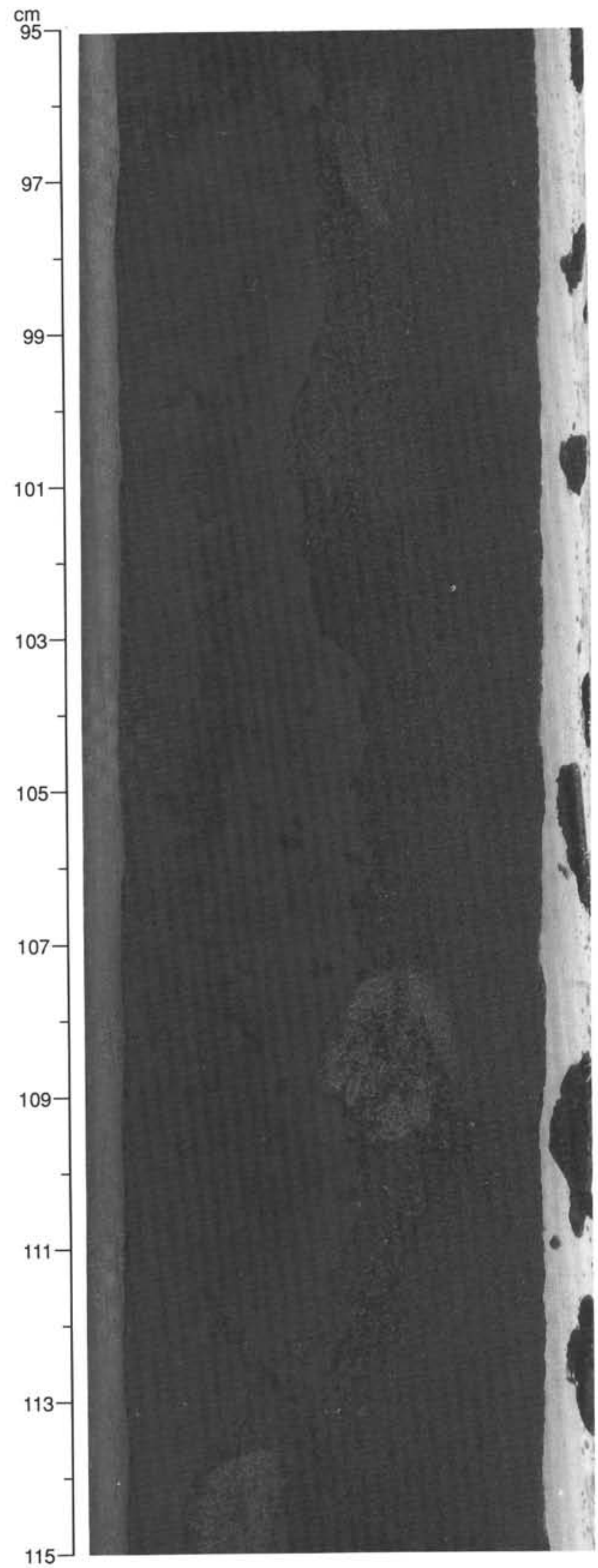

Figure 20. Core photograph, sandstone layer in Subunit IIC showing shallow to relatively deep scour structures and some load structures. Patchy zones of light-gray calcite cement occur in the coarsest sandstone at its base. Bedding orientation is nearly vertical in the core reference frame, with top to the right (Section 141-863B-44R-3, 95–115 cm).

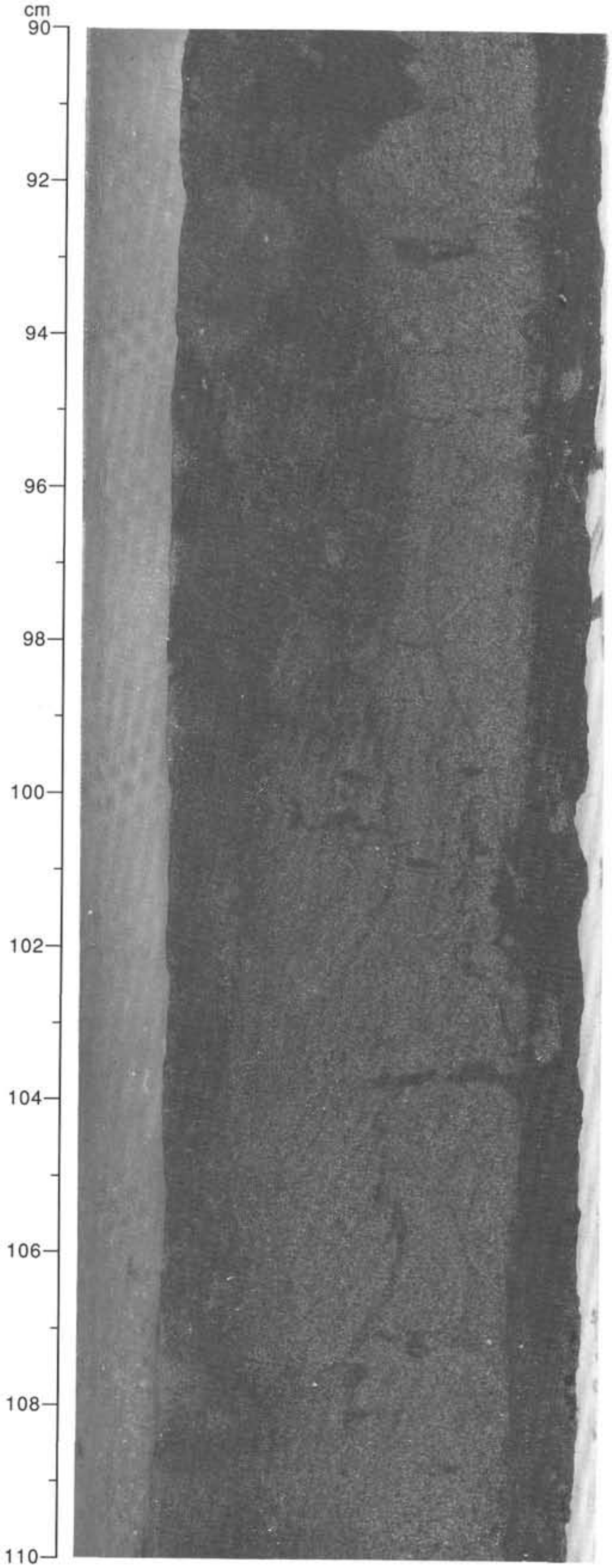

Figure 21. Core photograph, sandstone bed exhibiting upcore current directions. Mud-filled burrows are probably escape burrows created after sudden deposition of turbidite (Section 141-863B-39R-2, 90–110 cm).

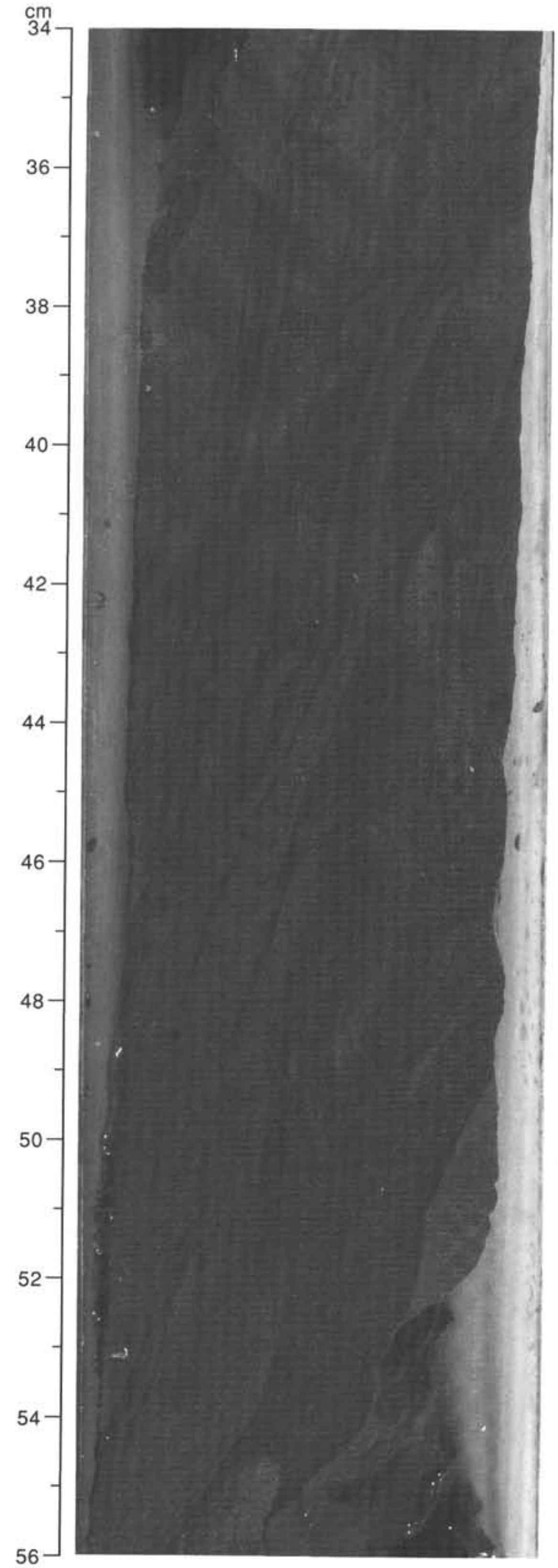

Figure 22. Core photograph, a typical fining-upward sequence in Subunit IIC that begins with cross-laminated fine-grained sandstone at the lower right. The basal contact is slightly scoured and is overlain by very fine-grained sandstone-siltstone that is convolute to horizontally laminated. The uppermost 7 cm is massive silty claystone (Section 141-863B-48R-3, 34–56 cm).

Table 4. X-ray diffraction mineralogy of sediments, Holes 863A and 863B.

Core, section, interval (cm)	Depth (mbsf)	Nonclay mineral phases						Phyllosilicates		
		Quartz	Feldspar	Hornbld.	Calcite	Amorph.	Pyrite	Smectite	Chlorite	Illite
141-863A-										
1H-4, 11–13	4.61	4	3	2	0	2	1	0	4	4
5H-2, 110–113	39.70	4	2	1	0	2	0	0	4	4
5H-2, 113–115	39.73	4	2	1	0	2	0	0	4	4
9X-1, 12–17	75.52	4	3	2	0	2	1	0	4	4
10X-CC, 3–5	85.13	4	3	1	0	1	0	0	4	4
15X-CC, 26–28	133.66	4	3	2	0	1	1	0	4	4
17X-CC, 29–32	153.34	4	3	2	0	2	0	0	4	4
18X-CC, 26–28	162.66	4	3	2	0	2	0	0	4	4
20X-CC, 13–18	181.73	4	4	2	0	1	0	0	4	4
24X-CC, 14–17	221.01	4	3	2	1	2	0	0	4	4
25X-1, 19–21	229.99	4	3	1	1	2	0	0	4	4
28X-1, 57–62	259.37	4	4	2	0	2	0	0	4	4
30X-2, 21–23	279.81	4	3	2	1	2	0	0	4	4
31X-CC, 21–23	288.49	4	3	1	0	2	1	0	4	4
141-863B-										
5X-CC, 3–5	335.63	4	4	2	1	2	1	0	4	4
9X-CC, 16–18	361.56	4	3	2	2	2	1	0	4	4
10R-1, 13–15	371.13	4	3	2	0	2	1	0	4	4
15R-2, 76–79	417.46	4	3	2	0	2	0	0	4	4
20R-CC, 4–6	466.58	4	3	2	1	2	1	3	4	3
25R-3, 110–112	515.80	4	2	2	1	2	1	4	3	3
31R-5, 56–58	576.16	4	3	2	2	2	1	4	4	3
35R-2, 68–70	609.88	4	3	1	0	2	1	4	4	3
40R-1, 15–17	656.05	4	3	1	0	2	0	4	3	3
43R-2, 27–29	686.57	4	3	2	0	2	1	4	2	0
49R-4, 93–95	738.63	4	3	2	2	2	1	4	3	3

Note: Numbers indicate: 4. dominant, 3. secondary, 2. minor, and 1. trace phases. 0 indicates phase absent.

localized patches of calcite-cemented sand (Fig. 20). Disseminated pyrite is found only in trace amounts. An unidentified amorphous phase is also present in all samples. The clay minerals likely to be present in the bulk samples are chlorite and illite, which appear to be present in roughly equal amounts. From Core 141-863B-20R to -49R (463.4–742.9 mbsf) the samples are dominated by smectite.

The separate analyses for clay minerals (Table 5) show that the main part of the fine fraction removed from sediments recovered in samples from Hole 863A and from Cores 141-863B-4X, -7N, and -10R in Hole 863B consists of illite and chlorite. The remaining portion (from 1% to 22%) consists of smectite. However, in sediments from Core 141-863B-15R (415.2 mbsf) and deeper cores, the fine fraction contains from 44% to 61% smectite (Fig. 23). The reason for this higher content of smectite in the lower part of Hole 863B is not obvious. Cristobalite, amphibole (hornblende), quartz, feldspar, and an amorphous phase are present in the fine fraction of all samples in minor amounts.

Diagenesis

In Subunit IB the black sulfide/organic-rich zones are dominated by diagenetic opaques including greigite(?) (see Paleomagnetism section, this chapter) and pyrite. Evidence of diagenesis, in addition to the authigenic opaques, includes dissolution of amphibole (cocks-comb structures), local micritization/recrystallization of nannofossils, and minor replacement of glassy fragments by zeolites. Rare, rounded, clusters of submicroscopic zeolites(?) are also present. The first carbonate cement occurs in Subunit IB at 75.5 mbsf (Section 141-863A-9X-CC, with associated pyrite). Within Subunit IC, nannofossils are locally recrystallized to micrite.

Diagenesis and cementation increase with sub-bottom depth throughout Unit II. One sandstone interval is pervasively cemented by carbonate (Section 141-863B-14R-1, 65 cm). Diagenetic observations in Subunit IIB include dissolution of amphibole, producing cocks-comb textures and alteration of glassy volcanic fragments to opaques and zeolites(?). Some sandstone beds are cemented by carbonate.

In Subunit IIC, volcanic glassy fragments are altered/replaced by clay minerals, carbonate, and zeolites(?). Nannofossils are recrystallized to micrite and sponge spicules are replaced by zeolites(?). Pyroxene and amphibole grains show evidence of dissolution. The sandstones are cemented by carbonate, zeolites (?), and in some instances clay minerals (thin birefringent rims). Veins filled with calcite, pyrite, silica, and zeolites are common throughout Subunit IIC. An open cavity lined with euhedral crystals of calcite and quartz occurs at 570 mbsf in Core 141-863B-31R (Fig. 24).

Interpretation

Unit I shows characteristics of hemipelagic background sedimentation associated with bottom-current activity and some slope-apron processes. Downhole facies distribution is somewhat variable. The alternating pyrite/organic-rich intervals and nannofossil-rich intervals may represent cycles of reducing and oxidizing environments, possibly due to fluctuations of paleo-ceanographic parameters such as the carbonate compensation depth (CCD) or oxygen-minimum zone. Sands in Unit I may be contourites or fine-grained turbidites. The slight coarsening-upward trend in clayey silt to clayey sand of Subunit IB may indicate events of rapid grain deposition from suspension. Subunit IA appears to be a slope apron that is being deposited very slowly or is being eroded, because the Quaternary section is either very thin (<18 cm) or entirely absent. The lack of post-upper Pleistocene microfossils at the top of Unit I is consistent with the hypothesis that this region is undergoing active tectonism and uplift.

The sedimentary structures found in Unit II are characteristic of outer fan lobes. The sandstones and sandy siltstones of Unit II represent turbidites, with partial Bouma sequences present throughout the unit (e.g., Bouma sequence in Core 141-863B-48R, Fig. 22). Distinct turbidite beds exhibit some relatively complete Bouma sequences but generally the beds lack the basal or middle parts of the Bouma sequence. For example, the sedimentary sequence in Core 141-863B-48R is interpreted to have formed in two distinct events. Scouring of massive silty clay occurred first. After that, a relatively complete Bouma sequence

Table 5. X-ray mineralogy of clay fractions, Holes 863A and 863B.

Core, section interval (cm)	Depth (mbsf)	Smectite (%)	Illite (%)	Chlorite (%)	Cristobalite*	Amphibole*	Quartz*	Feldspar*	Amorphous*
141-863A-									
1H-3, 130–132	4.30	5	53	42	TR	TR	M	M	M
5H-2, 116–118	39.76	1	59	33	TR	TR	M	M	M
10X-CC, 5–7	85.15	10	43	47	TR	TR	M	M	M
14X-2, 19–21	124.89	22	42	36	TR	TR	M	M	M
15X-CC, 28–30	133.68	17	47	36	TR	TR	M	M	M
21X-CC, 21–23	192.01	16	45	39	TR	TR	M	M	M
25X-1, 21–23	230.01	18	34	48	TR	TR	M	M	M
30X-2, 15–17	279.75	13	50	37	TR	TR	M	M	M
141-863B-									
4X-3, 76–78	329.66	13	41	46	TR	TR	M	M	M
7N-1, 31–33	355.21	16	48	36	TR	TR	M	M	M
10R-1, 15–17	371.15	18	40	42	TR	TR	M	M	M
15R-2, 76–79	417.46	57	23	20	0	0	TR	M	M
20R-CC, 4–6	466.58	61	22	17	TR	TR	M	M	M
25R-3, 112–113	515.82	54	20	26	TR	TR	M	M	M
31R-5, 58–59	575.18	48	25	27	TR	TR	M	M	M
35R-2, 66–68	609.86	44	30	26	TR	TR	M	M	M
40R-1, 17–19	656.07	54	23	23	TR	TR	M	M	M
49R-4, 93–95	738.63	26	34	40	TR	TR	M	M	M

Note : TR = trace amounts, M = minor amounts.
* Relative abundance

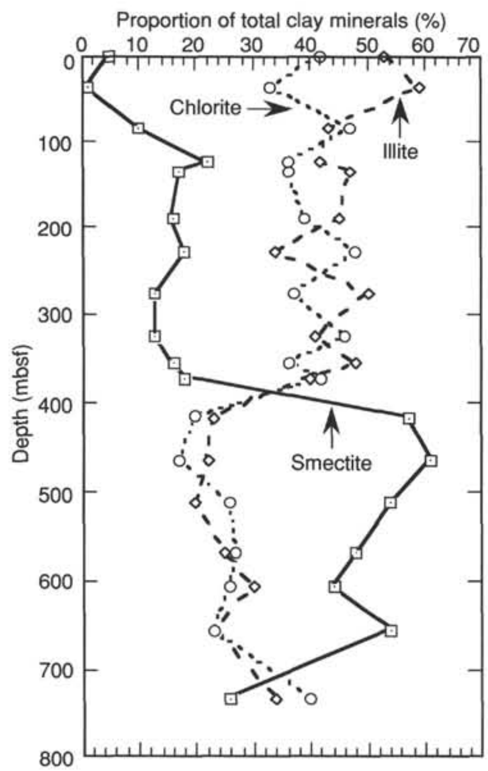

Figure 23. X-ray diffraction analyses of chlorite, illite, and smectite as percentage of total clay minerals. Near the top of Subunit IIC at 400 mbsf, the proportion of illite and chlorite drops off and smectite increases.

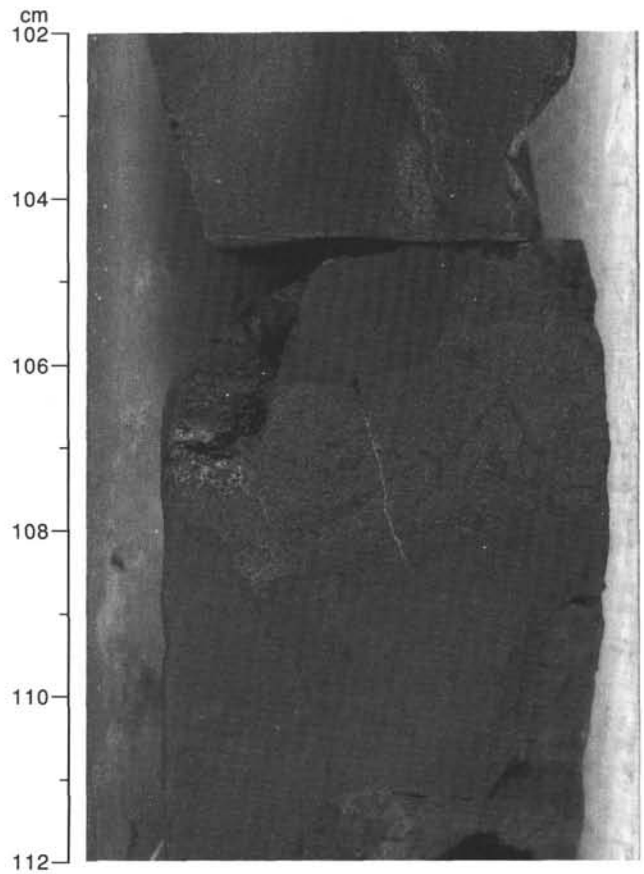

Figure 24. Open cavity lined with euhedral calcite and quartz crystals (105–106 cm), in sandstone and siltstone of Subunit IIC. A white calcite vein cuts the burrowed sandstone bed; sandstone is light gray from calcite cementation (Section 141-863B-31R-1, 102–112 cm).

was deposited as scour-fill. Massive sandstone (*Ta* turbidite) may be seen as a minor component and the sequence begins predominantly with cross-laminated to convolute-laminated fine-grained sandstone (T_c) succeeded by laminated siltstone and claystone (T_d). The uppermost massive silty claystone represents the low-density tail of this one distinct turbidity event (T_e). The sandy silty claystones in Subunit IIC were affected by post-depositional bioturbation mixing of sand and thin sand layers with silty clay and clay. Poor preservation of sedimentary structures is a function of the intensity of the bioturbation overprint.

Interpretation of current indicators in beds such as those shown in Figures 21 and 22 may permit the refinement of a depositional model for these units, if formation microscanner sonde (FMS) results permit bedding to be geographically oriented.

BIOSTRATIGRAPHY

Introduction

Preservation of siliceous and calcareous microfossils at Site 863 is similar to that of Site 859. Diatoms are preserved, albeit poorly, only in the upper 47 mbsf and two isolated occurrences below that depth, and could provide no age information. Radiolarians are preserved in either moderate or poor condition in the upper 74 mbsf, with barren zones and sporadic occurrences below. Only nine samples provided useful radiolarian ages at this site. Low diversified assemblages of well- to moderately-preserved planktonic foraminifers are observed in the upper 85.1 mbsf; they are poorly preserved or absent below 85.1 mbsf. The entire section drilled at Site 863 has been assigned to the *Globoconella inflata* Zone. Age determinations based on calcareous nannofossils were obtained by the shore-based studies of C. Müller. A summary of the biostratigraphy of diatoms, radiolarians, foraminifers, and calcareous nannofossils at Site 863 is presented in Figure 25.

Diatoms

Diatoms were encountered in the seven uppermost core-catcher samples at Site 863 with the exception of the sample from Core 141-863A-6H, which was barren. Large-sized specimens of *Coscinodiscus marginatus* were observed in the slide prepared for radiolarian analysis and thus concentrated in particles larger than 63 μm. There were traces of diatoms observed in Sample 141-863A-28X-CC. The diatom assemblages observed in Samples 141-863A-1H-CC through -7H-CC are poorly preserved and are dominated by broken valves of large and robust non-age-diagnostic species (e.g., *C. marginatus, Hemidiscus karstenii,* and *Thalassiosira eccentrica*). These are rare in all of these samples. All other cores were barren of diatoms. These circumstances make it very difficult or impossible to assign any ages.

Radiolarians

At Site 863, moderately preserved radiolarians are found down to Sample 141-863A-4H-CC (37 mbsf). They are followed by poorly preserved radiolarian assemblages down to Sample 141-863A-9X-CC (85 mbsf). The remainder of the sedimentary sequence drilled at Site 863 is barren of radiolarians with a few exceptions; Samples 141-863A-30X-CC, -863A-31X-CC, -863B-4X-CC, and -863B-39R-CC (Fig. 25) contain a few poorly preserved taxa.

Sample 141-863A-1H-CC contains *Axoprunum angelinum* and *Cycladophora davisiana davisiana.* The following five additional samples were examined from Core 141-863A-1H: Samples 141-863A-1H-1, 18–20 cm; -1H-3, 37–39 cm; -1H-3, 66–68 cm; -1H-3, 107–109 cm; and -1H-3, 127–129 cm contain *A. angelinum, C. d. davisinana, C. robusta, C. conica, Spongaster tetras, and Spongurus pylomaticus.* There is a high probability that they can be assigned to the upper Pliocene to lowermost Pleistocene (RN12–RN14), when stratigraphic ranges of the above three species of *Cycladophora* in this geographic area can be clarified in shore-based research. Both C. robusta and C. conica appear to occur in the Pliocene only, although this has to be confirmed. It should be noted here that Sample 141-863A-1H-1, 18–20 cm contains *Botryostrobus* cf. *miralestensis.* Some of the specimens of this taxa are similar to *Botryostrobus miralestensis* whereas the rest are similar to *B. acquilonaris.* It appears that the two species may have continuous gradation in their morphology.

Sample 141-863A-2H-CC can be placed in the Pleistocene to Pliocene based on the presence of *C. d. davisiana.* Samples 141-863A-3H-CC through -7X-CC contain less age-diagnostic taxa such as *Cycladophora robusta, Spongurus pylomaticus,* and *Saccospyris antarctica.* Samples 141-863A-8X-CC and -9X-CC cannot be provided with relevant age information because they only contain non-age-diagnostic taxa. Samples 141-863A-10X-CC through -863B-49R-CC are barren of radiolarians with the exception of four samples mentioned above.

Sample 141-863A-30X-CC is assigned to the *A. ypsilon* Zone (RN14), the lower Pleistocene, because it contains a dozen or more of *A. angelinum.* The three specimens of *Botryostrobus* cf. *miralestensis* that are considered to be of late Miocene age in tropical regions (Nigrini, 1991) are either reworked or are of different stratigraphic range.

Sample 141-863A-31X-CC is also assigned to the *A. ypsilon* Zone (RN14) of the lower Pleistocene. It contains *A. angelinum.*

Planktonic Foraminifers

At Site 863 analysis of planktonic foraminifers provided an age assignment to the *Globoconella inflata* Zone for the whole sequence cored in Holes 863A and 863B. In Hole 863A (Table 6) 29 samples were studied, 76% of which contain planktonic foraminifers. In Hole 863B (Table 7) 46 samples were examined, 72% of which contain planktonic taxa. Low-diversity assemblages in the core-catcher samples from both holes show variable abundance and preservation. The abundances are categorized as common in Samples 141-863A-1H-CC and -2H-CC, and as few from Samples 141-863A-3H-CC through -9X-CC. Below Core 141-863A-9X, the abundance strongly decreases. The sediments between Samples 141-863A-10X-CC and -22X-CC are mostly barren and down to the deepest sample of Hole 863A at 297.3 mbsf they contain only small amounts of planktonic foraminifers. In Hole 863B, which continued the drilled sequence below the bottom of Hole 863A, most of the samples contain rare planktonic foraminifers.

Preservation is good or moderate from the top of Hole 863A through to Sample 141-863A-9X-CC, it becomes poorer down toward Sample 141-863A-31X-CC, and remains poor in most of the samples from Hole 863B. In general, the planktonic foraminifers found in the sediments below Sample 141-863B-6X-CC have been strongly recrystallized and often flattened and broken, making identification of taxa difficult. Silica has partly replaced the carbonate of the shells. Inner parts of the shells often show residues of calcite. In samples containing high amounts of diagenetic carbonate only fragments of specimens or silicified shells were found.

G. inflata displays a constant background in the samples of Site 863. In the poorly preserved assemblages it is often the only foraminifer left, or dominates the assemblages. It seems to be very resistant against dissolution due to the microcrystal structure of its shell. Recent specimens of G. inflata are encrusted by a smooth calcite deposit. This crust is finally smoothed by an additional layer that is finely crystalline, in contrast to other planktonic species (Hemleben et al., 1988) and preserves the specimens in the sediments better than other taxa of planktonic foraminifers. G. inflata indicates temperate water of the southern Transition Zone between cold-water and warm-water regions (Be and Tolderlund, 1971), therefore the paleotemperatures of the sequences at Site 863 can be generally characterized as temperate.

Benthic Foraminifers

Benthic foraminifers are contained in 85% of the samples of Hole 863A (Table 8) and in 65% of the samples of Hole 863B (Table 9). Their abundances are categorized as common or few in the upper sequence drilled in Hole 863A down to Sample 141-863A-9X-CC at 85.1 mbsf. Below this interval they become rare throughout the remaining sequence of Site 863. The Holocene occurrence of Uvigerina peregrina, Bulimina mexicana,

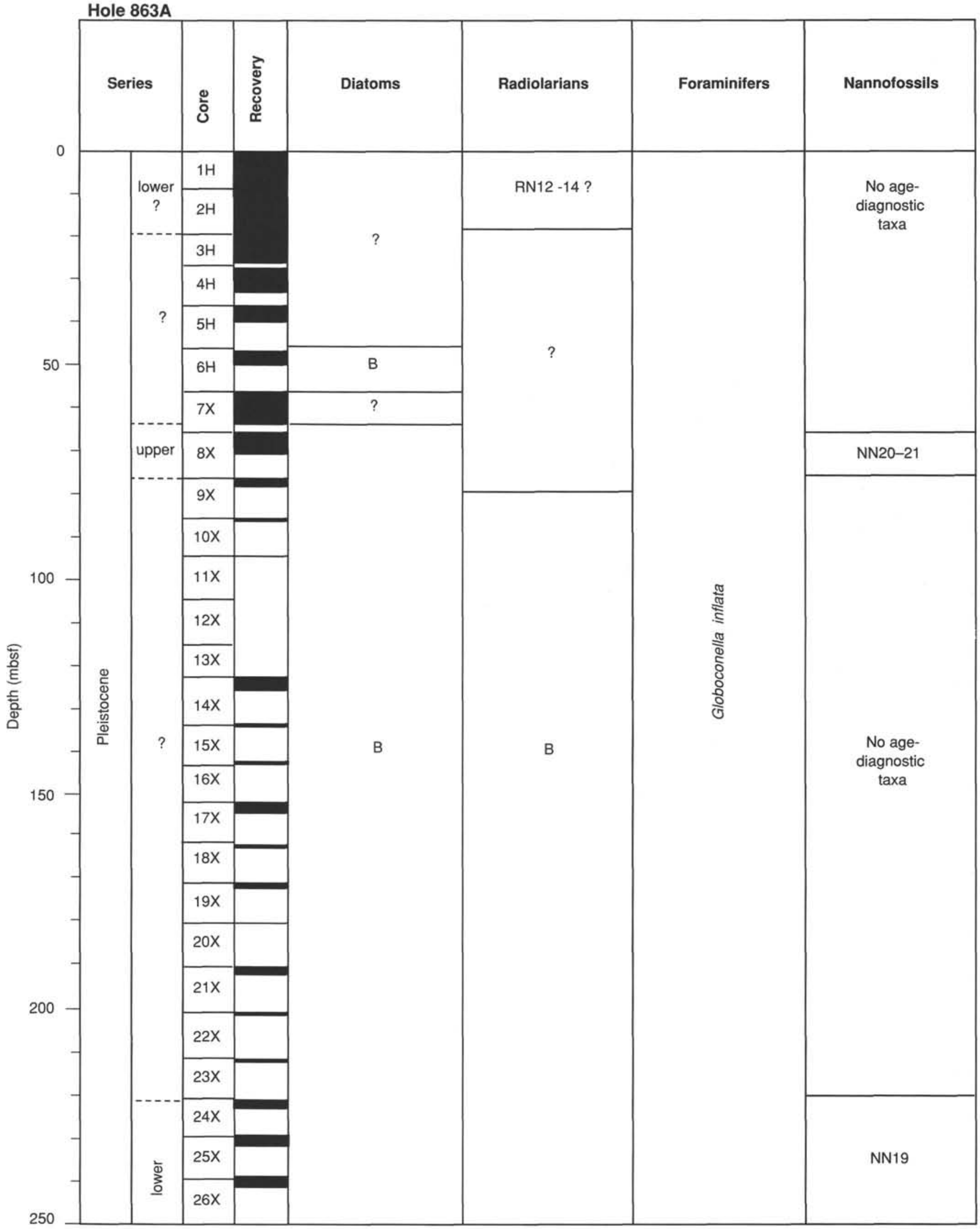

Figure 25. Summary of biostratigraphic age for the sediments recovered from Holes 863A and 863B.

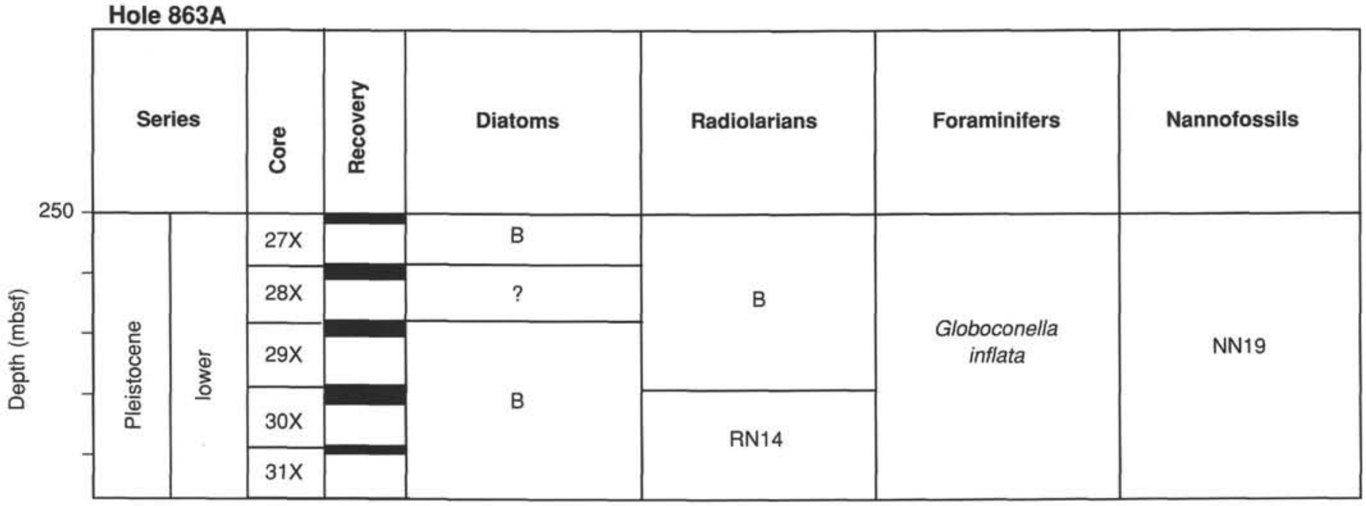

Figure 25 (continued).

Planulina wuellerstorfi, Melonis pompilioides, Pyrgo murrhina, Bulimina exilis and *Sphaeroidina bulloides* indicates a middle to upper bathyal paleoenvironment (van Morkhoven et al., 1986). They dominate the assemblages from the top down to 85.1 mbsf. Below 200 mbsf *Melonis pompilioides* and *Uvigerina* cf. *senticosa* constantly occur. Both are bathyal taxa, reaching in Holocene oceans down to lower bathyal depths. In the Peru-Chile Trench *U. senticosa* dominates at depths greater than 2400 m (Boersma, 1984). The shells of the bathyal benthic foraminifers are silicified in the same manner as has been described for planktonic foraminifers. *Nonionella chiliensis, Rosalina peruviana, Elphidium alvarezianum,* and *Bolivina costata* (Boltovskoy and Theyer, 1970; Boltovskoy et al., 1980) are neritic forms. Their occurrences indicate down-slope transport in the sequences of Site 863. Samples containing displaced foraminifers are marked by an asterisk in Tables 8 and 9. The neritic specimens are mostly preserved as calcitic fossils. Most of them contain a pyritic content. The two types of fossil-preservation frequently observed in one sample may be related to different degrees of transportation.

Calcareous Nannofossils

The results obtained from Hole 863A are based on investigation of 31 core-catcher samples. The sediments of the upper part of the sequence (Core 141-863A-1H to -23X) are poor in nannofossils. Only Sample 141-863A-8H-CC contains nannoplankton, with the following assemblage: *Gephyrocapsa ericsonii, G. carribeanica, G. oceanica, Helicosphaera carteri, Coccolithus pelagicus*, and *Cyclococcolithus leptoporus*. This assemblage indicates a late Pleistocene age (Zones NN20–NN21). From Core 141-863A-24X to Core 141-863A-31X well-preserved nannofossils are common to abundant. This sequence belongs to the lower Pleistocene (Zone NN19). The following species have been observed: *Cyclococcolithus leptoporus, Helicosphaera carteri, Gephyrocapsa ericsonii, G. oceanica, Syracosphaera pulchra,* and *Pseudoemiliania lacunosa*. Reworked nannofossils from the lower Miocene occur sporadically throughout the sequence. The top of the steeply dipping domain can be dated as Zone NN19, early Pleistocene.

Hole 863B was drilled about 10 m to the east of Hole 863A. Forty-nine core-catcher samples were studied. Nannofossils are abundant and they are of very small size. The assemblages observed from the top to the base of the sequence are the same. They are dominated by *Gephyrocapsa ericsonii*; *G. carribeanica, Cyclococcolithus leptoporus, Gephyrocapsa oceanica, Helicosphaera carteri,* and *Coccolithus pelagicus* are rare to few. The entire sequence in Hole 863B is attributed to the upper Pleistocene (Zones NN20–NN21).

PALEOMAGNETISM

Introduction

Pass-through cryogenic magnetometer measurements were not possible between Cores 141-863A-9X and -25X (75–240 mbsf) in Hole 863A due to very poor recovery. Better continuity of measurements was possible in Hole 863B. Alternating field demagnetization (AF) on archive-half sections was performed at a 10-cm interval using field intensities of 9, 12, and 15 mT. Discrete samples were measured with closely spaced demagnetization intervals up to a maximum of 50 or 60 mT. Susceptibility was measured as part of the multisystem track (MST) suite on whole-round sections.

Remanence and Susceptibility

Figures 26 and 27 record the variation with sub-bottom depth of natural remanent magnetization (NRM) inclination before demagnetization, and inclination and intensity after 15-mT demagnetization in Hole 863A. Prior to demagnetization, the NRM is biased to negative inclinations. After 15-mT cleaning of the archive-half sections, inclinations are consistently less steep, especially in the upper 20 mbsf. There is a thin interval of reversed polarity from 16.4 to 18 mbsf. Over the interval from 14 to 24 mbsf the demagnetized intensity record varies systematically over more than two orders of magnitude, with the minimum value coinciding with the interval of reversed polarity. Core 141-863A-5H (top at 37.1 mbsf) appears to contain part of a second cycle of rise and fall in intensity, although the limited recovery makes this more difficult to recognize. These patterns are repeated in the susceptibility data (Fig. 28), and in the proportion of NRM intensity remaining after demagnetization, and the Königsberger (Qn) ratio (Fig. 29).

The major peak in intensity and the other magnetic properties between 18 and 20 mbsf coincide with a layer of sulfide-rich clay. Sulfides are present in concentrated layers and as disseminations throughout the interval from 0 to 46.6 mbsf of Hole 863A, which constitutes lithologic Subunit IA (see Lithostratigraphy section, this chapter). The large variations in intensity and the other magnetic parameters over this interval may be related to dissolution of magnetite and the development of metastable magnetic iron sulfides (pyrrhotite and/or greigite).

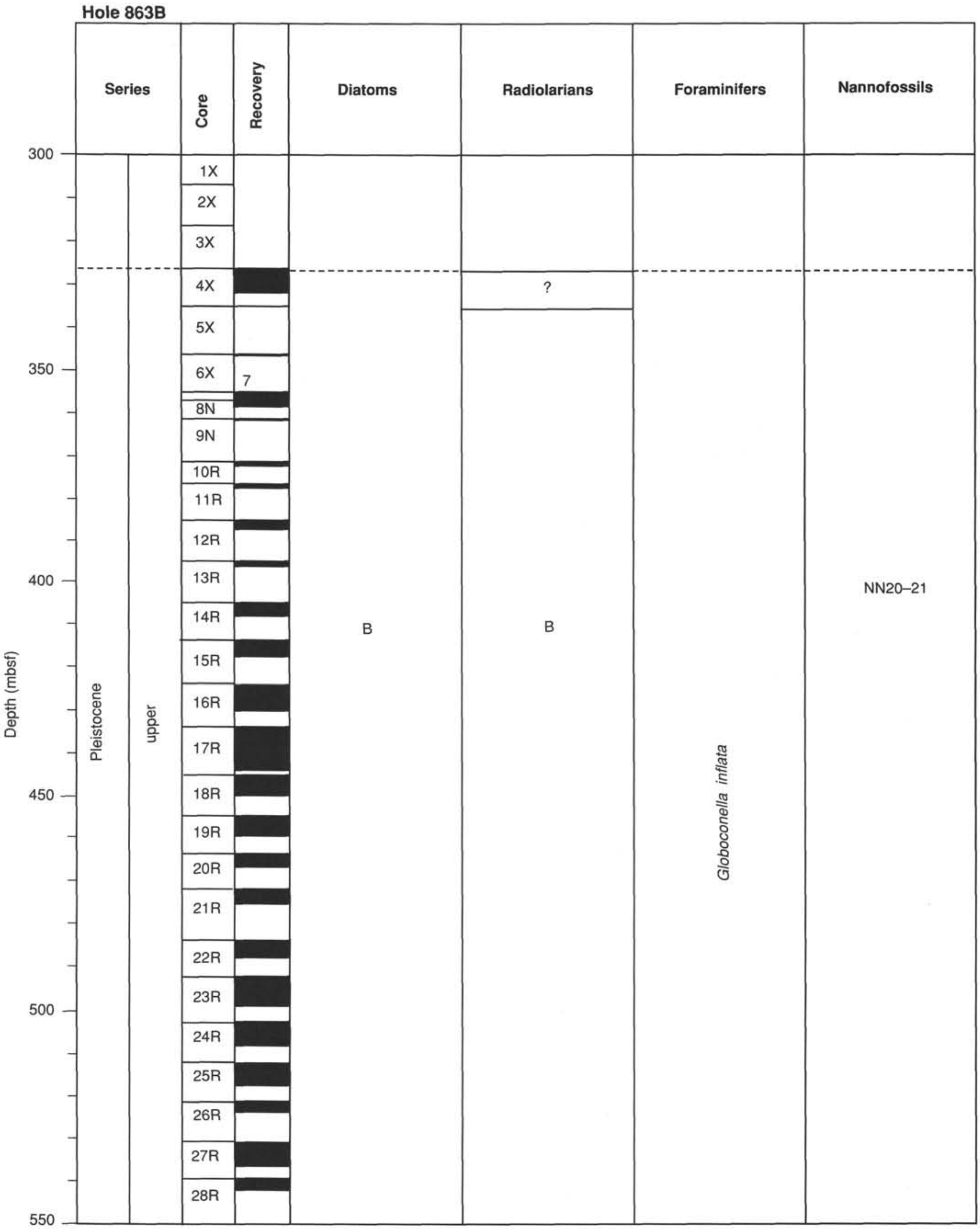

Figure 25 (continued).

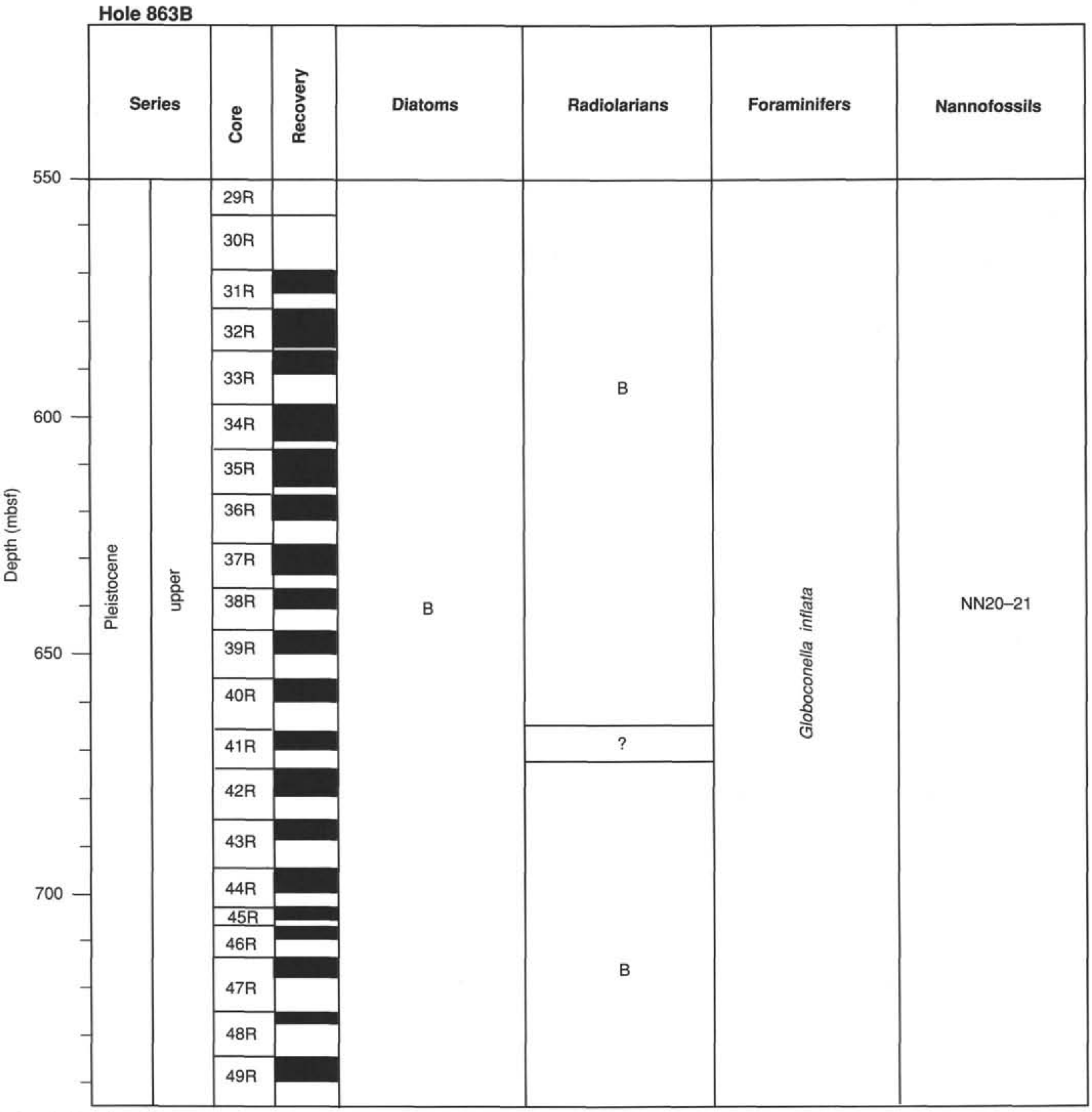

Figure 25 (continued).

No cryogenic magnetometer or susceptibility data are available in Hole 863A between 75 and 240 mbsf. Below 240 mbsf, NRM inclinations range between about –60° and –80°. Demagnetization at 15 mT reduces these inclinations, although almost all remain negative, and most fall between –45° and –75°. Bedding is nearly vertical below 259 mbsf (see Structural Geology section, this chapter), and we can anticipate that primary inclinations of ±65°, expected for this latitude, should have been rotated with the bedding to an angle ranging between about +25° and –25°, depending on the strike. Primary inclinations have apparently not been revealed by 15-mT demagnetization.

There is a gap in the susceptibility record in Hole 863A between 75 and 120 mbsf due to poor recovery. Susceptibility rises and falls over a broad cycle from 120 to 220 mbsf, then rises again to an average of around 7.5×10^{-3} S.I. at 250 mbsf. Suceptibility remains nearly constant from 250 to 280 mbsf, which may represent an interval through a single bed in the near-vertically bedded sequence.

Inclinations from Hole 863B measured by the pass-through magnetometer before and after 15-mT demagnetization are shown in Figure 30. Inclinations are once again almost all steeply negative, and demagnetization serves to consistently reduce the incli-

Table 6. Occurrence, preservation and estimated relative abundance of planktonic foraminifers in samples from Hole 863A.

Sample	Depth (mbsf)	Abundance	Preservation	*G. inflata*	*G. bulloides*	*G. crassaformis*	*G. scitula*	*O. universa*	*G. cariacoensis*	*N. pachyderma* D	*N. pachyderma* S	*G. crassula*	Paleotemperature	Zone
141-863A-														
1H-CC	8.6	C	G	C	F	R	R	R	R				Temperate	*Globoconella inflata*
2H-CC	18.1	C	M	C	C		R	F	R	R	R			
3H-CC	27.6	R	M	F	F	R	R			F	R			
4H-CC	37.1	F	M	R	F	R				F				
5H-CC	46.1	F	M	F	R	R								
6X-CC	56.7	F	M	R	F		R	R		R	R			
7X-CC	65.1	R	M	R	F					R	R			
8X-CC	75.4	C	G	C	R	R		R						
9X-CC	85.7	F	M	F	R	R	R			F	F	R		
10X-CC	94.7	B												
11X-CC	104.4	B												
14XJCC	123.7	R	P	R										
15X-CC	133.7	B												
16X-CC	143.0	R	P	R	R	R					R			
17X-CC	152.7	B												
18X-CC	162.4	B												
19X-CC	172.0	B												
20X-CC	181.6	R	P	R		R								
21X-CC	191.3	R	P								R			
22X-CC	200.9	B												
23X-CC	210.6	R	P								R			
24X-CC	220.3	R	P	R	R	R					R			
25X-CC	229.8	R	P	R						R	R			
26X-CC	249.2	R	P	R	F	R				R	F	R		
27X-CC	258.8	R	P	R		R					R			
28X-CC	268.4	R	P			R				R	R			
29X-CC	278.1	R	P	R		R						R		
30X-CC	287.6	R	P	R	R	R				R	R	R		
31X-CC	297.3	R	P	R		R						R		

Table 7. Occurrence, preservation, and estimated relative abundance of planktonic foraminifers in samples from Hole 863B.

Sample	Depth (mbsf)	Abundance	Preservation	*G. inflata*	*G. crassaformis*	*N. pachyderma* S	*G. bulloides*	*O.universa*	*G. crassula*	*N. pachyderma* D	Paleotemperatures	Zone
141-863B-												
4X-CC	335.60	R	P	R	R	R					Temperate	*Globoconella inflata*
5X-CC	345.20	R	P		R	R	R					
6X-CC	354.90	R	P	R	R	F	R					
7N-CC	357.40	R	P			R						
8N-CC	361.40	B										
9N-CC	371.00	B										
10R-CC	376.60	B										
11R-CC	386.30	B										
12R-CC	395.80	R	P	R								
13R-CC	405.50	B										
14R-CC	415.20	R	P	R								
15R-CC	424.70	R	P		R							
16R-CC	434.40	F	P	F		R						
17R-CC	444.00	B										
18R-CC	453.70	R	P	R								
19R-CC	463.40	R	P	R								
20R-CC	473.00	R	P	R	R							
21R-CC	482.70	R	P	R								
22R-CC	492.40	R	P	R	R							
23R-CC	502.00	R	P	R	R		R					
24R-CC	511.70	R	P	R								
25R-CC	521.40	R	P	R			R	R				
26R-CC	530.60	R	P	R								
27R-CC	540.20	R	P	R								
28R-CC	549.70	R	P	R								
29R-CC	559.40	R	P	R	R		R					
30R-CC	569.10	C	P	C	R		F	R	R	R		
31R-CC	578.80	R	P	R	P							
32R-CC	588.40	B										
33R-CC	598.10	R	P	R		R						
34R-CC	607.70	B										
35R-CC	617.40	B										
36R-CC	627.00	R	P	R		R						
37R-CC	636.60	B										
38R-CC	646.30	B										
39R-CC	655.90	R	P	R		R						
40R-CC	665.50	R	P	R	R	R						
41R-CC	675.20	R	P	R	R	R						
42R-CC	684.80	R	P	R	R							
43R-CC	694.50	R	P	R	R	R						
44R-CC	704.20	R	P	R			R					
45R-CC	706.80	R	P	R								
46R-CC	713.80	B										
47R-CC	723.50	B										
48R-CC	733.20	R	P	R	R		R					
49R-CC	742.90	F	P	F	R							

nation to less negative values. The NRM inclination record breaks up into intervals of less negative and more negative values, bounded at about 350, 500, 675, and 725 mbsf. Demagnetization increases the contrast between these intervals. Differences in inclination between these intervals may represent differences in bedding dip, or differences in magnetic mineralogy (reflected in coercivity of the viscous remanence, VRM) between beds. The latter interpretation is supported by the downhole variation in demagnetized intensity (Fig. 31), which can also be subdivided into the same intervals. Magnetic susceptibility also broadly follows the same pattern, although the contrast is less and an extra interval (marked by lower susceptibility) can be identified between 350 and 415 mbsf. The Königsberger (*Qn*) ratio and the ratio of intensity after 15-mT demagnetization to NRM intensity repeat the pattern (Fig. 32). The long extent (more than 50 m) of each of these intervals is a result of the near vertical bedding, which requires coring through many times the stratigraphic thickness to penetrate each bed. Demagnetized inclinations in the interval between 350 and 500 mbsf are sufficiently shallow (averaging around –10° to –20°) that they could represent primary inclinations from which VRM and other overprints have been thoroughly removed (note that negative inclinations do not necessarily denote normal polarity in the case of vertical bedding). Demagnetized remanence between about 700 and 715 mbsf may also record primary inclinations, as the inclination over this interval averages about –20° to –30°.

Demagnetization of Discrete Samples

Complicated demagnetization paths characterize samples from Cores 141-863A-1H through -5H (Fig. 33), suggesting the presence of multiple overprints that may be related to phases of reduction of magnetite to pyrite through intermediate metastable magnetic iron sulfides. Overprinting may result from chemical remanences acquired during magnetite reduction/iron sulfide generation or from an increased sensitivity of the iron sulfides to acquisition of high-coercivity remanences during drilling and sampling (Shipboard Scientific Party, 1991). Inclinations after maximum demagnetization at 50 or 60 mT are highly variable from sample to sample, and it is not clear whether a primary depositional magnetization has been isolated in any of these samples. Complex demagnetization behavior is also present in samples from Cores 141-863A-7X and -8X from lithologic Subunit IB (Fig. 34), suggesting that despite the decrease in concentration of sulfides in this subunit (see Lithostratigraphy section, this chapter), reduction of magnetite and sulfide generation still significantly affect the remanence in this part of the sequence.

Samples from lithological Unit II (below 104 mbsf) have far simpler demagnetization paths, consistent with much lower concentrations of sulfide minerals (Fig. 35). Many samples display long demagnetization trends in their stereonet plots, indicating the gradual removal of an overprint from a more stable magnetization. Demagnetization intensity plots of these samples are highly concave, demonstrating that low-coercivity components constitute a

Table 8. Occurrence, preservation, and estimated relative abundance of selected benthic foraminifers in samples from Hole 863A.

Sample	Depth (mbsf)	Abundance	Preservation	Displaced sediments	*Uvigerina peregrina*	*Bulimina mexicana*	*Planulina wuellerstorfi*	*Melonis pompilioides*	*Pyrgo murrhina*	*Bulimina exilis*	*Sphaeroidina bulloides*	*Bolivina costata*	*Uvigerina cushmani*	*Uvigerina senticosa*	*Ehrenbergina pupa*	*Nonionella chiliensis*	Paleoenvironment
141-863A-																	
1H-CC	8.6	C	G	*	R	R	F	C	R	R	R	R					Middle to upper Bathyal
2H-CC	18.1	C	M	*	F		R	R	R	R	R	R	R				
3H-CC	27.6	C	M		C	R		F		F							
4H-CC	37.1	C	M	*		R		F		R		R					
5H-CC	46.1	C	G		C	R		F		R							
6X-CC	56.7	F	M		F	R		R	R	R			R				
7X-CC	65.1	F	G		F			R		R							
8X-CC	75.4	F	G		F	R		R									
9X-CC	85,7	F	G		R	R	R	R					R				
10X-CC	94.7	B															(?)
11X-CC	104.4	B															
14X-CC	123.7	R	P		R			R									
15X-CC	133.7	B															
16X-CC	143.0	R	P		R												
17X-CC	152.7	B															
18X-CC	162.4	B															
18X-CC	172.0	B															
20X-CC	181.6	B															
21X-CC	191.3	R	P														
22X-CC	200.9	B															
23X-CC	210.6	R	P			R							R	R	R		Lower to middle Bathyal
24X-CC	220.3	R	P		R												
25X-CC	229.8	R	P		R	R		R									
26X-CC	249.2	R	P					R						R	R		
27X-CC	258.8	R	P	*				R								R	
28X-CC	268.4	R	P					R							R		
29X-CC	278.1	R	P												R		
30X-CC	287.6	R	P					R									
31X-CC	297.3	R	P					R									

Table 9. Occurrence, preservation, and estimated relative abundance of selected benthic foraminifers in samples from Hole 863B.

Sample	Depth (mbsf)	Abundance	Displaced sediments	Preservation	*Uvigerina peregrina*	*Ehrenbergina pupa*	*Melonis pompilioides*	Rosalina peruviana	Nonionella chiliensis	*Elphidium alvarezianum*	*Uvigerina* cf. *senticosa*	*Pyrgo murrhina*	Bulimina mexicana	Planulina wuellerstorfi	Paleoenvironment
141-863B-															
4X-CC	335.60	R	P		R										Bathyal
5X-CC	345.20	R	P			R	R								
6X-CC	354.90	R	M	*		R	R	R							
7N-CC	357.40	R	M	*	R		R	R	R						
8N-CC	361.40	B													
9N-CC	371.00	B													
10R-CC	376.60	B													
11R-CC	386.30	B													
12R-CC	395.80	B													
13R-CC	405.50	B													
14R-CC	415.20	R	P												
15R-CC	424.70	B													
16R-CC	434.40	B													
17R-CC	444.00	B													
18R-CC	453.70	R	P	*					R						
19R-CC	463.40	R	P	*			R		R						
20R-CC	473.00	R	P	*											
21R-CC	482.70	R	P	*	R			R	R	R	R				
22R-CC	492.40	R	P				R				R				
23R-CC	502.00	R	P				R								
24R-CC	511.70	R	P				R								
25R-CC	521.40	R	P	*			R								
26R-CC	530.60	R	P				R					R			
27R-CC	540.20	R	P	*		R			R						
28R-CC	549.70	B													
29R-CC	559.40	R	P				R				R				
30R-CC	569.10	R	M								R	R			
31R-CC	578.80	R	P				R								
32R-CC	588.40	B													
33R-CC	598.10	R	P		R		R								
34R-CC	607.70	B													
35R-CC	617.40	R	P		R										
36R-CC	627.00	R	P												
37R-CC	636.60	B													
38R-CC	646.30	B													
39R-CC	655.90	R	P								R		R		
40R-CC	665.50	R	P				R				R				
41R-CC	675.20	R	P				R				R				
42R-CC	684.80	R	P				R				R				
43R-CC	694.50	R	P		R		R								
44R-CC	704.20	R	P												
45R-CC	706.80	B													
46R-CC	713.80	B													
47R-CC	723.50	B													
48R-CC	733.20	R	P				R								
49R-CC	742.90	F	P				R	R			R	R		R	

large proportion of NRM. In some cases the direction of the magnetization vector is still changing systematically at 50 mT, implying that the overprint still has not been completely removed at this demagnetization level; in other cases the direction becomes stable at about 30–40 mT. Inclinations of the stable directions are generally around –30° to –45°.

Demagnetization intensity plots of samples from Cores 141-863B-7N and -17R are much more linear (Fig. 36), indicating that low-coercivity components are proportionally less significant in these samples. Demagnetization of these samples produces a smaller change in remanence direction; the direction at 50–60 mT appears to be stable, and constitutes the characteristic remanence (ChRM). Sample 141-863B-8N-1, 50–52 cm has a proportionally large component removed by 5-mT demagnetization, but then demagnetizes toward a similar stable ChRM. The inclination of the ChRM in these samples is low, between 0° and –20°, which would be consistent with this ChRM being a primary (depositional or early postdepositional) remanence in vertically dipping beds. These samples represent the interval between 350 and 500 mbsf, which was distinguished in the continuous cryogenic magnetometer record by low negative inclinations after 15-mT demagnetization.

The interval from 350 to 500 mbsf does not correspond to a single lithologic Subunit division (see Lithostratigraphy section, this chapter) so it is unlikely that differences in the coercivity spectra and degree of overprinting between this interval and the rest of lithological Unit II are related to differences in original sedimentary lithology. This interval corresponds to the upper part of Physical Properties Unit D, and is marked by a rapid downward decrease in porosity and by a zone of enhanced fluid chemical activity (see Physical Properties and Inorganic Geochemistry sections, this chapter). Differences in demagnetization behavior between this interval and the rest of the sequence at Site 863 may reflect chemical alteration of the magnetic mineralogy to leach out the carrier of the overprint.

STRUCTURAL GEOLOGY

Summary

Four structural domains can be defined at Site 863 (Fig. 37): an uppermost undisturbed domain (0–3.3 mbsf), a complexly faulted domain (3.3–46.6 mbsf), a gently dipping domain (46.6–258.8 mbsf) and a steeply dipping domain (258.8–742.9 mbsf). In the complexly faulted domain, normal faults consistently postdate reverse faults. There is a significant component of strike-slip movement involved in faulting. This may reflect a larger scale component of strike-slip in the forearc, which can be inferred from the obliquity of bedding and fault orientations to the margin and to the plate convergence vector. The steeply dipping domain comprises nearly 500 m depth of subvertically bedded turbidites. The bedding is cut by faults with normal, reverse, oblique, and strike-slip motions. Each fault may have had an earlier movement

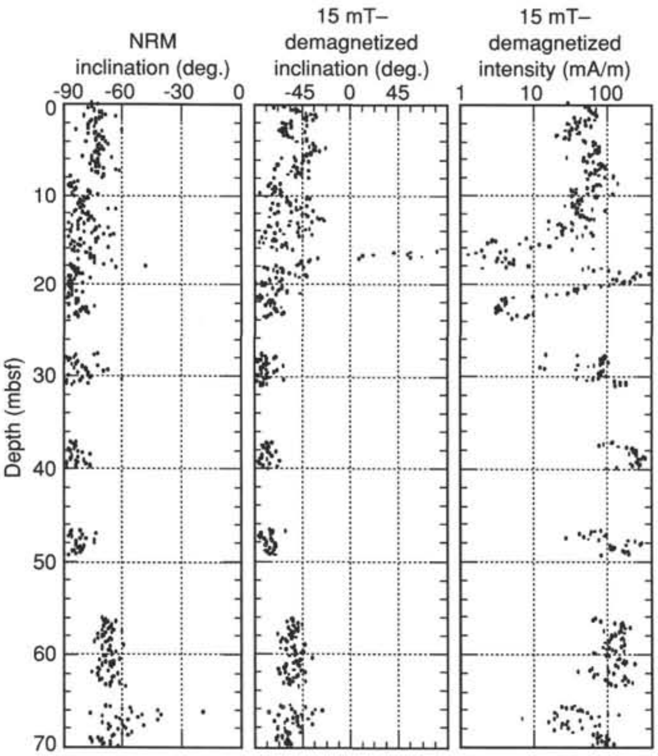

Figure 26. NRM inclination, and inclination and intensity after 15-mT demagnetization, of continuous sections from 0–70 mbsf of Hole 863A.

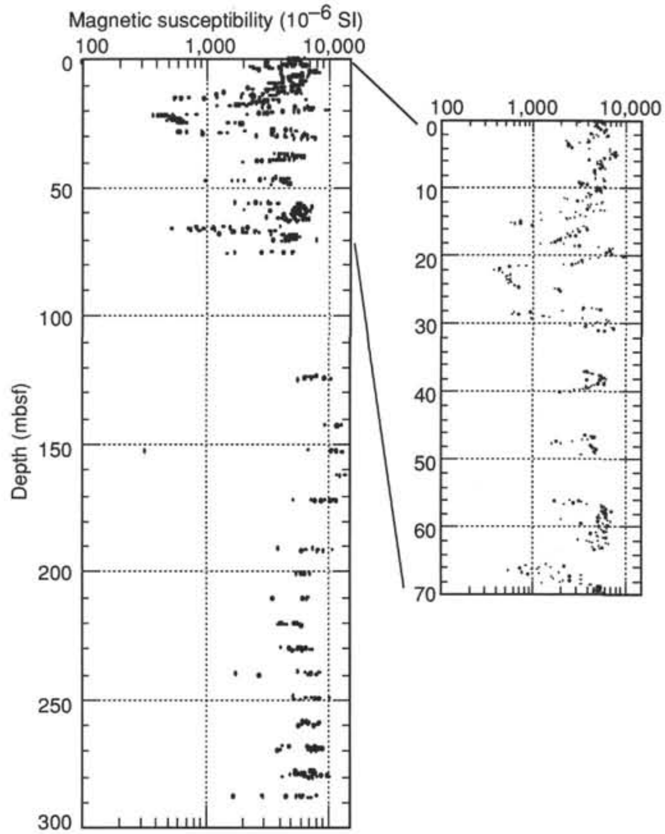

Figure 28. Magnetic susceptibility of whole-round sections, Hole 863A.

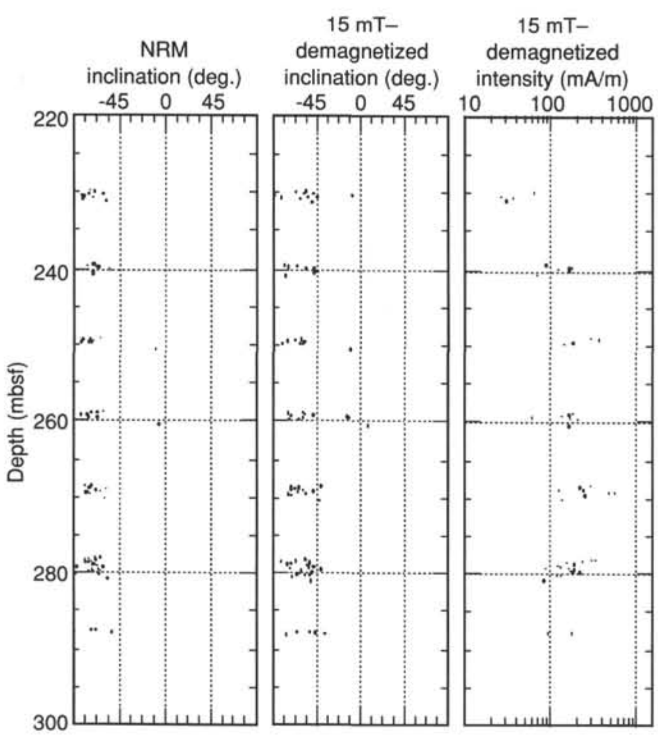

Figure 27. NRM inclination, and inclination and intensity after 15-mT demagnetization, of continuous sections from 220 mbsf to TD in Hole 863A.

history with different kinematics. Where cross-cutting relationships are observed the latest phase of faulting is normal. Deformation-band arrays with varying degrees of complexity and intensity are observed. Carbonate-filled veins are observed and relate to carbonate cementation in coarse sands. Deformation bands and carbonate veining are both more prevalent with depth and with proximity to major structures. Throughout Site 863, normal structures are the latest and are provisionally attributed to the superposition of spreading-ridge tectonics of the Chile Ridge on a previous accretionary history.

Detailed structural data for Holes 863A and 863B are presented in Table 10. Wherever possible, structural measurements have been reoriented into a geographical reference frame. Sections where reorientation was possible are shown in Figure 37.

Complexly Faulted Domain

This domain is characterized by complex and intense deformation related primarily to faults. Bedding is preserved through this domain. The domain underlies an interval (0–3.3 mbsf) of undisturbed sediment and covers Sections 141-863A-1H-3, 33 cm, through -5H-2, 147 cm (3.3–41.6 mbsf). The contact with the upper undisturbed domain corresponds to a fault. The lower contact is between Cores 141-863A-5H and -6H and its nature is unconstrained.

Faults

The distribution and character of faults within the complexly faulted domain is heterogenous, loosely corresponding to lithologic variations.

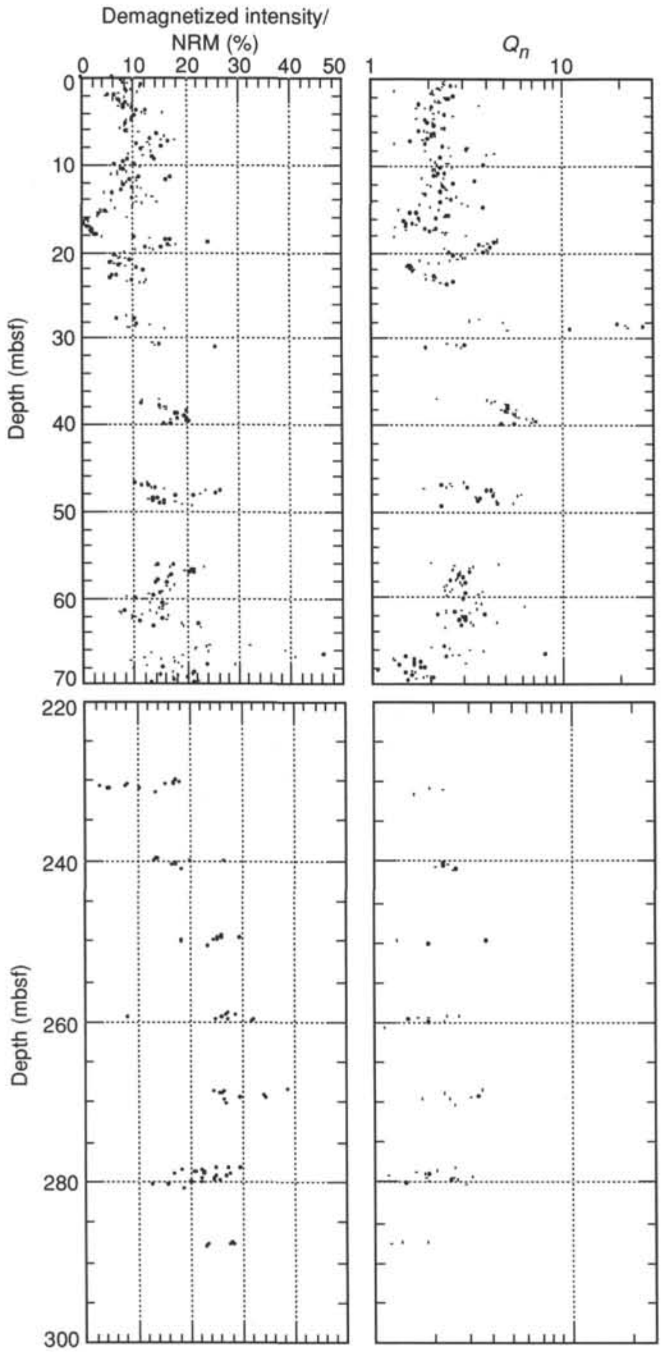

Figure 29. The ratio of intensity after 15-mT demagnetization to NRM intensity, and the Königsberger Q_n ratio, for sections from Hole 863A.

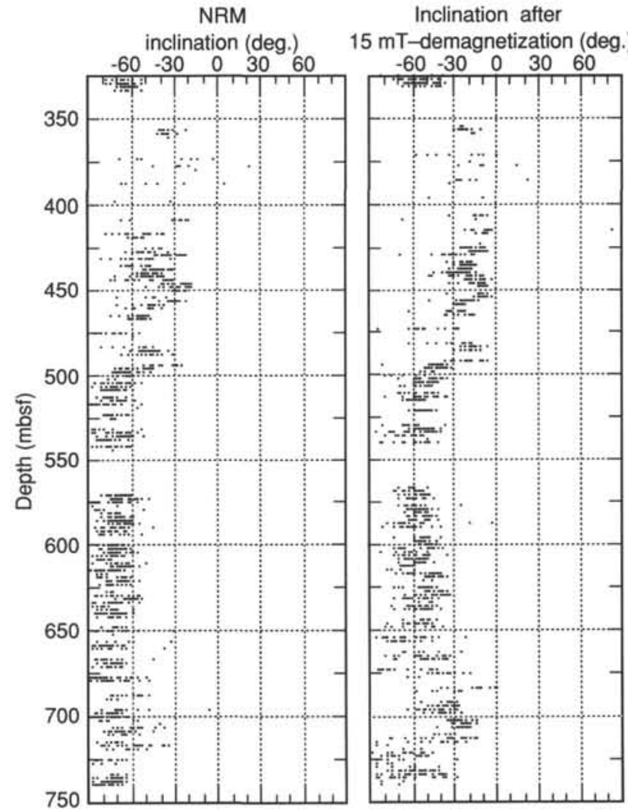

Figure 30. NRM inclination, and inclination after 15-mT demagnetization, for continuous sections from Hole 863B.

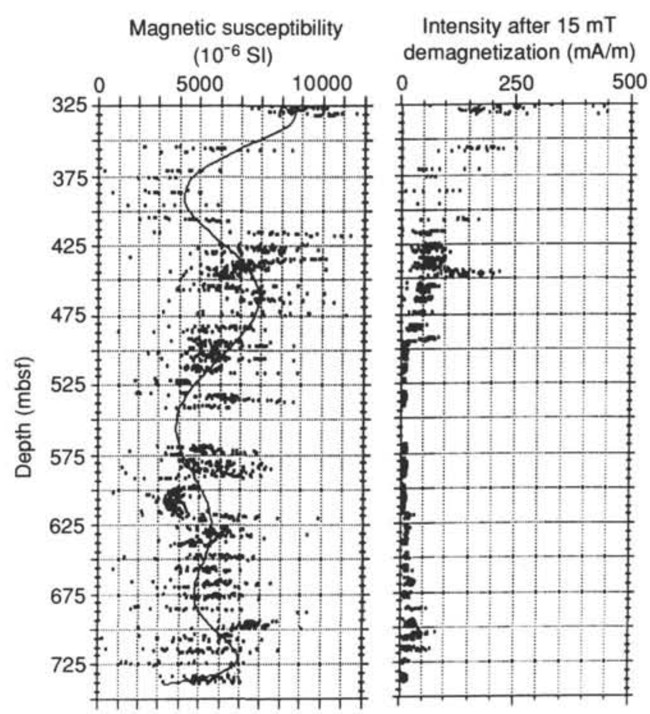

Figure 31. Magnetic susceptibility, and intensity after 15-mT demagnetization, for continuous sections from Hole 863B.

Sections 141-863A-1H-3, 33 cm, through -2H-4, 73 cm, are characterized by normal faults, reverse faults, and faults having mixed separations. Faults are generally defined by dark traces less than 1 mm thick. Normal faults are dominant and always post-date the reverse faults. Many of the normal faults are very steep and can be traced for up to 30 cm. Separations vary in size from submillimeter to 30 mm. Other normal faults, together with reverse faults and faults with mixed separations, are shallowly dipping. Some normal faults are listric. In one example, in Section 141-863A-1H-4, 35–46 cm, a listric normal fault is used as a

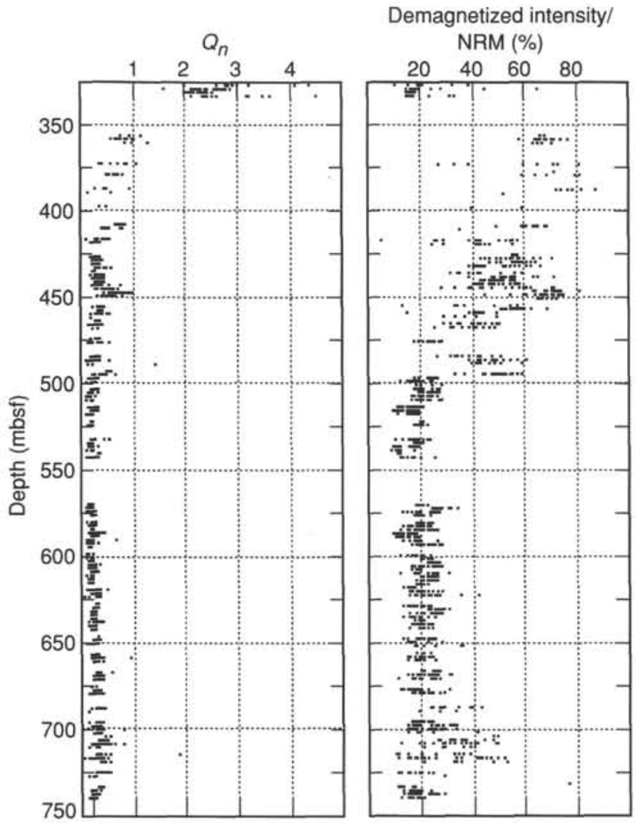

Figure 32. Königsberger Q_n ratio, and the ratio of intensity after 15-mT demagnetization to NRM intensity, for sections from Hole 863B.

detachment surface by faults having a reverse separation, dipping in an orientation conjugate to the main fault (Fig. 38). The separation on the main fault is about 20 mm; the antithetic reverse structures have up to a few millimeters separation. These structures cannot be explained satisfactorily by motion within the plane of observation: this would necessitate untenable volume changes within the structure. This structure, and probably many others where opposed separations are observed, must involve a component of strike-slip motion.

Sections 141-863A-3H-1, 0–140 cm, and -4H-1, 50 cm, through -CC, 32 cm, are complexly and intensively deformed. These zones correspond to a visually striking lithology characterized by a "marbling" pattern of dark layers and blebs (hydrous sulfides), with pale halos, in a gray clay (see Lithostratigraphy section, this chapter). Another similar zone may occur within Sections 141-863A-3H-5, 10 cm, through -3H-CC, 73 cm: this comprises thoroughly drilling-disturbed, "marbled" clay. One- to three-millimeter faults, spaced 2 to 15 cm, juxtapose packets where the marbling has a different style or orientation (Fig. 39). In some cases, the clays of the neighboring fault-bounded packets have different colors. In Sections 141-863A-4H-2, 60 cm, through -3, 35 cm, a prominent green clay with black layering is repeated four times in fault-bounded packets up to 10 cm thick. The thick faults have moderate dips in two conjugate orientations with a subhorizontal bisecting plane. Deflections of fabric neighboring these faults, together with extensional jogs (filled with fine black clay), generally indicate reverse movement, although individual separations cannot be discerned. The thick faults are consistently cut by finer (generally submillimeter) faults, spaced 1 to 20 mm apart. These faults dip moderately (some are parallel to the thick faults) to steeply. Most of these faults have normal separations of a few millimeters, others have reverse separations or more complex patterns where layers change thickness across a fault and both reverse and normal separations are observed.

Sections 141-863A-3H-1, 140 cm, through -3H-5, 10 cm, separate the marbled domains and are less deformed. This interval contains five or six shallowly dipping reverse faults, including one structure of greater significance in Section 141-863A-3H-2, 47–85 cm. Here, a major steep fault (Fig. 40) juxtaposes moderately to steeply dipping sands in the hanging wall vs. shallowly dipping clays and silts in the footwall. The fault is composed of 1 mm of dark clays that thicken to 5 mm of structureless sand. Minor faults in the hanging wall have reverse separations and lie parallel to the main fault, suggesting that this is also a reverse fault. In contrast, bedding in the footwall is deflected to indicate normal movement. The sand of the hanging wall is a 13-cm-thick horizon having well-defined bedding laminations. The top centimeter of the sand contains millimeter-scale isoclinal folds of bedding laminae within structureless sand. This major fault corresponds to an abrupt increase in bulk density (see Physical Properties section, this chapter) and to an inflection in the downhole temperature profile (see WSTP-ADARA Temperature Measurements section, this chapter). Less dense rocks in the hanging wall support a late phase of normal motion on this fault. The more complexly deformed "marbled" regions do not correspond to physical property changes, although their structure is suggestive of greater displacements, implying that the deformation in the marbled material is older. A sharp break in bulk densities at about 15 mbsf (see Physical Properties section, this chapter) corresponds to a zone of severe drilling disturbance. In this case, more-dense rock overlies less-dense rock, and a thrust may occur at this depth.

Sections 141-863A-5H-1, 15 cm, through -5H-3, 24 cm, are dominated by normal faults and faults having mixed separations. These faults occur in linked arrays, some having a major listric fault as detachment. The arrays are separated 10 to 15 cm, whereas individual faults within arrays are separated by a few millimeters to 2 cm. Some thick (2 to 3 mm) reverse faults are observed. The fault arrays abut against these or detach into them.

Orientation of Structures

Multishot orientations were available for Cores 141-863A-4H and 141-863A-5H. Rotations used to orient structural data into the geographical reference frame are shown in Table 11. In the Chile Triple Junction area the magnetic declination is 14° east. The data have not been corrected for the drift of the drill string from vertical. The multishot data show drifts of 5° and 6.2° for Cores 141-863A-4H and 141-863A-5H, respectively. Poles to bedding lie on a well-defined great circle (Fig. 41) oriented with a best-fit intersection axis plunging 00° toward 044°. Normal, reverse, and other faults do not fall into discrete orientations. Poles to faults also lie on a great circle with the same best-fit intersection axis as the bedding (Fig. 41).

Oblique-Slip in the Chile Triple Junction Forearc

If the multishot-oriented cores are typical of the complexly faulted domain, then the mean bedding and fault orientations are oblique to the trench, the slope, and the plate convergence direction. One explanation for these orientations is that they represent a component of strike-slip deformation in the forearc. Dextral-strike slip between the trench and the continental margin would lead to compression oblique to the trench and might explain the observed bedding and reverse fault orientations (Fig. 42). Strike-slip motion is supported by the observation of small-scale strike-slip structures in this domain. There are two possible mechanisms for development of strike-slip in the forearc:

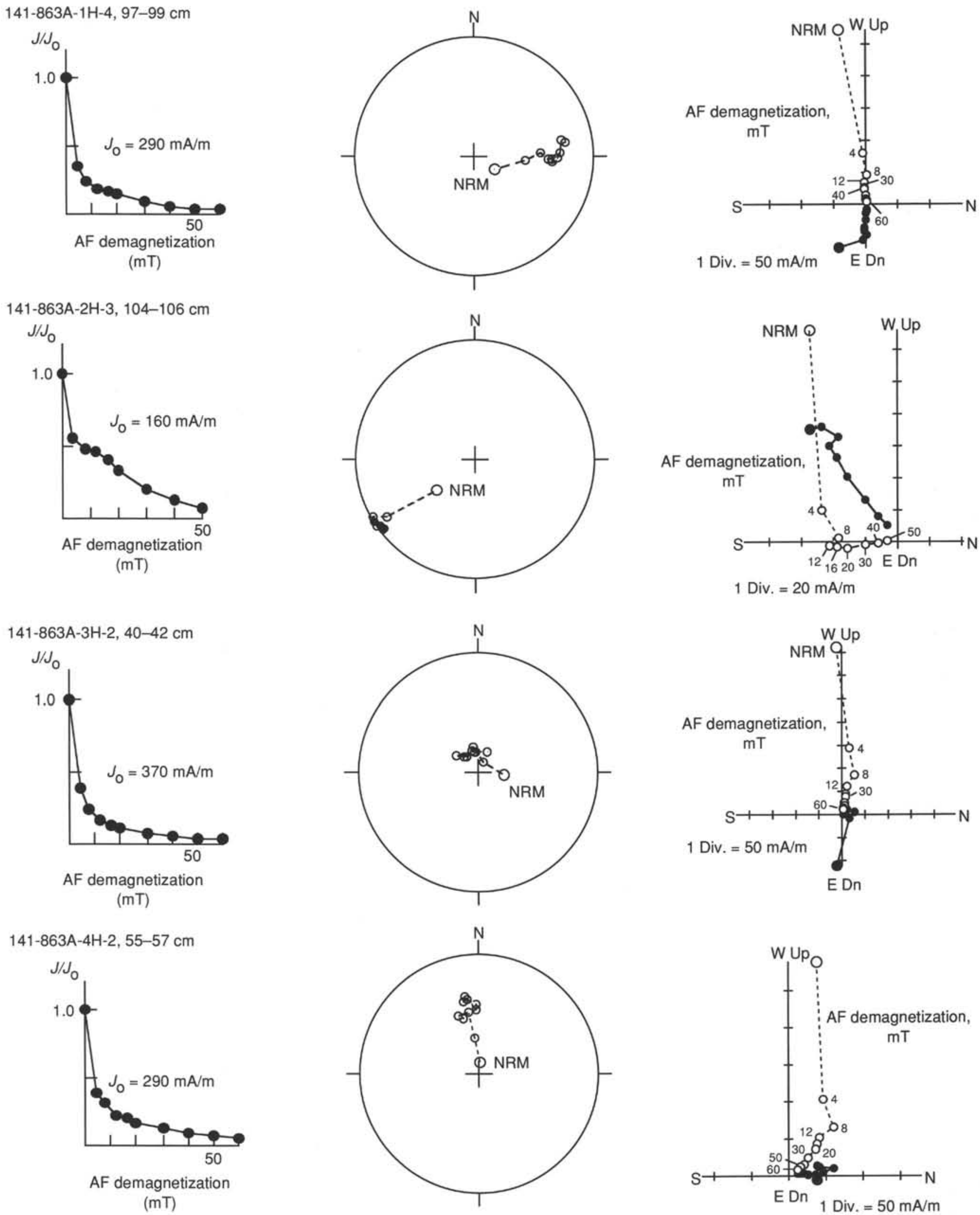

Figure 33. Zijderveld plots, stereograms, and demagnetization intensity plots for discrete samples from lithologic Subunit IA, displaying complex demagnetization behavior related to the presence of magnetic iron sulfides. Open symbols on the Zijderveld plots are on the vertical plane, closed symbols on the horizontal plane. Open symbols on the stereograms are in the upper hemisphere.

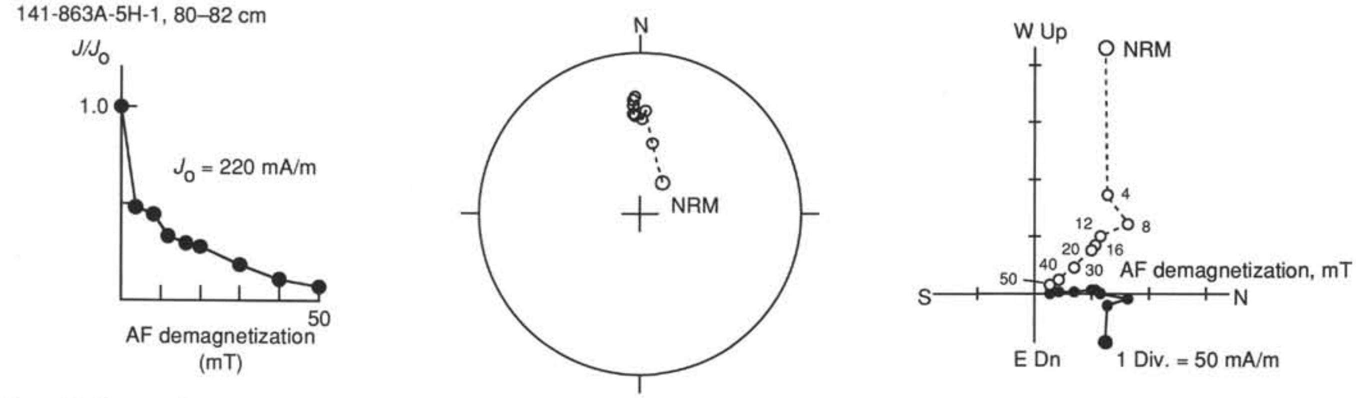

Figure 33 (Continued).

1. This motion is partitioned from the trench-parallel component of oblique subduction (potentially up to 20 mm/yr^{-1}).

2. The northward migration of the triple junction and its associated topographic anomaly, during its latest ridge-trench phase, has affected the kinematics within the forearc.

Gently Dipping Domain

This domain covers Cores 141-863A-6H through -27X (46.6–258.8 mbsf) and corresponds mostly to a zone of poor recovery. Bedding is observed wherever it has not been destroyed by drilling deformation and dips shallowly (Fig 43). Some small normal and reverse faults are observed. Multishot orientations were available for Core 141-863A-6H (Table 11). The small bedding data set from this core lies in the same band of orientations represented by bedding in the complexly faulted domain.

Steeply Dipping Domain

This domain extends from 259 mbsf in Hole 863A to the bottom of Hole 863B at 739.3 mbsf. The domain is characterized by very steep (normally subvertical) bedding together with considerable faulting, a variety of deformation bands and carbonate veining, and associated, localized cementation. Vertical bedding is first observed in Core 141-863A-29X. The first core assigned to this domain is Core 141-863A-28X. No bedding is observed in this core, but it contains deformation bands similar to those observed in the steeply dipping domain, but not observed in the gently dipping domain. The nature of the upper contact of the steeply dipping domain is unclear: it must be an unconformity or a fault.

Bedding and Younging

Bedding is generally subvertical (Figs. 44 and 45), varying slightly in orientation so that some of the succession is nominally upright, whereas some is nominally overturned. Erosive bases, bioturbation, graded bedding, and complete or partial Bouma sequences (see Lithostratigraphy section, this chapter) give clear younging information in individual cores, although the lack of core orientation means that we cannot at present assess the direction of younging in a geographical reference frame. Sedimentary structures indicate that current directions are parallel to the core axis and indicate flow up the core for bedding in its present vertical attitude. Shallowing of bedding orientations is only observed in the vicinity of faults.

Both logging (see Wireline Measurements section, this chapter) and a multishot drift survey (see Operations section, this chapter) indicate that Hole 863B drifted significantly (about 5°) toward 225° from vertical. It is possible that the drilling orientation may have been influenced by the bedding orientation.

Faults

Two major fault zones, at 496 and 687 mbsf, are identified in the steeply bedded domain, corresponding to zones where bedding is modified from the vertical.

Bedding becomes gradually shallower and overturned downward through Sections 141-863B-41R-2, 0 cm, through -41R-3, 90 cm, when approaching a major fault zone identified in Sections 141-863B-43R-1, 60 cm, through -43R-3, 75 cm (687 mbsf). The main fault zone is defined by breccia up to 2 m thick. The breccia varies from sand/siltstone with pervasive carbonate-filled submillimeter fractures spaced 2–20 mm to an aggregate of submillimeter to 20-mm angular clasts (Fig. 46). The breccia shows no preferred fracture orientations or fabrics.

Upright shallow bedding is observed in a fault-bounded packet in Sections 141-863B-23R-2, 18 cm, through -23R-3, 100 cm (496 mbsf). The interval contains several moderately dipping, slickenlined fault surfaces. The slickenlines indicate motion close to dip-slip and consistently contain steps indicative of normal displacements. Between two pairs of the fault-bounded packets are pervasively foliated clays 5 to 100 mm thick (Fig. 47).

The individual faults in the intensely faulted interval are typical of most faults in the steeply bedded domain. These have steep to moderate dips (Fig. 44) and a variety of slickenline orientations (Fig. 48), with stepping indicating the complete range of displacements, including reverse, normal, and strike-slip end members. The slickenlines are developed in submillimeter-thick, clay-rich planes that cause the core to break very sharply. These are commonly within thicker (up to 5 mm) networks of deformation structures (Fig. 49). Separations across individual faults cannot be identified. Faults in a subvertical orientation often juxtapose different lithologies and commonly run along bedding surfaces. Where faults are cross-cutting, it is nearly always those faults having normal displacements that are the latest. A good example is in Section 141-863B-37R-1, 30–70 cm. Here, two normal faults having separations larger than the core width, cut reverse faults that have separations of a few millimeters to a centimeter.

Fault orientations in the core reference frame are confusing. Most cores recovered from the steeply dipping domain are fairly continuous and contain bedding and younging information that will enable the data from separate cores to be reoriented relative to each other using bedding and younging as a datum. Absolute orientation of these data, in the geographical reference frame, may then be possible from FMS data (see Wireline Measurements section, this chapter).

Deformation Bands

Numerous styles and orientations of deformation bands are observed. The sediments recovered from the steeply dipping do-

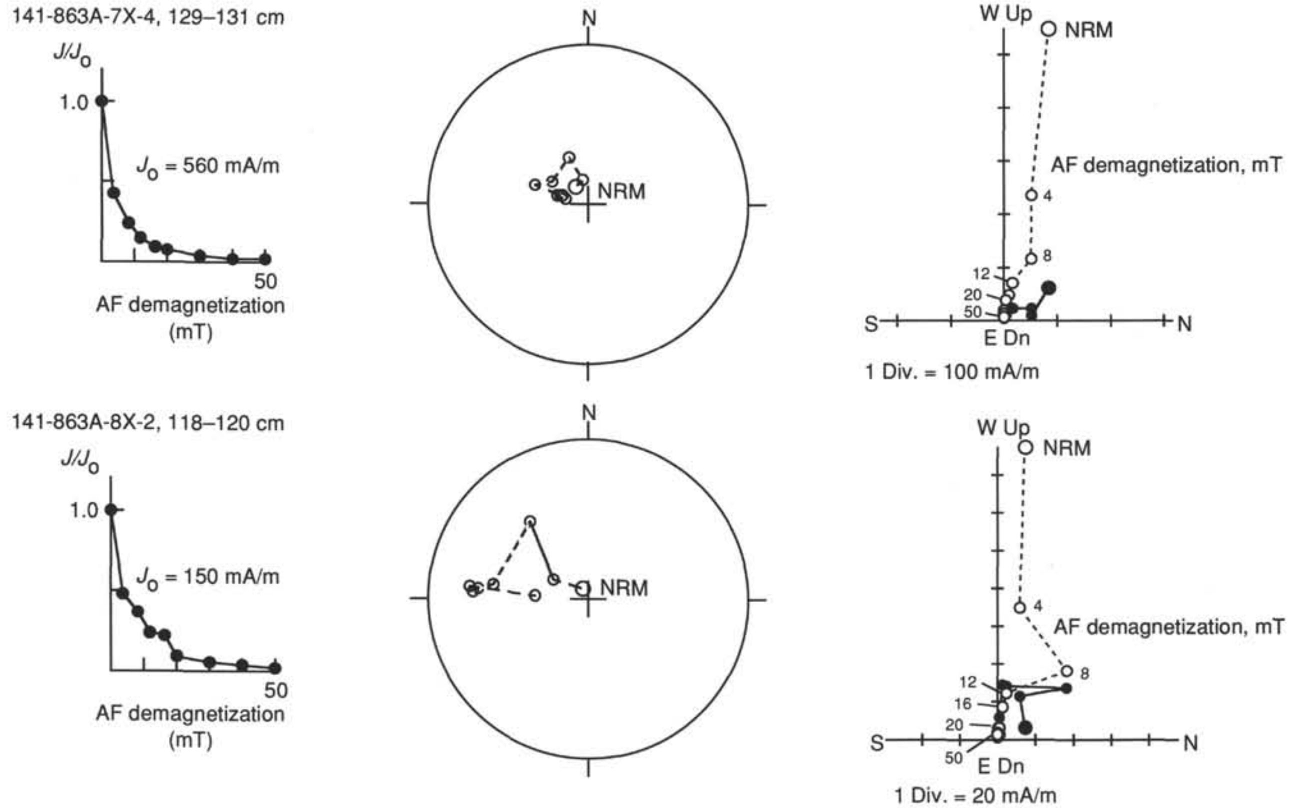

Figure 34. Zijderveld plots, stereograms, and demagnetization intensity plots for samples from lithologic Subunit IB, which also show complex demagnetization behavior related to the presence of magnetic sulfides. Symbols as for Figure 33.

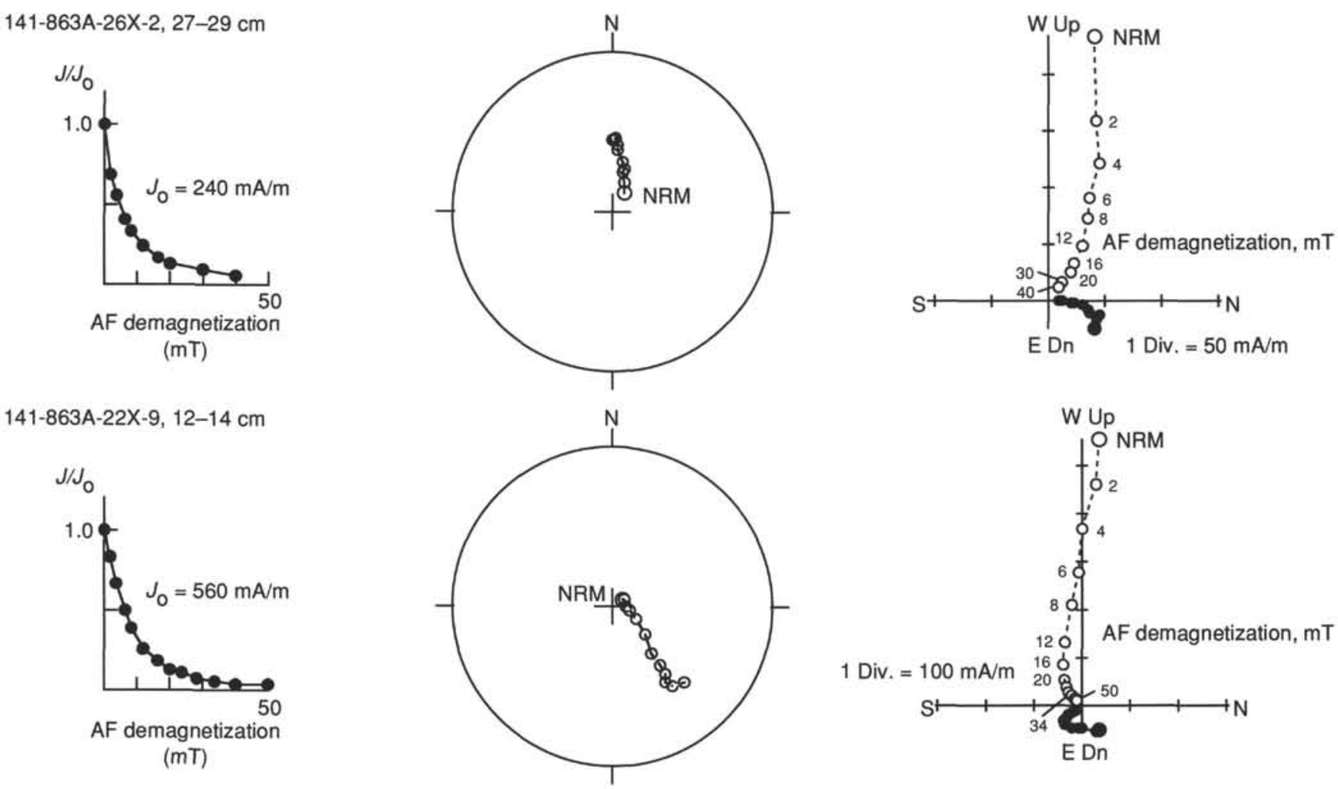

Figure 35. Zijderveld plots, stereograms, and demagnetization intensity plots of samples from lithologic Unit II. These have simpler demagnetization behavior, indicating the presence of a large normally polarized overprint. This overprint persists after 50-mT demagnetization in Sample 141-863A-22X-9, 12–14 cm. Symbols as for Figure 33.

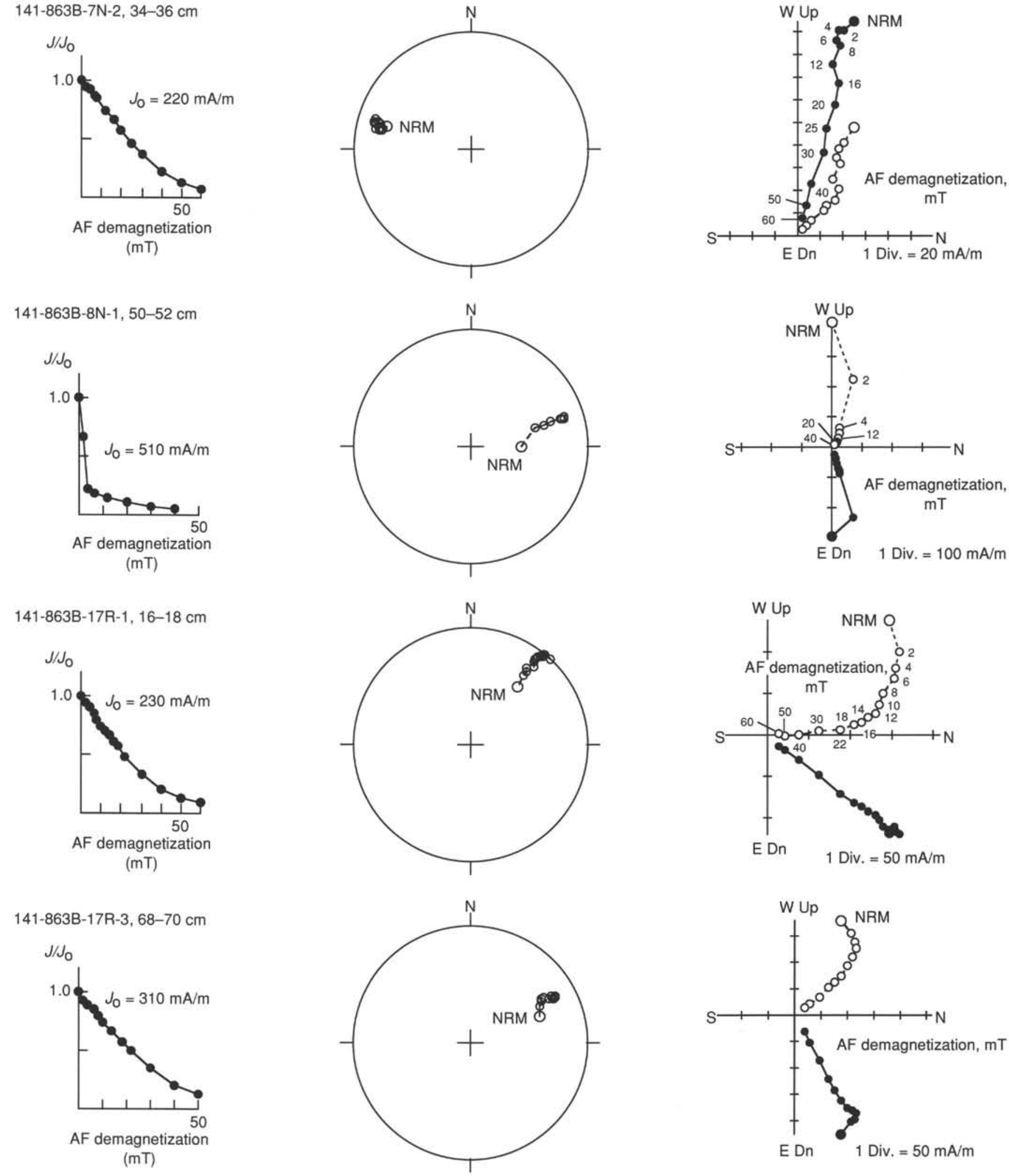

Figure 36. Zijderveld plots, stereograms, and demagnetization intensity plots of samples from the interval between 350 and 500 mbsf, in which the overprint is greatly reduced, and demagnetization isolates a ChRM which appears to be the primary magnetization. Symbols as for Figure 33.

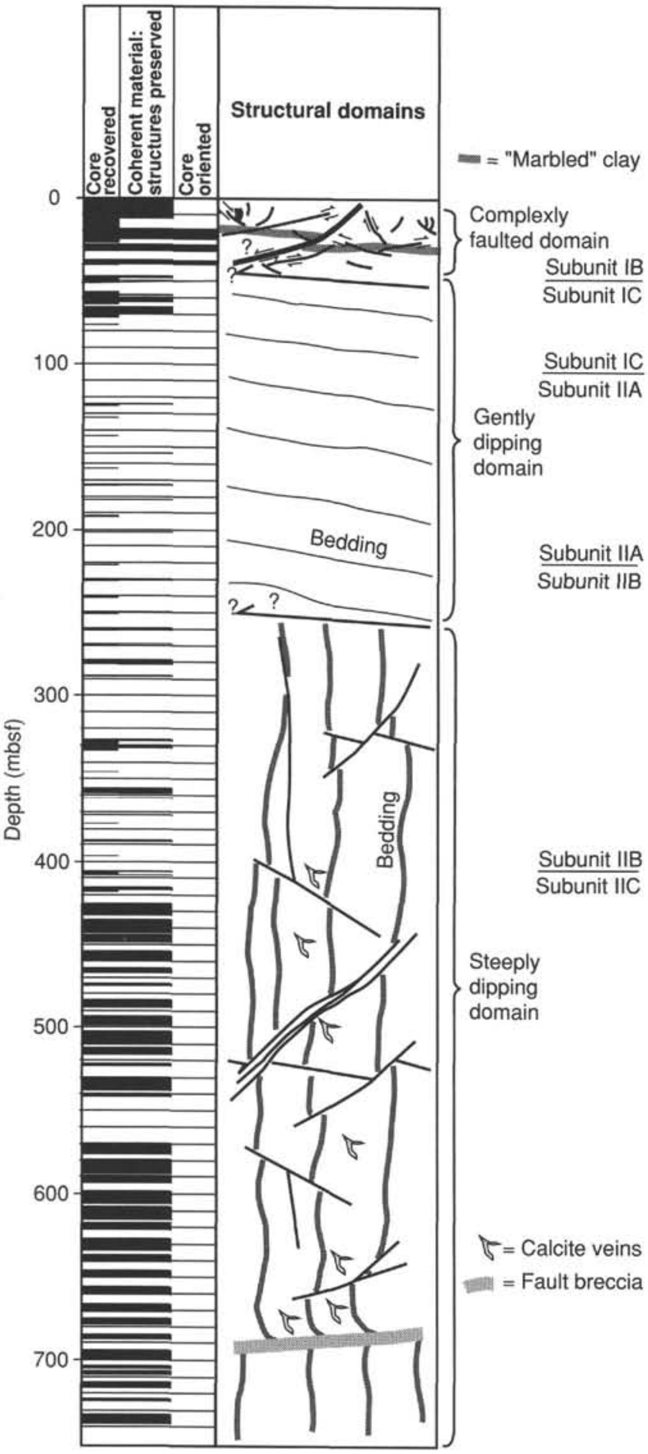

Figure 37. Schematic illustration of major structural features and changes at Site 863, plotted vs. depth. The first three columns show distribution of sediment recovery, the distribution of material sufficiently coherent to make structural observations, and the distribution of material in which structural measurements could be reoriented into a geographical reference frame. Approximate boundaries of lithologic subunits are shown for reference.

main show considerable lithologic variation including millimeter- and centimeter-scale variation as a result of bioturbation. As previously noted (see Structural Geology section, Site 860 chapter), lithologic variation has a considerable control upon the development of deformation bands, and this complicates the deformation band structure at Site 863 (Fig. 50). Rapid, high recovery from the steeply dipping domain at Site 863 means that deformation bands have not been analyzed in as much detail as we would like. Much more work remains, particularly with the relative and absolute reorientation of these data.

Planar bands having observable separations are the most common type of deformation band. These may be thought of as minor faults: the difference is semantic and these structures are included as deformation bands here to maintain consistency with structural descriptions at other sites of Leg 141. Planar deformation bands have moderate to steep dips. Some of the steep bands coincide with bedding surfaces, and separations are not observed. Generally, the moderately dipping deformation bands post-date the steep ones and show both reverse and normal separation of a few millimeters to a few centimeters (Fig. 51). Deformation bands extend into even the coarsest sandstones. This contrasts with deformation bands observed at other sites drilled during Leg 141, where deformation bands are absent from the sands.

Anastomosing networks of deformation bands (Figs. 50 and 52), similar to those characterized in detail at Site 860 (see Structural Geology section, Site 860 chapter), are most common in finer-grained sediments and in proximity to faults. Individual intervals show complex geometries and chronologies that have not yet been fully analyzed. The most intense development of deformation bands is observed in Sections 141-863B-41R-2, 0 cm, through 41R-3, 90 cm, corresponding to the immediate hanging wall of the major fault at 687 mbsf.

Mineral Veins

Discrete carbonate veins are observed in Sections 141-863B-13R-CC, 1–10 cm, and -16R-4, 80–100 cm. In Section 141-863B-13R-CC, 1–10 cm, carbonate veins having quartz-pyrite cores are irregular and up to 1 mm thick (Fig. 53), although they approximate to a moderate dip parallel to small deformation bands/faults having normal separations in the same interval. The veins cut across other deformation bands. In Section 141-863B-16R-4, 80–100 cm, the veins are post-dated by deformation bands with small (a few millimeters) separations.

In Core 141-863B-23R a fault has a 1-mm plane of carbonate slickencrysts. Stepping patterns define the motion as normal dip-slip. Throughout the steeply dipping domain, scoured bases of course sandstones and coarse sands in burrows are preferentially cemented with carbonate. Commonly, there are submillimeter-thick carbonate veins associated with this cementation (Fig. 54). The carbonate cement and veins show an orange fluorescence that relates to the presence of hydrocarbons (see Organic Geochemistry section, this chapter). Veins in the carbonate-cemented sandstones, together with more extensive and irregular cementation (Fig. 55), become more common in Sections 141-863B-41R-2, 0 cm, through -42R-3, 90 cm, approaching the major fault at 687 mbsf. The carbonate veins post-date deformation bands (Fig. 56). Carbonate veins are intensively developed in the breccia associated with the major fault and probably make up the cement to the breccia.

Tectonic Environment and Evolution of Site 863

The structural synthesis of Site 863 is preliminary because the orientation of fault and deformation-band structures and the interpretation of the microstructural evolution of these structures are of critical value.

Table 10. Detailed structural data on a section-by-section basis for Holes 863A and 863B.

Core, section, interval (cm)	Depth (mbsf)	X-Ref hand sheets	Photo?	ID	Identifier	Thickness (cm)	Core face orientation: App. dip	Core face orientation: Direction	Corrected core ref. frame: Strike	Corrected core ref. frame: Dip	Corrected core ref. frame: Dir.	Comments	Slick line: Plunge	Slick line: Trend
141-863A-														
1H-1, 21–21	0.21	1		B	Bedding		3	270	135	4	W			
1H-1, 44–44	0.44	2		B	Bedding		2	270	153	2	W			
1H-1, 60–61	0.6	3		B	Bedding		16	90	29	18	E			
1H-1, 84–85	0.84	4		Ft	Fault		58	270	208	61	W	Normal		
1H-1, 94–94	0.94	5		B	Bedding		2	270	207	2	W			
1H-2, 50–51	2	6		B	Bedding		11	270	160	12	W			
1H-2, 50–51	2	7		Ft	Fault		76	270	195	76	W	Normal		
1H-2, 123–124	2.73	8		B	Bedding		4	270	231	6	N			
1H-2, 140–140	2.9	9		B	Bedding		8	270	129	13	S			
1H-3, 10–11	3.1	10		B	Bedding		13	90	13	13	E			
1H-3, 33–37	3.33	11		Ft	Fault		35	270	166	36	W			
1H-3, 64–65	3.64	12		B	Bedding		5	270	119	10	S			
1H-3, 103–105	4.03	13		Ft	Fault		38	270	183	38	W			
1H-3, 106–110	4.06	14		Ft	Fault		39	90	12	40	E			
1H-3, 111–111	4.11	15		Ft	Fault		1	270	98	7	S			
1H-3, 126–126	4.26	16		Ft	Fault		3	90	45	4	E			
1H-3, 126–128	4.26	17		Ft	Fault		81	270	179	81	W	Reverse		
1H-3, 128–133	4.28	18		Ft	Fault		55	90	306	68	N	Parallel to B.P.		
1H-4, 24–26	4.64	19		Ft	Fault		55	270	191	55	W	Reverse		
1H-4, 25–25	4.65	20		Ft	Fault		9	270	129	14	S	Parallel to B.P.		
1H-4, 28–29	4.68	21		Ft	Fault		1	90	83	8	S			
1H-4, 40–47	4.8	22-1		Ft	Fault		2	90	80	11	S	Parallel to B.P.		
1H-4, 40–47	4.8	22-2		Ft	Fault		70	270	155	72	W	Normal, listric		
1H-4, 40–47	4.8	22-3		Ft	Fault		32	270	116	55	S	Normal, listric		
1H-4, 40–47	4.8	22-4		Ft	Fault		72	90	1	72	E	Normal, listric, antisetic		
1H-4, 40–47	4.8	22-5		Ft	Fault		7	270	95	53	S	Parallel to B.P.		
1H-4, 56–57	4.96	23		Ft	Fault		2	270	117	4	S	Parallel to B.P.		
1H-4, 56–61	4.96	24		Ft	Fault		43	270	178	43	W	Normal		
1H-4, 71–72	5.11	25		Ft	Fault		1	90	82	7	S	Parallel to B.P.		
1H-4, 81–84	5.21	26		Ft	Fault		84	90	2	84	E	Normal		
1H-4, 84–84	5.24	27		Ft	Fault		3	270	233	5	N	Parallel to B.P.		
1H-4, 60–95	5	28		Ft	Fault		75	270	151	77	W	Irregular, normal?		
1H-4, 110–115	5.5	29		Ft	Fault		48	270	186	48	W			
1H-4, 113–115	5.53	30		B	Bedding		29	270	182	29	W	Parallel to B.P.		
1H-4, 133–133	5.73	31		Ft	Fault		5	270	107	17	S			
1H-4, 133–135	5.73	32		Ft	Fault		19	270	160	20	W	Parallel to B.P.		
1H-4, 143–146	5.83	33		B	Bedding		7	270	111	19	S			
1H-5, 15–18	6.05	34		B	Bedding		28	270	171	28	W			
1H-5, 97–97	6.87	35		Ft	Fault		24	270	184	24	W	Normal		
1H-5, 100–107	6.9	36		Ft	Fault		88	270	180	88	W	Normal		
1H-5, 138–140	7.28	37		Ft	Fault		38	270	180	38	W	Parallel to B.P.		
1H-6, 3–5	7.43	38		Ft	Fault		29	270	187	29	W	Parallel to B.P.		
1H-6, 21–21	7.61	39		B	Bedding		14	270	184	14	W	Parallel to B.P.		
1H-6, 24–25	7.64	40		Ft	Fault		44	270	181	44	W	Reverse?		
1H-CC, 6–20	8.26	41		Ft	Fault		81	90	7	81	E	Parallel to B.P., core disturb.?		
2H-1, 52–55	9.12	1		B	Bedding		11	90	39	14	E			
2H-1, 67–79	9.27	2		Ft	Fault		59	90	358	59	E	Reverse?		
2H-1, 100–104	9.6	3		Ft	Fault		36	90	15	37	E	Parallel to B.P.		
2H-1, 120–122	9.8	4		Ft	Fault		33	90	15	34	E			
2H-1, 120–126	9.8	5		Ft	Fault		48	90	355	48	E			
2H-1, 132–134	9.92	6		Ft	Fault		57	90	10	57	E	Parallel to B.P.		
2H-2, 14–19	10.24	7		B	Bedding		12	90	318	16	E			
2H-2, 40–45	10.5	8		Ft	Fault		25	270	218	31	W			
2H-2, 112–120	11.22	9		Ft	Fault		46	90	12	47	E			
2H-2, 126–135	11.36	10		Ft	Fault		48	90	353	48	E			
2H-2, 139–140	11.49	11		Ft	Fault		16	270	227	23	N	Parallel to B.P.		
2H-3, 52–60	12.12	12		B	Bedding		7	90	16	7	E			
2H-3, 96–104	12.16	13		B	Bedding		28	90	13	29	E			
2H-4	13.05	NIL												
2H-5	14.55	NIL												
2H-6	16.05	NIL												
2H-7	17.55	NIL												
2H-CC	18	NIL												
3H-1, 0–2	18.1	1		Ft	Fault		25	270	154	27	W			
3H-1, 11–11	18.21	2		Ft	Fault		16	90	340	17	E	Parallel to B.P.		
3H-1, 12–14	18.22	3		Ft	Fault		3	270	243	7	N			
3H-1, 24–29	18.34	4		Ft	Fault		36	90	10	30	E			
3H-1, 29–29	19.39	5		B	Bedding		1	270	261	6	N			
3H-1, 30–35	18.4	6		Ft	Fault		31	270	213	35	W			
3H-1, 34–35	18.44	7		Ft	Fault		43	90	356	43	E	Reverse, with recumbent folds		
3H-1, 36–38	18.46	8		Ft	Fault		24	270	189	24	W			
3H-1, 38–42	18.48	9		Ft	Fault		14	270	164	15	W			
3H-1, 37–38	18.47	10		Ft	Fault		25	90	347	26	E			
3H-1, 41–42	18.51	11		Ft	Fault		1	270	101	5	S	Reverse		
3H-1, 45–47	18.55	12		Ft	Fault		25	270	184	25	W	Normal		
3H-1, 53–53	18.63	13		Ft	Fault		1	270	95	12	S			
3H-1, 54–54	18.64	14		Ft	Fault		14	90	47	20	S			
3H-1, 68–68	18.78	15		Ft	Fault		1	270	256	4	N			
3H-1, 73–74	18.83	16		Ft	Fault		6	90	315	8	E			
3H-1, 80–86	18.9	17		Ft	Fault		24	270	168	24	W			
3H-1, 85–86	18.95	18		Ft	Fault		16	90	346	16	E			
3H-1, 90–95	19	19		Ft	Fault		67	270	190	67	W	Normal		

Table 10 (continued).

Core, section, interval (cm)	Depth (mbsf)	X-Ref hand sheets	Photo?	ID	Identifier	Thickness (cm)	Core face orientation App. dip	Direction	Corrected core ref. frame Strike	Dip	Dir.	Comments	Slick line Plunge	Trend
141-863A-(Cont)														
3H-1, 93–94	19.03	20		Ft	Fault		28	90	358	28	E			
3H-1, 115–115	19.25	21		Ft	Fault		24	90	358	24	E			
3H-1, 135–135	19.45	22		Ft	Fault		51	90	346	52	E	Reverse		
3H-1, 137–137	19.47	23		B	Bedding		30	90	353	30	E			
3H-2, 20–23	19.8	24		Ft	Fault		48	270	182	48	W	Reverse		
3H-2, 24–24	19.84	25		B	Bedding		45	90	4	45	E			
3H-2, 50–53	20.1	26		Ft	Fault		39	270	204	42	W	Reverse		
3H-2, 55–62	20.15	27		B	Bedding		56	90	5	56	E			
3H-2, 64–72	20.24	28		B	Bedding		30	90	41	38	E			
3H-2, 68–78	20.28	29		Ft	Fault		60	270	182	60	W	Reverse		
3H-2, 98–99	20.58	30		Ft	Fault		78	270	172	78	W	Reverse		
3H-2, 99–99	20.59	31		Ft	Fault		8	90	32	9	E	Parallel to B.P.		
3H-2, 134–135	20.94	32		Ft	Fault		50	270	160	52	W	Reverse		
3H-2, 135–136	20.95	33		Ft	Fault		32	270	163	33	W			
3H-3, 18–20	21.28	34		Ft	Fault		53	270	183	53	W			
3H-3, 38–39	21.48	35		Ft	Fault		50	270	167	51	W	Normal?		
3H-3, 40–48	21.5	36		Ft	Fault		41	270	179	47	W	Parallel to B.P.		
3H-3, 47–53	21.57	37		Ft	Fault		41	270	172	41	W	Parallel to B.P.		
3H-3, 58–64	21.68	38		Ft	Fault		3	90	307	5	N			
3H-3, 99–101	22.09	39		Ft	Fault		61	90	4	61	E			
3H-4, 3–8	22.63	40		Ft	Fault		63	270	205	65	W			
3H-4, 37–42	22.97	41		B	Bedding		60	270	205	62	W			
3H-4, 65–73	23.25	42		B	Bedding		60	270	195	61	W			
3H-4, 111–111	23.71	43		Ft	Fault		2	90	286	7	N			
3H-4, 123–127	23.83	44		Ft	Fault		56	270	192	52	W	Reverse		
3H-4, 125–126	23.85	45		Ft	Fault		11	270	148	13	E	Parallel to B.P.		
3H-4, 128–134	23.88	46		Ft	Fault		20	270	216	24	W	Parallel to B.P.		
3H-5, 9–14	24.19	47		Ft	Fault		60	270	183	60	W	Parallel to B.P.		
3H-5, 14–16	24.24	48		Ft	Fault		13	90	290	34	N			
3H-6	25.6	NIL												
3H-CC	27.1	NIL												
4H-1, 1–3	27.61	1		Ft	Fault		48	270	181	48	W	Parallel to B.P., core disturb. ?		
4H-1, 3–4	27.63	2		Ft	Fault		22	90	22	22	E	Parallel to B.P., core disturb. ?		
4H-1, 25–30	27.85	3		Ft	Fault		48	90	347	49	E	Normal		
4H-1, 26–31	27.86	4		Ft	Fault		56	270	173	56	W	Normal?		
4H-1, 42–44	28.02	5		Ft	Fault		37	90	8	37	E	Parallel to B.P.		
4H-1, 49–53	28.09	6		Ft	Fault		67	270	159	68	W	Normal		
4H-1, 50–54	28.1	7		Ft	Fault		37	270	192	38	W	Normal, conjugate		
4H-1, 55–58	28.15	8		Ft	Fault		38	90	352	38	E			
4H-1, 60–65	28.2	9		Ft	Fault		43	270	187	43	W	Normal		
4H-1, 60–64	28.2	10		Ft	Fault		33	90	350	33	E			
4H-1, 65–67	28.25	11		Ft	Fault		76	90	4	76	E	Reverse		
4H-1, 70–71	28.3	12		Ft	Fault		2	270	108	6	W	Reverse		
4H-1, 70–76	28.3	13		Ft	Fault		56	90	349	56	E			
4H-1, 74–80	28.34	14		Ft	Fault		74	90	15	75	E	Normal		
4H-1, 88–97	28.48	15		Ft	Fault		83	90	355	83	E			
4H-1, 95–98	28.55	16		B	Bedding		31	90	10	31	E			
4H-1, 123–137	28.83	17		Ft	Fault		37	270	163	38	W			
4H-1, 123–137	28.83	18		Ft	Fault		55	90	356	55	E	Reverse, conjugate?		
4H-2, 6–7	29.16	19		B	Bedding		60	90	2	60	E			
4H-2, 6–10	29.16	20		Ft	Fault		34	270	181	34	W			
4H-2, 15–21	29.25	21		Ft	Fault		47	90	7	47	E			
4H-2, 60–64	29.7	22		Ft	Fault		30	270	177	30	W			
4H-2, 60–67	29.7	23		Ft	Fault		60	270	182	60	W	Normal		
4H-2, 65–70	29.75	24		Ft	Fault		45	270	182	45	W	Contact		
4H-2, 68–70	29.78	25		Ft	Fault		12	90	355	12	E	Parallel to B.P.		
4H-2, 68–70	29.78	26		Ft	Fault		33	90	9	33	E	Normal		
4H-2, 74–78	29.84	27		Ft	Fault		16	90	14	16	E	Contact		
4H-2, 78–84	29.88	28		Ft	Fault		63	90	19	64	E	Normal		
4H-2, 83–84	29.93	29		Ft	Fault		40	90	11	40	E	Parallel to B.P.		
4H-2, 85–96	29.95	30		Ft	Fault		45	90	3	45	E	Normal		
4H-2, 101–102	30.11	31		Ft	Fault		41	270	178	41	W	Reverse		
4H-2, 103–103	30.13	32		Ft	Fault		31	90	16	32	E	Parallel to B.P.		
4H-2, 105–108	30.15	33		Ft	Fault		50	270	176	50	W			
4H-2, 107–112	30.17	34		Ft	Fault		1	270	98	7	S	Contact		
4H-2, 110–114	30.2	35		Ft	Fault		47	90	357	47	E	Reverse		
4H-2, 115–112	30.25	36		Ft	Fault		31	270	188	31	W	Contact		
4H-2, 112–125	30.22	37		Ft	Fault		70	270	170	70	W	Contact		
4H-2, 130–135	30.4	38		Ft	Fault		46	270	175	46	W	Normal		
4H-2, 133–137	30.43	39		Ft	Fault		57	90	5	57	E	Contact		
4H-2, 136–140	30.46	40		Ft	Fault		53	270	195	54	W	Reverse		
4H-3, 13–15	30.73	41		Ft	Fault		70	270	176	70	W	Parallel to B.P.		
4H-3, 18–20	30.78	42		Ft	Fault		2	270	112	5	S			
4H-3, 25–27	30.85	43		Ft	Fault		50	270	192	51	W	Reverse, partly normal		
4H-3, 35–43	30.95	44		B	Bedding		61	270	182	61	W			
4H-3, 35–43	30.95	45		Ft	Fault		46	90	336	49	E	Reverse		
4H-CC, 10–12	32.11	46		Ft	Fault		9	270	192	9	W	Normal, low angle		
5H-1, 18–25	37.28	1		Ft	Fault		48	270	185	48	W			
5H-1, 23–33	37.33	2		Ft	Fault		54	90	356	54	E	Parallel to B.P.		
5H-1, 23–33	37.33	3		Ft	Fault		60	90	18	61	E	Parallel to B.P.		
5H-1, 23–33	37.33	4		Ft	Fault		64	90	13	65	E	Parallel to B.P.		
5H-1, 63–70	37.73	5		Ft	Fault		38	270	218	45	W	Reverse		

Table 10 (continued).

Core, section, interval (cm)	Depth (mbsf)	X-Ref hand sheets	Photo?	ID	Identifier	Thickness (cm)	Core face orientation		Corrected core ref. frame			Comments	Slick line	
							App. dip	Direction	Strike	Dip	Dir.		Plunge	Trend
141-863A-(Cont)														
5H-1, 63–70	37.73	6		Ft	Fault		23	90	36	28	E	Normal		
5H-1, 73–83	37.83	7		Ft	Fault		60	270	183	60	W	Reverse		
5H-1, 73–83	37.83	8		Ft	Fault		43	270	204	46	W	Reverse		
5H-1, 86–90	37.96	9		Ft	Fault		70	90	1	70	E	Normal, listric		
5H-1, 86–90	37.96	10		Ft	Fault		62	90	358	62	E	Normal, listric		
5H-1, 99–109	38.09	11		Ft	Fault		67	90	355	67	E			
5H-1, 99–109	38.09	12		Ft	Fault		64	90	358	74	E			
5H-1, 99–109	38.09	13		Ft	Fault		76	90	1	76	E			
5H-1, 116–123	38.26	14		Ft	Fault		59	90	8	59	E	Normal		
5H-1, 121–124	38.31	15		Ft	Fault		42	270	187	42	W	Reverse		
5H-2, 13–18	38.73	16		B	Bedding		42	90	4	42	E			
5H-2, 13–18	38.73	17		Ft	Fault		39	270	184	39	W	Normal		
5H-2, 13–18	38.73	18		Ft	Fault		22	270	185	22	W	Normal		
5H-2, 69–72	39.29	19		B	Bedding		40	90	12	41	E			
5H-2, 69–72	39.29	20		Ft	Fault		25	270	163	26	W	Normal		
5H-2, 69–72	39.29	21		Ft	Fault		17	270	193	17	W	Normal		
5H-2, 133–142	39.93	22		Ft	Fault		52	270	175	52	W	Normal, listric		
5H-2, 142–147	40.02	23		B	Bedding		10	90	310	15	N			
5H-2, 142–147	40.02	24		Ft	Fault		34	90	22	36	E	Normal		
5H-3	40.1	NIL												
5H-CC	41.6	NIL												
6H-1, 43–45	47.03	1		B	Bedding		17	270	167	17	W			
6H-1, 68–72	47.28	2		B	Bedding		37	270	196	38	W			
6H-1, 74–78	47.34	3		B	Bedding		33	270	200	35	W			
6H-1, 91–94	47.51	4		B	Bedding		36	270	185	36	W			
6H-1, 97–101	47.57	5		B	Bedding		23	270	173	23	W			
6H-1, 99–103	47.59	6		B	Bedding		23	270	192	23	W			
6H-1, 107–109	47.67	7		B	Bedding		18	270	174	18	W			
6H-2	48.1	NIL												
6H-CC	49.6	NIL												
7X-1, 43–45	56.53	1		Ft	Fault		50	270	142	57	W	Normal		
7X-1, 49–50	56.59	2		B	Bedding		8	90	45	11	E			
7X-1, 129–131	57.39	3		B	Bedding		18	90	345	19	E			
7X-2, 35–40	57.95	4		B	Bedding		11	90	28	12	E			
7X-2, 35–40	57.95	5		Ft	Fault		10	270	163	39	W	Normal		
7X-3, 49–51	59.59	6		B	Bedding		16	90	23	17	E			
7X-4, 134–138	61.94	7		Ft	Fault		5	270	219	6	W	Normal?		
7X-4, 134–138	61.94	8		B	Bedding		15	270	191	15	W			
7X-5	62.1	NIL												
7X-CC	63.6	NIL												
8X-1, 20–22	65.7	1		B	Bedding		42	90	28	46	E			
8X-1, 53–55	66.03	2		Ft	Fault		52	90	353	52	E	Normal		
8X-1, 53–55	66.03	3		B	Bedding		13	90	323	16	E			
8X-1, 134–136	66.84	4		B	Bedding		3	270	107	10	S			
8X-2, 20–24	67.2	5		Ft	Fault?		68	270	184	68	W	Normal		
8X-2, 20–24	67.2	6		B	Bedding		2	270	259	10	N			
8X-3	68.5	NIL												
8X-4	70	NIL												
8X-CC, 20–23	71.7	7		B	Bedding		17	90	319	22	E			
9X-1	75.4	NIL												
9X-CC	76.9	NIL												
11X-CC	94.7	NIL												
14X-1,	123.7	NIL												
14X-2,	125.2	NIL												
14X-CC, 29–32	126.99	1		B	Bedding		30	90	346	31	E			
15X-CC	133.4	NIL												
16X-CC	143	NIL												
17X-1,	152.7	NIL												
17X-CC	154.2	NIL												
18X-CC	162.4	NIL												
19X-1	172	NIL												
19X-CC	173.5	NIL												
20X-CC	181.6	NIL												
21X-1	191.3	NIL												
21X-CC	192.8	NIL												
22X-CC, 8–10	200.98	1		B	Bedding		32	90	1	32	E			
23X-CC	210.6	NIL												
24X-1	220.3	NIL												
24X-CC	221.8	NIL												
25X-1	229.8	NIL												
25X-2,	231.3	NIL												
25X-CC	232.8	NIL												
26X-1	239.5	NIL												
26X-2	241	NIL												
26X-CC	242.5	NIL												
27X-1, 31–35	249.51	1		B	Bedding		26	90	350	26	E			
27X-1, 43–48	249.63	2		Ft	Fault		87	90	346	87	E			
27X-1, 43–48	249.63	3		Ft	Fault		1	270	96	9	S	Normal		
27X-1, 61–61	249.81	4		B	Bedding		29	90	29	32	E			
27X-CC	250.7	NIL												
28X-1, 37–39	259.17	1		Ft	Fault		25	270	176	25	E			
28X-1, 45–46	259.25	2		Ft	Fault		31	270	175	31	W			

Table 10 (continued).

Core, section, interval (cm)	Depth (mbsf)	X-Ref hand sheets	Photo?	ID	Identifier	Thickness (cm)	Core face orientation App. dip	Core face orientation Direction	Corrected core ref. frame Strike	Corrected core ref. frame Dip	Corrected core ref. frame Dir.	Comments	Slick line Plunge	Slick line Trend
141-863A-(Cont)														
28X-1, 90–95	259.7	3		WS	Web Strand		28	90	338	30	E			
28X-1, 90–95	259.7	3		WS	Web Strand		34	90	26	37	E			
28X-1, 90–95	259.7	3		WS	Web Strand		6	270	198	6	W			
28X-1, 103–107	259.83	4		Ft	Fault		30	270	192	31	W			
28X-1, 105–110	259.85	5		WS	Web Strand		87	270	180	87	W			
28X-2, 22–26	260.52	6		WS	Web Strand		48	90	330	52	E			
28X-2, 28–31	260.58	7		WS	Web Strand		74	270	132	79	S			
29X-1, 10–20	268.5	1		Ft	Fault		28	90	9	29	E			
29X-1, 25–28	268.65	2		Ft	Fault		29	90	26	32	E			
29X-1, 28–28	268.68	3		Ft	Fault		4	270	236	7	N			
29X-1, 54–57	268.94	4		WS	Web Strand		73	270	169	73	W			
29X-2, 5–16	269.95	5		B	Bedding		74	270	196	75	W			
29X-CC	271.4	NIL												
30X-1, 52–54	278.62	1		Ft	Fault		21	90	335	23	E			
30X-1, 63–64	278.73	2		Ft	Fault		42	90	328	47	E			
30X-2, 30–33	279.9	3		B	Bedding		73	270	173	73	W			
30X-2, 33–35	279.93	4		Ft	Fault		40	90	6	40	E	Normal		
30X-2, 35–37	279.95	5		B	Bedding		71	270						
30X-2, 37–37	279.97	6		Ft	Fault		8	270	206	9	W	Normal?		
30X-2, 44–48	280.04	7		B	Bedding		79	90	357	79	E			
30X-2, 50–53	280.1	8		Ft	Fault		48	270	147	53	W	Normal?		
30X-2, 52–54	280.12	9		B	Bedding		82	90	11	82	E			
30X-2, 57–60	280.17	10		B	Bedding		35	90	55	51	S			
30X-2, 62–63	280.22	11		B	Bedding		85	90	50	87	E			
30X-2, 62–63	280.22	12		Ft	Fault		10	90	22	11	E	Normal		
30X-2, 62–64	280.22	13		B	Bedding		67	90	338	69	E			
30X-2, 62–64	280.22	14		B	Bedding		83	90	348	83	E			
30X-CC, 31–33	281.41	15		Ft	Fault		76	90	323	79	E	Vein?		
30X-CC, 33–35	281.43	16		Ft	Fault		82	90	323	84	E	Vein?		
30X-CC, 33–35	281.43	17		Ft	Fault		73	270	327	76	E	Vein?		
31X-1, 20–21	287.8	1		Ft	Fault		38	270	334	4	W			
31X-1, 20–25	287.8	2		Ft	Fault		62	270	194	63	W			
31X-1, 38–41	287.98	3		Ft	Fault		74	270	254	85	N			
31X-1, 62–64	288.22	4		Ft	Fault		74	90	320	78	E			
31X-2, 20–25	302.8	5		Ft	Fault		62	270	120	75	S			
31X-2, 35–50	302.95	6		Ft	Fault		61	270	205	63	W	Web strand, also		
141-863B-														
4X-1, 33–35	326.23	1		B	Bedding		71	90	351	71	E			
4X-1, 50–53	326.4	2		Ft	Fault		65	270	191	65	W			
4X-1, 97–99	326.87	3		Ft	Fault		57	270	221	64	W			
4X-1, 103–108	326.93	4		B	Bedding		81	270	165	81	W			
4X-1, 117–117	327.07	5		Ft	Fault		2	90	72	6	S			
4X-1, 131–133	327.21	6		B	Bedding		85	270	148	86	W			
4X-2	327.4	NIL												
4X-3, 120–122	330.1	7		B	Bedding		55	90	17	56	E			
4X-4, 58–61	330.98	8		B	Bedding		77	90	345	77	E			
4X-4, 102–104	331.42	9		B	Bedding		75	90	339	76	E			
4X-4, 102–106	331.42	10		B	Bedding		66	90	338	68	E			
4X-5, 5–11	331.95	11		B	Bedding		71	90	10	71	E			
4X-5, 35–70	332.25	12		B	Bedding		88	90	13	88	E			
4X-CC, 16–18	333.56	13		Ft	Fault		47	270	210	44	W	Web strand, also		
5X-CC, 12–15	335.72	1		B	Bedding		86	90	60	88	S			
5X-CC, 12–15	335.72	2		Ft	Fault		71	270	220	75	W			
6X-CC, 20–26	345.4	1		B	Bedding		87	90	347	87	E			
6X-CC, 36–43	345.56	2		B	Bedding		86	270	255	89	N			
7N-1, 85–100	355.75	1		B	Bedding		76	90	47	80	S			
7N-1, 85–100	355.75	2		Ft	Fault		81	90	59	85	S	Reverse		
7N-1, 85–100	355.75	3		Ft	Fault		81	90	32	82	E	Reverse		
7N-1, 85–100	355.75	4		Ft	Fault		85	90	58	87	E	Reverse		
7N-1, 85–100	355.75	5		B	Bedding		78	90	35	80	E			
7N-1, 85–100	355.75	6		Ft	Fault		60	270	220	66	W	Reverse		
7N-1, 85–100	355.75	7		Ft	Fault		82	90	34	83	E			
7N-1, 85–100	355.75	8		Ft	Fault		75	90	27	77	E			
7N-2, 8–9	356.48	9		Ft	Fault		22	270	192	22	W			
7N-2, 15–30	356.55	10		B	Bedding		72	90	345	73	E			
7N-2, 28–30	356.68	11		Ft	Fault		73	90	52	79	S			
7N-2, 40–50	356.8	12		Ft	Fault		77	90	40	80	E	Reverse		
7N-2, 44–47	356.88	13		Ft	Fault		66	270	161	67	W			
7N-2, 50–55	356.94	14		Ft	Fault		78	270	178	78	W	Reverse		
7N-2, 53–57	356.93	15		Ft	Fault		68	270	185	68	W			
7N-2, 52–55	356.92	16		Ft	Fault		71	90	308	81	N	Reverse		
7N-2, 55–65	356.95	17		Ft	Fault		68	270	168	68	W	Reverse		
7N-2, 64–75	357.04	18		B	Bedding		73	90	28	75	E			
7N-CC	357.3	NIL												
8N-1, 23–27	357.63	1		Ft	Fault		45	270	120	63	S	Reverse, second		
8N-1, 25–30	357.65	2		Ft	Fault		86	270	157	86	W	Parallel to B.P., first		
8N-1, 25–30	357.65	3		B	Bedding		88	90	327	88	E			
8N-1, 27–27	357.67	4		Ft	Fault		11	90	78	43	S	Reverse, third		
8N-1, 32–32	357.72	5		Ft	Fault		10	90	74	32	S	Reverse, third		
8N-1, 32–37	357.72	6		Ft	Fault		72	90	325	75	E	Reverse, second		
8N-1, 40–45	357.8	7		B	Bedding		86	270	148	87	W	True bedding		
8N-1, 40–45	357.8	8		B	Bedding		57	270	148	61	W	Cross bedding		

Table 10 (continued).

Core, section, interval (cm)	Depth (mbsf)	X-Ref hand sheets	Photo?	ID	Identifier	Thickness (cm)	Core face orientation		Corrected Core ref. frame			Comments	Slick line	
							App. dip	Direction	Strike	Dip	Dir.		Plunge	Trend
141-863B-(Cont)														
8N-1, 40–48	357.8	9		Ft	Fault		59	90	347	60	E	Normal		
8N-1, 50–53	357.9	10		B	Bedding		82	270	128	85	E	True bedding		
8N-1, 50–53	357.9	11		B	Bedding		67	270	152	69	W	Cross bedding		
8N-1, 56–59	357.96	12		Ft	Fault		70	90	345	71	E	Forth?		
8N-1, 52–71	357.92	13		Ft	Fault		72	270	178	72	W	Forth?		
8N-1, 85–80	358.25	14		B	Bedding		62	270	136	69	W			
8N-1, 85–80	358.25	15		Ft	Fault		64	270	145	68	W	Forth?		
8N-2	358.9	NIL												
8N-CC	360.4	NIL												
9X-CC, 5–10	361.45	1		B	Bedding		70	270	120	85	S			
10R-1, 75–86	371.75	1		Ft	Fault		42	90	51	55	S			
10R-1, 75–86	371.75	2		Ft	Fault		62	90	34	66	E			
10R-1, 75–86	371.75	3		Ft	Fault		72	90	27	74	E			
10R-1, 92–96	371.92	4		Ft	Fault		55	90	32	59	E			
10R-1, 102–108	372.02	5		Ft	Fault		56	270	173	56	W			
10R-1, 102–108	372.02	6		Ft	Fault		4	270	129	6	S			
10R-CC	372.5	NIL												
11R-1, 36–40	376.96	1		Ft	Fault		36	270	213	41	W			
11R-1, 37–44	376.97	2		Ft	Fault		54	90	336	57	E			
11R-1, 53–59	377.13	3		Ft	Fault		42	90	346	43	E			
11R-1, 64–69	377.24	4		Ft	Fault		65	270	222	71	W			
11R-1, 70–77	377.3	5		Ft	Fault		50	270	245	71	N			
11R-CC	378.1	NIL												
12R-1, 55–60	386.85	1		Ft	Fault		60	90	11	60	E			
12R-1, 55–60	386.85	2		Ft	Fault		85	270	126	87	S			
12R-1, 55–60	386.85	3		Ft	Fault		58	270	214	63	W	Normal		
12R-1, 90–95	387.2	4		Ft	Fault		37	270	126	52	S			
12R-1, 90–95	387.2	5		Ft	Fault		73	270	153	75	W	Normal		
12R-1, 90–95	387.2	6		Ft	Fault		19	90	32	22	E			
12R-1, 90–95	387.2	7		Ft	Fault		27	90	291	55	N			
12R-1, 95–105	387.25	8		Ft	Fault		36	90	300	56	N			
12R-1, 95–105	387.25	9		Ft	Fault		65	90	337	67	E	Normal		
12R-1, 95–105	387.25	10		Ft	Fault		73	270	191	73	W			
12R-1, 95–105	387.25	11		Ft	Fault		62	90	4	62	E	Parallel to B.P., wavy		
12R-CC	387.8	NIL												
13R-1, 30–35	396.1	1		Ft	Fault		23	90	305	36	E	Shear plane, normal step		
13R-1, 44–45	396.24	2		Ft	Fault		28	90	310	39	E	Shear plane, normal step	38	54
13R-1, 55–57	396.35	3		Ft	Fault		85	90	330	86	E	Normal		
13R-1, 59–62	396.39	4		Ft	Fault		66	270	135	73	W	Normal		
13R-1, 59–62	396.39	5		Ft	Fault		25	90	38	31	E			
13R-CC, 0–15	397.3	6		V	Vein		43	270	130	55	S	Calcite		
13R-CC, 0–15	397.3	7		V	Vein		52	270	130	63	S	Calcite		
13R-CC, 0–15	397.3	8		Ft	Fault		65	90	3	65	E			
13R-CC, 0–15	397.3	9		Ft	Fault		38	270	175	38	W	Normal		
13R-CC, 0–15	397.3	10		Ft	Fault		53	270	159	55	W			
13R-CC, 0–15	397.3	11		B	Bedding		86	270	202	86	W			
13R-CC, 0–15	397.3	12		Ft	Fault		2	90	272	52	N			
13R-CC, 0–15	397.3	13		Ft	Fault		85	270	220	85	W	Normal		
13R-CC, 0–15	397.3	14		Ft	Fault		48	270	175	48	W	Calcite		
14R-1, 56–59	406.06	1		Ft	Fault		34	270	240	54	N			
14R-1, 105–123	406.55	2		Ft	Fault		36	90	69	64	S			
14R-1, 105–123	406.55	3		Ft	Fault		27	270	107	60	S			
14R-1, 105–123	406.55	4		Ft	Fault		25	90	78	66	S	Normal, lower main fault		
14R-1, 105–123	406.55	5		Ft	Fault		50	270	252	76	N	Reverse		
14R-1, 105–123	406.55	6		Ft	Fault		66	90	24	68	E	Normal, upper main fault		
14R-1, 105–123	406.55	7		Ft	Fault		73	90	45	78	E	Normal lower main fault		
14R-2, 11–11	407.11	8		Ft	Fault		15	90	69	37	S			
14R-2, 52–60	407.52	9		Ft	Fault		63	270	127	73	S			
14R-2, 82–98	407.82	10		Ft	Fault		30	270	240	49	N			
14R-2, 82–98	407.82	11		Ft	Fault		54	270	105	79	S			
14R-2, 82–98	407.82	12		Ft	Fault		51	90	69	73	S	Normal		
14R-2, 82–98	407.82	13		Ft	Fault		57	270	237	70	N			
14R-3, 18–30	408.68	14		B	Bedding		72	90	340	73	E			
14R-CC	410	NIL												
15R-1, 34–35	415.54	1		Ft	Fault		8	90	276	51	N			
15R-1, 68–95	415.88	1		B	Bedding		81	90	20	82	E			
15R-2, 21–22	416.91	2		V	Vein		26	270	164	27	W	Calcite		
15R-2, 25–28	416.95	3		Ft	Fault		21	270	183	21	W			
15R-2, 30–36	417	4		Ft	Fault		27	270	121	44	S	Normal?		
15R-2, 45–50	417.15	5		B	Bedding		50	270	160	52	W			
15R-2, 70–80	417.4	6		B	Fault		86	270	113	88	S			
15R-2, 85–95	417.55	7		Ft	Fault		35	90	84	82	S	Normal		
15R-2, 95–98	417.65	8		Ft	Fault		48	270	239	65	N	Normal		
15R-2, 97–100	417.67	9		Ft	Fault		37	270	202	39	W	Normal		
15R-2, 97–98	417.67	10		Ft	Fault		56	270	220	63	W	Normal		
15R-2, 120–127	417.9	11		Ft	Fault		10	270	104	37	S	Normal		
15R-2, 120–127	417.9	12		Ft	Fault		62	270	168	63	W	Normal		
15R-2, 133–138	418.03	13		Ft	Fault		71	270	168	78	W			
15R-CC	418.2	NIL												
16R-1, 38–42	425.08	1		Ft	Fault		60	90	55	72	S	Normal		
16R-2, 25–40	426.45	2		Ft	Fault		72	90	7	72	E	Normal		

Table 10 (continued).

Core, section, interval (cm)	Depth (mbsf)	X-Ref hand sheets	Photo?	ID	Identifier	Thickness (cm)	Core face orientation		Corrected core ref. frame			Comments	Slick line	
							App. dip	Direction	Strike	Dip	Dir.		Plunge	Trend
141-863B-(Cont)														
16R-2, 25–40	426.45	3		B	Fault		81	270	165	81	W			
16R-3, 106–108	428.76	4		Ft	Fault		28	270	121	46	S			
16R-3, 108–110	428.78	5		Ft	Fault		21	270	123	35	S			
16R-4, 30–30	429.5	6		Ft	Fault		48	270	125	63	S			
16R-4, 30–35	429.5	7		B	Fault		73	90	345	74	E			
16R-4, 68–69	429.88	8		Ft	Fault		10	90	251	50	N			
16R-4, 62–72	429.82	9		Ft	Fault		77	270	153	78	W	Normal		
16R-4, 70–75	429.9	10		Ft	Fault		77	270	228	81	N			
16R-4, 70–75	429.9	11		Ft	Fault		5	270	141	6	W	Reverse		
16R-4, 75–85	429.95	12		Ft	Fault		85	90	332	86	E	Normal, cut vein		
16R-4, 75–85	429.95	13		Ft	Fault		25	270	241	44	N	Reverse		
16R-4, 75–85	429.95	14		Ft	Fault		56	270	152	59	W	Normal		
16R-4, 83–100	430.03	15		Ft	Fault		80	270	147	82	W	Normal	36	153
16R-4, 94–96	430.14	16		Ft	Fault		15	270	98	62	S	Reverse		
16R-4, 94–96	430.14	17		Ft	Fault		16	270	96	70	S			
16R-5, 20–75	430.9	18		Ft	Fault		84	270	190	84	W			
16R-5, 55–60	431.25	19		B	Fault		87	270	192	87	W			
16R-5, 64–73	431.34	20		Ft	Fault		55	270	144	60	W	Normal	40	173
16R-CC	432.2	NIL												
17R-1, 10–12	434.5	1		B	Bedding		13	270	256	44	N			
17R-1, 36–39	434.76	2		Ft	Fault		30	270	195	31	W			
17R-1, 98–100	435.38	3		B	Bedding		8	90						
17R-1, 109–110	435.49	4		Ft	Fault		4	270	268	60	N			
17R-1, 114–118	435.54	5		B	Bedding		55	90	304	69	N			
17R-1, 124–131	435.64	6		Ft	Fault		48	90	20	50	E			
17R-1, 129–133	435.69	7		Ft	Fault		30	90	315	39	E			
17R-2, 83–91	436.73	8		Ft	Fault		50	270	125	65	S			
17R-2, 100–140	436.9	9		Ft	Fault		86	270	181	86	W			
17R-2, 123–126	437.13	10		Ft	Fault		54	270	187	54	W			
17R-3, 62–69	438.02	11		Ft	Fault		58	90	32	62	E			
17R-3, 63–67	438.03	12		B	Bedding		40	270	150	44	W			
17R-3, 67–69	438.07	13		Ft	Fault		25	270	206	27	W			
17R-3, 99–109	438.39	14		Ft	Fault		43	90	308	57	N			
17R-3, 125–130	438.65	15		Ft	Fault		1	90	87	18	S			
17R-3, 124–132	438.64	16		Ft	Fault		48	90	329	52	E			
17R-4, 70–80	439.6	17		Ft	Fault		58	270	188	58	W			
17R-4, 112–113	440.02	18		B	Bedding		14	90	81	58	S			
17R-4, 112–113	440.02	19		B	Bedding		1	90	88	32	S			
17R-5, 41–52	440.81	20		Ft	Fault		50	90	311	61	N			
17R-5, 92–110	441.32	21		B	Bedding		58	270	107	79	S			
17R-6, 55–60	442.45	22		Ft	Fault		45	90	9	45	E	Normal		
17R-6, 55–60	442.45	23		Ft	Fault		51	270	169	51	W			
17R-7, 10–13	434.5	24		B	Bedding		10	90	272	77	N			
17R-7, 19–20	434.59	25		B	Bedding		6	270	265	50	N			
17R-7, 27–32	434.67	26		Ft	Fault		26	270	107	59	S	Normal		
18R-1	444	NIL												
18R-2, 25–40	445.75	1		Ft	Fault		10	90	354	70	E			
18R-2, 94–98	446.44	2		Ft	Fault		35	270	130	48	S			
18R-3, 27–73	447.27	3		Ft	Fault		83	270	180	83	W			
18R-3, 25–75	447.25	4		B	Bedding		76	270	195	76	W			
18R-4	448.5	NIL												
18R-CC	450	NIL												
19R-1, 25–45	453.95	1		B	Bedding		85	90	26	86	E			
19R-1, 45–75	454.15	2		B	Bedding		84	90	344	84	E			
19R-1, 73–105	454.43	3		B	Bedding		82	90	350	82	E			
19R-1, 115–135	454.85	4		B	Bedding		80	270	194	80	W			
19R-2, 35–42	455.55	5		Ft	Fault		47	90	302	64	N			
19R-3	456.7	NIL												
19R-4, 0–80	458.2	6		B	Bedding		90	90	45	90	E			
19R-5	459.7	NIL												
19R-CC	461.2	NIL												
20R-1, 105–120	464.45	1		B	Bedding		87	270	242	89	N			
20R-1, 32–34	463.72	2		Ft	Fault		55	270	225	64	W			
20R-2, 0–10	464.9	3		Ft	Fault		87	90	7	87	W	Normal		
20R-2, 0–15	464.9	4		B	Bedding		84	270	215	85	W			
20R-2, 20–40	465.1	5		B	Bedding		75	270	169	75	W			
20R-2, 40–47	465.3	6		Ft	Fault		35	270	170	35	W	Normal		
20R-2, 45–45	465.35	7		Ft	Fault		54	270	203	56	W			
20R-2, 43–49	465.33	8		Ft	Fault		67	270	181	67	W			
20R-2, 45–50	465.35	9		B	Bedding		87	270	188	87	W			
20R-2, 85–92	465.75	10		Ft	Fault		72	270	190	72	W			
20R-2, 97–97	465.87	11		Ft	Fault		50	270	166	51	W			
20R-3, 0–8	466.4	12		Ft	Fault		47	90	58	64	S	Reverse		
20R-3, 3–15	466.43	13		B	Bedding		37	270	196	38	W			
20R-3, 42–42	466.82	14		SP	Sandpipe		7	90	78	31	S			
20R-3, 43–45	466.83	15		B	Bedding		46	90	339	49	E			
20R-3, 45–49	466.85	16		Ft	Fault		47	90	66	69	S	Slump fault?		
20R-3, 50–52	466.9	17		B	Bedding		6	270	107	20	S			
20R-3, 54–60	466.94	18		B	Bedding		37	270	145	43	W			
20R-CC	467.9	NIL												
21R-1, 32–48	473.32	1		B	Bedding		88	270	218	88	W			
21R-2, 90–95	475.4	2		Ft	Fault		79	270	214	81	W			

Table 10 (continued).

Core, section, interval (cm)	Depth (mbsf)	X-Ref hand sheets	Photo?	ID	Identifier	Thickness (cm)	Core face orientation		Corrected core ref. frame			Comments	Slick line	
							App. dip	Direction	Strike	Dip	Dir.		Plunge	Trend
141-863B-(Cont)														
21R-3, 90–100	476.9	3		Ft	Fault		65	270	215	69	W			
21R-CC	477.5	NIL												
22R-1, 46–47	483.16	1		Ft	Fault		79	90	36	81	E			
22R-1, 45–47	483.15	2		Ft	Fault		37	270	10	38	W	Reverse		
22R-1, 45–50	483.15	3		Ft	Fault		45	270	22	48	W	Reverse?	12	12
22R-1, 58–62	483.28	4		Ft	Fault		61	90	1	61	E			
22R-1, 59–83	483.29	5		Ft	Fault		60	90	21	62	E		21	143
22R-2, 110–115	485.3	6		Ft	Fault		58	90	293	76	N			
22R-3, 35–45	486.05	7		Ft	Fault		57	90	336	59	E			
22R-4	487.2	NIL												
22R-CC	488.7	NIL												
23R-1, 78–80	493.18	1		Ft	Fault		38	270	241	58	N	Reverse		
23R-1, 83–85	493.23	2		Ft	Fault		37	270	242	58	N	Reverse		
23R-1, 85–95	493.25	3		Ft	Fault		81	270	170	81	W	Reverse, part of above		
23R-1, 110–120	493.5	4		Ft	Fault		80	270	178	80	W	Reverse, cut by normal		
23R-1, 110–120	493.5	5		Ft	Fault		56	270	205	59	W	Reverse		
23R-2, 0–10	493.9	6		Ft	Fault		58	90	321	64	E	Reverse		
23R-2, 0–10	493.9	7		Ft	Fault		86	270	152	86	W	Normal		
23R-2, 0–10	493.9	8		Ft	Fault		85	90	26	86	E			
23R-2, 0–10	493.9	9		B	Bedding		87	270	152	87	W			
23R-2, 18–25	494.08	10		Ft	Fault		59	270	344	60	W		59	238
23R-2, 18–32	494.08	11		Ft	Fault		64	90	330	65	E		49	0
23R-2, 30–38	494.2	12		Ft	Fault		58	90	332	61	E		41	0
23R-2, 62–65	494.52	13		Ft	Fault		33	90	76	68	S	Reverse step, vein	47	229
23R-2, 87–92	494.77	14		Ft	Fault		50	270	36	56	W			
23R-2, 93–94	494.83	15		Ft	Fault		8	90	83	48	S			
23R-3, 20–30	495.6	16		Ft	Fault		55	270	58	70	N		53	27
23R-3, 105–125	496.45	17		Ft	Fault		83	270	73	88	N		69	66
23R-4	496.9	NIL												
23R-5	498.4	NIL												
23R-CC	499.9	NIL												
24R-1, 3–9	502.03	1		Ft	Fault		51	90	326	56	E	Normal step	37	357
24R-1, 13–26	502.13	2		Ft	Fault		62	270	35	66	W		64	276
24R-1, 22–37	502.22	3		Ft	Fault		55	270	10	56	W		53	308
24R-1, 43–53	502.43	4		Ft	Fault		80	270	354	80	W		80	251
24R-1, 66–70	502.66	5		Ft	Fault		45	270	40	53	W			
24R-1, 80–90	502.8	6		Ft	Fault		50	90	46	60	E	Reverse step	31	204
24R-1, 80–90	502.8	7		Ft	Fault		30	90	78	69	S		48	103
24R-1, 80–90	502.8	8		Ft	Fault		63	90	56	71	S	Reverse step	26	227
24R-1, 102–104	503.02	9		Ft	Fault		25	270	248	51	N		5	252
24R-1, 112–113	503.12	10		Ft	Fault		30	270	168	31	W		22	304
24R-2, 80–83	504.3	11		Ft	Fault		61	270	138	67	N			
24R-2, 83–86	504.33	12		Ft	Fault		65	90	336	67	E			
24R-2, 80–90	504.3	13		Ft	Fault		61	270	22	63	W		48	349
24R-2, 88–100	504.38	14		Ft	Fault		73	270	32	76	W		5	12
24R-2, 97–105	504.47	15		Ft	Fault		21	90	58	33	S		34	150
24R-3, 30–40	505.5	16		B	Bedding		84	90	322	85	E			
24R-3, 83–90	505.83	17		Ft	Fault		10	90	88	81	S			
24R-3, 90–100	505.9	17		Ft	Fault		86	90	24	86	E			
24R-3, 130–135	506.3	18		Ft	Fault		51	90	64	71	S		58	100
24R-3, 133–150	506.33	19		Ft	Fault		72	90	18	54	W		7	203
24R-4, 13–18	506.63	20		Ft	Fault		32	90	59	50	S		47	166
24R-4, 15–33	506.65	21		Ft	Fault		65	90	45	72	E			
24R-4, 115–115	507.65	22		Ft	Fault		48	270	206	51	W			
24R-4, 115–123	507.65	23		Ft	Fault		50	90	327	55	E	Normal, listric		
24R-4, 123–130	507.73	24		Ft	Fault		60	270	204	62	W	Normal		
24R-5	508	NIL												
24R-CC	509.5	NIL												
25R-1, 7–28	511.77	1		Ft	Fault		41	270	152	45	W			
25R-1, 7–28	511.77	2		Ft	Fault		69	90	1	69	E			
25R-1, 35–39	512.05	3		Ft	Fault		52	270	188	52	W	Normal		
25R-1, 69–70	512.39	4		Ft	Fault		2	90	86	28	S	Reverse		
25R-1, 75–90	512.45	5		Ft	Fault		45	90	318	53	E			
25R-1, 75–90	512.45	6		Ft	Fault		13	90	332	15	E			
25R-1, 103–106	512.73	7		Ft	Fault		34	90	17	35	E			
25R-2, 12–22	513.32	8		Ft	Fault		51	90	7	51	E			
25R-2, 12–22	513.32	9		Ft	Fault		5	270	230	8	N			
25R-2, 30–40	513.5	10		Ft	Fault		57	90	306	69	N			
25R-2, 94–126	514.14	11		B	Bedding		11	90	359	83	E			
25R-3	514.7	NIL												
25R-4, 30–40	516.5	12		B	Bedding		12	90	49	43	S			
25R-CC	517.7	NIL												
26R-1	521.4	NIL												
26R-2, 65–148	523.55	1		B	Bedding		85	270	183	85	W			
26R-CC	524.4	NIL												
27R-1, 137–138	531.97	1		Ft	Fault		3	90	273	49	N			
27R-2, 21–23	532.31	2		Ft	Fault		14	270	209	16	W			
27R-2, 106–116	533.16	3		Ft	Fault		70	270	177	70	W			
27R-2, 115–117	533.25	4		Ft	Fault		32	270	118	53	S			
27R-3, 17–19	533.77	5		Ft	Fault		33	270	136	42	W			
27R-3, 23–24	533.83	6		B	Bedding		10	270	243	21	N			
27R-4, 45–53	535.55	7		B	Bedding		76	270	247	84	N			

Table 10 (continued).

Core, section, interval (cm)	Depth (mbsf)	X-Ref hand sheets	Photo?	ID	Identifier	Thickness (cm)	Core face orientation		Corrected core ref. frame			Comments	Slick line	
							App. dip	Direction	Strike	Dip	Dir.		Plunge	Trend
141-863B-(Cont)														
27R-4, 86–96	535.96	8		B	Bedding		56	270	193	57	W			
27R-4, 110–125	536.2	9		B	Bedding		70	90	55	78	S			
27R-5	536.6	NIL												
27R-CC	538.1	NIL												
28R-1, 0–40	540.2	1		B	Bedding		87	270	220	80	W			
28R-2	541.7	NIL												
28R-CC	543.2	NIL												
29R-CC	549.7	NIL												
30R-CC	559.4	NIL												
31R-1, 29–31	569.39	1		Ft	Fault		33	270	216	39	W			
31R-1, 41–46	569.51	2		Ft	Fault		32	270	191	32	W			
31R-1, 56–70	569.66	3		Ft	Fault		21	90	29	24	E			
31R-1, 56–70	569.66	4		Ft	Fault		18	270	211	21	W			
31R-1, 88–95	569.98	5		Ft	Fault		34	90	357	34	E			
31R-1, 130–132	570.4	6		B	Bedding		18	270	150	20	W			
31R-2, 108–115	571.68	7		Ft	Fault		64	270	223	70	W	Reverse		
31R-2, 135–140	571.95	8		Ft	Fault		42	90	349	43	E			
31R-2, 132–144	571.92	9		Ft	Fault		63	90	296	77	N			
31R-3, 23–33	572.33	10		Ft	Fault		55	270	228	65	N			
31R-3, 51–63	572.61	11		Ft	Fault		62	90	309	72	N			
31R-3, 100–107	573.1	12		Ft	Fault		33	270	222	41	N	Normal		
31R-3, 102–113	573.12	13		B	Bedding		78	90	337	79	E			
31R-4	573.6	NIL												
31R-5	575.1	NIL												
31R-CC	576.6	NIL												
32R-1	578.8	NIL												
32R-2, 60–75	580.9	1		B	Bedding		85	90	2	85	E			
32R-3, 52–90	582.32	2		B	Bedding		87	270	202	87	W			
32R-4	583.3	NIL												
32R-5, 45–55	585.15	3		B	Bedding		88	270	220	88	W			
32R-5, 70–72	585.4	4		Ft	Fault		40	90	25	43	E	Reverse		
32R-5, 75–76	585.45	5		Ft	Fault		14	270	206	16	W	Normal		
32R-6	586	NIL												
32R-7	587	NIL												
32R-CC	587.6	NIL												
33R-1, 77–100	588.4	1		B	Bedding		88	270	221	88	W			
33R-2	589.9	NIL												
33R-3, 33–35	591.73	2		Ft	Fault		84	270	186	84	W	Normal		
33R-3, 33–37	591.73	3		Ft	Fault		50	90	333	53	E	Normal		
33R-3, 52–62	591.92	4		Ft	Fault		58	90	308	69	N	Normal		
33R-3, 58–68	591.98	5		Ft	Fault		56	90	28	59	E	Normal	50	160
33R-3, 73–76	592.13	6		Ft	Fault		43	90	351	43	E			
33R-3, 73–77	592.13	7		Ft	Fault		46	90	6	48	E		13	182
33R-3, 75–90	592.15	8		Ft	Fault		84	90	7	74	E		29	15
33R-3, 83–90	592.23	9		Ft	Fault		71	90	24	72	E			
33R-3, 87–97	592.27	10		B	Bedding		66	90	355	66	E			
33R-4, 2–10	592.92	11		Ft	Fault		68	90	21	69	E		26	190
33R-4, 10–10	593	12		Ft	Fault		16	270	281	57	S		32	256
33R-4, 33–33	593.23	13		Ft	Fault		18	90	279	63	N			
33R-CC	594.4	NIL												
34R-1, 10–25	598.2	1		B	Bedding		87	90	18	87	E			
34R-1, 108–109	599.18	2		Ft	Fault		5	90	88	64	S	Normal step	28	104
34R-1, 114–130	599.24	3		Ft	Fault		83	90	12	83	E		59	24
34R-1, 128–136	599.38	4		Ft	Fault		50	270	7	50	W		18	352
34R-1, 133–140	599.43	5		Ft	Fault		45	270	4	46	W	Normal, vein, with synthetic n.f.	16	349
34R-1, 140–150	599.5	6		Ft	Fault		55	270	280	10	W		14	1
34R-2, 5–35	599.65	7		Ft	Fault		80	90	349	80	E		49	15
34R-3, 19–22	601.29	8		Ft	Fault		28	90	313	77	S		76	24
34R-3, 50–53	601.6	9		Ft	Fault		15	90	54	24	S			
34R-3, 60–62	601.7	10		Ft										
34R-3, 73–75	601.83	11		Ft	Fault		22	90	74	56	S			
34R-4, 30–55	603.9	12		F	Fault		78	270	330	80	W			
34R-4, 50–70	604.1	13		F	Fault		61	270	307	72	S		67	254
34R-5, 60–70	604.7	14		B	Bedding		87	90	346	87	E			
34R-5, 85–95	604.95	15		Ft	Fault		77	270	340	78	W		70	303
34R-5, 113–130	605.23	16		Ft	Fault		82	90	320	83	E			
34R-5, 129–133	605.39	17		Ft	Fault		48	90	322	56	E		44	44
34R-6	606.6	NIL												
34R-CC	607.1	NIL												
35R-1, 10–40	607.8	1		B	Bedding		81	90	6	81	E			
35R-1, 80–105	608.5	2		Ft	Fault		78	270	18	79	W		43	
35R-1, 120–130	608.9	3		Ft	Fault		52	270	169	53	W			
35R-1, 142–148	609.12	4		Ft	Fault		50	270	40	75	W		71	
35R-2, 53–58	609.73	5		Ft	Fault		48	270	46	58	W			
35R-2, 60–61	609.8	6		Ft	Fault		18	90	276	71	N		36	82
35R-3, 74–78	611.44	7		Ft	Fault		50	270	343	52	W			
35R-4, 25–30	612.45	8		Ft	Fault		48	90	336	51	E			
35R-4, 110–120	613.3	9		Ft	Fault		52	90	341	53	E		52	
35R-4, 118–125	613.38	10		Ft	Fault		51	90	357	52	E		51	84
35R-5	613.7	NIL												

Table 10 (continued).

Core, section, interval (cm)	Depth (mbsf)	X-Ref hand sheets	Photo?	ID	Identifier	Thickness (cm)	Core face orientation App. dip	Core face orientation Direction	Corrected core ref. frame Strike	Corrected core ref. frame Dip	Corrected core ref. frame Dir.	Comments	Slick line Plunge	Slick line Trend
141-863B-(Cont)														
35R-6, 33–44	615.53	11		Ft	Fault		57	90	336	59	E			
35R-CC	616.7	NIL												
36R-1, 17–30	617.57	1		B	Bedding		75	270	213	77	W			
36R-1, 83–92	618.23	2		Ft	Fault		68	270	38	72	W			
36R-1, 100–114	618.4	3		B	Bedding		66	270	150	69	W			
36R-1, 128–140	618.68	4		B	Bedding		86	90	333	86	E			
36R-2, 0–45	618.9	5		B	Bedding		76	270	19	78	W			
36R-3, 10–15	620.5	6		Ft	Fault		70	90	36	74	E			
36R-3, 60–80	620.7	7		B	Bedding		72	90	22	73	E			
36R-3, 90–105	621	8		Ft	Fault		70	270	20	72	W			
36R-4, 6–10	621.96	9		Ft	Fault		53	90	8	53	E			
36R-CC	623.4	NIL												
37R-1, 30–35	627.3	1		Ft	Fault		81	270	205	82	W			
37R-1, 43–45	627.43	2		Ft	Fault		38	90	49	50	S	Reverse		
37R-1, 50–53	627.5	3		Ft	Fault		33	90	58	51	S	Reverse		
37R-1, 60–63	627.6	4		Ft	Fault		28	270	239	46	N	Normal, cuts above reverse		
37R-1, 115–125	628.15	5		Ft	Fault		65	90	6	65	E			
37R-1, 130–136	628.3	6		Ft	Fault		37	270	344	40	W			
37R-2, 29–35	629.79	7		Ft	Fault		45	90	30	48	E		27	181
37R-2, 55–60	629.05	8		Ft	Fault		45	90	34	50	E		16	198
37R-2, 70–75	629.2	9		Ft	Fault		63	90	58	75	S		39	225
37R-2, 75–80	629.25	10		Ft	Fault		41	270	333	45	E		14	168
37R-3, 26–28	630.26	11		Ft	Fault		30	90	66	54	S		37	98
37R-3, 63–70	630.63	12		Ft	Fault		40	270	294	64	S		61	235
37R-3, 106–106	631.06	13		Ft	Fault		2	270	271	61	S		38	117
37R-4, 70–90	632.2	14		Ft	Fault		80	90	54	84	S			
37R-5, 60–73	633.6	15		Ft	Fault		60	90	347	60	E		35	10
37R-5, 132–150	634.32	16		B	Bedding		84	270	200	84	W			
37R-CC	634.5	NIL												
39R-1, 24–37	646.54	1		Ft	Fault		61	270	171	61	N	Reverse		
39R-1, 100–112	647.3	2		Ft	Fault		70	90	8	70	E			
39R-2, 0–150	647.8	3		B	Bedding		0	5	195	90	E			
39R-3	649.3	NIL												
39R-CC	650.8	NIL												
40R-1, 20–35	656.1	1		Ft	Fault		49	270	190	49	W			
40R-1, 20–35	656.1	2		Ft	Fault		82	270	120	86	S			
40R-2	657.4	NIL												
40R-3	658.9	NIL												
40R-CC	660.4	NIL												
41R-1, 74–94	666.24	1		Ft	Fault		30	90	296	53	N			
41R-2, 20–33	667.2	2		B	Bedding		70	90	359	70	E	Overturned		
41R-2, 33–34	668.83	3		Ft	Fault		8	270	217	10	W			
41R-2, 100–120	669.5	4		V	Vein		48	90	308	61	N			
41R-2, 100–120	669.5	5		V	Vein		42	90	305	57	N			
41R-2, 100–120	669.5	6		V	Vein		36	90	355	36	E			
41R-2, 110–111	669.6	7		Ft	Fault		42	90	296	64	N			
41R-2, 115–116	669.65	8		B	Bedding		73	90	15	74	E	Overturned		
41R-2, 120–137	669.7	9		Ft	Fault		17	270	158	18	W			
41R-3	670	NIL												
41R-4	671.5	NIL												
41R-CC	673	NIL												
42R-1, 53–61	675.73	1		Ft	Fault		65	90	39	70	E	Sheared below here		
42R-1, 60–67	675.8	2		Ft	Fault		9	270	135	13	W			
42R-1, 63–70	675.83	3		Ft	Fault		42	90	14	43	E	Reverse		
42R-1, 75–78	675.95	4		Ft	Fault		55	270	160	57	W			
42R-1, 60–80	675.8	5		Ft	Fault		75	90	38	78	E	Normal		
42R-1, 80–95	676	6		Ft	Fault		45	270	137	54	W	Bed overturned		
42R-1, 114–116	676.34	7		Ft	Fault		87	90	329	87	E	Normal		
42R-1, 114–116	676.34	8		B	Bedding		35	270	144	41	W	Overturned		
42R-2, 44–50	677.14	9		B	Bedding		61	270	197	62	W	Overturned		
42R-2, 70–80	677.4	10		B	Bedding		65	270	11	66	W	Overturned		
42R-2, 82–90	677.52	11		Ft	Fault		61	270	24	64	W			
42R-3, 0–4	678.2	12		B	Bedding		38	90	59	56	S			
42R-3, 69–73	678.89	13		Ft	Fault		68	90	204	70	W	Reverse		
42R-3, 85–90	679.05	14		Ft	Fault		77	270	332	78	E			
42R-3, 76–91	678.96	15		V	Vein		80	90	323	82	E	Reverse sense		
42R-CC	679.7	NIL												
43R-1	684.8	NIL										Shear zone		
43R-2	686.3	NIL										Shear zone		
43R-3	687.8	NIL										Shear zone		
43R-CC	689.3	NIL										No shear		
44R-1, 30–40	694.8	1		B	Bedding		80	90	33	82	E			
44R-1, 48–50	694.98	2		Ft	Fault		28	90	302	45	N		17	321
44R-1, 80–90	695.3	3		B	Bedding		89	90	25	89	E			
44R-2	696	NIL												
44R-3, 40–40	697.9	4		B	Bedding		10	90	284	37	N			
44R-3, 41–42	697.91	5		Ft	Fault		20	90	40	25	E	Erosion surface of channel		
44R-4, 5–10	699.05	6		Ft	Fault		50	270	331	54	W		31	305
44R-4, 60–70	699.06	7		B	Bedding		87	270	151	87	W			
44R-4, 110–115	700.1	8		Ft	Fault		33	270	34	37	W			
44R-5, 5–15	700.55	9		Ft	Fault		85	90	324	86	E			
44R-CC	702	NIL												
45R-1, 28–38	704.48	1		Ft	Fault		60	90	0	60	E			
45R-1, 76–76	704.96	2		Ft	Fault		85	90	343	85	E			

Table 10 (continued).

Core, section, interval (cm)	Depth (mbsf)	X-Ref hand sheets	Photo?	ID	Identifier	Thickness (cm)	Core face orientation		Corrected core ref. frame			Comments	Slick line	
							App. dip	Direction	Strike	Dip	Dir.		Plunge	Trend
141-863B-(Cont.)														
45R-2, 10–20	705.8	3		Ft	Fault		60	270	180	60	W			
45R-2, 15–23	705.85	4		Ft	Fault		70	270	180	70	W			
45R-2, 20–35	705.9	5		B	Bedding		87	90	355	87	E			
45R-2, 38–42	706.08	6		B	Bedding		82	90	20	82	E			
45R-2, 65–70	706.35	7		B	Bedding		90	90	355	89	E			
45R-CC	707.2	NIL												
46R-1, 42–43	707.22	1		Ft	Fault		40	270	334	45	W			
46R-1, 74–76	707.54	2		Ft	Fault		39	270	45	48	E		31	189
46R-1, 106–110	707.86	3		Ft	Fault		53	90	348	53	E			
46R-2, 45–55	708.75	4		B	Bedding		80	90	297	85	N			
46R-CC	709.8	NIL												
47R-1, 30–48	714.1	1		B	Bedding		81	90	354	81	E			
47R-2, 110–115	716.4	2		Ft	Fault		16	270	214	19	W	Reverse		
47R-2, 115–125	716.45	3		Ft	Fault		65	90	29	68	E	Reverse		
47R-3	717.8	NIL												
47R-CC	718.3	NIL												
48R-1	723.5	NIL												
48R-2, 22–30	725.22	1		Ft	Fault		62	270	143	67	W			
48R-2, 65–72	725.65	2		Ft	Fault		75	270	168	75	W			
48R-3, 5–13	726.55	3		Ft	Fault		84	270	160	84	W			
48R-3, 33–45	726.83	4		Ft	Fault		85	90	25	85	E			
48R-3, 35–45	726.85	5		B	Bedding		83	270	156	84	W			
48R-3, 50–59	767	6		B	Bedding		65	270	180	65	W			
49R-1	733.2	NIL												
49R-2, 16–18	734.86	1		B	Bedding		11	90	82	54	S			
49R-3, 127–131	737.47	2		B	Bedding		47	270	244	68	N			
49R-4, 56–58	738.26	3		V	Vein		20	90	71	49	S			
49R-4, 85–87	738.55	4		V	Vein		12	90	283	44	N			
49R-CC	739.2													

It is clear that Site 863 has had a complex deformation history over a relatively short time (post-early Pleistocene). Reverse, normal, and strike-slip components of motion are all observed, although throughout the site it is the normal components that are the youngest. It is tempting to suggest that the normal components of motion relate to the current tectonic environment: a forearc toe underlain by an actively spreading oceanic ridge.

The displacements observed correspond to discrete portions of the fault rock of any individual fault, and it is possible that faults have experienced more complex histories. Microstructural studies may resolve the kinematic evolution, together with the changing environmental and deformational conditions, and constrain better models for structural evolution.

The steeply dipping domain is anomalous. Significant tectonic units with vertical bedding have not been described from so close to the toe of any accretionary complex, and this geometry must relate to an unusual array of kinematic parameters. This domain also provides a problem in structural analysis in that we cannot ascertain whether the faults that cut the sediments pre- or post-date the tilting of those sediments to their current vertical orientation.

None of the structures or structural domain boundaries below about 50 mbsf correspond to changes in physical properties (see Physical Properties and Wireline Measurements sections, this chapter) or changes in fluid chemistry (see Inorganic Geochemistry and Organic Geochemistry sections, this chapter). In contrast, there are changes in all of these parameters that do not correspond to structural geology. Most notable is an abrupt change in specimen and downhole sonic velocities (see Physical Properties and Wireline Measurements sections, this chapter) at about 400 mbsf. There are corresponding, although less dramatic, changes in lithology and clay mineralogy, fluid chemistry, and paleomagnetism (see Lithostratigraphy, Inorganic Geochemistry, and Paleomagnetism sections, this chapter). These changes occur entirely within the steeply dipping domain and do not correspond to any structural break. The changes are provisionally assigned to a diagenetic front within the borehole. If this is correct, then the implication is that the diagenesis post-dates all the deformation below about 50 mbsf and dominates the sediment physical properties.

ORGANIC GEOCHEMISTRY

Shipboard organic geochemical analyses of sediments from Holes 863A and 863B included measurements of volatile hydrocarbon and nonhydrocarbon gases, organic matter fluorescence, and analysis of total hexane soluble lipid/bitumen, inorganic carbon, total carbon, nitrogen, and sulfur. The instrumentation, operating conditions, and procedures are summarized in the Explanatory Notes chapter (this volume).

Volatile Gases from Sediments

Volatile gases (hydrocarbons, CO_2, H_2S, N_2, CS_2, O_2) released by the sediments recovered at Holes 863A and 863B were continuously measured by gas chromatography as part of the shipboard safety and pollution monitoring program. We used the headspace technique, in which a sediment plug is heated in a sealed vial to drive off gases (Emeis and Kvenvolden, 1986). The results are listed in Table 12 and Figure 57. The methane concentrations in the headspace volumes range between less than 2 and 34,789 ppm. In the uppermost part (4.4–60.5 mbsf) methane concentration was low and ranged from slightly above detection limit to 7 ppm, and no ethane nor heavier gaseous hydrocarbons were detected. Low methane content and high sulfate concentrations in interstitial water (see Inorganic Geochemistry section, this chapter) indicate that for this uppermost layer environmental conditions were not adequate for any significant methanogenesis.

From about 68.3 down to 124.7 mbsf, methane contents increased (2,966 to 34,783 ppm) with ethane levels of 3 to 107 ppm

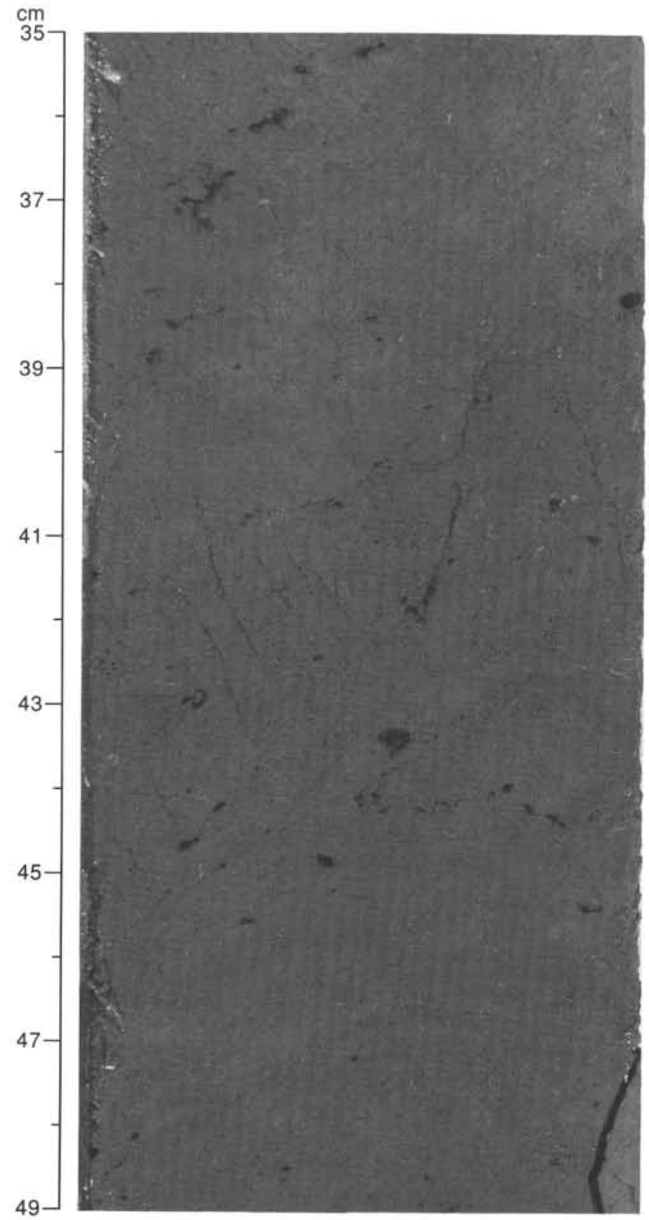

Figure 38. Core photograph, Section 141-863A-1H-4, 35–49 cm. A listric normal fault runs from top right and intersects the core-liner on the left-hand side at about 46 cm. The fault has an inflection at about 40 cm. Reverse faults in the hanging wall have antithetic orientations and detach into the main listric fault. Dark irregular marks are fine-grained hydrous sulfides.

and C_1/C_2 ratios of 179 to 989, which are suggestive of a biogenic origin. Gas content is relatively high at 0.232 cm^3 gas/cm^3 sediment.

Methanogenic bacteria are generally active after complete sulfate depletion by sulfate-reducing bacteria (Claypool and Kaplan, 1974). The sulfate content in interstitial waters is relatively low, with almost complete sulfate depletion by between 68.4 and 76.05 mbsf (see Inorganic Geochemistry section, this chapter). Therefore, over the high-methane content interval from 68.3 to 124.7 mbsf, environmental conditions were favorable for methanogenesis via CO_2 reduction, the major process by which microbial methane is produced in deep-sea sediments.

Core recovery was considerably low (12.3%) from about 143.1 to 345.2 mbsf, an interval of highly tectonized sediments. The recovered sediments had a very low gas content (< 0.001 cm^3 gas/cm^3 sediment) with low methane concentrations (5–341 ppm), and no ethane nor higher hydrocarbons were detected. The only exceptions were three atypical samples that in addition to ethane and higher hydrocarbons contained ethylene and higher olefins. The origin of these unsaturated hydrocarbons was related to overheating of the extended core barrel (XCB) shoe resulting in thermal cracking of sediments in the core catcher. After recovery of Core 141-863B-5X, the XCB shoe was retrieved and observed to have suffered severe mechanical deformation, having lost its cutting elements and undergone thermal deformation resulting in an almost 1-cm decrease in diameter. Upon opening the core catcher, we found the bottom part of the sediment next to the deformed section to have a strong pungent odor, to be very hard, and to have a heated clay aspect (Sample 141-863B-5X-CC, 26–29 cm) that differed significantly from the immediately overlying sediment (Sample 141-863B-5X-CC, 16–19 cm; Table 12). Analysis of headspace gases showed the presence of ethylene and heavier unsaturated hydrocarbons up to C_{6+} and confirmed that the organic matter of Sample 141-863B-5X-CC, 26–29 cm, had undergone extensive thermal cracking.

The thermal effect is localized, as the immediately overlying sediments (10 cm above the heated zone) showed no evidence of thermal alteration. The presence of cracked gases of similar composition in the next core (Sample 141-863B-6X-CC, 0–3 cm) may indicate that overheating continued or that the drilling-related thermal event generated enough downhole cracked gases to be sufficient to contaminate the next few centimeters of core. The return to normal gas composition in Core 141-863B-7N, associated with a change to the motor-driven core barrel (MDCB, indicated by the suffix "N" on core identification) confirmed that the unsaturated anomalous gas composition was due to overheating and drilling-related core alterations. The atypical presence of ethylene in Sample 141-863A-19X-CC, 10–13 cm (also a low-recovery zone) could also be associated with some degree of incipient thermal cracking due to drilling-related overheating. The appearance of atypical olefinic hydrocarbons could provide early warning of drilling-related difficulties.

From about 356.3 to 737.5 mbsf the gases contained in the sediments had a significantly different composition; with methane 10 to 4502 ppm (v/v), ethane 3 to 192 ppm (v/v) (Table 12 and Fig. 57), and very low C_1/C_2 ratios (0.3 to 86) (Fig. 58).

From about 456.5 mbsf the presence of C_3 and heavier hydrocarbons was observed to increase with sub-bottom depth, with C_1/C_3 ratios ranging from 0.7 to 346, and ratios of 1 to 3.7 for the heavy-gas-rich interval from 521.8 to 715.3 mbsf. This interval is coincident with a steeply-dipping, stratigraphically narrow sedimentary sequence (see Lithostratigraphy section, this chapter). This sedimentary section had a significant amount of heavier gasoline-range volatile hydrocarbons (Table 12) extending beyond C_7 (heptane), well within the natural gasoline range. As indicated before (Organic Geochemistry Section, Site 861 chapter, this volume), due to limitations in the chromatographic method the carbon range cut-off for gasoline hydrocarbons is about C_7, but heavier C_{7+} gasoline-range hydrocarbons are present in the sediments, as shown by solvent extractable bitumen analysis (see below). Due to the extended gasoline-range hydrocarbon series present in some of the gas samples and the lack of corresponding reference hydrocarbons on board the ship, some hydrocarbons had to be assigned the same response factors as the nearest reference compound available and their concentrations added.

The downhole profiles for headspace methane, ethane, and propane plus heavier hydrocarbons are also shown in Figure 57.

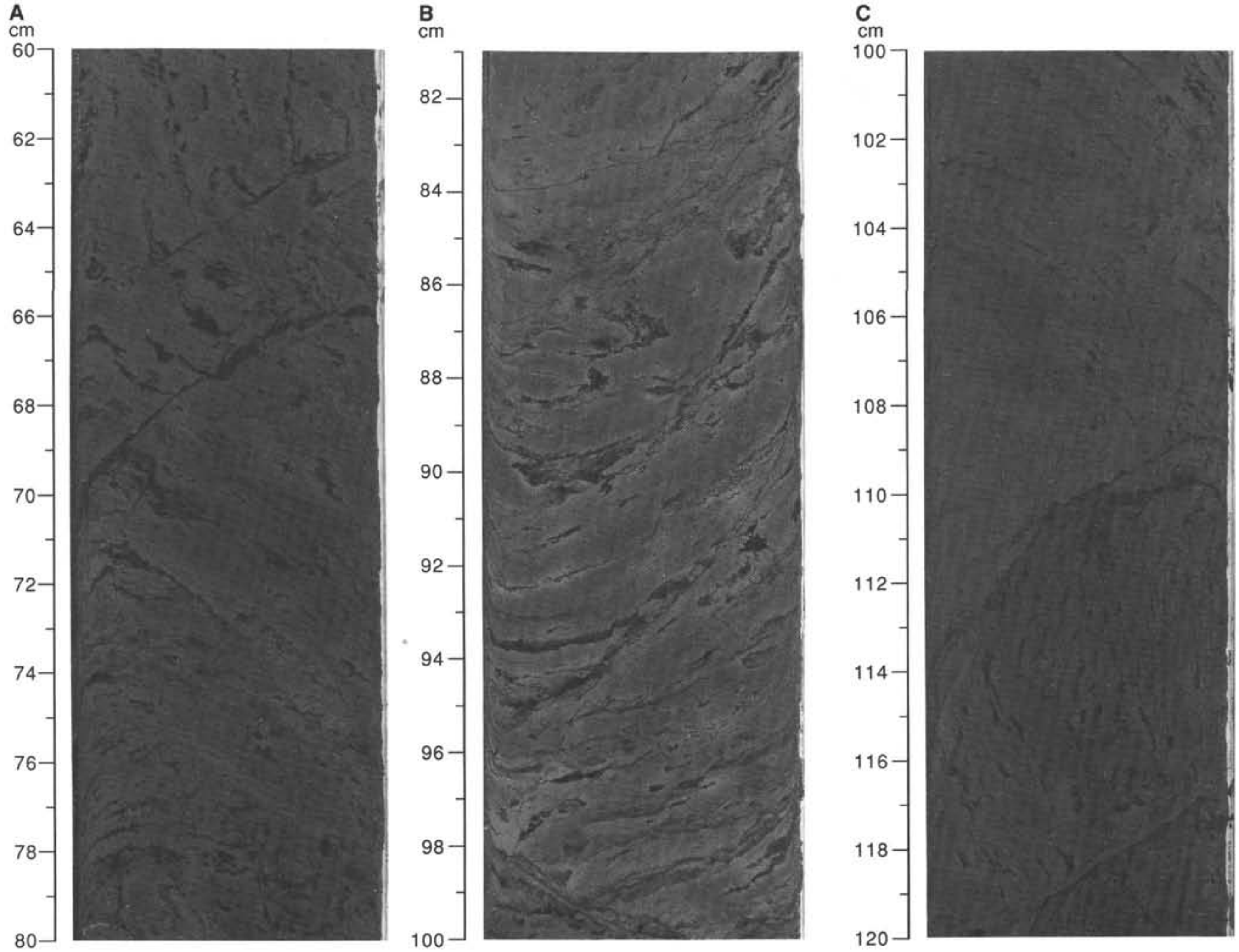

Figure 39. Core photographs, Section 141-863A-4H-2. **A.** 60–80 cm; **B.** 81–100 cm; **C.** 100–120 cm. Complex faulting within marbled clays. The marbled pattern of black layers and blebs with pale halos is caused by fine-grained hydrous sulfides. The marbling is cut by numerous faults. Thick, moderately-dipping faults are mostly reverse faults. Other faults mostly have normal separations.

The total gas and methane content of the recovered sediments from this section is relatively low, and frequently methane content is lower than C_2 and C_3 as indicated by C_1/C_2 and C_1/C_3 ratios < 1.0 (Table 12). This would indicate that the measured gas and the methane levels are most probably controlled by lithology, porosity, and degassing during core retrieval. An undetermined amount of gas is lost to drilling fluids during drilling and recovery, and therefore in-situ gas content is higher than measured on board. For the indurated sediments drilled in the lower sections of Site 863, this effect is compounded by the lack of the core-sediment seal normally present in soft unconsolidated sediments.

Carbon dioxide was present at concentrations that range from 68 to 2553 in the gases desorbed from sediments by the headspace method (Table 12). A somewhat lower CO_2 level was found in the deeper section of Hole 863B, and the highest concentration was observed for the drilling-altered sample at 345.2 mbsf. Even higher amounts of free CO_2 could have been present in the sediments and pore waters prior to the depressurization that occurs during core retrieval. Large fluctuations in CO_2 concentration were observed throughout the sequence of recovered sediments, suggesting possible alterations due to drilling fluid contamination (seawater), degassing during depressurization, core sectioning and air contamination at sample introduction in headspace containers. No H_2S was detected in the chromatographic analysis of Site 863 gases even though some cores from the upper layers of Hole 863A had a pungent sulfur-compound-like smell upon splitting.

Fluorescence

The bitumen extract colors (*n*-hexane soluble organic matter) decreased in intensity from yellow to pale yellow for the 4.4- to 586.2-mbsf interval, then increased again in yellow intensity with increasing depth in the hole. The fluorescence of the extracts went from a weak white for the upper section of the hole turning to a intense blue-white fluorescence from 356.3 mbsf down to total depth. Two intermediate samples, Samples 141-863A-4H-2, 142–145 cm, and 141-863A-5H-1, 137–140 cm, showed a yellow-orange fluorescence. Yellow fluorescence is interpreted to indicate incipient thermal maturation of bitumen to the early mature stage, and white (or blue-white) fluorescence has been associated with mature and overmature bitumen, enriched in polynuclear aromatic hydrocarbons (PAH) (Shipboard Scientific Party, 1982). Based on the color and fluorescence intensities of the extracts as well as the relative intensities of chromatograms of extractable organic

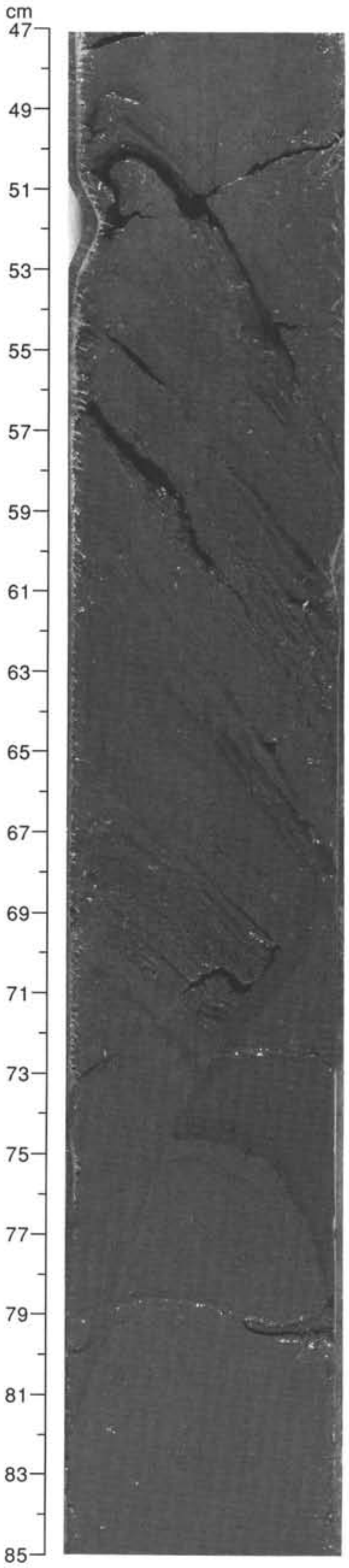

Figure 40. Core photograph, Section 141-863A-3H-2, 47–85 cm. A major fault intersects the core liner at 69 cm on the right side and 82 cm on the left side. Minor faults in the hanging wall (mostly too small to see) have reverse separations. At 75 cm, deflection of footwall bedding suggests normal motion.

Table 11. Rotations used to reorient structural data from the core reference frame into the geographic reference frame, Hole 863A.

Core	Rotation	Method
141-863A		
-4H	061°	Multishot
-5H	037°	Multishot
-6H	–036°	Multishot

Note: All rotations are around vertical axes and are clockwise looking down-axis.

matter (see below), the concentrations of extractable organic matter are low for the upper section of the sequence increasing with sub-bottom depth below 356.3 mbsf.

Gas in Core Expansion Voids

After core retrieval on deck, gas expansion voids were observed in the core-liner-contained core. The gas was sampled directly from the gas voids by piercing the core liner with a sampling needle and collecting the gases in pre-evacuated Vacutainers. Upon chromatographic analysis, the expansion-void gases (EVG) for some samples were found to contain hydrocarbons in the C_1 to C_7 range (Table 13).

For some samples EVG hydrocarbon contents (up to 839003 ppm; 83.9% vol.) were found to reach significantly higher concentration levels than headspace gas and presented different C_1/C_2 gas ratios for equivalent depths (Tables 12 and 13). Due to low core recovery and/or lack of core to core-liner seal EVG gas recovery was low and sporadic and has, therefore, low geochemical diagnostic relevance for Site 863.

At Site 863 the water sampler temperature probe (WSTP) was deployed, and gas samples were obtained from the overflow chamber on two occasions (WSTP runs after Cores 141-863A-10X and 141-863A-16X). The gases were analyzed (Table 13) and found to contain methane through C_{6+}. The presence of ethylene in one of the samples (141-863A-16X-WSTP) would suggest incipient cracking due to downhole drilling-related effects (see above).

Bitumen Analyses and Organic Matter Characterization

The hexane extracts (500 µL) of the samples from the fluorescence assessment were concentrated under a stream of helium to about 25 to 400 µL. These concentrates were analyzed by high-resolution gas chromatography and examples of chromatographic traces are shown in Figure 59. In the upper section (4.4–76 mbsf) the dominant compound series in the total extracts are hydrocarbons ranging from n-C_{15} to n-C_{36} with some samples where pristane ($C_{19}H_{40}$) and phytane ($C_{20}H_{42}$) are the major isoprenoid alkanes identifiable on board. As a general trend, the n-alkanes $>C_{26}$ have a significant predominance of homologues having odd carbon numbers and carbon preference indexes CPI > 1.0 (Table 14), typical for immature hydrocarbons that originate from terrestrial higher plants (Simoneit, 1977, 1978). The contribution of bitumen of marine origin, derived from alteration of microbial lipids of marine origin ($<C_{24}$; maxima about C_{20}) is more significant in the 124.7–181.7 mbsf interval.

The value of the carbon preference index (CPI) decreases with geothermal maturation approaching values of CPI≈ 1 for crude oils and mature organic matter. The CPI had to be calculated for the range C_{26}–C_{35} because in some samples n-C_{25} coeluted with a contaminant that is more abundant in samples taken from split cores and that thus is most likely associated with plastic-derived contaminants originating from core-liner fragments incorporated during core splitting.

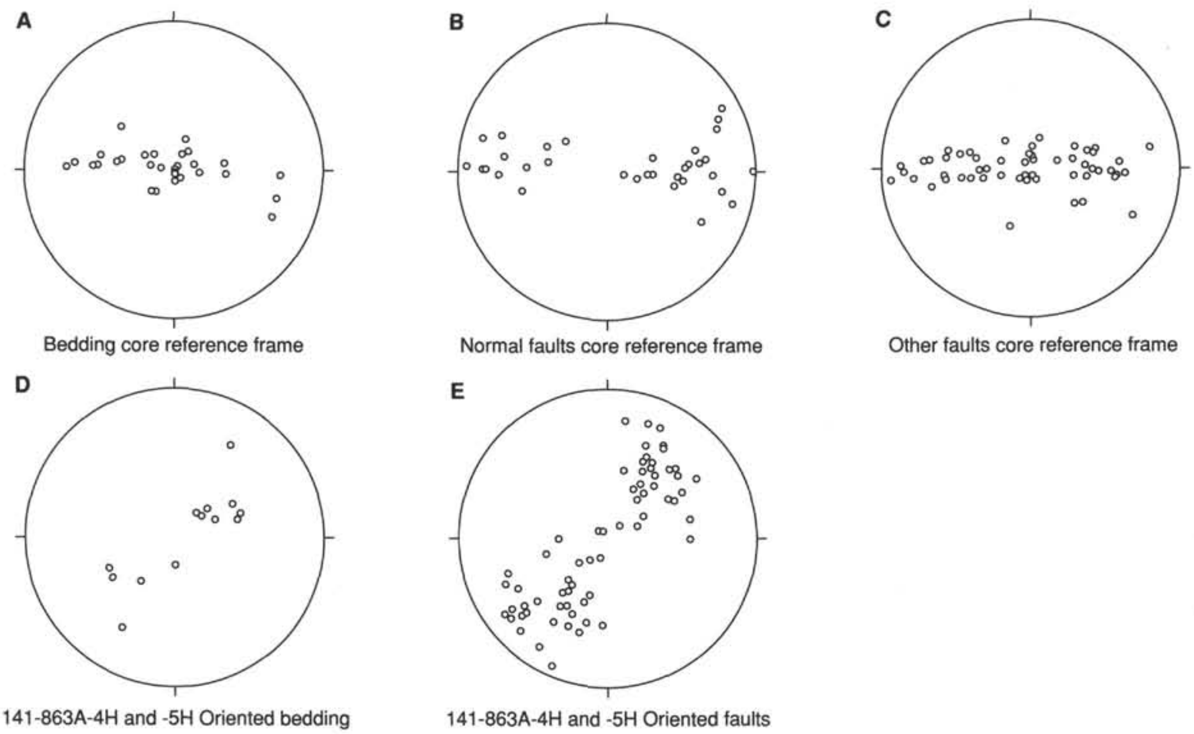

Figure 41. Stereonet of structural data from the complexly-faulted domain. Plots (**A**), (**B**), and (**C**) show poles to bedding, normal faults, and all other faults respectively. These data are from all cores from Core 141-863A-1H through Core 141-863A-5H and are oriented in the core reference frame. (**D**) and (**E**) show data from Cores 141-863A-4H and 141-863A-5H that have been oriented in the geographical reference frame using multishot data. Poles to bedding are plotted in (**D**) and poles to all faults in (**E**).

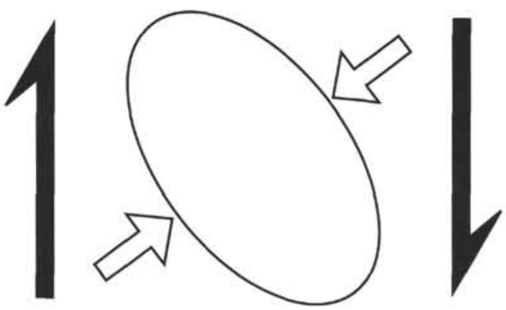

Figure 42. Directions of maximum compressive strain (open arrows) and finite-strain ellipse for dextral simple shear with a shear strain of 0.6: the approximate shear strain integrated over 1 m.y. if the component of plate convergence parallel to trench is all partitioned into a 30-km-wide zone of the forearc.

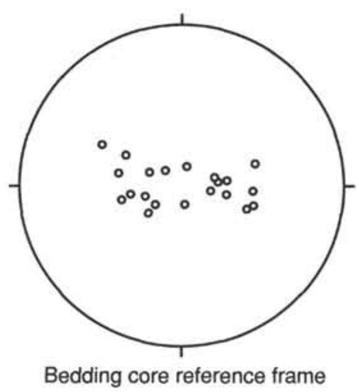

Figure 43. Poles to bedding for bedding data from the gently-dipping domain. Data are from Cores 141-863A-6H through 141-863A-27X and are oriented in the core reference frame.

For Site 863, CPI indexes of the organic matter extracted from the sediments have a great variability. Thus, in the upper section, some samples that have a low degree of geothermal maturity with higher CPI values are interlayered with samples having lower CPI indexes and general hydrocarbon distributions suggestive of higher degrees of maturation (Table 14 and Fig. 59). For the lower section (depth >330.2 mbsf) several samples have CPI indexes significantly lower than 1.0, which is probably associated with an increased content of aromatic hydrocarbons and their co-elution with some even-carbon-numbered hydrocarbons.

The isoprenoid to normal hydrocarbon ratios (Pr/n-C_{17} and Ph/n-C_{18}) and the pristane to phytane ratios (Pr/Ph) are low—to about 330.2 mbsf—then increase with depth down the hole (Table 14). However, pristane to phytane ratios are highly formation-dependent (Farrington et al., 1988); they have been reported to be an indicator that responds to maturation (Simoneit et al., 1981), as well as an indicator of anoxic conditions of sedimentation (Didyk et al., 1978).

Analysis of gases released in the core liner as well as gases released from sediments by headspace analysis indicated the

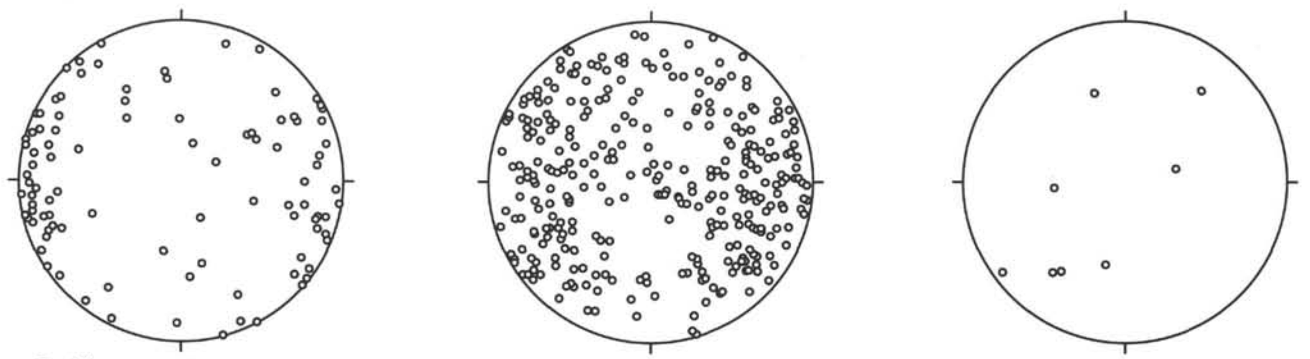

Figure 44. Poles to bedding, all faults and deformation bands, and carbonate veins from the steeply-dipping domain. Data are from Cores 141-863A-28X through 141-863A-31X and all cores in Hole 863B. Data are oriented in the core reference frame.

presence of gasoline-range hydrocarbons and suggested the presence of heavier gasoline-range compounds. The presence of these heavier natural gasoline-type thermogenic hydrocarbons was also corroborated by the extraction analyses, which show that abundant hydrocarbons within the carbon-atom range for natural gasoline and/or condensate can be observed on the gas chromatograms (Fig. 59) when contrasted with the solvent extraction blank. The relative amount of gasoline- and/or condensate-range hydrocarbons increases with sub-bottom depth and is indicative of an increased thermal stress and/or the existence of a deeper-located source of thermogenic hydrocarbons.

The actual nature of this deeper source of thermogenic hydrocarbons might be related to a conventional, slowly matured hydrocarbon source located deeper in the sedimentary sequence. Alternatively, the thermogenic hydrocarbons may be generated by a high-temperature source (Simoneit et al., 1981) and/or by petroleum hydrocarbon generation through action of hydrothermal fluids upon immature sedimentary organic matter (Didyk and Simoneit, 1989).

Organic Carbon Content

Because the Rock-Eval pyrolysis analyzer was inoperable during Site 863, the total organic carbon (TOC) content of the sediments was measured by means of the NCS analyzer.

The concentrations of inorganic, total, and organic carbon in the sediments recovered from Holes 863A and 863B are presented in Table 15. The percentage of calcium carbonate (%$CaCO_3$) was calculated from the inorganic concentrations by assuming that all carbonate is in the form of calcite. Total nitrogen and total sulfur concentrations are also included in Table 15.

The total organic carbon (TOC) contents were found to be relatively low—ranging from 0.12% to 0.78%, with most sediments containing less than 0.5%. The total organic carbon contents have been plotted vs. depth in Figure 60 and show no depth-related trend. Sediments at 22.8 and 66.2 mbsf have slightly higher TOC values (>0.5%), which suggests the possible existence of narrow zones of slightly higher organic contents.

Conclusions

Biogenic gas composed mainly of methane and ethane was detected in the upper zone of the sedimentary section of Site 863 (from 68.3 to 124.7 mbsf). Abundant thermogenic hydrocarbons extending into the natural gasoline range and/or condensate range are present in the lower section (around 356.3 mbsf to total penetration depth). The organic matter content of the sediments is relatively low. Localized maturational and organic anomalies suggest the occurrence of migrational processes and a deeper source of thermogenic hydrocarbons.

INORGANIC GEOCHEMISTRY

The primary purposes of the pore-water program at Site 863 were to evaluate the effects of hydrothermal circulation on the nature and geochemistry of sediments and fluids directly above the recently subducted ridge axis, to determine if pore-fluid compositions provide information about fluid sources and migration pathways during deformation of the toe of the accretionary prism, and to contrast diagenesis in this presumably high-temperature regime with precollision Site 859 and the upper slope Sites 860 and 861. The pressure core sampler (PCS) was not run at Site 863 as gas hydrates were not anticipated (and none were encountered). Fluids were obtained from squeezing whole rounds of APC, XCB, and RCB cores and from the water sampler temperature probe (WSTP). These were analyzed for salinity, sodium, calcium, magnesium, potassium, strontium, lithium, ammonia, chloride, sulfate, pH, alkalinity, boron, silica and fluoride. The whole-round squeezed interstitial water data are presented in Table 16 and Figure 61.

The water sampler temperature probe (WSTP) was deployed five times in the water-plus-temperature configuration to collect in-situ water samples in Hole 863A. Samples from both the titanium coil and the overflow chamber were analyzed, and the results of these analyses are presented in Table 17 and in Figure 62. In all cases, we collected large volumes in the overflow chamber, an indication of significant drill-fluid contamination of the sample coils. In the first two deployments (27.6 and 56.1 mbsf), the concentrations of all constituents correspond to those obtained from squeeze cakes. However, these values also correspond to seawater concentrations; thus, the possibility of drill-fluid contamination cannot be ruled out.

The subsequent three WSTP runs correspond to a zone of extremely poor recovery and therefore no comparison with interstitial water data from squeeze cakes can be made. The values in these samples also correspond to the seawater concentration of the parameters measured; thus, it is possible that we have drill-fluid contamination. On the other hand, the in-situ temperature data indicate that the tool penetrated the formation, and except for one deployment there seems to be no thermal evidence of drill-fluid contamination (see WSTP-ADARA Temperature Measurements section, this chapter). Therefore, an alternative explanation is that the samples were collected in a zone of very high water content associated with structural deformation and that the composition of the fluids does not differ significantly from seawater values. This possibility cannot be ruled out as the fluid samples

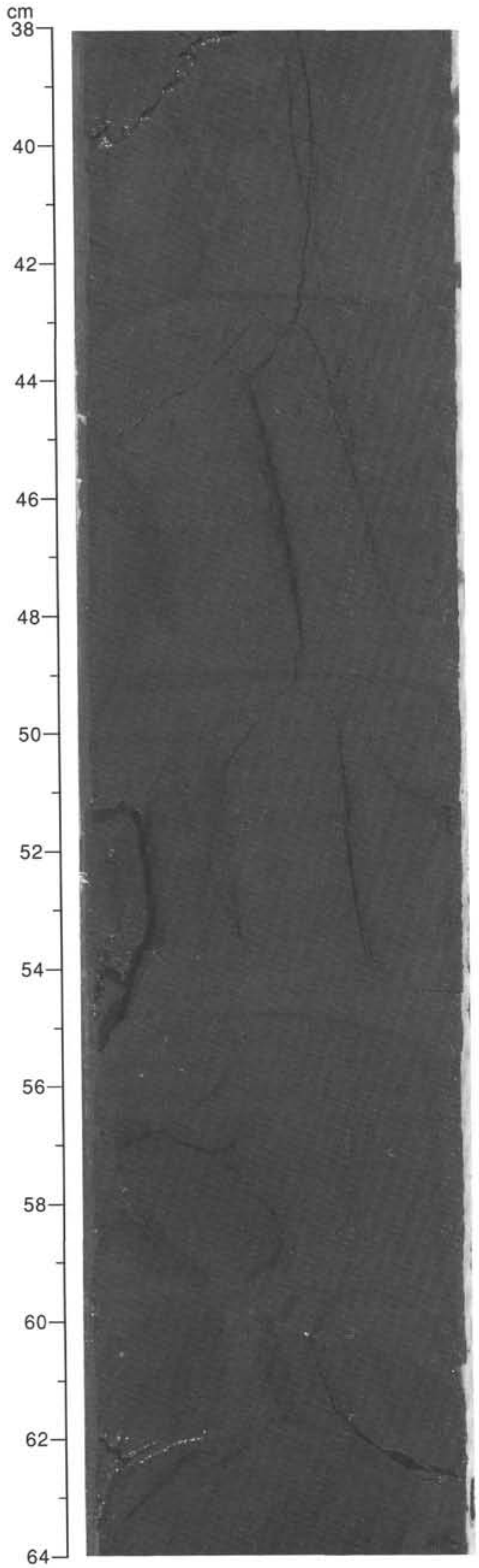

Figure 45. Core photograph, Section 141-863A-30X-2, 38–64 cm. Six drilling biscuits containing steeply dipping beds. The uppermost biscuit shows the development of pale deformation bands within the fine sandstone.

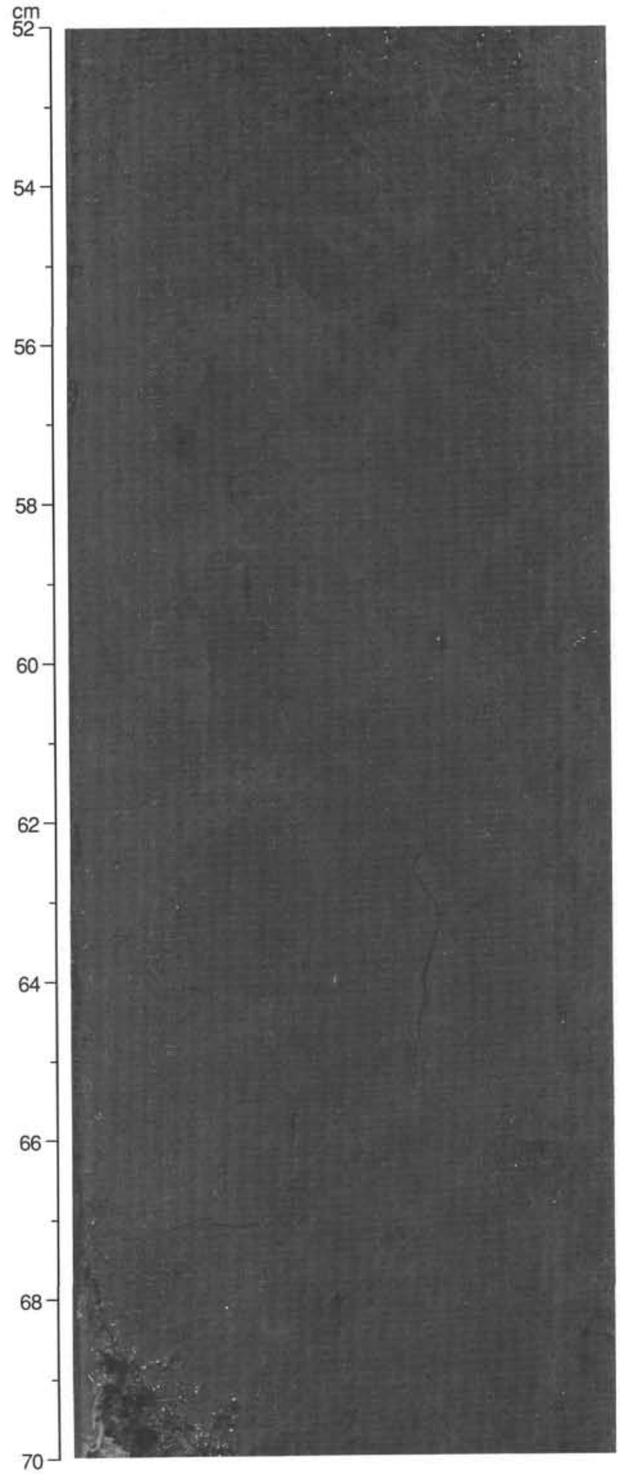

Figure 46. Core photograph, Section 141-863B-43R-3, 52–70 cm. Part of the breccia relating to a major fault at 687 mbsf. The breccia is heterogeneous. Coarser angular fragments dominate the lower part of the image. These are separated by planar bands of very fine breccia. In the top of the picture the breccia becomes more pervasively fine-grained.

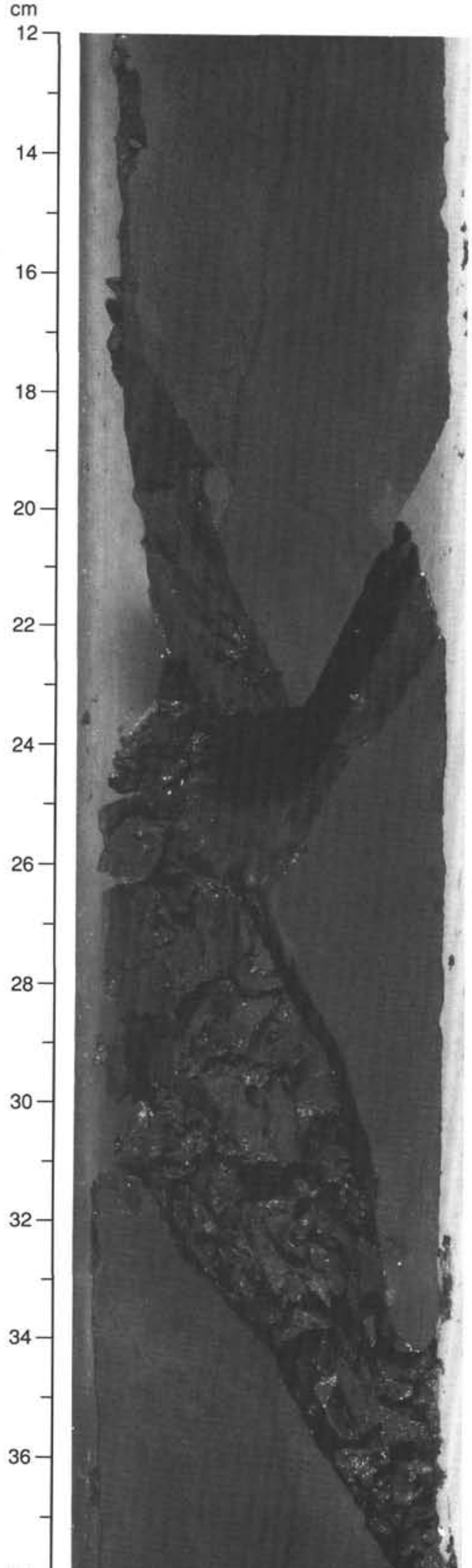

Figure 47. Core photograph, Section 141-863B-23R-2, 12–38 cm. Faults in a major fault zone at 496 mbsf. Rubbly material in the lower half of the photo is pervasively foliated and lineated clay. This is bound by two slickenlined fault surfaces indicating dip-slip motion. The upper fault marks the upper boundary of the fault zone. Above this, bedding is vertical, as can be seen in the upper piece. Within the fault zone bedding is shallow.

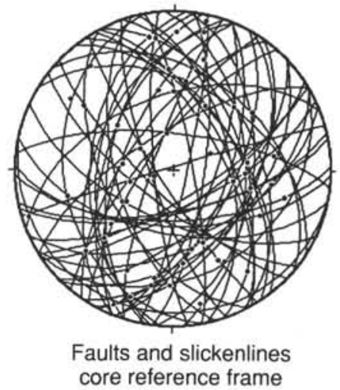

Figure 48. Great circles to faults in the steeply dipping domain. Points mark slickenline orientations where they were measured.

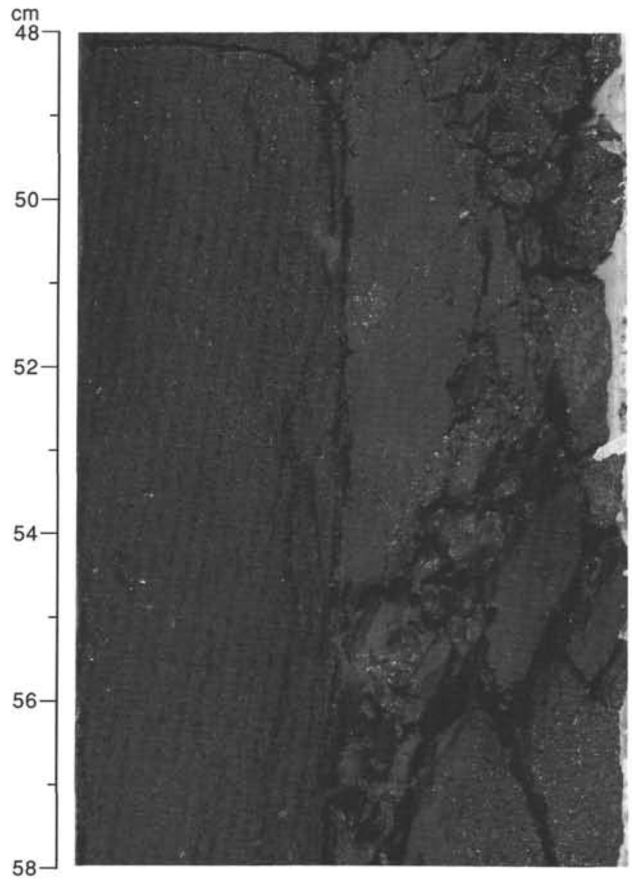

Figure 49. Core photograph, Section 141-863B-16R-5, 48–58 cm. Bedding-parallel fault in the steeply-dipping domain. Slickenlined fault surfaces are contained within the submillimeter dark clay that forms the sharpest fault contact. The fault zone is wider overall, with thicker and more irregular seams either side of the sharp break.

obtained from the squeeze cakes below the zone of poor recovery have a composition similar to that of seawater (Fig. 62).

Gas samples were collected from the headspace of the overflow chamber in the two deployments for which there was positive pressure on retrieval. Gas samples were also collected after the fluids were removed from the titanium coil through a syringe. All these samples were analyzed for their hydrocarbon composition and the data are presented in Table 18. Note that in the two

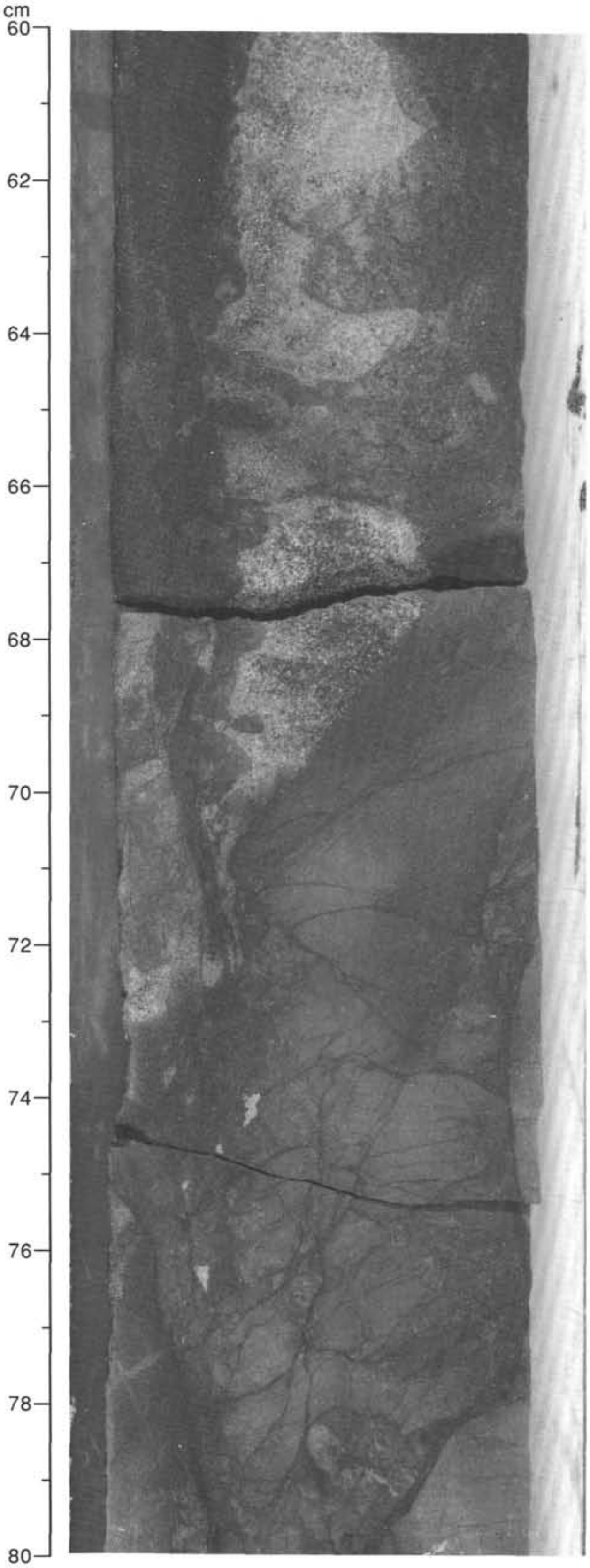

Figure 50. Core photograph, Section 141-863B-18R-3, 60–80 cm. Complex deformation bands show lithologic controls on their intensity in bioturbated sediments on the lower right side of the photo. Paler material above is the cemented material within bioturbated coarser sands.

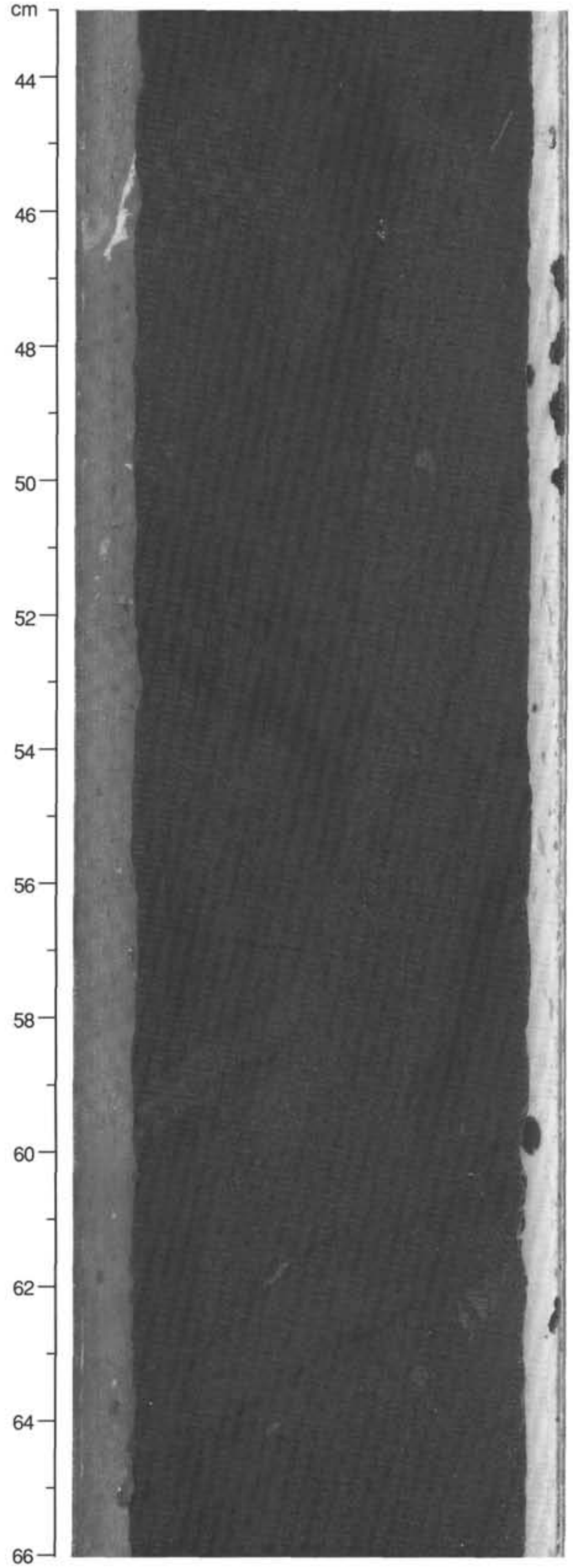

Figure 51. Core photograph, Section 141-863B-37R-1, 43–66 cm. A deformation band forms the vertical contact between coarse sand on the right and fine sand on the left. This is cut and offset by reverse and normal deformation bands with a moderate dip.

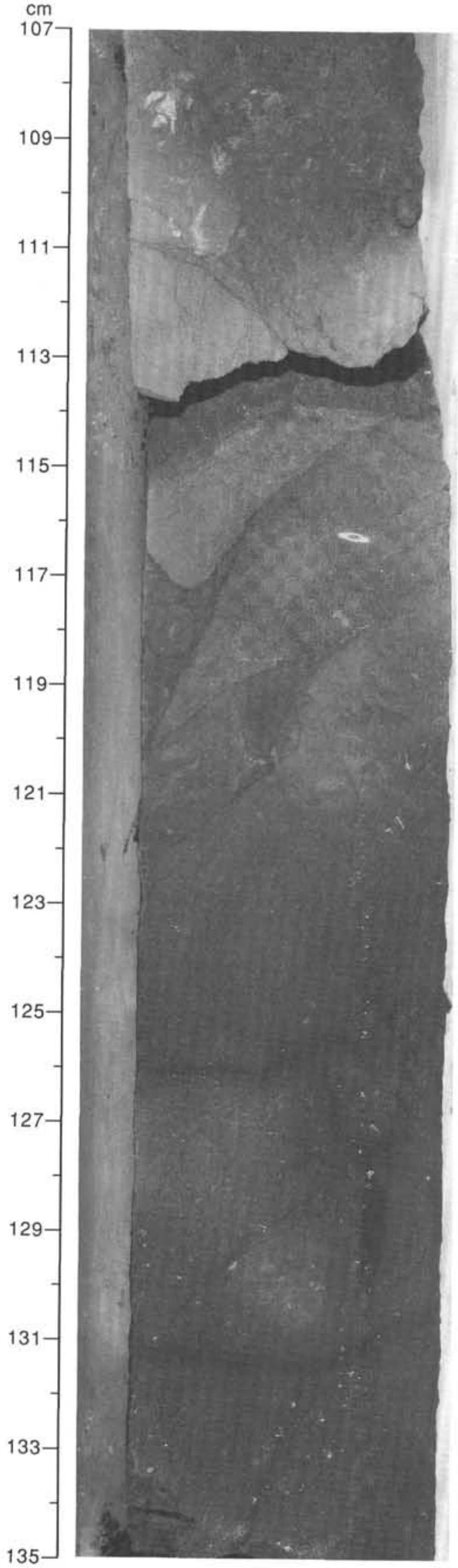

Figure 52. Core photograph, Section 141-863B-18R-1, 107–135 cm. Anastomosing deformation bands in fine sandstone/siltstone.

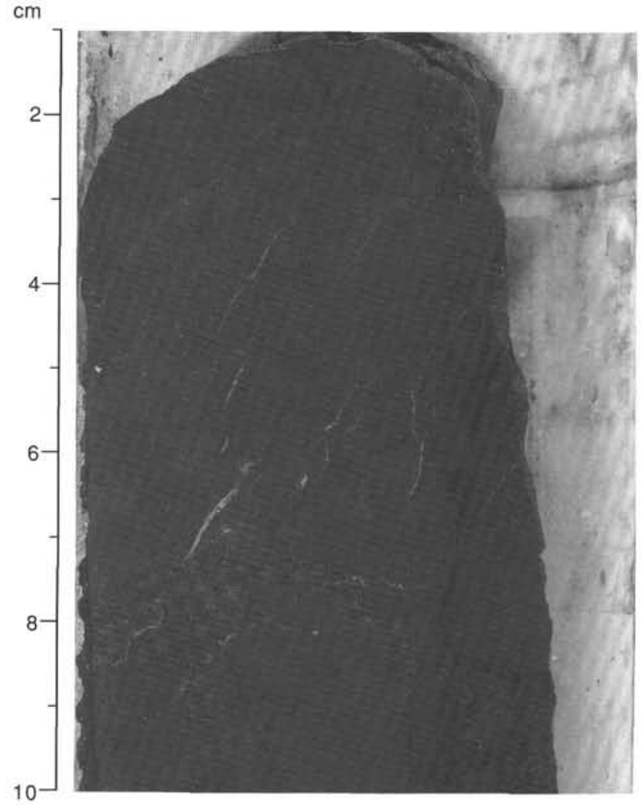

Figure 53. Core photograph, Section 141-863B-13R-CC, 1–10 cm. Irregular carbonate veins cross-cut deformation band. The dark blebs in the cores of the veins are aggregates of pyrite and quartz.

deployments where gas samples were collected from both the titanium coil and the headspace in the overflow chamber, the gas compositions are very different. These results indicate that the hydrocarbons in the overflow chamber represent the composition of the gases sampled from the formation by in-situ gas separation in the evacuated chamber. The extremely poor recovery in this section did not allow for collection of gas from the core by vacutainers, and thus comparison of the gases sampled with the WSTP, with the composition of vacutainer samples is not possible.

Interstitial water profiles from the squeezed intervals demonstrate the presence of at least five separate fluid regimes (Fig. 61). There is little evidence in the interstitial water chemistry for active hydrothermal circulation, but the bottom several hundred meters do display extreme chemical characteristics that are likely related to hydrothermal reactions below recovery or in communication via lateral fluid flow. In addition, past high-temperature fluid circulation is evidenced by the presence of silicified planktonic foraminifers and cross-cutting calcite and quartz veins localized in deformation bands and fault traces. Because of the marked difference between the composition of seawater and that encountered in the interstitial fluids at Site 863, we plotted the sum of cation charges vs. the sum of anion charges to ensure no large systematic analytical errors (Fig. 63).

In the interval from 0 to about 60 mbsf, sulfate reduction leads to downward-decreasing sulfate concentrations, with increasing ammonia and alkalinity. This interval is characterized by free hydrogen sulfide, iron monosulfide, and biogenic gas compositions, and is clearly undergoing active sulfate diagenesis. At the base of this layer, the interval from 60–80 mbsf is characterized by very high alkalinities and ammonium concentrations and by

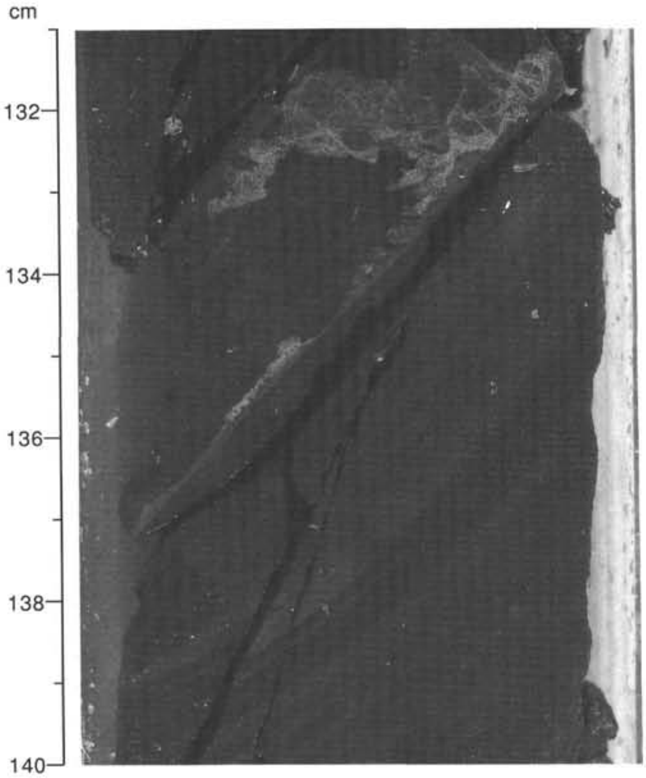

Figure 54. Core photograph, Section 141-863B-34R-1, 131–140 cm. Carbonate veins associated with cementation of a small irregular coarse sandstone in a fault-bound block. Faults run from top right to bottom left between 131 and 137 cm.

sulfate depletion, consistent with methanogenesis. Strong calcium, magnesium, and strontium depletions are related most likely to in-situ diagenetic calcite precipitation and volcanic glass alteration. These profiles suggest "normal" diagenetic reactions with diffusion between the overlying seawater and the interval below 60 mbsf.

Between 80 and 147 mbsf no interstitial water samples were recovered, but the dramatic difference in the pore-fluid characteristics, especially the sharp contact at about 65 mbsf, suggest that the interval from 60 to about 147 mbsf may be a thrust sheet composed of strata that fills the small basin landward of the drill site. This interval corresponds to the onset of structural deformation, to a zone of high porosity, and to a temperature anomaly indicative of lateral fluid flow in this interval (see Structural Geology, WSTP-ADARA Temperature Measurements, and Lithostratigraphy sections, this chapter). In addition, the low salinity and low total cation and anion balances in the part of this interval with better recovery (68–76 mbsf) suggest lateral flow (Fig. 64).

In the interval from 147 to about 400 mbsf, sulfate concentrations are similar to those in the uppermost layer, suggesting past sulfate reduction but the absence of contemporary methanogenesis. Calcium, magnesium, potassium, sodium, strontium, and fluoride concentrations are near seawater values in the upper portion of this interval, but display dramatic diffusion gradients downward into the interval below 400 mbsf. Boron also decreases downsection, suggesting a sink for boron below 400 mbsf.

In the interval from 400 to about 500 mbsf, sulfate is virtually depleted, suggesting the presence of active methanogenesis, and calcium, magnesium, potassium, silica, and boron gradients suggest a strong sink for these elements near the base of this interval. Salinity, total cations, and total anions display a distinct minimum

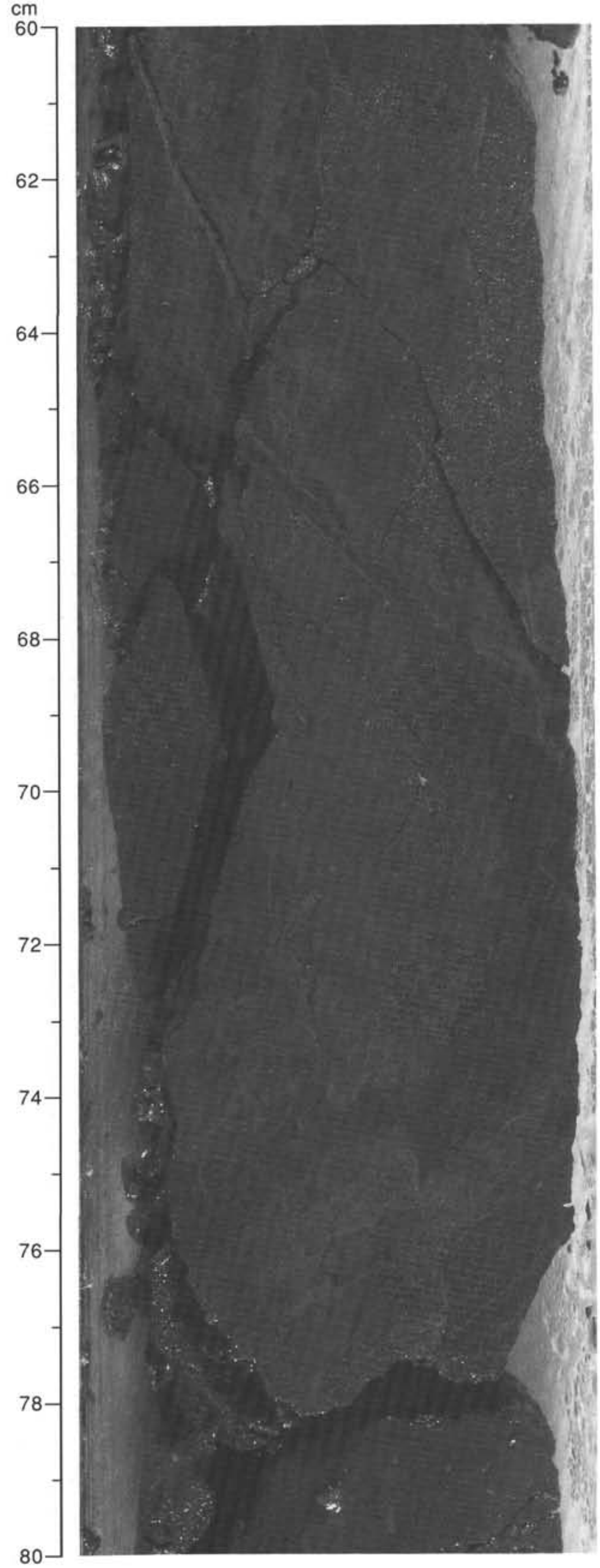

Figure 55. Core photograph, Section 141-863B-42R-1, 60–80 cm. Irregular and veinlike cementation in material in the immediate hanging wall of a major fault at 687 mbsf. Cementation is still concentrated in coarser sands, but extends into finer material.

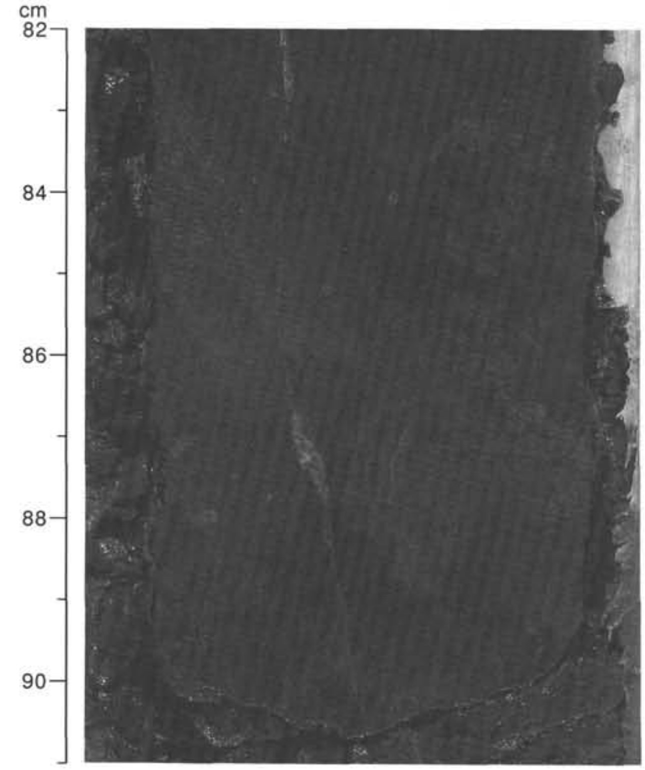

Figure 56. Core photograph, Section 141-863B-42R-3, 82–91 cm. Irregular cementation and carbonate veins in material in the immediate hanging wall of a major fault at 687 mbsf. The veins cut across a steep deformation band.

in this interval, requiring lateral migration from a low-salinity source (Fig. 64). Sodium, however, decreases downward below 400 mbsf along a linear gradient. As sodium and chloride gradients are not coupled, the reactions involving Na and Cl below recovery are not due to isochemical salt concentration-dilution phenomena (e.g., phase separation in hydrothermal plumbing), but most likely to albitization of oceanic basement (Na-uptake) with charge-coupled diffusion.

Both magnesium and potassium are almost completely depleted below about 500 mbsf. The shapes of these Mg and K gradients, coincident with strong inflections in the gradients of Ca, Li, SO_4, Sr, F, Si, B and a steep pH increase, suggests the presence of a reaction front or lateral fluid flow at this level. This front coincides with an increase in the smectite content of the sediments from 30% to 60% of the clay fraction (see Lithostratigraphy section, this chapter). As this change in clay composition occurs within an almost vertical bedding plane it is hard to call upon a change in depositional conditions to explain its occurrence. Instead, a diagenetic front involving smectite formation from glass alteration consistent with the Mg and K profiles seems to be a likely scenario. At this depth there is also a marked change in the resistivity logs (see Wireline Measurements section, this chapter) which also could be related to an increase in clay-cementation of sandstones.

On the other hand, the sediments collected for squeezing in this section were less consolidated and showed indications of a larger degree of fracturing relative to the samples above and below. The borehole temperature logs also show a break in the gradient at this interval (see Wireline Measurements section, this chapter). These observations suggest the presence of hydrothermally altered fluid flow through this zone, perhaps isolated at about 500 mbsf.

Below 500 mbsf, pH values increase to almost 10.5 and boron approaches maximum values of almost 1 mM at 600 mbsf. Titration alkalinity remains below about 4 mM. Apparently there is no carbonate alkalinity, and almost all alkalinity is composed of OH^- and $B(OH)_4$-, requiring an unusual combination of alkaline fluid sources derived from reactions below recovery. In addition, these high pH values are likely to be at least partly responsible for past and present in-situ silica replacement reactions (silicified foraminifers).

The interval below about 260 mbsf contains a vertically-tilted, monotonously-bedded clay-silt/sandstone that is presumably fairly porous and permeable, even though partially cemented. This unit could provide fluid conduits for rapid vertical and/or horizontal exchange along the sandstone beds. The dramatic changes in interstitial water chemistry within this 500 m-thick unit suggest that the vertical fluid history is more complex than a single vertical chimney structure plumbed between 260 and 740 mbsf. There are several potential scenarios. One possibility is that the interval between about 400 and 500 mbsf is a lateral fluid conduit with top (400 mbsf) and bottom (500 mbsf) boundaries tapping dramatically different fluid sources. The difficulty with this scenario is the linear (diffusion?) Na gradient that extends from 400 mbsf to total depth, which would seem to eliminate the possibility of lateral flow, as this Na gradient must reflect albitization of basalt basement. However, the temperature logs do show a "cold" anomaly in this interval.

A second possibility is that the entire section below 220 mbsf was initially perfused with hydrothermally-driven fluids after this block was underthrust by the east wall of the ridge axis and tilted 90° into its present orientation, permitting the bedded sandstones to act as vertical pipes for hot fluid conductance upward from the basement ridge axis contact. Past high-temperature, alkaline, silica- and calcium-rich fluid circulation upsection to at least 325 mbsf is evidenced from the presence of silicified foraminifers and veins of calcite, quartz, and other authigenic minerals localized in fault traces and deformation bands. Further evidence of migration of hot fluids is the overprinting of paleomagnetic inclinations—suggesting a thermochemical remagnetization event—and the high concentration of migrated gasoline-range hydrocarbons (see Paleomagnetism and Organic Geochemistry sections, this chapter). Subsequently, with burial and smothering of the MOR circulation system and development of thrust faults at 147 mbsf and along the basement contact (décollement?), the fluid stopped circulating and its composition evolved via low-temperature diagenetic fronts that have migrated from both ends of the pipe (i.e., top and bottom), and are now located between 400 and 500 mbsf. In support of this notion of an upward-migrating diagenetic front, we note that below about 405 mbsf there is a dramatic increase in the smectite content of the clay fraction, the occurrence of zeolites, and concentrations of heavy hydrocarbons.

A third possibility is that fluids do not convect (and have not convected) vertically or horizontally through Site 863, and that the chemical and thermal characteristics of this site reflect purely transient fluctuations in basal boundary conditions that are transmitted up the "pipe" conductively (diffusively). This scenario would then be similar to the moving diagenetic front model, with the additional constraint that the chemical reactions are poised on isotherms that are moving up and down the section with the vertical propagation of fluctuating bottom boundary conditions, presumably imparted by the downgoing oceanic crustal slab.

Unique aspects of fluid chemistry below 500 mbsf include the high pH (up to 10.5), low alkalinity, and high B, F, and Li in a solution that is a $CaCl_2$ brine devoid of K and Mg. Almost all alkalinity is comprised of OH^- and $B(OH)_4$-, with little or no carbonate alkalinity - all carbonate has been precipitated, a process still occurring at the top of the presently-active diagenetic

Table 12. Composition of headspace gases for sediments from Holes 863A and 863B.

Core, section, interval (cm)	Depth (mbsf)	Hydrocarbon concentration (ppm)												
		C_1	C_2	C_2=	C_3	i–C_4	n–C_4	i–C_5	n–C_5	C_{6+}	CO_2	C_1 (cm^3/cm^3)	C_1/C_3	C1/C3
141-863A-														
1H-3, 137–140	4.4	tr	0	0	0	0	0	0	0	0	640	0.000		
2H-3, 142–145	13.0	tr	0	0	0	0	0	0	0	0	690	0.000		
3H-3, 137–140	22.5	4	0	0	0	0	0	0	0	0	411	0.000		
4H-2, 142–145	30.5	7	0	0	0	0	0	0	0	0	734	0.000		
5H-1, 137–140	38.5	6	0	0	0	0	0	0	0	0	703	0.000		
6H-1, 137–140	48.0	6	0	0	0	0	0	0	0	0	943	0.000		
7X-3, 137–140	60.5	5	0	0	0	0	0	0	0	0	715	0.000		
8X-2, 132–135	68.3	19,152	107	0	0	0	0	0	0	0	881	0.128	179	
9X-1, 62–65	76.0	3,390	12	0	0	0	0	0	0	0	124	0.023	283	
10X-CC, 10–13	85.2	2,966	3	0	0	0	0	0	0	0	143	0.020	989	
11X-CC, 10–13	94.8	6,234	13	0	0	0	0	0	0	0	198	0.042	480	
14X-1, 97–100	124.7	34,783	40	0	0	0	0	0	0	0	495	0.232	870	
16X-CC, 10–13	143.1	325	0	0	0	0	0	0	0	0	466	0.002		
17X-CC, 10–13	153.2	341	0	0	0	0	0	0	0	0	68	0.002		
18X-CC, 10–13	162.5	26	0	0	0	0	0	0	0	0	476	0.000		
19X-CC, 10–13	172.8 *	26	4	3	3	0	0	0	0	0	558	0.000	6.5	8.7
20X-CC, 10–13	181.7	16	0	0	0	0	0	0	0	0	549	0.000		
21X-1, 42–45	191.7	14	0	0	0	0	0	0	0	0	500	0.000		
22X-CC, 40–43	201.4	16	0	0	0	0	0	0	0	0	271	0.000		
23X-CC, 22–25	210.8	14	0	0	0	0	0	0	0	0	130	0.000		
24X-1, 49–52	220.8	10	0	0	0	0	0	0	0	0	236	0.000		
25X-1, 40–43	230.2	9	0	0	0	0	0	0	0	0	nd	0.000		
26X-1, 56–59	240.1	8	0	0	0	0	0	0	0	0	558	0.000		
27X-1, 79–82	250.0	11	0	0	0	0	0	0	0	0	374	0.000		
28X-1, 109–112	259.9	19	0	0	0	0	0	0	0	0	388	0.000		
29X-1, 67–70	269.1	8	0	0	0	0	0	0	0	0	675	0.000		
30X-1, 132–135	279.4	11	0	0	0	0	0	0	0	0	307	0.000		
31X-1, 60–63	288.2	13	0	0	0	0	0	0	0	0	514	0.000		
141-863B-														
4X-3, 132–135	330.2	10	0	0	0	0	0	0	0	0	408	0.000		
5X-CC, 16–19	335.8	5	0	0	0	0	0	0	0	0	134	0.000		
5X-CC, 26–29	335.9 *	28	13	8	59	59	26	37	15	50	809	0.000	2.2	0.5
6X-CC, 0–3	345.2 *	70	12	20	24	6	14	4	3	2	2553	0.000	5.8	2.9
7N-1, 137–140	356.3	14	4	0	0	0	0	0	0	0	483	0.000	3.5	
8N-2, 0–3	358.3	19	7	0	0	0	0	0	0	0	370	0.000	2.7	
9X-CC, 10–13	361.4	10	4	0	0	0	0	0	0	0	742	0.000	2.5	
10R-1, 26–36	371.3	11	11	0	0	0	0	0	0	0	606	0.000	1.0	
11R-1, 8–11	376.7	13	17	0	0	0	0	0	0	0	557	0.000	0.8	
12R-1, 100–103	387.3	11	38	0	0	0	0	0	0	0	633	0.000	0.3	
13R-1, 17–20	396.0	12	44	0	0	0	0	0	0	0	609	0.000	0.3	
14R-1, 132–135	406.8	15	55	0	0	0	0	0	0	0	499	0.000	0.3	
15R-1, 137–140	416.6	68	64	0	0	0	0	0	0	0	681	0.000	1.1	
16R-2, 132–135	427.5	260	66	0	0	0	0	0	0	0	686	0.002	3.9	
17R-4, 0–4	438.9	398	58	0	0	0	0	0	0	0	781	0.003	6.9	
18R-1, 137–140	445.4	321	82	0	0	0	0	0	0	0	824	0.002	3.9	
19R-2, 132–135	456.5	1,180	192	0	0	1	0	0	0	0	481	0.008	6.1	
20R-2, 105–108	465.9	412	112	0	0	2	0	0	0	0	807	0.003	3.7	
21R-1, 93–96	473.9	386	100	0	0	0	0	0	0	0	893	0.003	3.9	
22R-3, 82–85	486.5	3,154	142	0	0	3	2	0	0	0	912	0.021	22	
23R-3, 137–140	496.7	4,502	92	0	13	10	3	11	3	25	983	0.030	49	346
24R-1, 132–135	503.3	1,199	16	0	8	4	2	7	2	11	1010	0.008	75	150
25R-2, 132–135	514.5	258	3	0	13	4	2	7	2	10	225	0.002	86	20
26R-1, 42–45	521.8	98	3	0	36	9	4	16	5	31	278	0.001	33	2.7
27R-3, 137–140	535.0	44	10	0	59	13	6	20	6	35	282	0.000	4.4	0.7
28R-1, 55–58	540.8	41	11	0	49	10	5	15	5	25	492	0.000	3.7	0.8
29R-CC, 0–3	549.7	79	32	0	96	24	10	29	8	53	482	0.001	2.5	0.8
30R-CC, 0–3	559.4	109	51	0	152	38	14	44	13	154	109	0.001	2.1	0.7
31R-3, 132–135	574.9	161	75	0	183	43	14	37	12	114	140	0.001	2.1	0.9
32R-5, 135–140	586.2	262	89	0	221	57	20	58	18	236	104	0.002	2.9	1.2
33R-1, 102–105	589.4	181	64	0	149	37	14	40	14	182	149	0.001	2.8	1.2
34R-3, 132–135	602.4	253	76	0	200	52	17	49	14	215	nd	0.002	3.3	1.3
35R-3, 148–150	612.2	89	33	0	91	25	8	29	8	112	265	0.001	2.7	1.0
36R-3, 137–140	621.8	117	33	0	94	27	9	27	8	92	81	0.001	3.5	1.2
37R-4, 132–135	632.8	95	20	0	66	19	6	21	6	63	146	0.001	4.8	1.4
38R-2, 137–140	639.6	108	27	0	106	35	13	41	13	155	93	0.001	4.0	1.0
39R-1, 124–125	647.5	153	21	0	68	21	9	21	6	65	717	0.001	7.3	2.3
40R-1, 102–105	656.9	50	10	0	44	17	6	20	5	57	228	0.000	5.0	2.9
41R-1, 132–135	666.8	112	28	0	84	26	8	25	6	45	139	0.001	4.0	1.3
42R-1, 137–140	676.6	122	53	0	123	38	12	30	11	55	263	0.001	2.3	1.0
43R-2, 82–85	687.1	95	35	0	67	20	8	19	5	30	779	0.001	2.7	1.4
44R-2, 147–150	697.5	257	59	0	75	23	10	17	5	23	308	0.002	4.4	3.4
45R-2, 0–3	705.7	358	71	0	97	31	13	22	6	28	189	0.002	5.0	3.7
46R-1, 22–25	707.0	594	135	0	225	68	35	54	15	85	409	0.004	4.4	2.6
47R-1, 147–150	715.3	345	70	0	133	45	24	38	12	54	152	0.002	4.9	2.6
48R-1, 26–27	723.8	529	69	0	103	34	18	23	6	25	100	0.004	7.7	5.1
49R-3, 132–135	737.5	423	38	0	48	15	7	10	3	6	88	0.003	11	8.8

* = Thermally cracked gas due to drill bit overheating

C_3 and n–C_4 peaks include olefins and other unidentified hydrocarbons.

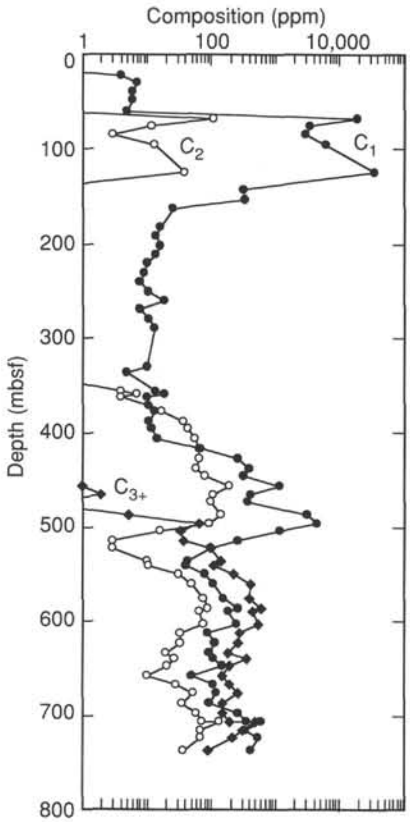

Figure 57. Composition of headspace gases vs. sub-bottom depth (mbsf) for sediments from Holes 863A and 863B.

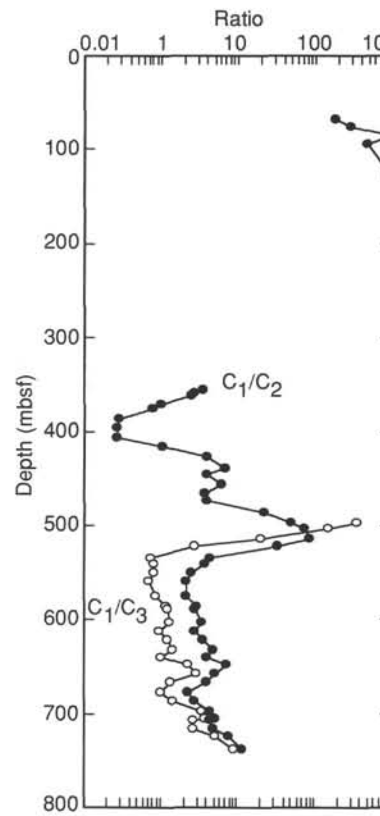

Figure 58. Methane/ethane (C_1/C_2) and methane/propane (C_1/C_3) ratios vs. sub-bottom depth of gases from sediments in Holes 863A and 863B.

Table 13. Composition of gases from core expansion voids of sediments and the WSTP from Holes 863A and 863B.

Core, section, interval (cm)	Depth (mbsf)	Hydrocarbon concentration (ppm)												
		C_1	C_2	$C_2=$	C_3	i–C_4	n–C_4	i–C_5	n–C_5	C_6+	CO_2	C1/C_2	C_1/C_3	C_1/n–C_4
141-863A-														
3H-3	22.1	7	0	0	0	0	0	0	0	0	566			
8X-4	70.3	836,885	2118	0	0	0	0	0	0	0	924	395		
10X-WSTP	85.1[a]	5,798	8	0	0	0	10	0	0	21	375	725		580
14X-1	124.5[a]	24,026	11	0	0	0	2	0	0	0	507	2184		12,013
16X-WSTP	143.0[b]	548	9	4	7	4	120	5	5	36	952		78	5
141-863B-														
4X-3	332.4[b]	417	52	41	52	4	14	2	0	3	773	8	8	30
7N-1	355.3[a]	6	0	0	0	0	5	0	0	3	493			1
8N-1	357.9	0	0	0	0	0	0	0	0	0	959			
14R-1	406.8[a]	5	6	0	0	0	1	0	0	1	378	1		5
16R-4	429.8[a]	46	8	0	0	0	2	0	0	2	351	6		23
17R-5	441.6[a]	49	3	0	0	0	4	0	0	3	527	16		12
18R-2	446.7	317	32	0	0	0	0	0	0	0	610	10		
19R-3	457.6	83	6	0	0	0	0	0	0	0	330	14		
20R-2	465.3	29	3	0	0	0	0	0	0	0	482	10		
22R-2	485.3	149	4	0	0	0	0	0	0	0	960	37		
3R-2	571.2[a]	5	tr	0	tr	tr	2	0	0	10	413			3

[a] n–C_4 peak includes unidentified hydrocarbon with lower retention time.
[b] C_3 and n–C_4 peaks include olefins and other unidentified hydrocarbons.

Ca-profile (~480 mbsf). In addition, diagenetic fronts for removal of K and Mg (~500 mbsf) may reflect present-day formation of K-Mg-OH silicate phases ("greensands"?), zeolites, or Mg-rich smectites and sepiolite. In addition, the high pH and behavior of F, B, Cl and SO_4 suggest fluids sourced from a sequence of reactions involving Mg-depleted fluids much deeper in the subduction zone (Janecky and Seyfried, 1986), perhaps involving retrograde metasomatic alteration of serpentinized ultramafics, followed by flow through the off-axis remnants of hydrothermal deposits with hydration and dissolution of anhydrite or iron hydroxy chloride phases. These pH values are higher than expected for basalt hydrolysis reactions in the presence of Mg, and suggest some component of these fluids is sourced from much deeper (Seyfried et al., 1984; Fryer et al., 1990; Fryer, 1992).

Table 14. Extractable bitumen of sediments from Holes 863A and 863B.

Core, section (cm)	Depth (mbsf)	C_{max}	C_{range} C_i–C_f	Pr/Ph	Pr/n-C_{17}	Ph/n-C_{18}	CPI
141-863A-							
1H-3	4.4	21 & 31	10–36	0.95	1.38	0.86	3.02
6H-1	48.0	31	10–36	0.75	2.00	1.60	1.82
9X-1	76.0	27	10–36	0.91	3.50	4.60	1.01
14X-1	124.7	19	10–36	0.63	1.43	1.33	1.96
16X-CC	143.1	28	16–36	0.29	0.33	0.39	0.73
20X-CC	181.7	20 & 34	10–36	0.56	0.45	0.47	1.15
24X-1	220.8	31	10–36	1.17	2.33	0.27	1.47
29X-1	269.1	27	10–36	1.42	4.25	1.20	2.70
31X-1	288.2	27	12–36	0.59	3.71	4.00	1.68
141-863B-							
4X-3	330.2	27	10–36	0.28	1.80	2.00	2.63
11R-1	376.7	28	10–36	0.34	4.73	6.33	0.38
14R-1	406.8	28	15–36	0.42	8.62	14.78	0.52
21R-1	473.9	25	10–36	0.97	1.60	1.10	1.10
23R-3	496.7	25	10–36	1.31	17.80	11.33	1.68
30R-CC	559.4	27	10–36	1.22	18.33	9.00	1.86
32R-5	586.2	27	10–36	1.17	7.25	9.00	1.70
37R-4	632.8	27	10–36	1.69	15.88	10.00	1.68
42R-1	676.6	27	10–36	1.27	11.00	9.45	1.98
47R-1	715.3	19	10–34	2.09	19.71	13.20	0.42
49R-3	737.5	21	10–34	1.47	12.00	5.29	0.95

PHYSICAL PROPERTIES

General

The Explanatory Notes of this volume explain in full the procedures used to measure physical properties at Site 863. As at other Leg 141 sites, at Hole 863A the shallow subsurface occurrence of sediments with low porosity and low water content sediment forced an early change in core-recovery technique from hydraulic piston core (APC) to extended core barrel (XCB). As a consequence, APC cores (in which disturbance is relatively small) were collected to a depth of only 56.1 mbsf, below which XCB coring extended to the bottom of Hole 863A at a depth of 297.3 mbsf. In contrast to the other drilling sites located on the continental slope (i.e., Sites 859, 860, and 861), gas expansion at Site 863 did not disrupt the semiconsolidated sediment recovered in APC cores. As a consequence, for the first time on Leg 141, useful downhole acoustic-velocity data were obtained with the digital sound velocimeter (DSV).

XCB coring at Hole 863A introduced core disturbance that seriously degraded readings of bulk density and acoustic velocity by the gamma-ray attenuation porosity estimator (GRAPE) and *P*-wave logger (PWL) sensors. Because intact sedimentary material could usually be identified in split cores, drilling-disturbed cores did not in general impair the collection of accurate physical property data from discrete samples. More seriously, XCB coring was largely unsuccessful in recovering material between Cores 141-863A-10X and -13X, thus virtually no physical property data are recorded between a depth of 85 and 124 mbsf.

At Hole 863B, XCB, RCB, and MDCB coring was employed to recover sediment to a depth of 742.9 mbsf. Poor core-recovery at the top of Hole 863B produced a second but smaller gap in physical property data from roughly 297 to 326 mbsf. However, rotary-cone drilling below 376.6 mbsf typically returned cores with intact sedimentary fabric and commonly 3 to 7 m in length. Thus material both representative of the stratigraphic sequence and lending itself to the measurement of good-quality in-situ physical properties was recovered from the lower half of the sedimentary section penetrated at Site 863.

Physical properties data collected at Site 863 are described below under three headings: (1) index properties, which comprise porosity, water content, grain density, and bulk density (including GRAPE) information, (2) acoustic velocity data that integrate the PWL, DSV, and Hamilton-Frame velocity measurements, and (3) thermal conductivity measurements.

Based on the physical characteristics of core sediment, the sedimentary sequence drilled at Site 863 has been subdivided into four physical properties units:

Unit A, from 0 to 100 mbsf, of weakly-consolidated silty clay and clayey silt;

Unit B, 100–190 mbsf, semilithified section of siltstone;

Unit C, 190–350 mbsf, a transitional sequence of weakly consolidated silty clay and clayey silt with minor sandstone and siltstone beds; and,

Unit D, from 350 to 740 mbsf, lithified siltstone and sandstone beds.

Physical properties Unit A is effectively equivalent to lithologic Unit I (see Lithostratigraphy section, this chapter). Unit I is conspicuously dark gray in color and rich in iron sulfides.

Lithologic Unit II comprises physical properties Units B, C, and D.

Index Properties

Index properties of selected samples from Holes 863A and 863B are combined on Table 19. Plots of the vertical distribution of porosity, water content, bulk density, and grain density for both holes are combined in Figure 65.

Most of the physical property unit boundaries correspond to breaks in the porosity profile apart from the upper boundary of Unit D, which corresponds to a change in sonic velocity.

Porosity decreases downward through the upper 80 mbsf of section (Unit A) from approximately 52% at the surface to 42% at 80 mbsf. With notable deviations, the downsection decrease in porosity continues to the base of Hole 863B (742.9 mbsf), where the measured porosity is approximately 25%. The net change in porosity from the top to the bottom of Hole 863B is thus only 25%.

The distinct upper low-porosity zone between 100 and 190 mbsf (Unit B), coincident with a section of lithified siltstone, is interposed between two sections of less-lithified beds dominated by silty clays (Units B and C). The other break in porosity and water content across the boundary between Subunits D1 and D2 at 400 mbsf is less distinct, but the boundary also corresponds to a substantial break in the thermal conductivity profile (Fig. 65).

The vertical distribution of water content mimics the shape of the porosity profile. At the seafloor, approximately 30% of the mass of the sediment consists of interstitial water, whereas at the base of the Site 863 section intergranular water accounts for only about 10% of the rock mass. Water content less than 5% occurs in sandstone layers well-cemented by calcite, commonly found in the lower part of Unit C and the upper beds of Unit D.

No systematic change in average grain density with depth was measured by the analyses of discrete sediment samples (Table 19). The average grain density for the sedimentary section penetrated at Site 863 clusters approximately around 2.75 g/cm^3, identical within measuring limits to that established at other Leg 141 sites. There is no particular association of higher grain density with sandstone beds, as has been observed at other sites less rich in coarse-textured deposits, e.g., Sites 859, 860, and 861.

The shape of the downsection profile of bulk density is virtually the inverse of that of wet-sediment water content and porosity. Bulk density distribution defines with less distinction the breaks bounding the physical properties units most clearly delimited by porosity and water content. Between about 350 mbsf and 600 mbsf, calcite-cemented sandstone beds (CS on Fig. 65) of Units C and D are conspicuously dense (~2.7 g/cm^3). Similar cemented sandstone beds were not always sampled (but do occasionally occur) in the lower part of Unit D.

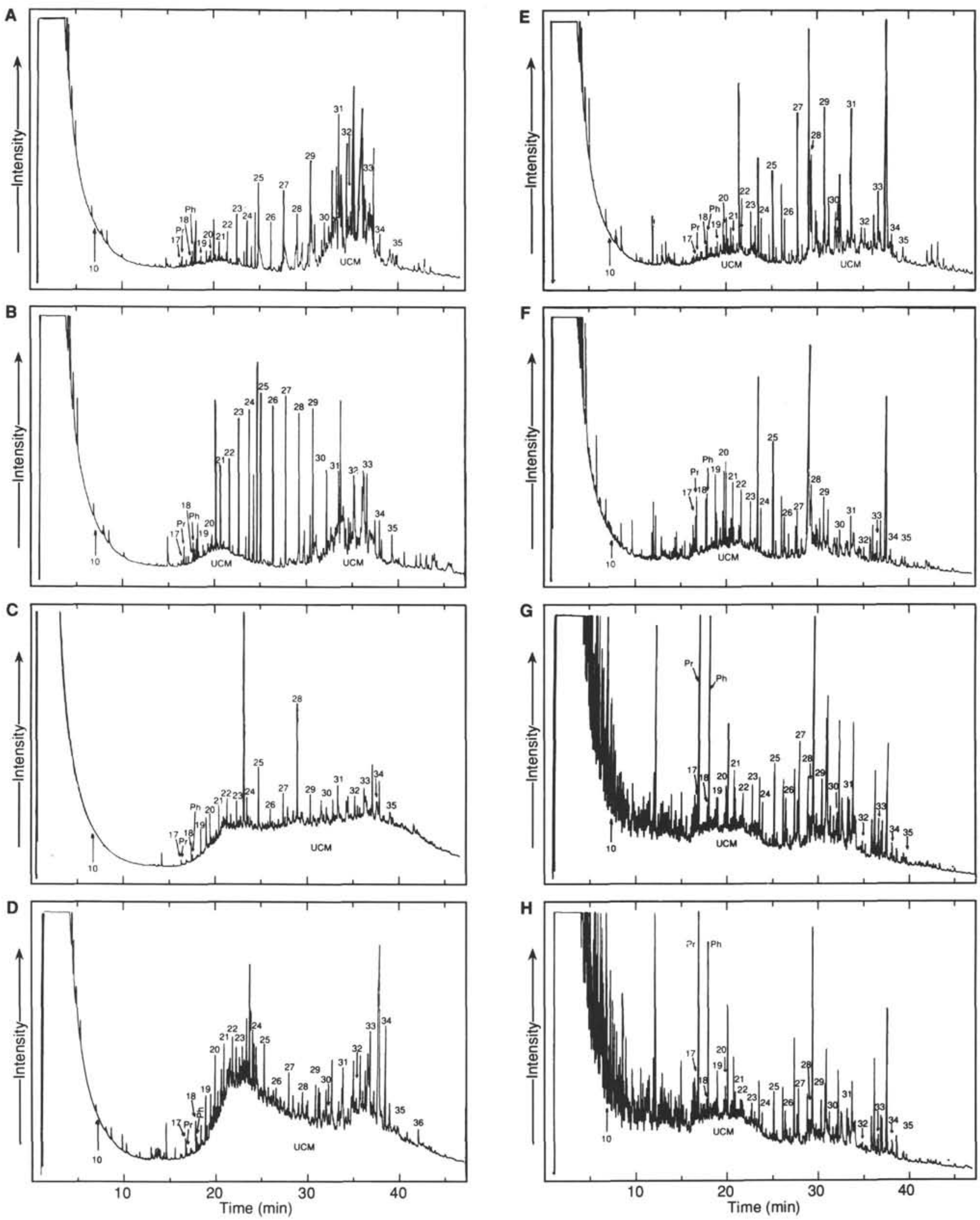

Figure 59. Gas chromatographic traces of the bitumen (hexane soluble matter) of sediments from Holes 863A and 863B: (**A**) Sample 141-863A-6H-1, (**B**) Sample 141-863A-9X-1, (**C**) Sample 141-863A-16X-CC, (**D**) Sample 141-863A-20X-CC, (**E**) Sample 141-863B-4X-3, (**F**) Sample 141-863B-21R-1, (**G**) Sample 141-863B-30R-CC, and (**H**) Sample 141-863B-32R-5 (numbers refer to carbon chain length of *n*-alkanes, Pr = pristane, Ph = phytane, UCM = unresolved complex mixture of branched and cyclic compounds).

Table 15. Total organic and inorganic carbon, and total nitrogen and sulfur of sediments from Holes 863A and 863B.

Core, section, interval (cm)	Depth (mbsf)	Total carbon (%)	Inorganic carbon (%)	Organic carbon (%)	$CaCO_3$ (%)	Total nitrogen (%)	Total sulfur (%)	OrgC/N	OrgC/S
141-863A-									
1H-1, 11–13	0.1	0.35	0.09	0.26	0.7	0.04	0.41	6.50	0.63
1H-1, 141–143	1.4	0.40	0.07	0.33	0.6	0.04	0.15	8.20	2.20
1H-2, 134–136	2.8	0.50	0.10	0.40	0.8	0.04	0.39	10.00	1.00
1H-4, 22–24	4.7	0.25	0.04	0.21	0.3	0.02	0.20	10.00	1.00
1H-6, 38–40	7.9	0.42	0.06	0.36	0.5	0.03	0.28	12.00	1.30
2H-1, 42–44	9.0	0.28	0.06	0.22	0.5	0.04	0.19	5.50	1.10
2H-4, 56–58	13.7	0.56	0.07	0.49	0.6	0.05	0.51	9.80	0.96
3H-1, 5–7	18.2	0.52	0.03	0.49	0.2	0.19	0.29	2.60	1.70
3H-4, 24–26	22.8	1.43	0.65	0.78	5.4	0.06	0.55	13.00	1.40
4H-3, 30–32	30.9	0.35	0.07	0.28	0.6	0.03	0.25	9.30	1.10
5H-1, 103–105	38.1	0.34	0.06	0.28	0.5	0.03	0.16	9.30	1.70
6H-1, 48–50	47.1	0.38	0.09	0.29	0.7	0.04	0.48	7.20	0.60
7X-1, 97–99	57.1	0.35	0.02	0.33	0.2	0.05	0.19	6.60	1.70
8X-1, 71–73	66.2	1.17	0.50	0.67	4.2	0.08	0.33	8.40	2.00
9X-CC, 1–3	76.2	0.56	0.25	0.31	2.1	0.04	0.53	7.70	0.58
14X-2, 45–47	125.2	0.25	0.08	0.17	0.7	0.02	0.14	8.50	1.20
15X-CC, 17–19	133.6	0.42	0.19	0.23	1.6	0.01	0.07	23.00	3.30
17X-1, 24–26	152.9	0.24	0.09	0.15	0.7	0.02	0.10	7.50	1.50
19X-1, 12–14	172.1	0.16	0.04	0.12	0.3	0.02	0.18	6.00	0.66
21X-1, 8–10	191.4	0.50	0.14	0.36	1.2	0.02	0.08	18.00	4.50
23X-CC, 36–38	211.0	0.55	0.19	0.36	1.6	0.03	0.12	12.00	3.00
25X-1, 12–14	229.9	0.81	0.42	0.39	3.5	0.03	0.08	13.00	4.90
27X-1, 33–35	249.5	0.96	0.52	0.44	4.3	0.04	0.12	11.00	3.60
29X-1, 51–53	268.9	0.54	0.22	0.32	1.8	0.03	0.07	10.00	4.60
31X-1, 30–32	287.9	0.63	0.23	0.40	1.9	0.04	0.11	10.00	3.60
141-863B-									
4X-1, 59–61	326.5	0.54	0.32	0.22	2.7	0.03	0.11	7.30	2.00
7N-1, 98–100	355.9	0.84	0.47	0.37	3.9	0.05	0.13	7.40	2.80
10R-1, 6–8	371.1	0.41	0.18	0.23	1.5	0.03	0.13	7.60	1.70
14R-1, 88–90	406.4	1.02	0.59	0.43	4.9	0.05	0.17	8.60	2.50
17R-1, 7–8	434.5	0.56	0.32	0.24	2.7	0.03	0.35	8.00	0.68
20R-1, 103–105	464.4	0.57	0.37	0.20	3.1	0.03	0.34	6.60	0.59
23R-1, 58–60	493.0	0.70	0.39	0.31	3.2	0.05	0.11	6.20	2.80
26R-1, 1–3	521.4	0.66	0.37	0.29	3.1	0.05	0.14	5.80	2.10
28R-1, 48–49	540.7	0.72	0.37	0.35	3.1	0.05	0.18	7.00	1.90
31R-1, 16–18	569.3	0.29	0.16	0.13	1.3	0.02	0.17	6.50	0.76
34R-1, 14–16	598.2	0.33	0.13	0.20	1.1	0.03	0.10	6.60	2.00
36R-2, 16–19	619.1	0.34	0.14	0.20	1.2	0.04	0.15	5.00	1.30
38R-3, 74–76	640.3	0.42	0.14	0.28	1.2	0.05	0.08	5.60	3.50
41R-1, 42–44	665.9	0.34	0.22	0.12	1.8	0.02	0.11	6.00	1.10
45R-1, 69–71	704.9	0.46	0.23	0.23	1.9	0.04	0.10	5.70	2.30
49R-1, 48–50	733.7	0.36	0.24	0.12	2.0	0.02	0.14	6.00	0.86

GRAPE scanning of whole-round core sections provided useful bulk-density measurements for the semiconsolidated silty clay and clayey silt beds of Unit A recovered by APC coring at Hole 863A (Fig. 66). In the upper 50 mbsf two discordances (*X* and *Y* in Fig. 66) in the bulk density data stand out. These appear to correspond to major structural features in the core associated with the black, sulfide-rich region (see discussion below). Virtually no meaningful GRAPE bulk-density measurements were extracted from XCB and RCB cores from Holes 863A and 863B.

Sonic (V_P) Velocity

A relatively good suite of velocity measurements was collected down through the section at Holes 863A and 863B (Table 20). In the region from 0 to 50 mbsf both the digital sound velocimeter (DSV) and *P*-wave logger (PWL) results are available (Fig. 67). The two methods of recording *P*-wave velocity show trends that have similar form. However, the DSV results are shifted to higher velocities from the average PWL velocity by approximately 50 m/s. This could be a basic calibration problem or a real effect of the direction in which the velocity measurements were made. The DSV measurements were made parallel to the core axis, whereas PWL velocities are perpendicular to the core axis.

At deeper levels, velocities slowly increase downhole (Fig. 65) from 1550 to 1700 m/s in the near surface to 1900–2000 m/s at approximately 300–350 mbsf (with some major gaps in the data). At approximately 350 mbsf (top of the transitional boundary between physical properties Units C and D), a rapid increase in velocity occurs to above 2500 m/s. Below 350 mbsf the velocities are uniformly high, increasing to 2800 to 3300 m/s by the base of the hole. This distinct increase in velocity also shows up in the logging data (see Wireline Measurements section, this chapter) and occurs at the Unit C/Unit D boundary.

Thermal Conductivity

The thermal conductivity data can be split into two major trends, both of which demonstrate that thermal conductivity increases slowly with sub-bottom depth (Fig. 65). The two trends are separated by a large discordance at 400 mbsf where the thermal conductivity rapidly increases with sub-bottom depth over a short interval. We checked to see if this discordance corresponded with a change in the method of conductivity measurement from the whole-to half-space method and found that we had started to use the whole-space method higher up in the hole (see Table 21). Thus, this sharp discordance appears to reflect a real physical change in the sediment and occurs across the boundary between physical property Subunits D1 and D2.

Discussion and Overview

Physical properties Unit B comprises mostly clay and silty clay and is closely associated with both the black sulfide-rich sediment and a region of complex deformation. The discordance in GRAPE bulk density data at 22 to 23 mbsf (*Y* in Fig. 66) is associated with

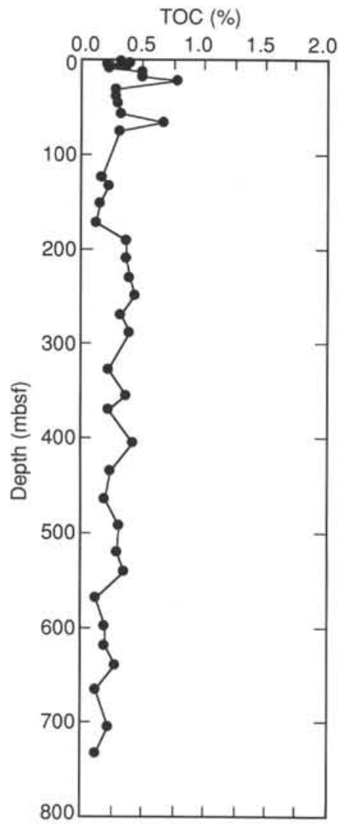

Figure 60. Total organic carbon content vs. depth of sediments from Holes 863A and 863B.

both a major normal fault and a thermal anomaly (see WSTP-ADARA Temperature Measurements and Structural Geology sections, this chapter). The form of the density discordance is consistent with the observed normal fault, with the juxtaposition of originally shallow-buried low- density material in the hanging wall over denser footwall material.

The break in bulk density at 16 mbsf (*X* in Fig. 66) is associated with a complex zone of deformation comprising both normal and reverse faults (as well as some core disturbance associated with core flow-in at the base of the piston core). Although structural observations (see Structural Geology section, this chapter) indicate that the normal faults generally postdate the reverse faults at this level, our observation of dense material over lower density material at 16 mbsf is consistent with the reverse component being dominant.

The discordance in porosity and bulk density between physical properties Unit B and the units above and below are quite large (Fig. 65). Unfortunately, the contact regions are zones of particularly poor core recovery. In general, physical properties Unit B contains less clay than the units above and below (see Lithostratigraphy section, this chapter) and perhaps higher permeabilities have allowed this unit to compact more efficiently. The base of physical properties Unit B is also the site of a relatively large break in the temperature profile. This was also the location of the largest deviation of the borehole and where the drill pipe was eventually trapped. Based on the general coincidence of the temperature anomalies with structures at this site (see WSTP-ADARA Temperature Measurements section, this chapter), and the anomalous behavior of the hole itself, we speculate this contact may be a fault zone.

Physical properties Unit C comprises silt to silty clay, and relatively small gradients in porosity and bulk density occur down though this unit to 400 mbsf (Fig. 65). This is despite the large structural discordance between the shallow-dipping beds above approximately 250 to 260 mbsf and the vertical sequences below this level (see Structural Geology section, this chapter). This observation suggests that the tectonic activity that created this major structural discordance occurred long enough in the past for the sediment to dewater and achieve a uniform compaction gradient.

The transitional boundary between physical properties Units C and D is complex in terms of both physical properties and other parameters, such as inorganic geochemistry, and is separated out as Subunit D1 (see Inorganic Geochemistry section, this chapter). In terms of porosity and bulk density, Subunit D1 is transitional and coincides with a break in slope that corresponds to a more rapid porosity decrease and density increase into the top of Subunit D2 (Fig. 65). The boundaries of Subunit D1 are particularly distinct in both velocity and thermal conductivity data (Fig. 65) and in the density and velocity logs (Fig. 80, see Wireline Measurements section, this chapter). The sharp increase in discrete sample velocity at approximately 350 mbsf (Fig. 65) is coincident with the sudden appearance of thin calcite-cemented sandstone intervals (which have very high velocities) and a general induration of the sediment at the Unit C/Subunit D1 boundary. Thermal conductivity also similarly increases, but across a slightly deeper discontinuity, situated closer to 400 mbsf, coincident with a large jump in the formation resistivity (see Wireline Measurements section, this chapter). In the region between 350 and 400 mbsf an apparent increase in zeolite mineralization was also observed, along with a rapid increase in the smectite component of the clays, and important changes in the geochemistry of the pore fluids (see Lithostratigraphy and Inorganic Geochemistry sections, this chapter).

Sonic velocity is the physical parameter most sensitive to any cementation in the rock, and is thus the best measure of the upper boundary of the diagenetic front that we propose is responsible for the changes in so many of the measured parameters in the depth range between 350 to 400 mbsf (Subunit D1).

In Unit D the general increase in density down to approximately 500 mbsf (Subunit D1) and the vertical trend below this level to the base of the hole probably relate to both consolidation and other diagenetic processes. Little or no major discordance in physical properties is measured across several large zones of breccia in the basal part of the hole (see Structural Geology section, this chapter) and we suggest that these zones formed sufficiently long ago that any physical property discordances have died away.

WSTP-ADARA TEMPERATURE MEASUREMENTS

Site 863 is positioned directly above the oceanic spreading axis that is currently being thrust beneath the toe of the accretionary wedge. Considerable hydrothermal activity was expected to cause measurable anomalies in downhole temperature at Site 863. Specific objectives of the temperature measurement program were:

1. To determine the possible nature of the heat-transfer processes in the wedge toe (conductive vs. advective).
2. To identify any temperature anomalies associated with channelized fluid flow.
3. To provide constraints for geochemical and other studies relating to the movement of fluids though the wedge and the thermal maturation of the sediments in the wedge.

Because of the expected rapid temperature variations, 10 WSTP runs were conducted in the top 293 mbsf of the sediment column, with an additional four ADARA runs in the near-surface

Table 16. Interstitial water data obtained from squeezing whole rounds in titanium squeezers for Site 863.

Core, section, interval (cm)	Depth (mbsf)	IW vol. (mL)	pH	Alk (mM) (Gran)	Sal (Refr)	Cl (mM) (Tit'n)	SO_4 (mM) ($BaSO_4$)	NH_4 (μM) (Spec)	Si (μM) (Spec)	Mg (mM) (Tit'n)	Ca (mM) (Tit'n)	K (mM) (AES)	Sr (μM) (AES)	F (μM) (ISE)	B (mM) (Spec)	Na (mM) (AES)	Li (μM) (AES)
141-863A-																	
1H-3, 145–150	4.45	29.0	8.18	3.65	34.5	556	28.7	62	437	49.90	10.20	13.1	85	65.2	0.58	492.0	34
2H-3, 145–150	13.05	22.0	7.99	3.88	35.0	560	28.1	111	477	50.60	10.40	12.9	85	52.4	0.54	494.0	32
3H-3, 145–150	22.55	32.0	7.86	4.13	35.0	553	28.8	280	585	50.10	10.50	12.9	89	40.0	0.58	482.0	28
4H-2, 145–150	30.55	22.0	8.45	5.32	35.5	559	28.3	616	551	50.10	10.40	12.4	87	38.3	0.52	483.0	24
5H-1, 145–150	38.55	18.0	7.91		35.5	556	27.5	1440	543	50.10	10.50	11.7	87	37.1	0.55	485.0	23
6H-1, 140–150	48.00	38.0	7.99	6.22	35.0	553	27.5	3016	525	50.40	10.30	10.1	92	38.0	0.60	483.0	22
7X-3, 140–150	60.50	24.0	8.09	7.04	36.0	557	26.6		505	49.10	9.75	9.6	94	40.2	0.70	493.0	22
8X-2, 140–150	68.40	28.0	8.00	20.79	33.0	547	0.4	7636	709	37.40	2.15	8.8	37	40.3	0.64	491.0	19
9X-1, 65–75	76.05	18.0			33.0	549	0.4	8244	609	31.20	2.17	9.0	44	41.3	0.62	478.0	27
17X-1, 30–35	153.00	3.0			35.5	549	27.4	142	355	50.70	10.60	11.4	85	45.1	0.32	485.0	35
19X-1, 57–65	172.60	8.0			35.0	550	26.3	155	401	51.60	10.50	11.1	89	44.7	0.31	482.0	35
21X-1, 45–50	191.70	9.0			34.5	547	26.2	239	396	52.00	9.93	10.6	83	46.5	0.27	484.0	45
23X CC, 25–30	210.80	12.0			36.0	549	27.0	424	545	51.20	11.30	10.9	87	45.4	0.27	480.0	44
24X-1, 52–57	220.80	10.0			35.5	549	27.3	511	708	51.40	12.10	10.4	91	45.2	0.30	486.0	45
25X-1, 43–53	230.20	13.0			35.0	559	26.4	452	603	52.10	11.80	10.8	91	47.1	0.22	482.0	68
26X-1, 64–74	240.10	12.0			35.0	555	27.2	350	554		11.60	10.4	92	45.2	0.27	483.0	38
27X-1, 82–92	250.20	10.0			35.0	560	26.7	537	533	50.90	12.50	10.7	94	48.0	0.24	482.0	50
28X-1, 112–126	259.92	1.0				557	26.3	602				10.0		45.2	0.30	498.0	38
29X-1, 70–80	269.10	8.0			35.5	550	26.1	653	525		12.70	10.1	91	44.4	0.24	481.0	42
30X-1, 140–150	279.50	12.0	8.16	4.83	35.0	556	26.8	466	605	51.70	12.80	10.0	96	43.3	0.24	476.0	44
31X-CC, 15–20	288.40	12.0			35.0	557	26.9	373	646	52.00	12.40	9.3	92	38.3	0.21	483.0	42
141-863B-																	
4X-3 140–150	330.30	12.0			35.0	559	25.7	2315	809	45.70	14.40	9.4	107	45.4	0.42	491.0	140
7N-1, 140–150	356.30	10.0	8.83	3.92	36.0	559	25.3	1433	576	46.80	11.84	8.1	100	40.6	0.19	493.0	50
8N-1, 79–89	358.20	9.0			34.5	555	24.2	1596	600	46.20	12.05	8.3	104	41.5	0.19	492.0	50
10R-1, 26–36	371.30	12.0	8.80	5.54	35.0	559	25.0	1687	607	44.20	11.90	8.4	102	41.3	0.19	492.0	43
11R-1, 11–18	376.70	15.6	8.72	4.64	34.5	558	23.8	1531	716	45.20	12.20	7.7	105	43.1	0.17	486.0	48
12R-1, 103–113	387.30	5.3			34.5	558	21.8	1642		41.20	10.90	8.0	100	43.1	0.12	493.0	49
13R-1, 20–30	396.00	7.5			34.0	554	19.4	1704	627	39.00	10.60	6.9	98	43.1	0.16	492.0	42
14R-1, 140–150	406.90	7.8			34.0	549	18.8	1535	574	41.30	10.30	6.5	104	43.0	0.15	489.0	45
15R-1, 140–150	416.60	20.0	8.56	5.01	32.5	562	2.1	2446	286	35.10	11.90	5.0	117	43.3	0.18	467.0	55
16R-2, 140–150	427.60	14.3			33.0	563	1.6	2555	247	35.00	13.40	5.4	113	43.7	0.17	477.0	55
17R-3, 135–150	438.70	6.0			32.0	568	1.1	2341	265	38.40	14.50	3.7	117	42.0	0.11	460.0	57
18R-1, 140–150	445.40	3.0			32.0	557	1.1	2165		38.10	15.60	3.2	128		0.08	448.0	52
19R-2, 140–150	456.60	17.0	9.03	3.65	32.0	558	1.2	2568	158	36.60	16.40	3.3	122	48.4	0.14	471.0	58
20R-2, 108–118	465.80	7.5			32.0	556	1.5	2504	151	36.20	17.30	3.2	129	50.2	0.11	458.0	60
21R-1, 96–108	474.00	4.5			32.0	564	2.7	2720		35.50	17.10	3.3	128		0.15	470.0	59
22R-3, 90–100	486.30	9.0			32.5	561	0.9	2309	125	34.20	26.40	2.2	146	51.4	0.10	450.0	70
23R-3, 140–150	496.80	11.0	9.41	2.16	35.0	570	0.6	1963	134	22.70	43.00	1.1	124	49.6	0.12	452.0	99
24R-1, 135–145	503.30	17.3	9.25	1.58	34.5	578	3.8	1959	136	17.50	50.70	0.9	98	52.8	0.17	463.0	115
25R-2, 140–150	514.60	18.0			35.0	583	9.0	1959	129	4.48	75.50	0.7	67	58.3	0.30	446.0	138
26R-1, 45–55	521.80	13.5			36.5	583	13.1	1866	135	1.70	85.40	0.7	65	59.3	0.37	438.0	129
27R-3, 140–150	535.00	16.2	9.82	3.08	37.0	578	18.3	1897	160	2.01	95.60	0.8	61	76.7	0.63	428.0	100
28R-1, 63–73	540.80	18.0			37.0	581	19.2	1932	146	3.67	95.20	0.7	65	82.1	0.82	433.0	92
31R-3, 140–150	573.50	4.5			38.0	595	15.4	1724		1.14	113.00	1.1	70	80.5	0.88	416.0	88
32R-5, 140–150	586.20	8.5			37.5	589	14.4	1691		0.20	113.00	0.6	65	84.7	0.94	399.0	86
33R-1, 105–115	589.40	10.0	10.25	3.47	37.0	582	15.2	1835		2.40	108.00	0.8		86.4	0.98	408.0	88
34R-3, 140–150	602.50	7.5				586	14.1	1732		2.80	114.00	0.5	68	71.7	0.93	398.0	78
35R-3, 138–148	612.10	7.0			37.5	579	15.2	1897		2.40	112.00	0.6	68	73.2	0.94	390.0	77
36R-3, 140–150	621.30	7.0			37.5	581	16.5	1691		2.10	119.00	0.5	83	69.7	0.77	387.0	82
37R-4, 140–150	632.90	8.0	10.46	4.16	37.0	573	17.7	1831		2.00	117.00	1.1	100	73.4	0.79	388.0	90
38R-2, 140–150	639.50	6.7			38.0	573	18.7	1794		0.10	118.00	0.7	105	73.4	0.69	390.0	86
39R-1, 125–140	647.50	12.0			38.0	577	19.1	2000		1.00	117.00	0.7	107	77.9	0.88	387.0	91
40R-1, 110–120	657.00	6.1			38.0	572	19.6	1959		1.40	124.00	0.4	102	76.4	0.71	373.0	88
41R-1, 135–150	666.80	1.5			37.5	580	18.7			0.40	122.00	0.7			0.62	383.0	85
42R-1, 140–150	676.60	2.0			38.0	592	18.5	2185		0.10	135.00	0.7	122	72.6	0.67	373.0	94
43R-2, 90–100	687.20	0.7			40.0	614				0.60	143.00				0.49		
44R-2, 137–147	697.30	3.5			36.5	588	11.6	2000		1.80	131.00	0.5	115	79.8	0.70	361.0	84
45R-1, 90–100	705.10	1.0			36.5		10.8			1.50	126.00	1.0				363.0	
46R-1, 12–22	706.90	2.5			38.0	590	10.9	1349		1.80	131.00	0.7	124	75.2	0.54	362.0	87
47R-2, 0–10	715.30	2.6			37.5	576	9.9	1691		0.10	127.00	0.5	118	67.0	0.69	356.0	81
48R-1, 32–46	723.80	1.5			39.0	575	10.2	1446		1.10	136.00	1.1	135		0.58	344.0	88
49R-3, 135–150	737.50	8.2	10.44		37.0	576	9.3	1774		0.10	135.00	0.7	148	66.5	0.69	350.0	73

region. The WSTP was deployed both in its newer format and its old format (with Uyeda temperature probe only).

WSTP Temperature Measurements

The quality of the WSTP temperature measurements at this site is variable. A small number exhibited unusually pronounced temperature fluctuations during the temperature decay sequence after insertion in the formation. Of the ten WSTP runs, however, seven produced results than could be used to constrain the temperature profile at this site.

The deployment of the newer WSTP tool at 27.6 mbsf produced a good initial penetration and temperature decay profile over 8 min that extrapolates in 1/t space to 5.26°±0.04°C (Fig. 68). At long time intervals a small temperature anomaly produces a deviation from the initial linear trend (a "data hook"—see WSTP-ADARA Temperature Measurements section, Site 859 chapter). The "data hook" itself trends toward approximately 5.7°C. The measurement with the newer WSTP at 56.1 mbsf is not of the highest quality (Fig. 69) because the temperature spike on formation penetration is small and the 1/t fit is not very linear. The record is included here because, relative to the local WSTP and ADARA measurements immediately above and below, it records generally high temperatures that range between 8.75°C and 9°C at this level of the borehole. As the borehole fluid is close to seawater bottom temperatures of approximately 2°C, the generally raised-temperature in this portion of the borehole must reflect locally higher formation temperatures. A best attempt at a linear fit though the early part of the 1/t fit extrapolates to

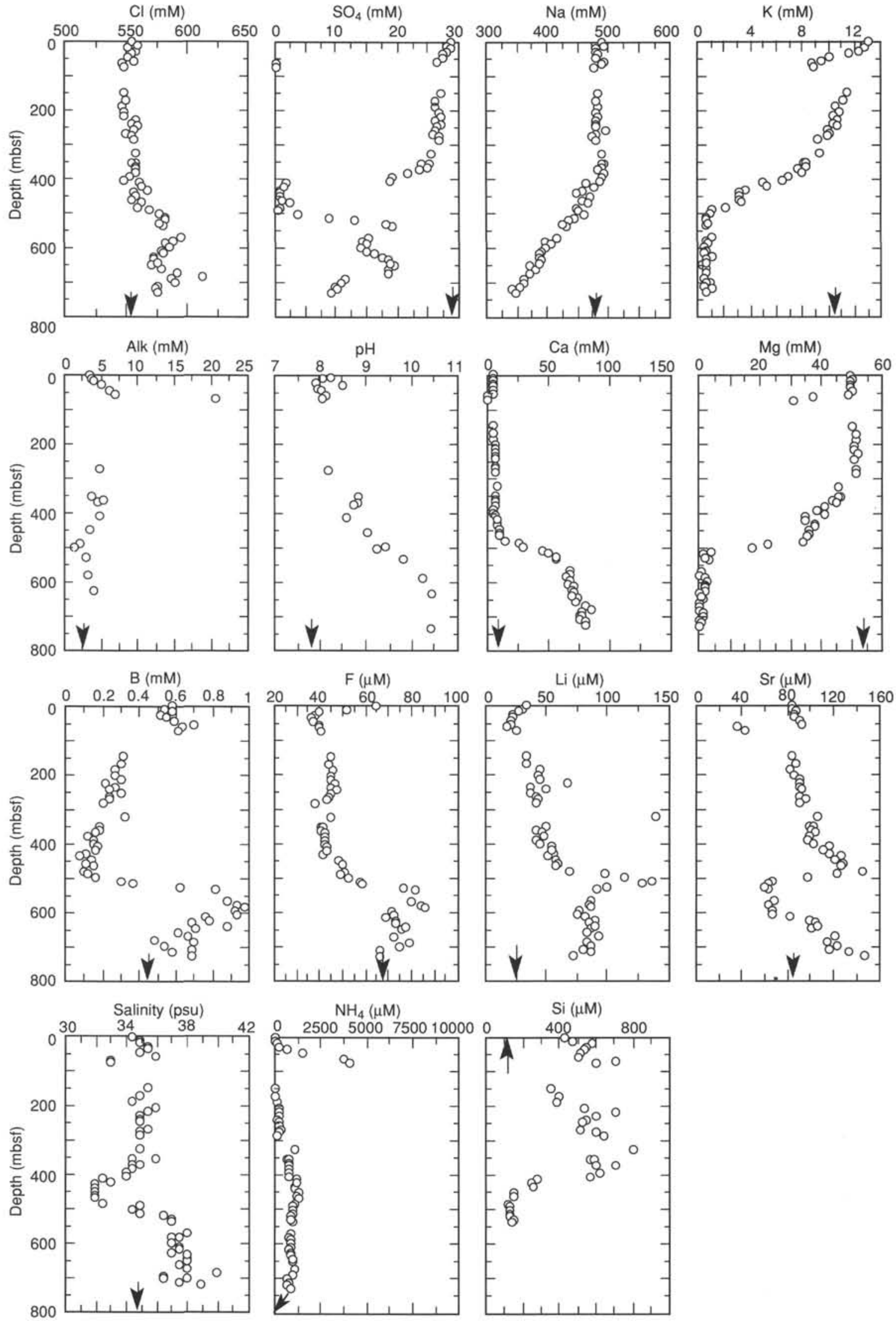

Figure 61. Interstitial water compositions vs. sub-bottom depth for Site 863. All data are from squeezed whole rounds of APC, XCB, and RCB cores. Arrows on axes indicate seawater concentrations for each constituent, where appropriate.

Table 17. Interstitial water data obtained from WSTP runs for Site 863.

Core	Depth (mbsf)	Designation	Volume (mL)	Salinity (Refr)	Cl (mM)	SO_4 (mM)	Mg (mM)	Ca (mM)	F (μM)	B (mM)	Sr (μM)	Li (μM)
141-863A-												
4H	27.6	WT	6	33	551	28.3	52.8	10.5	77.3	0.37	92	32
		WO	400	28	460	23.9	44.4	8.75	52	0.3	78	69
7X	56.1	WT	7.5	34	555	26.5	52.5	10.3	86.1	0.49	98	21
		WO	79.5	14	232	11.4	21.9	4.3	58	0.18	50	99
10X	85.1	WT	5.5	34	539	25.7	50.5	8.97	67.6	0.44	87	27
		WO	850	32	508	25	47.5	8.77	63	0.9	79	33
13X	114	WT	7	33	536	26.9	50.7	10.1	63.2	0.43	89	25
		WO	860	30	488	24.9	46.3	9.24	61	0.37	85	32
16X	143	WT	6	33	538	27.8	51.5	10	62.9	0.34	85	26
		WO	1100	32	517	26.6	48.5	9.61	63	0.33	79	30

WT - titanium coil. WO - overflow chamber.

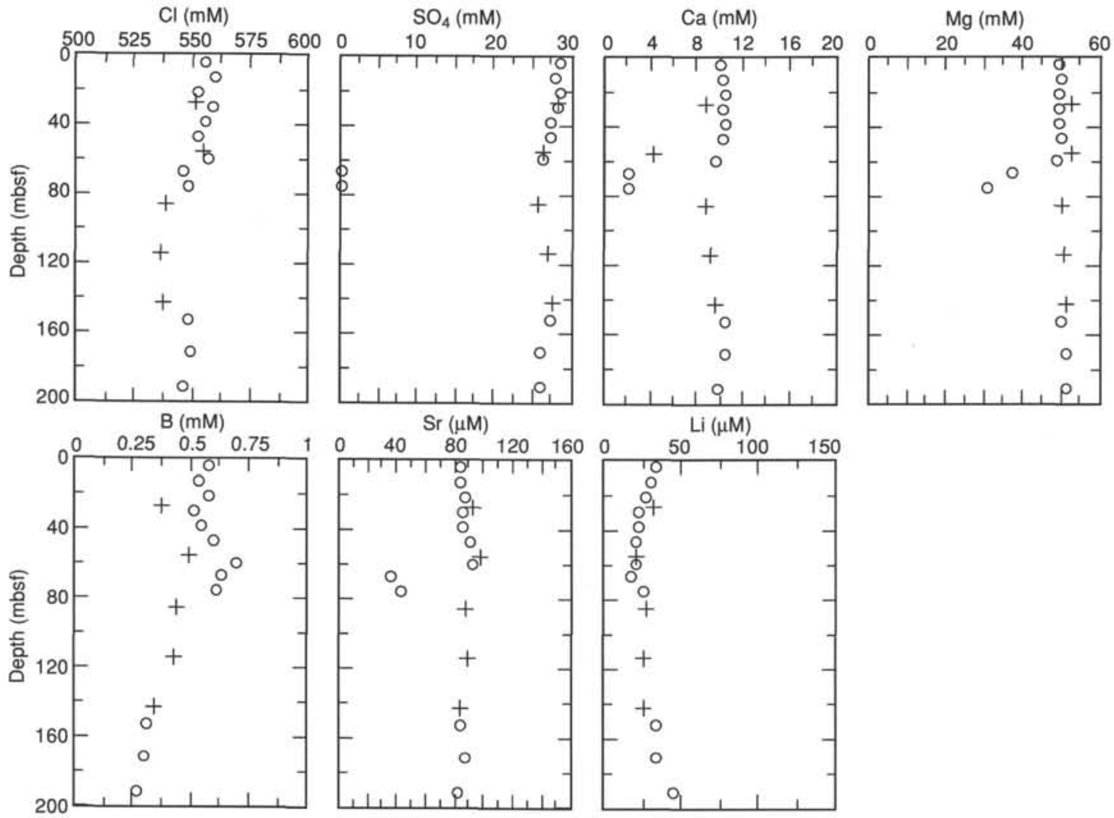

Figure 62. Comparison of interstitial water data from squeezed whole rounds (open circles) and from the WSTP (crosses).

approximately 8.75°C, while an extrapolation from the data hook at low 1/t values trends toward approximately 9.1°C. As a consequence, we suggest that the actual formation temperature must be at, or higher than, an average 8.9°± 0.2°C in this region of the borehole.

The measurement with the newer WSTP tool at 85.1 mbsf is of moderate quality (Fig. 70). Although the temperature spike and decay look reasonable, the linear fit is not particularly good after the first 5 to 6 min of data. The initial linear extrapolation indicates a formation temperature of 9.24°C. The subsequent data hook trends to a slightly higher temperature of approximately 9.42°C over a period of over 17 min. We suggest that the formation temperature is bounded by these two extrapolated temperatures because we would not expect the temperature of a cracked formation to be so stable over such a long time (the two extreme values differ by less than 0.2°C). Thus we have taken an average of the two extrapolated trends for a formation temperature of 9.33°± 0.09°C.

The deployment of the older WSTP tool at 143 mbsf resulted in a high-quality measurement (Fig. 71), with over 11 min of data on the linear extrapolation to a formation temperature of 12.0°± 0.05°C. The deployment of the older WSTP tool at 200.9 mbsf produced a moderate-quality measurement (Fig. 72). From the form of the overall temperature record, there initially appears to be a good penetration and subsequent cooling trend. The rather short 1/t fit to the first 5 min produces a linear extrapolation to a formation temperature of 16.2°±0.05°C. The subsequent data hook is, however, substantial and trends toward 17.0°±0.08°C.

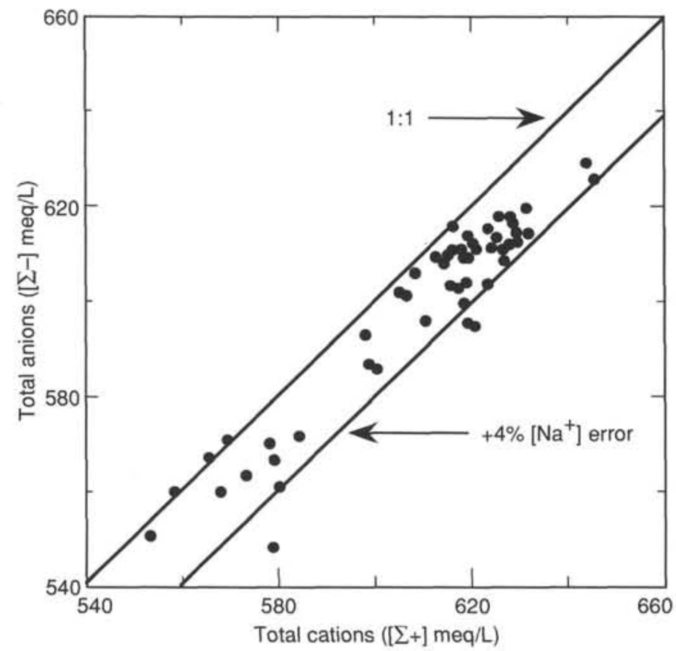

Figure 63. Total cation charges plotted vs. total anion charges for Site 863 interstitial water samples. Since solutions must be electrically neutral, all data should fall along the 1:1 line. All data appear to 2±2% off the line toward cation-rich (anion-poor) errors. Thus, the sums of systematic errors for the major cations and anions can not exceed ~4%. The most likely source of this offset is either +2% error in Na-determinations or –2% error in Cl determinations, or some combination.

Given the short initial linear profile and the subsequent large data hook in 1/t space, it is possible that tool disturbance may have allowed some borehole fluid to have penetrated the formation during the initial stages of the deployment. The data hook may then relate to later warming of the water toward formation temperatures in the latter part of the penetration period. Note, however, that the previous deployment at 143 mbsf was of high quality (Fig. 71) and also had a late data hook that had an initial trend toward higher temperatures in 1/t space. Due to the problems of interpreting the record at 200.9 mbsf, we provisionally average the two extreme possibilities to give a formation temperature of 16.6°±0.4°C.

Both the measurements performed with the older WSTP tool at 229.8 and 239.5 mbsf (Figs. 73 and 74, respectively) are of high quality, with more than 22 min of data on the linear extrapolation to formation temperatures of 25.84°±0.08°C and 26.77°±0.10°C, respectively. During the penultimate deployment at 239.5 mbsf, the tool did not appear to penetrate the formation. During the last deployment, the collet system in the downhole assembly broke and the old WSTP tool was lost during the attempted recovery, ending drilling at Hole 863A.

ADARA Measurements

Of the four attempted ADARA measurements, three provided useful results. Due to the scatter in the thermal conductivity data in the top 50 mbsf (see Physical Properties section, this chapter), we use thermal conductivities of 1.2 and 1.3 W/m·K and average the two resulting temperature estimates obtained from the APCTFIT program. The very high thermal conductivities (around 1.4–1.6 W/m·K) periodically recorded at this level were from localized regions rich in black sulfides, and we do not consider them to be a reflection of the average thermal conductivity of this interval. In general, however, varying the thermal conductivity only caused very minor variations in the extrapolated temperatures from the ADARA tool.

The deployment at 27.6 mbsf was of moderate quality with a slight disturbance of the tool requiring the fitting of two portions of the decay curve. The fit to the upper portion of the curve (x on Fig. 75) gave temperatures of 5.49°C and 5.37°C using thermal conductivities of 1.2 and 1.3 W/m·K, respectively. The fit to the lower portion of the curve (y on Fig. 75) gave temperatures of 5.48°C and 5.5°C with thermal conductivities of 1.2 and 1.3 W/m·K, respectively. The average formation temperature at this depth is then 5.46°± 0.09°C.

The deployment at 37.1 mbsf is of very high quality (Fig. 76), and the extrapolated fit to the decay curve gave temperatures of 4.42°C and 4.29°C using thermal conductivities of 1.2 and 1.3 W/m·K, respectively. The average formation temperature at this depth is then 4.36°± 0.07°C. The deployment at 46.6 mbsf is also of very high quality (Fig. 77), with the extrapolated fit to the decay curve giving temperatures of 5.72°C and 5.60°C using

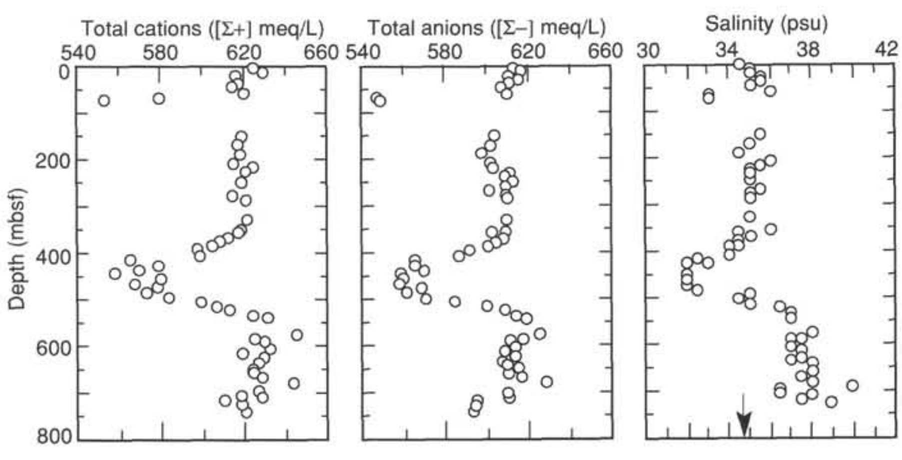

Figure 64. Sum of total cation charges, total anion charges, and salinity, all plotted vs. depth for Site 863 interstitial water samples. Total cations and total anions are a more accurate measure of "salinity" than refractive index for pore-fluid compositions that are very different from NaCl (seawater) composition. Arrow indicates seawater salinity.

Table 18. Composition of gases trapped inside the WSTP titanium coils as a result of gas expansion.

Core	Designation	Depth (mbsf)	C_1 (ppm)	C_2 (ppm)	i-C_4	n-C_4	i-C_5	n-C_5	n-C_6	CO_2
141-863A-										
4H	WT	27.6	56.3	0	0	0	0	0	0	558
10X	WT	56.1	289915	485	0	0	0	0	0	
10X	WO	56.1	5798	8.33	0	9.7	0	0	2.69	375
13X	WT	114	28402	13.87	0	2.13	0	0	0	
16X	WT	143	623	0	0	0	0	0	0	520
16X	WO	143	547	8.97	4.15	117	1.95	5.1	2.33	951

WT = gases from titanium coil. WO = gases from overflow chamber.

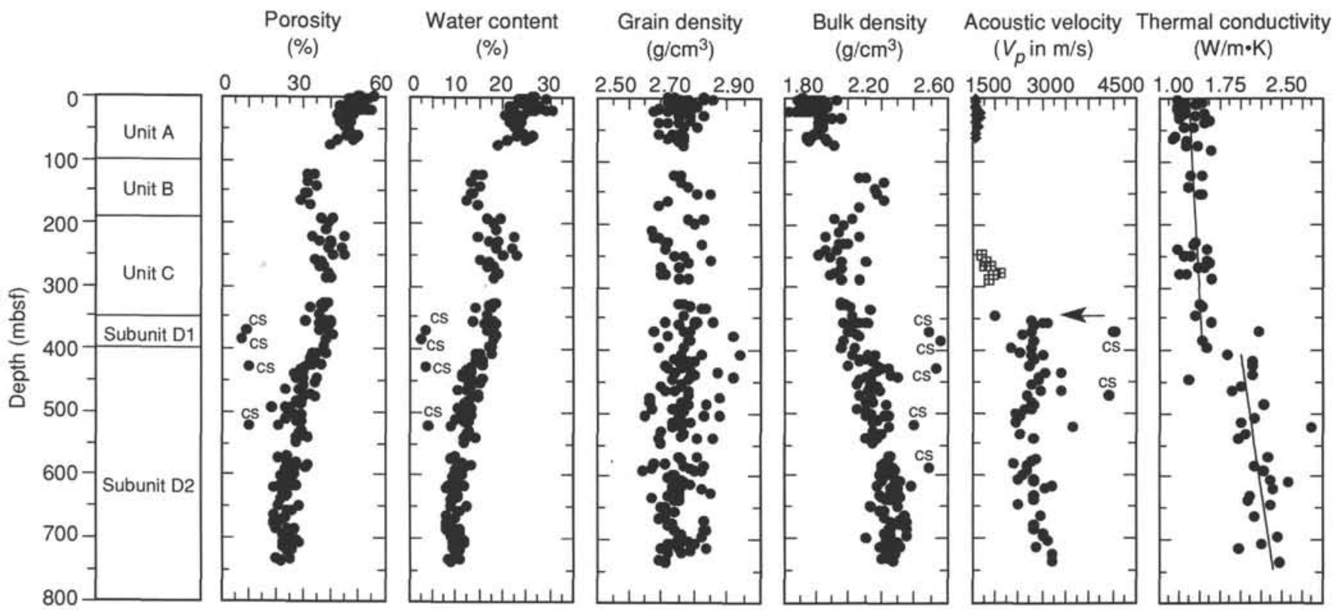

Figure 65. Physical properties units, discrete-sample porosity, water content, grain density, bulk density, acoustic velocity, and thermal conductivity. Data for Holes 863A and 863B are combined. CS denotes calcite-cemented sandstone layers. In the acoustic velocity chart, diamonds indicate DSV measurements From Hole 863A; boxes indicate Hamilton Frame (HF) measurements from Hole 863A; dots indicate HF measurements from Hole 863B.

thermal conductivities of 1.2 and 1.3 W/m·K, respectively. The average formation temperature at this depth is then 5.66°±0.06°C.

Discussion

The results from the WSTP and ADARA tools are presented in Table 22 and are plotted against sub-bottom depth on Figure 78. The profile is not very linear with peaks in the temperature profile at approximately 27 and 56 mbsf and in the region of 230–240 mbsf. This is not a conductive profile, and lateral fluid movement though this section must be substantial to produce temperature fluctuations of this size. These peaks in temperature are also broadly consistent with similar inflection points in the temperature profiles obtained from logging the hole (see Wireline Measurements section, this chapter) and discontinuities in the geochemical profiles at around 60 mbsf (see Inorganic Geochemistry section, this chapter).

The two relatively sharp peaks in temperature in the upper part of the profile broadly correspond to a structurally complex region rich in black sulfides, that lies between 0 and 65 mbsf (see Lithostratigraphy section, this chapter). In this sulfide-rich region there is evidence, in the form of black sulfide dilational-jog fillings (see Structural Geology section, this chapter), that fracture-controlled fluid flow is important. In detail, the upper of these two temperature anomalies is defined by both the ADARA and WSTP probe and is positioned (on the scale at which the temperature measurements were made) very close to a major structural and physical property discontinuity (see Structural Geology and Physical Properties sections, this chapter) located at approximately 22 to 23 mbsf. This discontinuity corresponds to a large normal fault (see Fig. 40).

The lower of the two temperature anomalies corresponds to the base of the complexly deformed sediments comprising the sulfide-rich region (see Structural Geology and Physical Properties sections, this chapter). Note that this lower temperature reading is not of the best quality, and it probably represents a minimum formation temperature at this level. This warm water is associated with anomalously low salinity fluids that are probably associated with lateral advection (see Inorganic Geochemistry section, this chapter).

In the region between 60 and 200 mbsf the temperature profile is substantially more linear, and it is tempting to attribute this to a remnant conductive profile existing before the localized anomalies associated with the shallow sulfide-rich region developed. A rough linear extrapolation can, for example, be drawn through the readings at 37.1, 46.6, 85.1, and 200.9 mbsf that gives a temperature gradient of approximately 73°C/km (Fig. 79). This is not a particularly high gradient, considering the position of Site 863 directly over the oceanic spreading axis. The wireline logging temperatures, however, suggest that the actual overall gradient is higher than this, perhaps a little above 85°C/km, and that the

Table 19. Index physical properties for combined Holes 863A and 863B.

Core, section, interval (cm)	Depth (mbsf)	Wet-bulk density (g/cm^3)	Dry-bulk density (g/cm^3)	Grain density (g/cm^3)	Wet-sediment porosity (%)	Dry-sediment porosity (%)	Wet-sediment water content (%)	Dry-sediment water content (%)	Wet-sediment void ratio	Dry-sediment void ratio
141-863A-										
1H-1, 7	0.07	1.92	1.41	2.72	49.8	49.2	26.6	36.2	0.99	0.96
1H-1, 139	1.39	2.13	1.56	2.74	55.7	49.7	26.7	36.5	1.26	0.98
1H-2, 41	1.91	1.93	1.41	2.83	50.5	50.5	26.8	36.7	1.02	1.01
1H-2, 132	2.82	1.96	1.44	2.78	50.8	49.8	26.5	36.1	1.03	0.98
1H-3, 52	3.52	1.89	1.34	2.83	53.6	53.4	29.1	41.1	1.15	1.13
1H-3, 98	3.98	1.99	1.50	2.76	47.8	47.1	24.6	32.7	0.92	0.88
1H-5, 41	6.41	1.97	1.47	2.78	49.5	48.7	25.7	34.6	0.98	0.94
1H-6, 53	8.03	1.98	1.47	2.72	49.7	48.2	25.8	34.7	0.99	0.92
1H-CC, 16	8.48	1.94	1.43	2.74	49.9	49.2	26.4	35.8	1.00	0.96
2H-1, 40	9.00	1.94	1.43	2.72	49.8	48.8	26.2	35.6	0.99	0.95
2H-3, 20	11.80	2.01	1.52	2.80	47.6	47.0	24.3	32.1	0.91	0.88
2H-4, 53	13.63	2.06	1.62	2.75	43.1	42.5	21.4	27.2	0.76	0.73
2H-4, 130	14.40	2.07	1.60	2.81	45.6	44.7	22.6	29.2	0.84	0.80
2H-5, 60	15.20	1.91	1.37	2.77	52.4	51.7	28.1	39.2	1.10	1.06
3H-1, 8	18.18	1.97	1.47	2.74	48.7	47.9	25.4	34.0	0.95	0.91
3H-2, 84	20.44	1.90	1.37	2.69	51.8	50.7	28.0	38.8	1.07	1.02
3H-2, 143	21.03	1.84	1.27	2.77	55.1	54.8	30.7	44.3	1.23	1.20
3H-3, 20	21.30	1.88	1.33	2.75	53.6	52.9	29.3	41.4	1.16	1.11
3H-3, 77	21.87	1.96	1.44	2.79	51.2	50.1	26.7	36.5	1.05	0.99
3H-4, 100	23.60	2.05	1.61	2.72	43.7	42.7	21.8	27.8	0.77	0.74
3H-4, 21	22.81	1.93	1.44	2.68	48.5	47.8	25.7	34.6	0.94	0.91
3H-5, 86	24.96	2.03	1.57	2.77	44.8	44.4	22.6	29.3	0.81	0.79
3H-6, 31	25.91	2.05	1.60	2.78	44.7	44.0	22.3	28.7	0.81	0.78
4H-1, 105	28.65	2.03	1.55	2.83	47.1	46.5	23.7	31.1	0.89	0.86
4H-1, 105	28.65	2.02	1.52	2.75	48.5	47.0	24.7	32.7	0.94	0.88
4H-2, 130	30.40	2.10	1.64	2.75	45.5	43.5	22.1	28.4	0.83	0.76
4H-3, 27	30.87	2.15	1.71	2.79	42.7	41.3	20.4	25.6	0.75	0.70
4H-CC, 8	31.35	2.03	1.57	2.79	45.0	44.6	22.7	29.3	0.82	0.80
5H-1, 100	38.10	2.05	1.58	2.79	45.4	44.6	22.7	29.4	0.83	0.80
5H-2, 127	39.87	2.04	1.59	2.69	43.4	42.5	21.8	27.9	0.77	0.73
5H-2, 50	39.10	2.02	1.53	2.75	47.7	46.4	24.2	32.0	0.91	0.86
5H-CC, 4	40.37	2.05	1.59	2.72	45.4	43.9	22.7	29.3	0.83	0.78
6H-1, 50	47.10	2.05	1.59	2.81	44.8	44.4	22.4	28.8	0.81	0.79
6H-1, 124	47.84	2.01	1.53	2.77	46.5	45.9	23.7	31.1	0.87	0.84
7X-1, 100	57.10	2.02	1.54	2.75	46.5	45.5	23.6	30.8	0.87	0.83
7X-2, 100	58.60	1.99	1.51	2.73	46.8	46.0	24.1	31.7	0.88	0.84
7X-3, 100	60.10	1.98	1.50	2.69	47.3	46.1	24.4	32.3	0.90	0.85
7X-4. 65	61.25	1.95	1.44	2.73	50.0	48.9	26.3	35.6	1.00	0.95
7X-5, 58	62.68	2.06	1.59	2.77	45.9	44.6	22.8	29.5	0.85	0.80
8X-1, 68	66.18	1.94	1.43	2.72	49.3	48.6	26.1	35.3	0.97	0.94
8X-2, 100	68.00	1.96	1.47	2.75	48.4	47.8	25.2	33.8	0.94	0.91
8X-3, 130	69.80	2.07	1.63	2.77	42.9	42.4	21.3	27.0	0.75	0.73
9X-CC, 4	76.19	2.12	1.71	2.77	40.3	39.7	19.4	24.1	0.67	0.65
14X-1, 43	124.13	2.30	1.97	2.76	31.5	30.8	14.1	16.4	0.46	0.44
14X-2, 42	125.12	2.26	1.91	2.74	34.4	33.2	15.6	18.4	0.52	0.49
15X-CC, 14	133.54	2.42	2.09	2.76	32.0	29.8	13.5	15.6	0.47	0.42
16X-CC, 14	143.14	2.36	2.00	2.78	35.0	32.8	15.2	17.9	0.54	0.49
17X-1, 20	152.90	2.37	2.04	2.85	31.4	30.6	13.6	15.7	0.46	0.44
17X-1, 26	152.96	2.38	2.05	2.81	31.7	30.5	13.7	15.8	0.46	0.43
18X-CC, 7	162.47	2.42	2.12	2.72	29.1	27.3	12.3	14.0	0.41	0.37
19X-1, 10	172.10	2.27	1.93	2.69	33.1	31.8	14.9	17.6	0.49	0.46
21X-1, 7	191.37	2.22	1.85	2.83	36.6	36.1	16.9	20.3	0.58	0.56
21X-CC, 7	191.87	2.12	1.70	2.78	41.0	40.4	19.8	24.8	0.70	0.67
22X-CC, 24	201.14	2.17	1.77	2.80	39.0	38.4	18.4	22.6	0.64	0.62
23X-CC, 38	210.98	2.14	1.74	2.67	38.7	37.5	18.6	22.8	0.63	0.59
24X-1, 36	220.66	2.06	1.60	2.69	45.5	43.6	22.6	29.2	0.83	0.77
24X-CC, 47	221.34	2.27	1.93	2.68	33.2	31.8	15.0	17.7	0.50	0.46
25X-1, 10	229.90	2.17	1.75	2.72	40.5	38.9	19.2	23.7	0.68	0.63
25X-2, 3	230.36	2.14	1.76	2.71	36.4	36.0	17.4	21.1	0.57	0.56
25X-CC, 28	231.22	2.20	1.78	2.82	40.2	39.1	18.8	23.1	0.67	0.64
26X-1, 28	239.78	2.06	1.61	2.71	44.1	42.9	22.0	28.1	0.79	0.74
26X-2, 20	240.44	2.13	1.72	2.71	39.3	38.4	18.9	23.3	0.65	0.62
27X-1, 36	249.56	2.02	1.55	2.74	45.1	44.6	22.9	29.7	0.82	0.80
27X-CC, 50	250.62	2.08	1.66	2.77	41.3	41.0	20.3	25.5	0.70	0.69
28X-1, 16	258.96	2.30	1.95	2.85	34.2	33.5	15.2	18.0	0.52	0.50
28X-CC, 35	260.41	2.16	1.79	2.78	36.8	36.6	17.4	21.1	0.58	0.57
29X-1, 49	268.89	2.15	1.77	2.75	37.9	37.4	18.0	22.0	0.61	0.59
29X-2, 40	269.60	2.16	1.80	2.70	35.6	35.0	16.9	20.3	0.55	0.53
30X-1, 117	279.27	2.12	1.72	2.71	39.1	38.4	18.9	23.3	0.64	0.62
30X-2, 71	280.31	2.09	1.69	2.70	39.3	38.8	19.3	23.9	0.65	0.63
31X-1, 30	287.90	2.26	1.84	2.78	40.5	38.1	18.4	22.5	0.68	0.61
31X-CC, 23	288.46	2.16	1.77	2.75	38.7	37.8	18.3	22.5	0.63	0.60
1H-3, 96	3.96	2.02	1.51	2.86	49.0	48.3	24.9	33.2	0.96	0.92
1H-4, 17	4.67	2.04	1.56	2.86	46.8	46.4	23.6	30.8	0.88	0.86
1H-4, 76	5.26	2.06	1.57	2.75	48.0	46.0	23.9	31.4	0.92	0.84
141-863B-										
4X-1, 54	326.44	2.16	1.78	2.75	38.0	37.2	18.0	21.9	0.61	0.59
4X-2, 7	327.47	2.15	1.74	2.77	39.2	38.6	18.7	23.0	0.64	0.62
4X-3, 102	329.92	2.18	1.80	2.79	37.1	36.7	17.4	21.1	0.59	0.57
4X-CC, 12	332.76	2.21	1.83	2.82	37.7	37.0	17.5	21.2	0.61	0.58
5X-CC, 18	335.78	2.33	1.99	2.84	32.3	31.7	14.2	16.6	0.48	0.46
6X-CC, 28	345.48	2.22	1.85	2.77	36.1	35.2	16.7	20.0	0.56	0.54

Table 19 (continued).

Core, section, interval (cm)	Depth (mbsf)	Wet-bulk density (g/cm^3)	Dry-bulk density (g/cm^3)	Grain density (g/cm^3)	Wet-sediment porosity (%)	Dry-sediment porosity (%)	Wet-sediment water content (%)	Dry-sediment water content (%)	Wet-sediment void ratio	Dry-sediment void ratio
141-863B-(Cont)										
7N-1, 97	355.87	2.23	1.82	2.86	40.0	38.8	18.4	22.5	0.67	0.63
7N-1, 120	356.10	2.30	1.91	2.80	38.3	36.2	17.1	20.6	0.62	0.56
7N-2, 75	357.15	2.27	1.88	2.81	37.7	36.2	17.0	20.5	0.60	0.5
8N-1, 17	357.57	2.32	2.00	2.71	31.4	30.0	13.8	16.0	0.46	0.42
8N-2, 12	358.41	2.17	1.76	2.80	40.1	39.1	18.9	23.3	0.67	0.64
9X-CC, 29	361.69	2.23	1.86	2.75	36.0	34.9	16.5	19.8	0.56	0.53
10R-1, 96	371.96	2.21	1.80	2.79	39.6	38.2	18.4	22.5	0.66	0.61
10R-1, 7	371.07	2.20	1.83	2.68	36.3	35.0	16.9	20.3	0.57	0.53
10R-1, 60	371.60	2.69	2.60	2.77	9.4	9.2	3.6	3.7	0.10	0.10
11R-1, 52	377.12	2.26	1.85	2.92	39.9	38.8	18.1	22.0	0.66	0.63
11R-1, 4	376.64	2.25	1.83	2.72	40.8	37.9	18.5	22.8	0.69	0.61
12R-1, 4	386.34	2.17	1.78	2.78	38.1	37.6	18.0	22.0	0.62	0.60
12R-1, 40	386.70	2.77	2.69	2.79	7.7	7.4	2.8	2.9	0.08	0.08
13R-1, 10	395.90	2.15	1.77	2.69	37.4	6.5	17.8	21.7	0.60	0.57
13R-1, 60	396.40	2.24	1.86	2.77	37.5	36.0	17.1	20.7	0.60	0.56
14R-1, 89	406.39	2.22	1.83	2.94	38.6	38.5	17.8	21.7	0.63	0.62
14R-2, 46	407.46	2.32	1.96	2.82	34.8	33.5	15.4	18.2	0.53	0.50
14R-3, 44	408.44	2.36	2.01	2.76	33.4	31.6	14.5	17.0	0.50	0.46
15R-1, 130	416.50	2.30	1.94	2.75	34.5	33.0	15.4	18.2	0.53	0.49
15R-1, 42	415.62	2.27	1.94	2.74	32.4	31.5	14.6	17.1	0.48	0.46
15R-2, 107	417.77	2.35	2.02	2.80	32.4	31.1	14.1	16.4	0.48	0.45
15R-CC, 12	418.24	2.26	1.91	2.78	34.4	33.5	15.6	18.4	0.52	0.50
16R-1, 80	425.50	2.37	2.00	2.78	36.7	34.0	15.8	18.8	0.58	0.51
16R-2, 63	426.83	2.20	1.86	2.71	33.9	33.3	15.8	18.7	0.51	0.50
16R-3, 98	428.68	2.41	2.09	2.72	31.0	28.9	13.2	15.2	0.45	0.40
16R-4, 126	430.46	2.74	2.63	2.76	10.5	10.0	3.9	4.1	0.12	0.11
16R-5, 40	431.10	2.44	2.13	2.79	29.4	27.9	12.4	14.1	0.42	0.38
17R-1, 8	434.48	2.37	2.07	2.87	29.3	29.0	12.6	14.5	0.41	0.41
17R-2, 20	436.10	2.35	2.04	2.74	30.4	29.2	13.3	15.3	0.44	0.41
17R-5, 102	441.42	2.46	2.18	2.80	27.0	25.9	11.3	12.7	0.37	0.35
17R-7, 40	443.30	2.50	2.22	2.92	27.6	26.8	11.3	12.8	0.38	0.36
18R-1, 23	444.23	2.32	2.02	2.79	29.0	28.7	12.8	14.7	0.41	0.40
18R-2, 12	445.62	2.31	2.03	2.73	27.9	27.4	12.3	14.1	0.39	0.38
18R-4, 15	448.65	2.34	2.03	2.78	30.2	29.4	13.2	15.2	0.43	0.41
18R-2, 101	446.51	2.26	1.90	2.78	34.8	33.9	15.8	18.8	0.53	0.51
19R-1, 144	455.14	2.25	1.90	2.76	34.0	33.3	15.5	18.3	0.55	0.49
19R-3, 40	457.10	2.33	2.01	2.70	30.5	29.2	13.4	15.5	0.44	0.41
19R-5, 16	459.36	2.38	2.07	2.76	30.2	28.9	13.0	14.9	0.43	0.40
20R-1, 102	464.42	2.32	2.02	2.71	29.3	28.5	13.0	14.9	0.42	0.39
20R-2, 65	465.41	2.34	2.05	2.78	28.6	28.1	12.5	14.3	0.40	0.39
20R-3, 52	466.46	2.39	2.14	2.74	24.0	23.7	10.3	11.5	0.32	0.31
21R-1, 58	473.58	2.27	1.94	2.78	32.3	31.8	14.6	17.0	0.48	0.46
21R-2, 82	474.90	2.34	2.03	2.88	30.4	30.3	13.3	15.4	0.44	0.43
21R-CC, 9	475.40	2.34	1.99	2.66	34.1	31.5	14.9	17.6	0.52	0.46
22R-1, 105	483.75	2.30	2.01	2.66	27.8	27.1	12.4	14.2	0.39	0.37
22R-2, 94	484.84	2.35	2.05	2.76	29.8	28.8	13.0	14.9	0.42	0.40
22R-4, 7	486.47	2.43	2.14	2.78	28.7	27.3	12.1	13.7	0.40	0.37
22R-3, 35	485.75	2.43	2.13	2.84	29.1	28.1	12.3	14.0	0.41	0.39
23R-1, 61	493.01	1.95	1.69	2.73	25.3	29.3	13.3	15.4	0.34	0.41
23R-2, 109	494.99	2.25	2.02	2.74	23.4	24.3	10.6	11.9	0.31	0.32
23R-4, 102	497.92	2.31	2.06	2.77	24.5	25.0	10.9	12.2	0.32	0.33
24R-1, 128	503.28	2.33	2.04	2.83	29.0	28.9	12.7	14.6	0.41	0.40
24R-2, 27	503.72	2.30	1.99	2.65	29.8	28.6	13.3	15.4	0.43	0.40
24R-3, 121	506.16	2.42	2.11	2.75	29.8	28.1	12.6	14.5	0.43	0.39
24R-4, 34	506.79	2.45	2.17	2.88	27.0	26.5	11.3	12.7	0.37	0.36
25R-2, 100	514.20	2.35	2.06	2.79	27.7	27.4	12.1	13.7	0.38	0.37
25R-1, 46	512.16	2.37	2.13	2.76	23.3	23.3	10.1	11.2	0.30	0.30
25R-3, 26	514.96	2.35	2.05	2.73	29.5	28.4	12.9	14.8	0.42	0.39
26R-1, 4	521.44	2.60	2.49	2.73	10.8	10.7	4.3	4.5	0.12	0.12
26R-2, 84	522.79	2.44	2.22	2.76	21.0	20.8	8.8	9.7	0.27	0.26
27R-4, 80	535.90	2.40	2.09	2.76	30.1	28.6	12.9	14.8	0.43	0.40
27R-1, 30	530.90	2.35	2.05	2.70	29.8	28.5	13.0	14.9	0.43	0.39
27R-3, 80	534.40	2.39	2.09	2.77	28.7	27.7	12.3	14.0	0.40	0.38
28R-2, 34	541.27	2.30	1.97	2.81	32.1	31.6	14.3	16.7	0.47	0.46
28R-2, 53	541.46	2.34	2.06	2.86	27.6	27.9	12.1	13.7	0.38	0.38
28R-1, 48	540.68	2.37	2.08	2.69	28.7	27.2	12.4	14.1	0.40	0.37
29R-CC, 2	549.72	2.35	2.07	2.70	27.6	26.6	12.0	13.7	0.38	0.36
31R-1, 19	569.29	2.44	2.19	2.75	24.4	23.6	10.2	11.4	0.32	0.31
31R-5, 19	574.79	2.45	2.23	2.76	21.5	21.1	9.0	9.9	0.27	0.27
31R-1, 39	569.49	2.46	2.21	2.81	24.3	23.8	10.1	11.3	0.32	0.31
32R-1, 103	579.83	2.42	2.16	2.71	24.8	23.8	10.5	11.8	0.33	0.31
32R-4, 114	584.44	2.40	2.07	2.77	31.7	29.9	13.6	15.7	0.47	0.42
32R-6, 38	586.68	2.44	2.15	2.83	27.9	27.1	11.8	13.3	0.39	0.37
32R-2, 133	581.63	2.43	2.15	2.68	27.5	25.7	11.6	13.1	0.38	0.34
32R-CC, 1	587.89	2.70	2.38	2.67	31.2	26.0	11.8	13.4	0.45	0.35
33R-2, 143	590.98	2.41	2.13	2.82	27.3	26.7	11.6	13.1	0.38	0.36
33R-1, 75	589.15	2.47	2.20	2.79	25.9	24.9	10.8	12.0	0.35	0.33
33R-3, 25	591.30	2.44	2.20	2.80	23.7	23.3	9.9	11.0	0.31	0.30
33R-4, 16	592.21	2.48	2.22	2.64	25.6	23.5	10.6	11.8	0.34	0.31
34R-1, 17	598.27	2.39	2.11	2.73	26.9	26.0	11.5	13.0	0.37	0.35
34R-6, 82	606.33	2.48	2.22	2.76	25.7	24.3	10.6	11.9	0.35	0.32
34R-2, 64	600.24	2.43	2.19	2.74	23.8	23.1	10.0	11.2	0.31	0.30
34R-4, 62	603.22	2.42	2.20	2.72	22.0	21.5	9.3	10.3	0.28	0.27

Table 19 (continued).

Core, section, interval (cm)	Depth (mbsf)	Wet-bulk density (g/cm^3)	Dry-bulk density (g/cm^3)	Grain density (g/cm^3)	Wet-sediment porosity (%)	Dry-sediment porosity (%)	Wet-sediment water content (%)	Dry-sediment water content (%)	Wet-sediment void ratio	Dry-sediment void ratio
141-863B-(Cont)										
35R-3, 40	611.10	2.41	2.16	2.77	24.4	23.9	10.3	11.5	0.32	0.31
35R-1, 136	609.06	2.52	2.28	2.75	24.1	22.7	9.8	10.8	0.32	0.29
35R-5, 21	613.91	2.49	2.25	2.79	23.9	23.1	9.9	10.9	0.31	0.30
35R-CC, 32	616.08	2.48	2.21	2.76	26.1	24.8	10.8	12.1	0.35	0.33
36R-3, 53	620.41	2.46	2.26	2.82	19.4	19.7	8.1	8.8	0.24	0.24
36R-1, 53	617.93	2.38	2.09	2.73	27.9	26.8	12.0	13.6	0.39	0.36
36R-4, 87	622.25	2.50	2.27	2.73	22.4	21.3	9.2	10.1	0.29	0.27
36R-2, 27	619.17	2.59	2.37	2.74	21.8	20.3	8.6	9.4	0.28	0.25
37R-1, 119	628.19	2.46	2.23	2.75	22.4	21.7	9.3	10.3	0.29	0.28
37R-2, 89	629.39	2.50	2.26	2.85	23.2	22.8	9.5	10.5	0.30	0.29
37R-4, 81	632.31	2.39	2.14	2.72	24.6	24.0	10.5	11.8	0.33	0.31
37R-5, 140	634.40	2.52	2.28	2.67	23.2	21.5	9.4	10.4	0.30	0.27
38R-1, 47	637.07	2.40	2.16	2.75	24.0	23.6	10.3	11.4	0.32	0.31
38R-2, 64	638.74	2.46	2.23	2.74	22.3	21.7	9.3	10.3	0.29	0.27
38R-2, 105	639.15	2.43	2.21	2.75	22.0	21.6	9.0	10.2	0.28	0.27
39R-2, 73	648.43	2.34	2.05	2.71	28.5	27.6	12.5	14.3	0.40	0.38
39R-3, 84	649.97	2.50	2.28	2.70	21.3	20.3	8.8	9.6	0.27	0.25
40R-1, 30	656.20	2.39	2.14	2.71	24.3	23.7	10.4	11.6	0.32	0.31
40R-3, 38	658.98	2.42	2.15	2.74	26.1	25.1	11.1	12.4	0.35	0.33
41R-1, 44	665.94	2.54	2.34	2.71	19.4	18.5	7.8	8.5	0.24	0.23
41R-2, 22	667.22	2.42	2.18	2.69	23.5	22.7	10.0	11.1	0.31	0.29
41R-4, 25	670.25	2.51	2.28	2.83	22.6	22.0	9.2	10.1	0.29	0.28
42R-2, 31	677.01	2.46	2.24	2.73	21.4	20.8	8.9	9.8	0.27	0.26
42R-1, 110	676.30	2.55	2.35	2.73	19.6	18.7	7.9	8.5	0.24	0.23
42R-3, 39	678.37	2.52	2.32	2.72	19.6	18.8	8.0	8.7	0.24	0.23
43R-1, 68	685.48	2.56	2.35	2.83	20.0	19.5	8.0	8.7	0.25	0.24
43R-2, 58	686.88	2.45	2.21	2.84	24.3	23.9	10.1	11.3	0.32	0.31
43R-3, 2	687.32	2.46	2.18	2.74	26.7	25.2	11.1	12.5	0.36	0.33
44R-1, 36	694.86	2.42	2.15	2.76	26.2	25.3	11.1	12.5	0.36	0.34
44R-2, 94	696.94	2.44	2.19	2.75	24.6	23.7	10.3	11.5	0.33	0.31
44R-3, 117	698.67	2.46	2.20	2.76	26.0	24.7	10.8	12.1	0.35	0.33
44R-3, 19	697.69	2.55	2.32	2.82	22.6	21.6	9.1	10.0	0.29	0.27
44R-4, 56	699.51	2.30	2.05	2.47	24.0	22.6	10.7	12.0	0.32	0.29
45R-1, 72	704.92	2.44	2.15	2.75	28.1	26.6	11.8	13.4	0.39	0.36
45R-2, 30	705.50	2.43	2.16	2.78	26.5	25.5	11.2	12.6	0.36	0.34
46R-1, 121	708.01	2.44	2.15	2.80	28.2	27.0	11.8	13.4	0.39	0.37
46R-2, 58	708.88	2.50	2.26	2.73	23.0	21.9	9.4	10.4	0.30	0.28
46R-2, 70	709.00	2.49	2.25	2.72	22.7	21.7	9.4	10.3	0.29	0.27
47R-1, 114	714.94	2.39	2.14	2.70	25.2	24.3	10.8	12.1	0.34	0.32
47R-2, 10	715.40	2.45	2.22	2.75	22.6	22.0	9.4	10.4	0.29	0.28
47R-2, 70	716.00	2.51	2.24	2.84	26.0	25.0	10.6	11.9	0.35	0.33
47R-3, 70	717.50	2.44	2.16	2.79	26.5	25.6	11.1	12.5	0.36	0.34
48R-2, 25	724.21	2.49	2.24	2.72	24.4	23.0	10.1	11.2	0.32	0.30
48R-2, 55	724.51	2.43	2.18	2.76	24.7	23.9	10.4	11.6	0.33	0.31
49R-1, 50	733.70	2.40	2.13	2.69	25.5	24.5	10.9	12.3	0.34	0.32
49R-1, 140	734.60	2.45	2.25	2.71	20.1	19.6	8.4	9.1	0.25	0.24
49R-4, 13	737.83	2.47	2.24	2.71	21.8	21.0	9.1	10.0	0.28	0.26

temperature gradient is higher at this site than at Site 859. In addition, given the observations of other thermal anomalies deeper in the hole (see below, and the Wireline Measurements section, this chapter), an assumption of a linear conductive gradient at this site may well be in error.

At the base of the temperature profile (Fig. 78) there is again a sharp increase in temperature gradient between 200 and 230 mbsf. This is a zone of particularly poor core recovery and substantial hole deviation. It also corresponds to a relatively substantial discontinuity in the physical properties (see Physical Properties section, this chapter), and we suggest that it may well correspond to a major structure.

In summary, the temperature profile at Site 863 indicates rapid lateral advection of warm fluids out though localized conduits in the toe of the wedge along structural and physical property discontinuities at three levels at least. In particular, the advecting warm fluids are spatially associated with a distinct region between 0 and 60 mbsf, which is both structurally very complex and rich in black sulfides. In this region, structural observations of probable sulfide infillings along dilation-fault-jogs indicate that fluid pathways may be predominantly fracture controlled and associated with substantial faults.

WIRELINE MEASUREMENTS

Introduction

Wireline measurements were conducted at this site to measure the in-situ properties of sediments within the toe of the accretionary wedge where they have been thrust directly above the Chile Ridge seafloor-spreading center. These rocks were expected to have undergone considerable alteration due to active hydrothermal circulation processes of the ridge, and possible recent ridge-volcanism. Of particular interest were the hydrothermally-induced lithification and mineralization of these rocks and the structural fabrics that developed during subduction of the rift axis. We also anticipated exceptionally high borehole temperatures, due to the expected high temperatures of the zero-age oceanic crust directly beneath the site. Downhole measurements at this site complement observations from the cores to correlate chemical, structural, physical, and thermal properties of these rocks with tectonic and hydrothermal diagenetic processes.

A stuck drill pipe prevented most logging in the upper 232 m of the hole (see Operations section, this chapter); however, good logs were acquired within the open borehole between 232 and 733

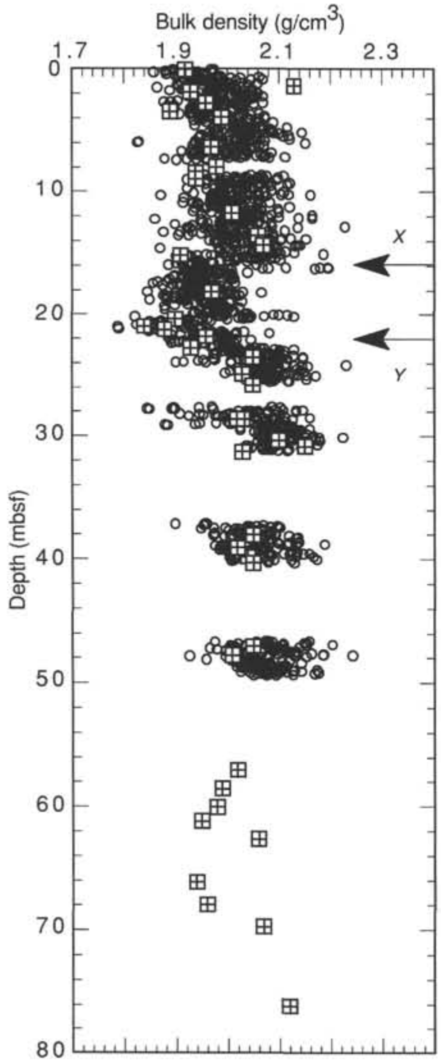

Figure 66. Discrete-sample (boxes) and GRAPE (dots) measurements of wet-sediment bulk density vs. depth in APC cores of physical properties Unit A, recovered in the upper part of Hole 863A.

mbsf. Four tool strings were run to acquire a full set of geophysical, geochemical, and formation microscanner sonde (FMS) logs. The Lamont temperature tool (TLT) was run on two tool strings, with a series of six discrete temperature stations added to the second run to more accurately constrain the temperature of the borehole.

Log Quality

The log data from Hole 863B cover the interval from the base of the drill string (232.0 mbsf) to near the base of the hole (732.7 mbsf). They are all of generally high quality. The borehole through most of the logged interval is nearly circular with the diameter varying between 10 and 11 in. (25–28 cm). This is within the normal range of the calipers on the tools that must, to acquire good data, be pressed to the borehole wall. Occasional washouts produced short intervals of large hole diameter and poor density/porosity data. There is an unusually high incidence of either cycle skipping or noise interference in the sonic velocity log data. The velocity log was acquired as the geophysical string was being lowered to the bottom of the hole. Normally the data collected on the upward logging run are preferred, but the sonic tool failed at

Table 20. Acoustic velocity data derived from digital sediment sound (DSV) and Hamilton Frame velocimeters.

Core, section, interval (cm)	Depth (mbsf)	Velocity (m/s)
141-863A-		
1H-2, 92	2.42	1609.5
1H-5, 97	6.97	1611.3
2H-4, 75	13.85	1645.1
3H-4, 84	23.44	1714.9
3H-1, 84	18.94	1609.5
4H-1, 84	28.44	1637.5
4H-3, 55	31.15	1714.9
5H-2, 128	39.88	1643.2
6H-1, 115	47.75	1660.5
7X-2, 112	58.72	1628.0
7X-CC, 16	63.76	1639.4
27X-1, 70	249.90	1718.0
28X-1, 14	258.94	1809.0
29X-1, 40	268.80	1793.0
29X-1, 49	268.89	1908.0
30X-1, 98	279.08	2117.0
30X-2, 71	280.31	1962.0
31X-CC, 28	288.51	1863.0
141-863B-		
6X-CC, 5	345.25	2022.0
7N-1, 20	355.10	2768.0
7N-2, 10	356.50	3116.0
8N-1, 52	357.92	3017.0
9X-CC, 4	361.44	2829.0
10R-1, 20	371.20	2795.0
10R-1, 59	371.59	4518.0
10R-1, 60	371.60	4571.0
11R-1, 40	377.00	2611.0
12R-1, 20	386.50	2828.0
13R-1, 41	396.21	2375.0
13R-CC, 2	396.53	2782.0
14R-1, 63	406.13	2542.0
14R-3, 32	408.32	2767.0
14R-3, 34	408.34	3006.0
15R-3, 44	415.64	2818.0
16R-3, 15	424.85	2716.0
16R-3, 64	426.84	2727.0
17R-2, 50	436.40	3070.0
17R-3, 60	438.00	3425.0
18R-2, 2	445.52	2949.0
18R-3, 74	447.74	2956.0
19R-1, 76	454.46	2771.0
20R-1, 98	464.38	2986.0
20R-3, 56	466.50	3416.0
21R-1, 74	473.74	4411.0
21R-1, 86	473.86	2710.0
21R-2, 78	474.86	4433.0
22R-1, 105	483.75	2803.0
22R-4, 8	486.48	2844.0
23R-1, 110	493.50	2802.0
23R-3, 36	495.76	2666.0
24R-1, 114	503.14	2461.0
24R-3, 12	505.07	2527.0
25R-3, 48	515.18	2466.0
26R-2, 85	522.80	3669.0
27R-3, 80	534.40	2539.0
28R-1, 47	540.67	2847.0
31R-3, 128	573.38	2862.0
32R-1, 8	578.88	2776.0
32R-1, 133	580.13	2415.0
32R-4, 114	584.44	2672.0
33R-CC, 6	592.86	2700.0
34R-1, 16	598.26	2606.0
34R-6, 11	605.62	2829.0
34R-6, 13	605.64	2474.0
35R-3, 38	611.08	2831.0
36R-2, 56	619.46	3209.0
36R-3, 53	620.41	3102.0
37R-3, 129	631.29	2836.0
38R-1, 116	637.76	2816.0
39R-2, 20	647.90	2487.0
41R-1, 43	665.93	2985.0
42R-3, 45	678.43	2847.0
43R-2, 76	687.06	2860.0
44R-1, 40	694.90	3027.0
44R-3, 48	697.98	3015.0
45R-1, 50	704.70	3139.0
47R-1, 80	714.60	2878.0
48R-3, 43	725.17	3220.0
49R-4, 14	737.84	3207.0

Note: All Hole 863A data points are DSV measurements: those for Hole 863B are Hamilton Frame determinations.

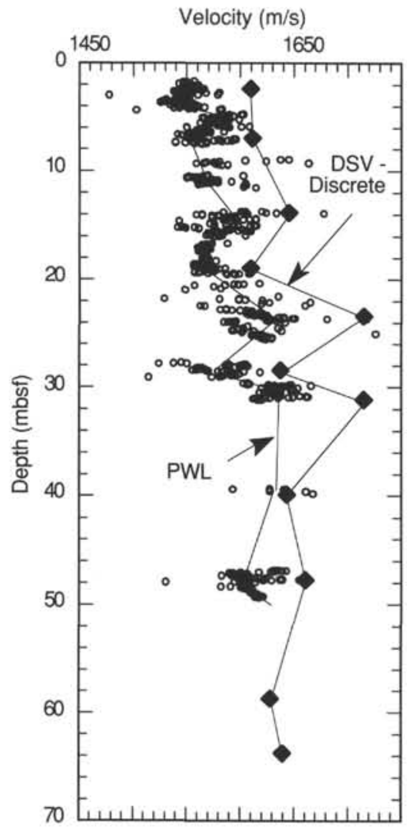

Figure 67. Acoustic velocity measurements in the upper part of physical properties Unit A using core-scanning PWL and at discrete depth intervals using the DSV.

the bottom of the hole. The noise problems are predominantly localized to specific depths and we anticipate that many of the problems with noise can be overcome by close examination of the sonic waveforms after the cruise.

Each log was shifted in depth, by correlating the gamma-ray logs between runs, to correct for differences in the stretch of the logging cable. All logs were then corrected to the base of the drill pipe by subtracting the distance from rig floor to seafloor roughly (2577 m). These depths should be accurate to within ± 2 m.

Sub-bottom depths during both runs of the TLT were determined using the pressure recorded in the instrument and a depth vs. pressure table derived from pressure readings at depths noted during logging. An additional constraint on the sub-bottom depths of the temperature data will come from the Schlumberger depth vs. time record. The six temperature stations recorded during the second run were occupied for 10 min each at preselected sub-bottom depths.

All temperature values above 232 mbsf were recorded while the tool was inside the drill pipe and may not accurately reflect the temperature of the borehole because of the isolation of the TLT in the drill pipe and the thermal influence of the pipe. The depth calibration of the data measured in the drill pipe was difficult because of the uncertainty of the effect on the apparent pressure when the tool is moving inside. Individual pressure readings are not believed to be an accurate indicator of depth.

Logging Results

Five log units were identified (Fig. 80) using the geophysical and geochemical logs. The units are defined primarily on the basis of the resistivity, density, and gamma-ray logs. The velocity log, even though noisy, was used to determine average velocities and

Table 21. Thermal conductivity measurements for combined Holes 863A and 863B.

Core, section, interval (cm)	Depth (mbsf)	Thermal conductivity (W/m·K)	Method
141-863A-			
1H-2, 71	2.21	1.31	
1H-4, 71	5.21	1.24	
1H-6, 71	8.21	1.53	
2H-2, 100	11.10	1.46	
2H-5, 100	15.60	1.32	
2H-7, 50	18.10	1.32	
2H-2, 50	10.60	1.29	
2H-5, 50	15.10	1.25	
2H-7, 68	18.28	1.23	
2H-CC, 26	18.61	1.31	
3H-3, 100	22.10	1.29	
3H-5, 100	25.10	1.56	
3H-CC, 52	26.52	1.32	
4H-1, 100	28.60	1.46	
4H-3, 50	31.10	1.28	
4H-CC, 25	31.52	1.27	
5H-1, 100	38.10	1.63	
5H-2, 100	39.60	1.56	
6H-1, 100	47.60	1.43	
6H-2, 100	49.10	1.33	
7X-4, 100	61.60	1.20	
8X-1, 99	66.49	1.18	
8X-4, 55	70.55	1.36	
9X-1, 40	75.80	1.35	
9X-CC, 21	76.36	1.48	
10X-CC, 21	85.31	1.64	
14X-CC, 15	125.45	1.39	
14X-CC, 25	125.55	1.54	
16X-CC, 6	143.06	1.38	
17X-1, 17	152.87	1.52	
17X-CC, 18	153.23	1.55	
25X-1, 25	230.05	1.46	
25X-CC, 13	231.07	1.45	
26X-1, 26	239.76	1.23	
26X-CC, 10	240.66	1.59	
27X-1, 70	249.90	1.41	
27X-CC, 34	250.46	1.32	
28X-1, 15	258.95	1.59	
28X-CC, 18	260.24	1.62	
29X-1, 36	268.76	1.50	
29X-CC, 13	269.99	1.57	
30X-1, 100	279.10	1.35	
30X-CC, 10	280.59	1.25	
31X-2-CC, 41	288.64	1.66	HS
141-863B-			
4X-2, 78	328.18	1.51	
4X-5-58	332.48	1.55	
6X-CC, 10	345.30	1.46	
8N-1, 26	356.00	1.67	HS
10R-1, 56	371.56	2.24	HS
12R-1, 61	386.91	1.55	HS
13R-1, 4	395.84	1.59	HS
14R-1, 10	405.60	1.85	HS
15R-2, 55	417.25	2.15	HS
16R-1, 129	425.99	2.16	HS
17R-4, 100	439.90	2.14	HS
18R-2, 100	446.50	1.38	HS
19R-5, 1	459.21	2.02	HS
20R-2, 1	464.77	1.89	HS
22R-3, 68	486.08	2.30	HS
24R-4, 94	507.39	2.19	HS
25R-3, 40	515.10	2.03	HS
26R-2, 88	522.83	2.89	HS
27R-3, 66	534.26	2.08	HS
28R-1, 49	540.69	2.00	HS
31R-1, 118	570.28	2.35	HS
32R-4, 100	584.30	2.18	HS
33R-2, 116	590.71	2.30	HS
34R-6, 73	606.24	2.38	HS
35R-1, 120	608.90	2.60	HS
36R-2, 60	619.50	2.39	HS
37R-3, 132	631.32	2.13	HS
38R-2, 120	639.30	2.10	HS
39R-2, 63	648.33	2.38	HS
41R-1, 34	665.84	2.19	HS
49R-4, 116	738.86	2.49	HS
44R-3, 5	697.55	2.45	HS
46R-1, 65	707.45	2.27	HS
47R-3, 2	716.82	1.98	HS

Note: HS indicates measurement by the half-space method; all other measurements are full space.

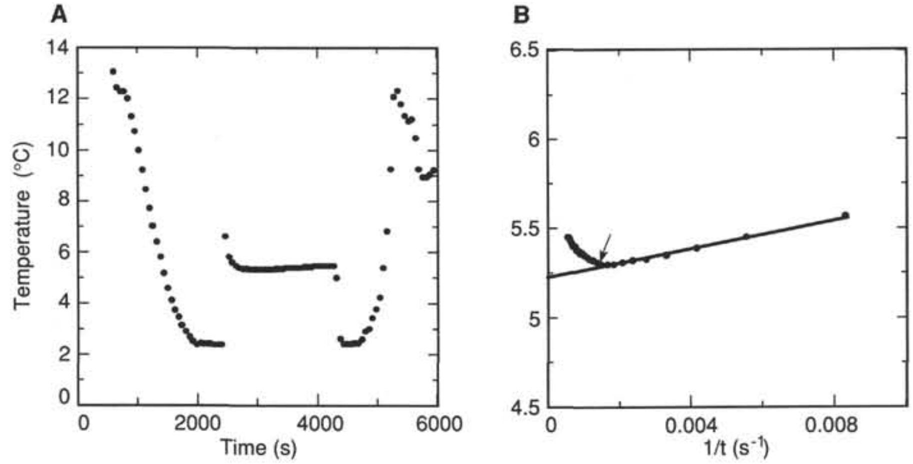

Figure 68. Temperature vs. time (**A**) and 1/t fit to data (**B**) at 27.6 mbsf, Hole 863A. Arrow marks departure (data "hook") from main trend at small 1/t time intervals.

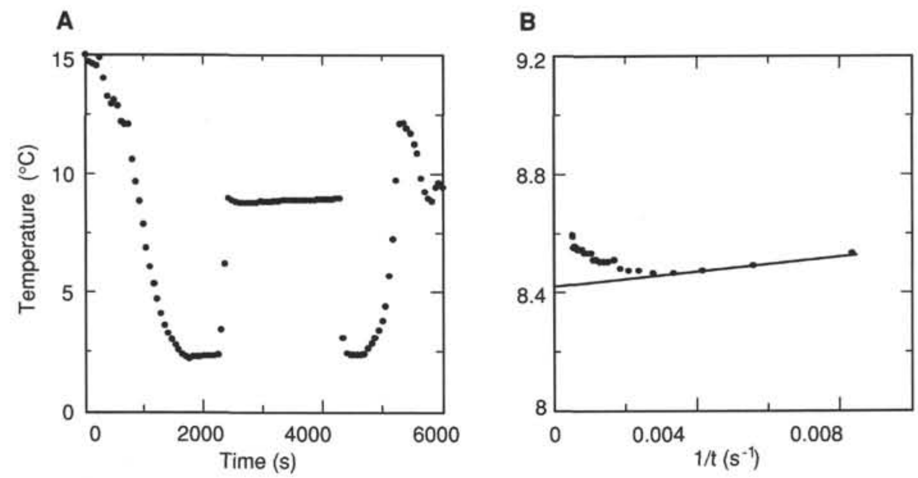

Figure 69. Temperature vs. time (**A**) and 1/t fit to data (**B**) at 56.1 mbsf, Hole 863A. Arrow marks departure (data "hook") from main trend at small 1/t time intervals.

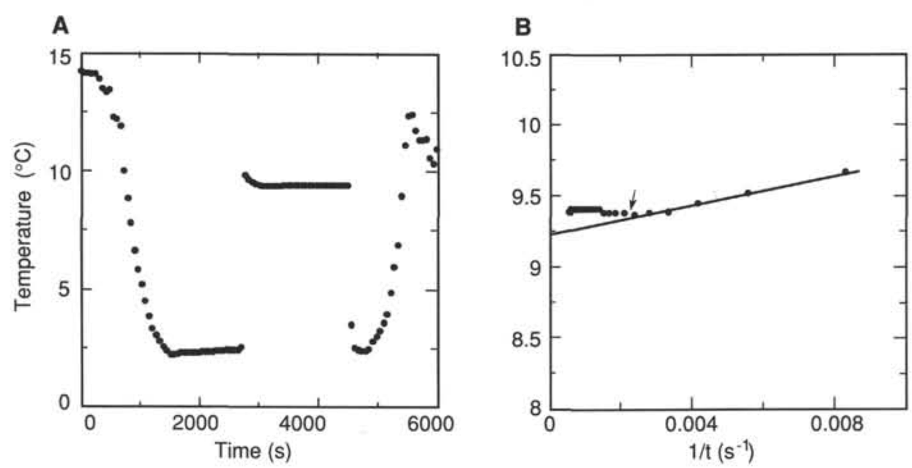

Figure 70. Temperature vs. time (**A**) and 1/t fit to data (**B**) at 85.1 mbsf, Hole 863A . Arrow marks departure (data "hook") from main trend at small 1/t time intervals (WSTP temperature probe only).

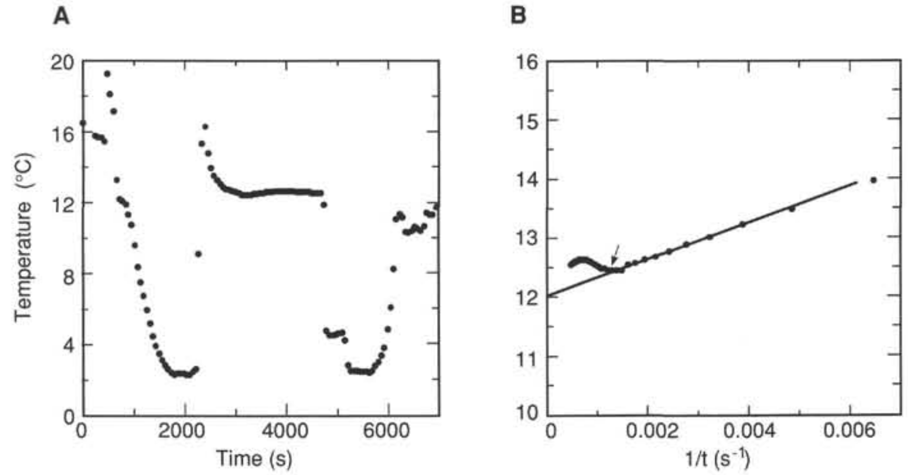

Figure 71. Temperature vs. time (**A**) and 1/t fit to data (**B**) at 143 mbsf, Hole 863A. Arrow marks departure (data "hook") from main trend at small 1/t time intervals.

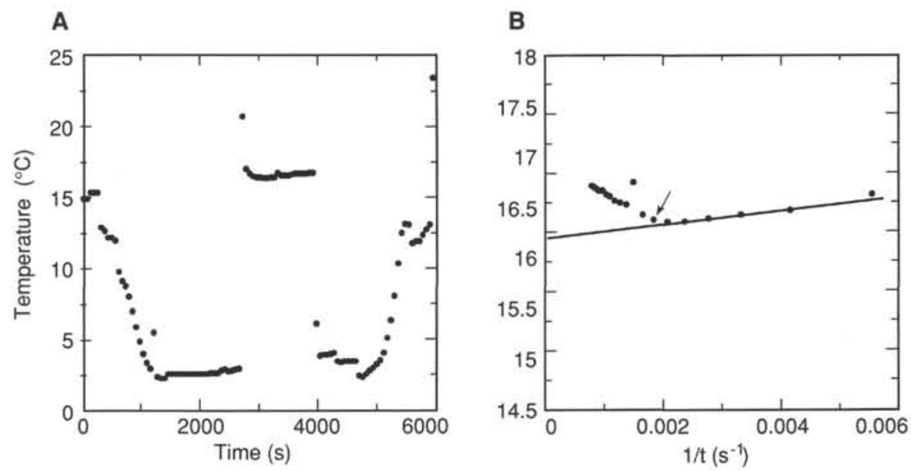

Figure 72. Temperature vs. time (**A**) and 1/t fit to data (**B**) at 200.9 mbsf, Hole 863A. Arrow marks departure (data "hook") from main trend at small 1/t time intervals.

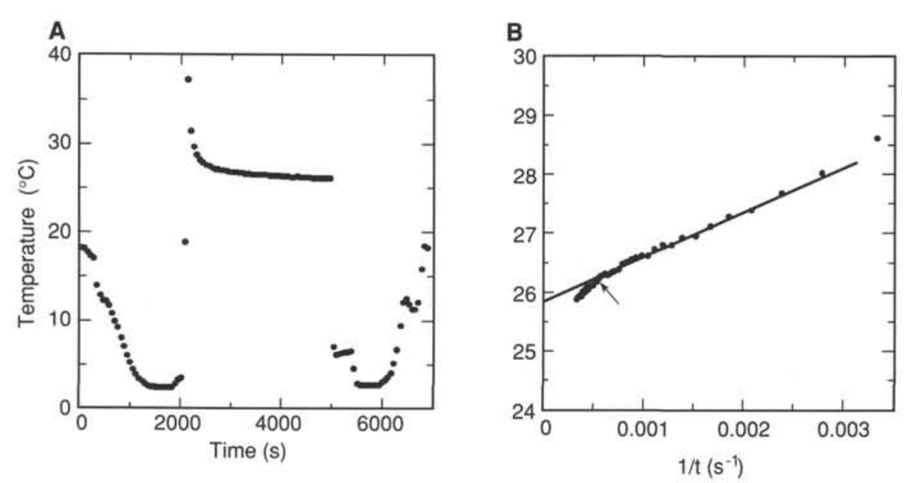

Figure 73. Temperature vs. time (**A**) and 1/t fit to data (**B**) at 229.8 mbsf, Hole 863A. Arrow marks departure (data "hook") from main trend at small 1/t time intervals.

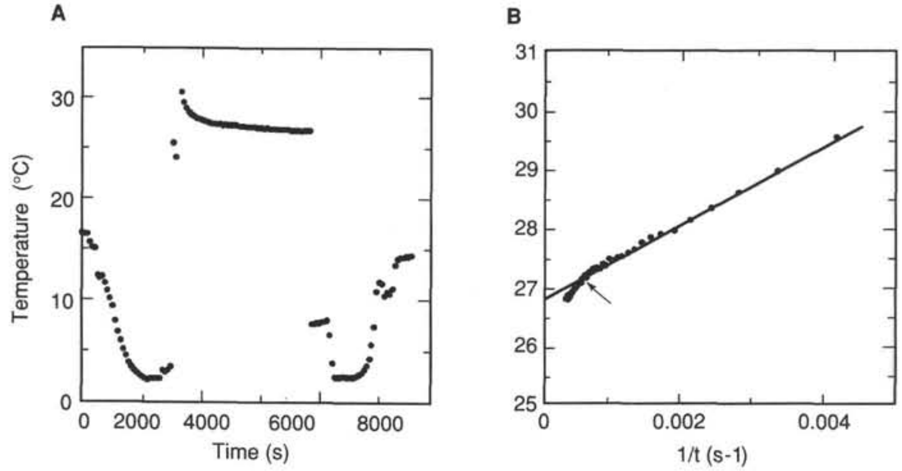

Figure 74. Temperature vs. time (**A**) and 1/t fit to data (**B**) at 239.5 mbsf, Hole 863A. Arrow marks departure (data "hook") from main trend at small 1/t time intervals.

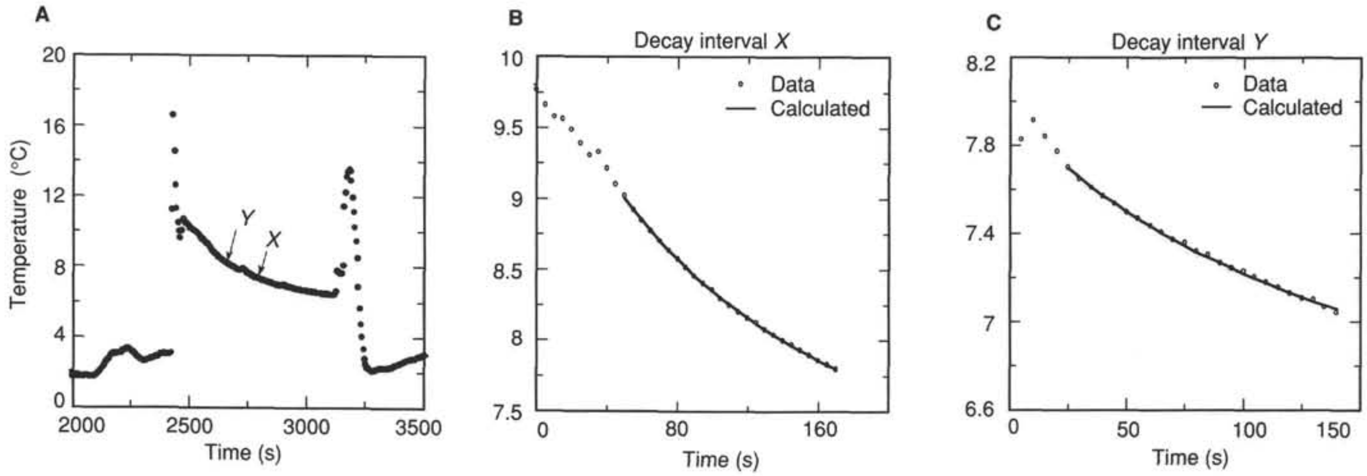

Figure 75. ADARA deployment at 27.6 mbsf, Hole 863A, has a nonlinear temperature decay profile (**A**). The two portions of the decay curve (*X* and *Y*) are shown fitted (**B,C**). Both portions of the curve were fitted using thermal conductivities of 1.2 and 1.3 W/m·K. The 1.3 W/m·K fit is illustrated.

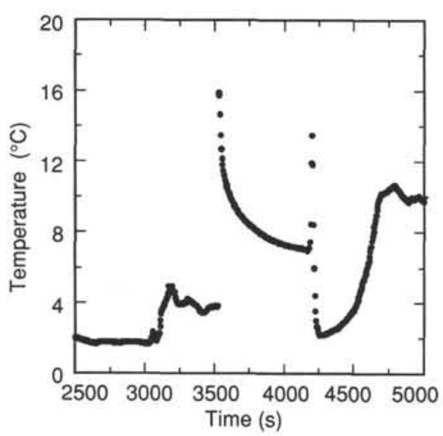

Figure 76. ADARA deployment at 37.1 mbsf, Hole 863A, has a good temperature decay profile. The decay curve was fitted using thermal conductivities of 1.1 and 1.2 W/m·K.

trends, and the silicon, iron, and calcium logs (Fig. 81) were used to define the lowermost unit. Distinctive changes on more than one log at similar sub-bottom depth determined the boundaries between the logging units.

Log Unit 1— Base of Pipe (232.0 mbsf) to 400.6 mbsf

This unit is characterized by average resistivities of 1.5 oh-m·m. Seismic velocity, which appears to increase linearly with depth, varies between 2.1 km/s at 335 mbsf, and 2.7 km/s at 398 mbsf near the base of the unit. The density log is affected by irregular hole size at the top of the log unit, but between 300 mbsf and the bottom of the unit averages about 2.1 g/cm.

Log Unit 2—400.6 to 420.0 mbsf

Unit 2 is characterized by a resistivity increase from 1.5 ohm·m at the bottom of Unit 1 to an average of about 2.5 ohm·m in the upper part of Unit 2. There is a pronounced drop in density from 2.1 to 1.75 g/cm^3 at 401 mbsf, accompanied by a slight decrease in the gamma-ray log from 50 to 44 API units. Smear-slide analysis of sediments at this depth indicates a decrease in both clay and volcanic glass. The top of the log unit is approximately

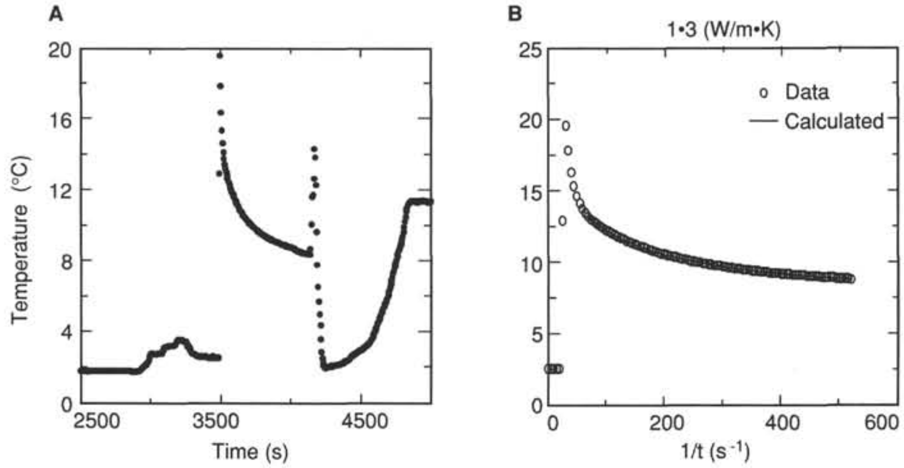

Figure 77. ADARA deployment at 46.6 mbsf, Hole 863A. **A.** A well-behaved temperature decay profile. Decay curve was fitted using thermal conductivities of 1.1 and 1.2 W/m·K. **B.** The 1.3 W/m·K fit.

Table 22. WSTP and ADARA temperature data for Site 863.

Depth (mbsf)	WSTP temperature (°C)	ADARA temperature (°C)	± Error	"Hook" temperature (°C)
0.0		1.70		
27.60	5.26		0.04	5.70
27.60		5.46	0.09	
37.10		4.36	0.07	
46.60		5.66	0.06	
56.10	8.91		0.20	9.10
85.10	9.33		0.09	9.40
143.00	12.00		0.05	13.10
200.90	16.60		0.40	16.95
229.80	25.85		0.08	24.90
239.50	26.77		0.10	26.00

equivalent to the top of lithostratigraphic Subunit IIC, which lies at 405.5 mbsf.

Log Unit 3—420.0 to 560.0 mbsf

The top of this log unit is marked by an abrupt increase in all three (shallow, medium, and deep) resistivity logs from 2.5 to 3.5 ohm·m, a decrease in the gamma-ray log from 52 to 39 API units, and an increase in density from 2.2 to 2.3 g/cm^3. The velocities within this interval vary from 2.9 km/s at the top of the unit to 2.7 km/s near the bottom at 558 mbsf.

Log Unit 4—560.0 to 702.5 mbsf

The top of Log Unit 4 is characterized by a step-increase in the medium and deep resistivity logs from 3.0 to 3.5 ohm·m, and from 3.5 to over 5.0 ohm·m in the shallow resistivity. The density log also exhibits a baseline shift from 2.1 g/cm^3 at the top to approximately 2.4 g/cm^3 within the log unit, and is accompanied by a decrease in porosity from 25% to 20%. This is consistent with the cementation increase and porosity decrease with depth noted in the cores (see Lithostratigraphy and Physical Properties sections, this chapter). The velocity log is degraded significantly by numerous cycle-skipping events in the upper and lower part of the unit, but generally increases with depth.

Log Unit 5—702.5 to 732.7 mbsf

This unit is identified primarily on the basis of the geochemical and spectral gamma-ray logs. The top of the unit is marked by a slight increase in the gamma-ray log from 45 to 50 API units, an increase in potassium, and in the calcium, iron, and sulfur yields. The silicon yield is depressed near the top of this unit, but then gradually increases at the bottom of the logged interval (715.0–732.7 mbsf). Most of the geophysical logs (i.e. velocity, density, sonic) do not appear to be affected by the lithologic changes observed in the geochemical logs.

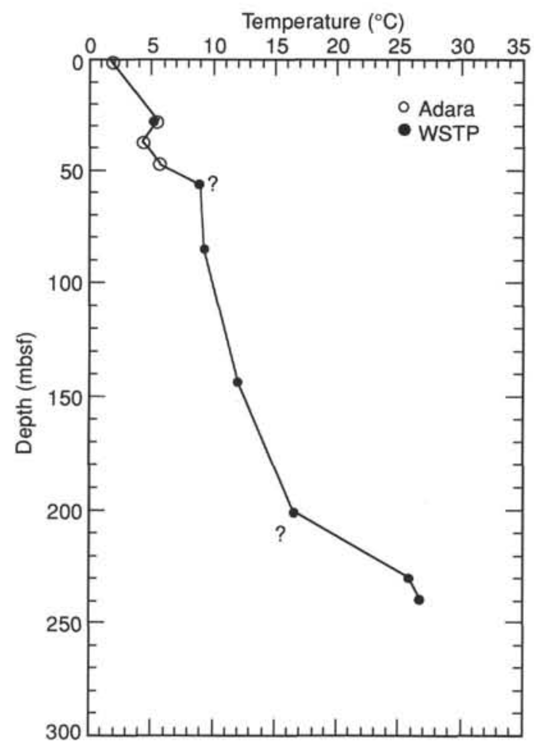

Figure 78. Temperature vs. sub-bottom depth at Site 863. The WSTP (solid circles) and ADARA (open circles) temperatures are both shown. Errors limits for temperature are too small to clearly represent on this scale.

Temperature Logs

Borehole temperatures were acquired down to the bottom of the hole (742 mbsf) on two downhole runs of the TLT. The bottom of the drill pipe was stuck at 232 mbsf so the portion of the

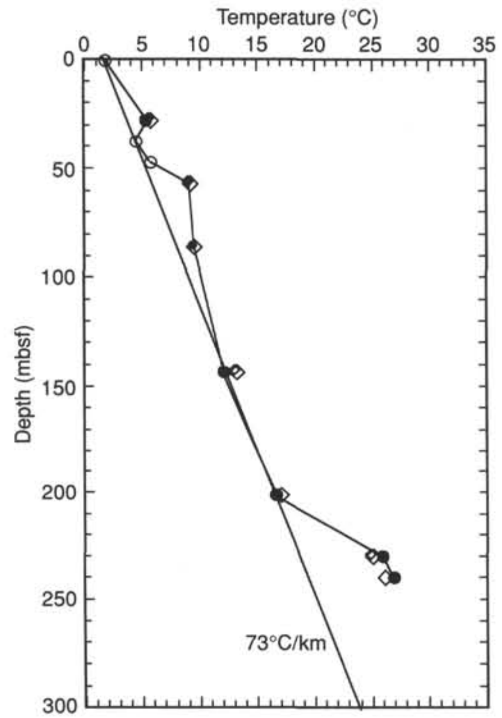

Figure 79. Temperature vs. depth at Site 863. The WSTP (solid circles) and ADARA (open circles) temperatures are both shown together with the estimated temperatures from linear extrapolations of the late data "hooks" (diamonds). A linear extrapolation through the data away from the obvious thermal anomalies is shown. It suggests that there may have been a pre-existing conductive profile corresponding to a temperature gradient of 73°C/km.

temperature data between seafloor and 232 mbsf was acquired with the tool inside the drill pipe. The TLT was run on the first tool string, which was run in the hole only 3 hours after drilling-fluid circulation had stopped. During the trip down, a blockage was encountered that prevented the tool string from moving down the pipe. In an attempt to dislodge the blockage, drilling fluid was pumped through the pipe for approximately 20 min. The temperatures were certainly disturbed between the seafloor and the base of the drill pipe. The disturbance was probably not significant in the deeper part of the hole. The second run of the temperature tool was 28 hr after the first run (31 hr after circulation stopped). During this run the tool string was stopped at selected depths to acquire temperature readings at a set of six discrete stations. At the stations the temperature of the TLT was allowed to equilibrate with the borehole for 10 min. These data have been used to fit an exponential equilibration curve to predict an equilibrium borehole temperature at each station (Fig. 82).

Despite the added complication of logging in the drill pipe, the borehole temperature profile within the upper 232 mbsf shows similar characteristics with that of the formation temperature profile (Fig. 83). The uppermost approximately 70 m of the hole shows a relatively steep gradient of about 100°C/km. Although this is slightly less than that observed from the formation temperatures, the depth to which this steep gradient persists is within reasonable agreement. Below 70 mbsf the gradient decreases to less than half that of the upper 70 m. This uppermost 70 m roughly corresponds to a zone of high concentrations of black sulfide minerals that are observed in the upper 46 m of Hole 863A (see Lithostratigraphy section, this chapter). The high thermal gradient probably reflects the infiltration of hydrothermal fluids along a complexly faulted domain inferred from sedimentary structures (see Structural Geology section, Fig. 37, this chapter) and physical properties (see Physical Properties section, this chapter). The localized variations in the thermal gradient determined from for-

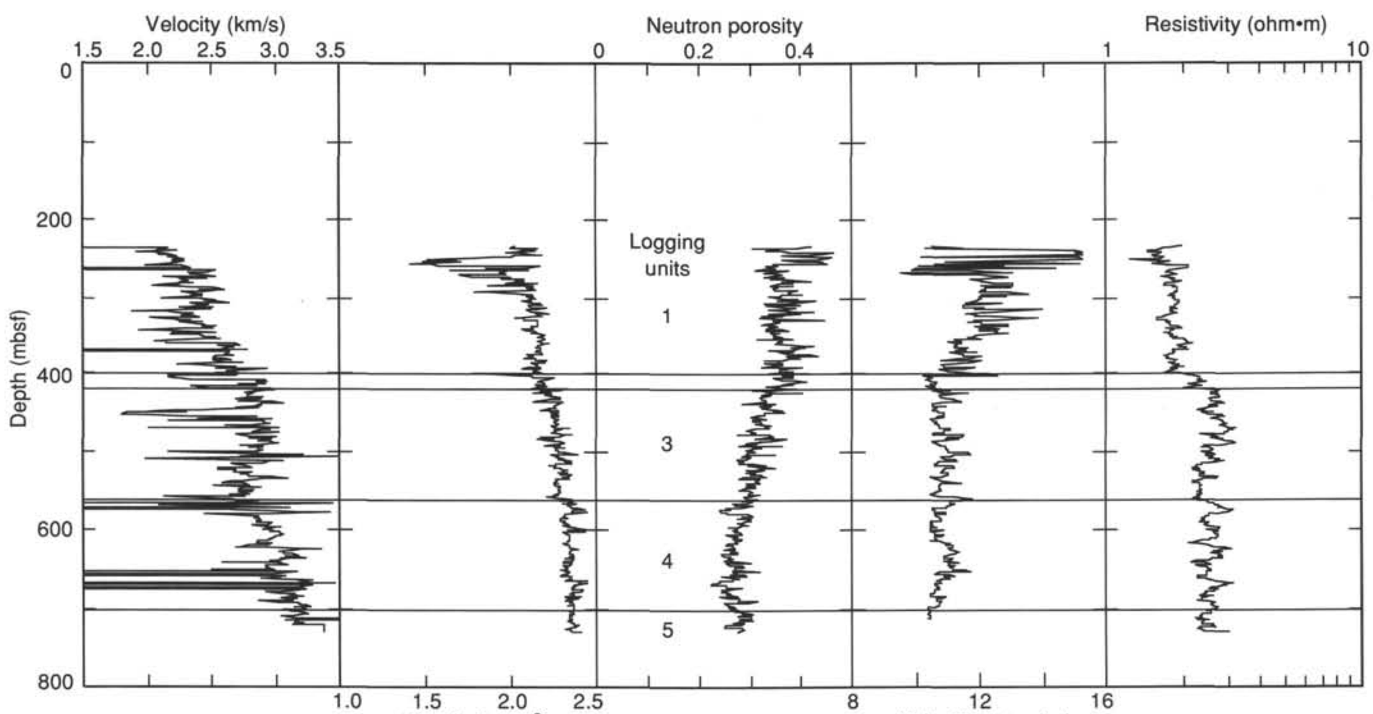

Figure 80. Synthesis of key physical properties logs showing division into logging units. The resistivity log is the shallow-focused resistivity. Porosity is neutron porosity. Velocity is based on the transit time for the near-receiver set. Note that there is significant cycle skipping in the data, as indicated by wild velocity swings. Hole diameter is from the MCD. Unit 2 lies between 400.6 and 420.0 mbsf.

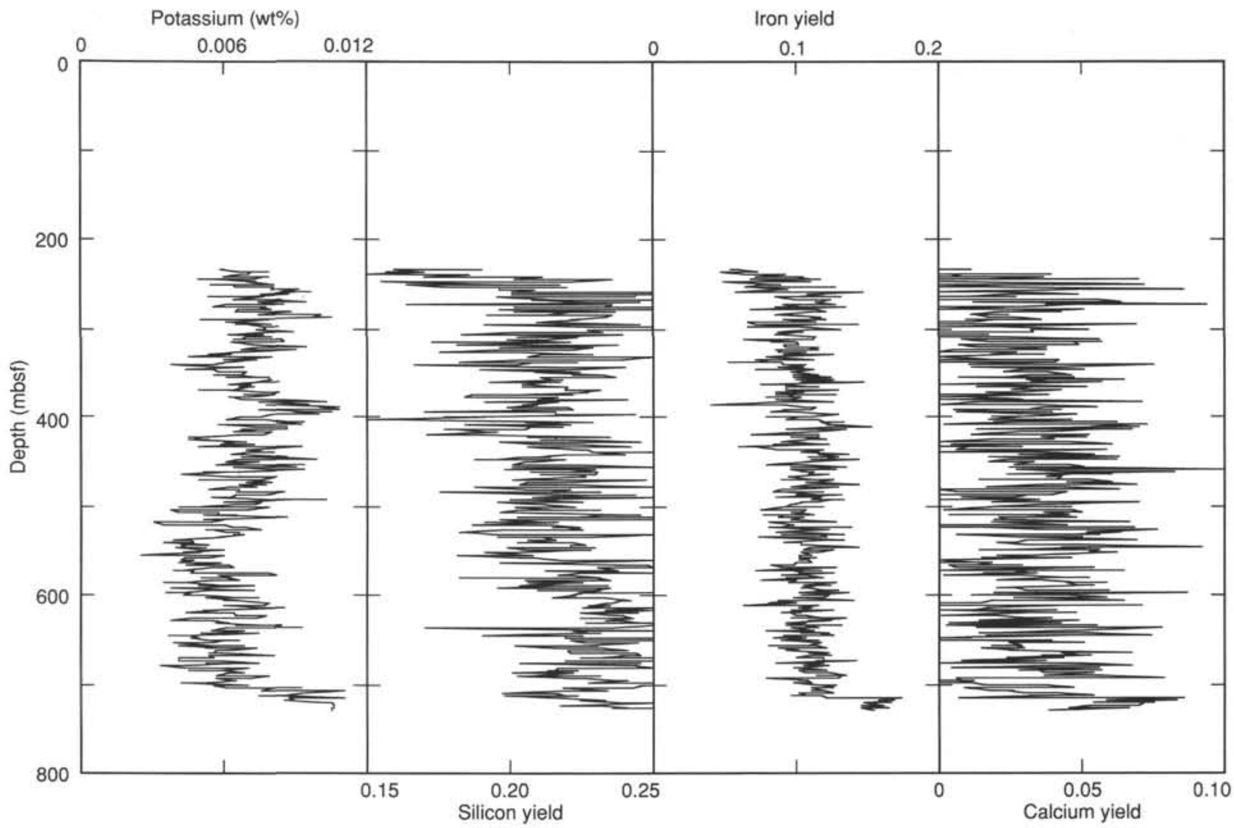

Figure 81. Potassium (wt%), and silicon, iron, and calcium yield logs from Hole 863B.

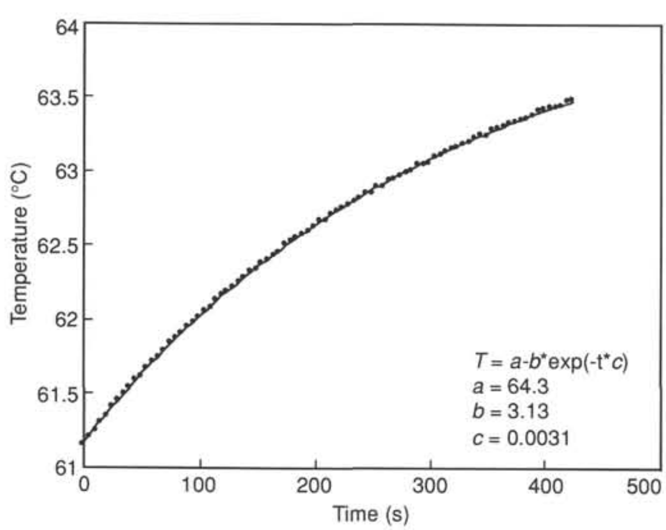

Figure 82. Equilibrium decay curve for a temperature station at the bottom of the borehole (742 mbsf). An exponential temperature curve (T) is fitted to the data to predict an equilibrium temperature of 64.3°C at a time (t) of infinity.

mation temperatures observed at 38–50 mbsf do not appear in the TLT data, as they may be too localized for the tool to detect as it moves through the borehole.

Temperature log data show an increase in thermal gradient below about 220 mbsf. Inflections in the log temperature profile occur at the same sub-bottom depths as those determined in the formation (see WSTP-ADARA Measurements section, this chapter; Fig. 83), but the change in gradient is considerably less pronounced. This boundary corresponds with the top of lithologic Unit II (see Lithostratigraphy section, this chapter), in which bedding is tilted nearly vertical.

Temperatures between the base of the pipe and the bottom of the hole differ considerably between the descent and the ascent of the TLT. The temperature station at 500 mbsf provides a good constraint on the borehole temperature at this depth (Fig. 83). This point implies that the temperatures recorded during the ascent are slightly closer to the actual borehole temperature, but both are systematically shifted by as much as 8°C. The temperatures recorded while the tool moved are clearly too high on the ascent and too low on the descent, but we expect trends in the temperatures should reflect real variations in borehole temperatures, especially during the ascent where a slower, consistent tool speed was maintained. The trends recorded during the ascent of the tool show a slight increase in the gradient at approximately 400 mbsf. This sub-bottom depth corresponds to an abrupt boundary where diagenesis is implied to be more advanced, as an increase in clay alteration is indicated by a large increase in the smectite clay fraction (see Lithostratigraphy section, this chapter).

A temperature of 65°C was measured at a station at the bottom of the hole. This implies an overall temperature gradient from the surface to the bottom of the hole of 85°C/km. The overall gradient at Site 863 is considerably greater than that measured at Site 860 (35°C/km) (Wireline Measurements section, Site 860 chapter, this volume), and nearly identical to that at Site 859, where it is 83°C/km (Wireline Measurements, Site 859 chapter, this volume). The measured temperature at the base of Hole 863B may also be biased toward lower temperatures than that at Hole 859B, because of the shorter period between the end of circulation and logging. A 20°C increase in temperature is observed between the

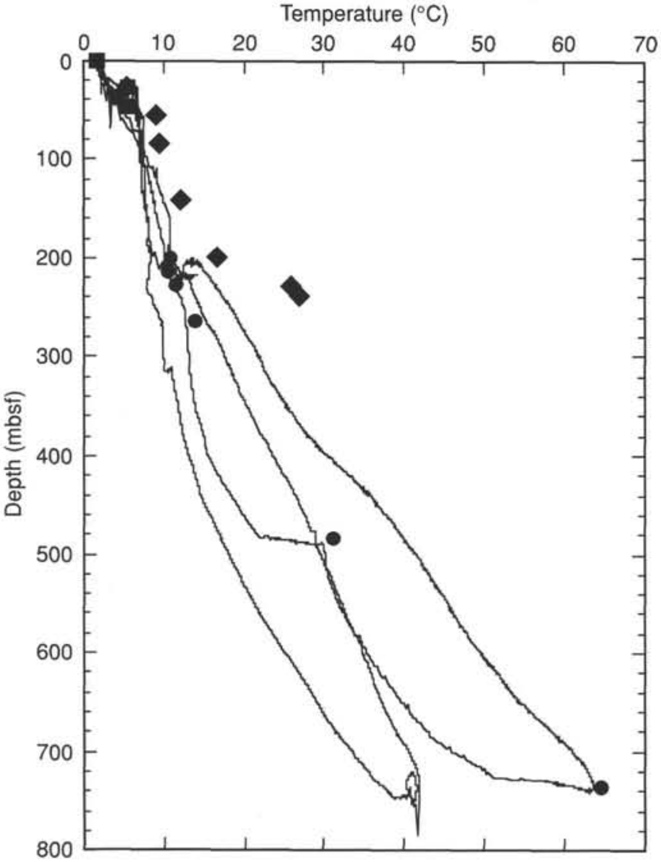

Figure 83. Compilation of the wireline temperature measurements from two Lamont temperature tool runs and WSTP tool (diamonds) and ADARA tool (squares) formation temperatures. The circles are borehole temperatures derived from temperature stations, where the tool was held stationary for 10 min to allow an equilibration curve to be established so that equilibrium temperatures could be predicted.

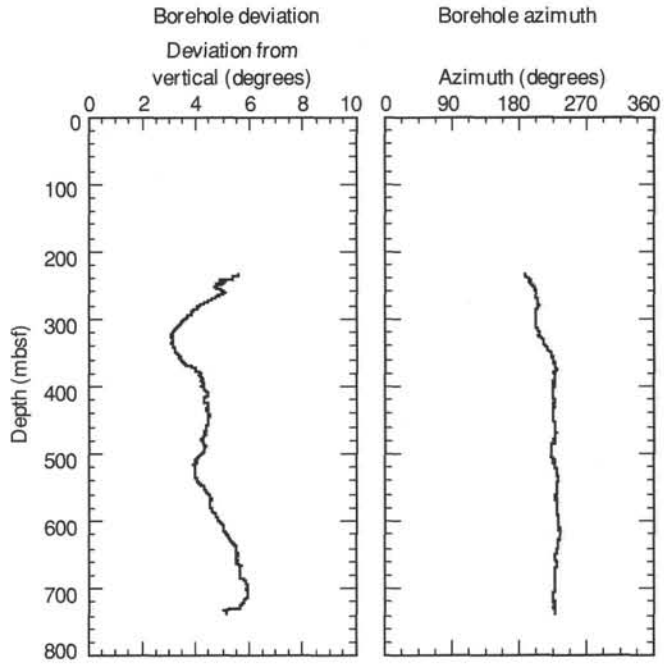

Figure 84. Borehole deviation and azimuth observed by the FMS. These data may be folded into the interpretation of strike and dip for sedimentary structures.

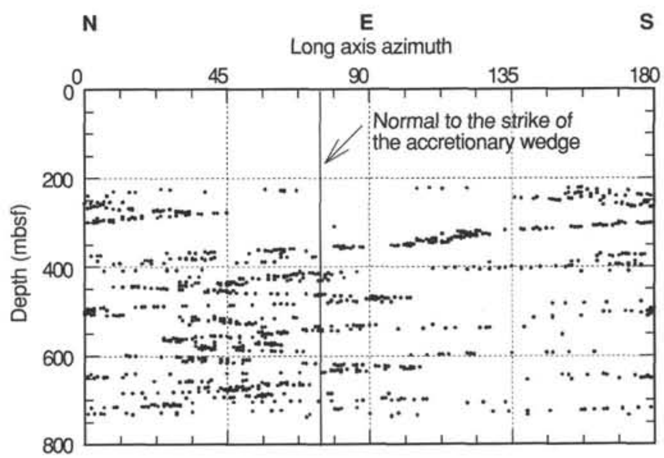

Figure 85. Azimuth of the long axis of the elliptical borehole as a function of sub-bottom depth. The data cluster weakly around 45° in the bottom part of the hole. There is little consistency to the data in the upper part of the logged interval.

two runs, and the borehole was probably still warming relatively quickly at the time of the second run.

Borehole Direction and Shape

FMS data indicate that the borehole deviates by up to 9° from the vertical (Fig. 84). The deviation is measured using three orthogonal accelerometers that work equally well in or out of drill pipe. The FMS tool was run up into the drill pipe to the mudline to provide a continuous record of the deviation. The deviation increases from about 1° at the mudline to about 9° at about 183 mbsf. It diminishes to 4°–6° deeper in the borehole. Over the open-hole logging interval, the borehole azimuth varies from south-southeast to southwest (Fig. 84). Azimuth data are not available from drill pipe because the three component magnetometer will not work in the drill pipe. As bedding in the interval below the drill pipe is nearly vertical with respect to the borehole (see Lithostratigraphy section, this chapter), the drill hole is likely to be contained within the plane of bedding.

The FMS tool will tend to orient itself in the borehole so that one pair of its calipers are pointing along the long axis of the borehole. The long axis can be determined by examination of the orientation of the calipers and hole size in each direction. Between the bottom of the hole and about 400 mbsf the hole is 25–28 cm in diameter and varies between circular and slightly elliptical. Between 400 mbsf and the bottom of the drill pipe, the hole is generally much more washed out, elliptical, and between 28 and 31 cm, and 31 and 38 cm in diameter. Where it is elliptical, the data from the two FMS runs indicate that the tool had the same orientation in the borehole.

Hole 863B is elliptical over most of its length and there is a slight tendency of the long axis of the ellipse to be oriented northeast-southwest (Fig. 85). The alignment is not as well developed as that observed in Hole 859B and it is rotated somewhat from the roughly east-west orientation observed there (see Wireline Measurements section, Site 859 chapter, this volume). The orientation in Hole 863B is roughly 60° from the strike direction of the margin. The borehole ellipticity may be due to the weakness of the formation in the bedding direction. This seems most likely, as the drill bit was guided along the bedding plane.

SUMMARY AND CONCLUSIONS

Site 863 is located at the base of the trench slope of the Chile Trench at the point where the Chile Ridge is being subducted (Fig. 1; location in Fig. 2). The purpose of drilling at Site 863 was to determine the lithologies and depositional environments of the sediment sequences at the base of the trench slope that have been modified by hydrothermal circulation and near-trench volcanism, and to identify the structural fabrics and deformation caused by rift subduction. Extremely vigorous hydrothermal effects were anticipated at Site 863 because the rift axis has been subducted roughly 3 km beneath the base of the trench slope here. Fluids and heat emanating from the spreading ridge were expected to have produced extensive mineralization and elevated thermal gradients in the overlying sediment at Site 863. While evidence of fluid flow, cementation, and mineralization were recognized in the sediment section drilled at Site 863, the temperature gradient was not as steep as anticipated. The temperature gradient at Site 863 is similar to that of Site 859, despite the fact that Site 859 lies approximately 30 km north of the triple junction.

Two lithostratigraphic units were defined at Site 863 (Fig. 86):

Unit I is composed of silt- and clay-sized sediment, both lithified and unlithified, to a depth of 104.4 mbsf. Unit I is further divided into two subunits:

Subunit IA, defined between the seafloor and 46.6 mbsf, is composed of about 4 m of Quaternary unlithified, undeformed silty clay to clayey silt, deposited as slope cover on the more intensely deformed sediments of the accretionary wedge, overlying lower (?) Pleistocene sulfide/organic-rich silty clay to clayey silt, with minor sand. The lower (?) Pleistocene section is complexly faulted and deformed. The base of Subunit IA is a fault. The deformed sequence of Subunit IA represents the uppermost strata involved in the intense deformation associated with subduction.

Lithologic Subunit IB, defined between 46.6 and 104.4 mbsf, is upper Pleistocene silty claystone to clayey siltstone, with minor sandstone. The base of Subunit IB was not recovered.

Deformation in Subunit IA is dominated by reverse faults, with offsets larger than the scale of the core. Faults typically bound individual lithological sequences. Some reverse faults accommodate later-stage normal motion, showing bedding offset in a reverse sense, but with drag into the fault that indicates recent normal displacement.

One well-developed flower structure, with fault strands documenting both reverse and normal offsets, was found in Core 141-863A-1H. These faults cannot be restored by a two-dimensional reconstruction in the plane of the core face: their restoration requires an oblique strike-slip component of motion. This suggests that other complex fault zones that display reverse and normal offsets in the plane of the core face may actually accommodate an oblique component of motion.

Diatoms and radiolarians are poorly preserved at Site 863, except in APC cores. Only the most robust foraminifer forms are preserved, such as *Globoconella inflata,* with shells often completely replaced by silica during diagenesis. Pyritized shelf benthic foraminifer species were recovered. They were likely deposited and altered in an oxygen-minimum zone on the upper continental rise, upslope from Site 863, and transported and redeposited downslope. Benthic foraminifers that are not likely to have been reworked indicate a lower bathyal depositional environment. The entire drilled section at Site 863 is Pleistocene in age.

Lithologic Unit II extends from 104.4 to 742.9 mbsf and is composed of lower and upper Pleistocene sandstone and bioturbated siltstone, with sandy silty claystone. Bedding in Unit II is predominantly steep to vertical, with intervals of broken formation that mark fault zones. Hole was 863B drilled for 640 m through Unit II in a direction nearly parallel to bedding. Hole 863B probably penetrated approximately 60 m of section. Biostratigraphic order is inverted in the near vertical sequence; lower Pleistocene lies above upper Pleistocene, the break occurring between 290 and 325 mbsf.

Unit I was likely deposited as contourites, with Unit II being the product of distal turbidite (outer fan) deposition. No conglomerate units were recovered. Unit II is heavily bioturbated. Bouma sequences were sampled in Cores 141-863B-41R and -49R.

The steeply dipping domain, extending from 250 to 742.9 mbsf, is characterized by prevalent deformation bands and web structures in the sandstone units. The first appearance of vertical bedding is at about 265 mbsf. Vertical bedding extends to total depth (TD). Faults have moderate dips or they parallel bedding. Many well-developed slickenlines indicate normal offsets on faults. If these (apparent) normal faults predate bedding tilt, then they could actually be early reverse faults. In either case, normal faulting now dominates the most recent deformation.

Some faults contain secondary calcite mineralization bands 1–2 mm wide, often showing slickencrysts. Quartz-pyrite mineralization also occurs along faults. These observations suggest that fluid flow and mineralization along the fault surfaces were synchronous with deformation.

Multishot orientation of Cores 141-863A-4H, -5H, and -6H allows for the orientation of structures in the geographic coordinate system: both bedding and faults strike northwest-southeast in these cores, at a large angle to both local topographic slopes and to the plate convergence direction. This orientation may reflect strike-slip faulting in the forearc, extending to within 5 km of the base of the trench slope. The Liquiñe-Ofqui fault on land is an active right-lateral strike-slip fault that parallels the trench about 160 km inshore (Leslie, 1986). The entire forearc may represent a broad shear zone that takes up trench-parallel plate motion. The strike-slip component of plate motion in this region is about 20 mm/yr (Chase, 1978). Such a rate distributed over the 160 km-wide forearc implies strain rates of about 4×10^{-15}/s, a strain rate similar to that within other orogenic zones.

A steeply inclined, normally polarized overprint dominates the NRM through most of the sequence, and this still persists after 15-mT demagnetization. Between 350 and 500 mbsf, however, the steeply inclined overprint is greatly reduced, and a low-inclination component is revealed. It probably represents the primary magnetization in this near-vertically bedded part of the sequence. This interval has been a zone of enhanced fluid chemical activity (see below), and it may be that the carrier of the overprint has been leached out. Wide variations in magnetic intensity, coercivity, and the Königsberger ratio, and complex AF-demagnetization paths, suggest the presence of magnetic iron sulfides in the sulfide-rich sediment of lithologic Unit I.

Inorganic geochemical observations suggest that several chemically distinct fluid zones are present at Site 863:

From the seafloor to 60 mbsf there is a zone of sulfate diagenesis that is typical of microbial hemipelagic diagenesis. A methanogenic layer exists between about 60 and 147 mbsf, where the calcium content drops to 20% of seawater. In the zone between 60 and 147 mbsf, pore- fluid characteristics are dramatically different from overlying units, suggesting that this interval may be a thrust sheet composed of strata deposited further landward. Downward diffusion gradients of Ca, Mg, K, Na, Sr, and F characterize the lower interval between 147 and 400 mbsf. Boron also decreases downsection, suggesting a boron sink below 400 mbsf. Both Mg and K are nearly depleted below about 500 mbsf, which coupled with a steep pH increase and inflections in the gradients of other constituents, suggests the presence of a reaction front or lateral fluid flow at this depth.

Below 490 mbsf, fluids comprise a strongly alkaline brine; chlorine contents are up to 15% above seawater, pH increases to 10.5 in the lower 150 m of the hole, and calcium reaches concentrations up to 150 mM, suggesting nearby reactions with basalt or retrograde alteration of serpentinized ultramafics.

Organic geochemical data define zones dominated by either biogenic gas or thermogenic gas likely to have migrated into the region of Site 863. The depth interval between 0 and 60 mbsf contains little methane or other hydrocarbon gases. Some biogenic gas is present between 60 and 125 mbsf, with C_1/C_2 ratios of about 800. Starting at about 350 mbsf there is an increase in ethane, and the C_1/C_2 ratio drops to about 5. Propane and higher hydrocarbons up to and beyond C_7 appear in the interval between 460 mbsf and TD. The C_1/C_2 ratio drops to less than 1 in some cases. The overall gas composition is one of thermogenic gas with gasoline-range hydrocarbons. The vertically-bedded sequence drilled at the bottom of Hole 863B likely represents a preferential migration pathway for hydrocarbons sourced at depth or in a zone of hydrocarbon preservation.

The organic matter content of the drilled section between 0 and 350 mbsf is comprised of both terrestrial and marine components. Hydrocarbon gases superimposed on a more mature overall organic hydrocarbon profile were encountered between 430 mbsf and TD, but the bitumen in the sediment remained immature. These observations indicate that mature hydrocarbons migrated into the region of the drill site, probably from further downdip in the subduction zone.

Carbonate cementation is the dominant control over the gradients in physical properties at Site 863. Porosity decreases from approximately 60% to 35% between the seafloor and 150 mbsf, reflecting cementation with carbonate (micritic) cement. The porosity decreases from 40% to 25% between 300 mbsf and TD, with short intervals of heavily-cemented sections with porosities as low as 5%–10%. Compressional-wave velocities are 1600 m/s at the seafloor, linearly increasing from 1750 to 3200 m/s between 250 mbsf and TD. Some calcareous units have velocities up to 4500 m/s.

Site 859, in a similar tectonic position as Site 863, exhibits a higher degree of compaction than Site 863. The sediment at Site 859 exhibits 10%–15% lower porosity at any given sub-bottom depth relative to Site 863, but the same gradient of porosity decrease with sub-bottom depth applies to both sites. The sediment at Site 863 is much sandier than at Site 859 except in the upper 70 m, which is identical at the two sites.

The overall temperature gradient of the top 250 m of Site 863 is at least 73°C/km. Superimposed on this minimum gradient are (1) high-temperature anomalies at about 30 and 60 mbsf, coresponding to a sulfide-rich, complexly deformed zone; and (2) a zone of steep temperature gradient from about 200 to 240 mbsf, coresponding to the top of the interval of steeply dipping bedding.

Wireline measurements at Site 863 were hampered by a stuck drill pipe that precluded logging the upper 232 m of the hole, but four string runs acquired good logging data in the interval 232–733 mbsf.

Five log units were defined, largely based on data from the geophysical and geochemical logs, primarily the resistivity, gamma-ray, and density logs.

Borehole temperatures were measured by the LDGO temperature tool (TLT) during two tool-string deployments in Hole 863B. The first temperature run occurred only 3 hr after the cessation of fluid circulation in the hole; thus, downhole equilibrium temperatures were not measured during this run. However, the first temperature run was followed 28 hr later by the second run, during which the tool string was stopped at a series of depths so that the temperature tool could measure the actual downhole temperature at those depths without the effects of tool response.

A temperature of 65°C was measured at the bottom of Hole 863B, constraining the overall minimum temperature gradient at this site to be about 85°C/km. The bottomhole temperature increased about 20°C between the two temperature measurements, suggesting that equilibrium temperature had not yet been reached at the time of the second run.

Borehole orientation data were acquired during FMS tool-string runs. These data show that the borehole deviates up to 9° from vertical, and the azimuth of the hole varies from south-southeast to southwest over the open interval of the hole.

Conclusions

The sequence of deformational events observed at Site 863 lends support to the hypothesis formulated prior to drilling that the ridge-trench collision produces subduction erosion of the forearc within the collision zone. Large normal faults, thought to accommodate subsidence of the forearc in response to the subduction of material near the plate interface (Fig. 3), are likely to be the large-scale manifestation of the same process that is recognized in the cores from Site 863. Early-stage deformation of the sandstone at Site 863 was primarily compressive, with reverse/thrust faulting dominant in the cores. This deformation is likely to be related to frontal accretion of these turbidites following deposition in the Chile Trench. Uplift and tilting of the sedimentary strata was probably a result of subduction of the ridge with its steep topography. The latest phase of deformation recognized in the cores, high-angle normal faulting, including the reactivation of pre-existing reverse faults, reflects the subsidence of the forearc immediately following ridge subduction.

Geochemical analysis of Site 863 samples indicates, as did the results from Sites 859, 860, and 861, that a substantial amount of fluid, including hydrocarbon gas, is migrating upward from deep within the subduction zone to the shallow structural levels drilled during Leg 141.

The thermal anomaly expected at Site 863, and the accompanying hydrothermal circulation and mineralization, were not observed. Although deformation was intense, with near-vertical bedding drilled for roughly 600 m, the strong thermal effects expected of ridge subduction were not detected. This is all the more unusual when seen in comparison with Site 859, which is roughly 30 km north of the triple junction. Site 859 has a similar overall geothermal gradient (roughly 100°C/km) as that of Site 863; however, Site 859 exhibited evidence of much higher volumes and/or rates of hot fluid flow, with narrow downhole intervals of very high temperatures and with large deviations from a linear temperature gradient with depth.

The deformation sequence at Site 859 indicates that subduction erosion has not yet begun. The lack of Quaternary sediment incorporated in the thrust system at Site 859, however, may mean that subduction accretion at that location has ceased, and that this portion of the margin is in transition from accretion to erosion. Site 863 sediments are undergoing extensional deformation as the latest phase of their deformational history. This, together with the observations from seismic reflection images, strongly indicates that at Site 863 subduction erosion is taking place. Thus, the transition from subduction accretion to subduction erosion along the Chile Trench in this region occurs over a distance along strike of about 30 km, and over a period of about 3 m.y.

REFERENCES

Bé, A.W.H., and Tolderlund, D.S., 1971. Distribution and ecology of living planktonic foraminifera in surface waters of the Atlantic and Indian Oceans. *In* Funnell, B.M., and Riedel, W.R. (Eds.), *The Mi-*

cropaleontology of Oceans: Cambridge (Cambridge Univ. Press), 105–149.

Boersma, A., 1984. *Handbook of Common Tertiary Uvigerina:* Stoney Point, NY (Microclimate Press).

Boltovskoy, E., Giussani, G., Wantanabe, S., and Wright, R. 1980. *Atlas of Benthic Shelf Foraminifera of the Southwest Atlantic:* The Hague (Dr. W. Junk bv Publishers).

Boltovskoy, E., and Theyer, F., 1970. Foraminiferos Recientes de Chile Central. *Rev. Mus. Argent. Cienc. Nat. "Bernardino Rivadavia," Hidrobiol.,* 2:279–379.

Chase, C.G., 1978. Plate kinematics: the Americas, East Africa, and the rest of the world. *Earth Planet. Sci. Lett.,* 37:355–368.

Claypool, G.E., and Kaplan, I.R., 1974. The origin and distribution of methane in marine sediments. *In* Kaplan, I.R. (Ed.), *Natural Gases in Marine Sediments:* New York (Plenum Press), 99–139.

Didyk, B.M., and Simoneit, B.R.T., 1989. Hydrothermal oil of Guaymas Basin and implications for petroleum formation mechanisms. *Nature,* 342:65–68.

Didyk, B.M., Simoneit, B.R.T., Brassell, S.C., and Eglinton, G., 1978. Organic geochemical indicators of palaeoenvironmental conditions of sedimentation. *Nature,* 272:216–222.

Emeis, K.C., and Kvenvolden, K.A., 1986. Shipboard organic geochemistry on JOIDES Resolution. *ODP Tech. Note,* 7: College Station, TX (Ocean Drilling Program).

Farrington, J.W., Davis, A.C., Tarafa, M.E., McCaffery, M.A., Whelan, J.K., and Hunt, J.M., 1988. Bitumen molecular maturity parameters in the Ikpikpuk well, Alaskan North Slope. *Org. Geochem.,* 13:303–310.

Fryer, P., 1992. Mud volcanoes of the Marianas. *Sci. Am.,* Feb. 1992:46–52.

Fryer, P., Pearce, J.A., Stokking, L.B., et al., 1990. *Proc. ODP, Init. Repts.,* 125: College Station, TX (Ocean Drilling Program).

Hemleben, C., Spindler, M., and Anderson, O.R., 1988. *Modern Planktonic Foraminifera:* New York (Springer).

Janecky, D.R., and Seyfried, W.E., 1986. Hydrothermal serpentinization of peridotite within the oceanic crust: experimental investigations of mineralogy and major element chemistry. *Geochim. Cosmochim. Acta,* 50:1357–1378.

Leslie, R.B., 1986. Tectonics of the Southern Chile Trench and the Chile Margin Triple Junction [Ph.D. dissert.]. Columbia Univ., New York.

Nigrini, C.A., 1991. Composition and biostratigraphy of radiolarian assemblages from an area of upwelling (northwestern Arabian Sea, Leg 117). *In* Prell, W.L., Niitsuma, N., et al., *Proc. ODP, Sci. Results,* 117: College Station, TX (Ocean Drilling Program), 89–126.

Seyfried, W.E., Janecky, D.R., and Mottl, M.J., 1984. Alteration of the oceanic crust: implications for geochemical cycles of lithium and boron. *Geochim. Cosmochim. Acta,* 48:557–569.

Shipboard Scientific Party, 1982. Guaymas Basin: Sites 477, 478, and 481. *In* Curray, J.R., Moore, D.G., et al., *Init. Repts. DSDP,* 64 (Pt. 1): Washington (U.S. Govt. Printing Office), 210–415.

———, 1991. Site 806. *In* Kroenke, L.W., Berger, W.H., Janecek, T.R., et al., *Proc. ODP, Init. Repts.,* 130: College Station, TX (Ocean Drilling Program), 291–367.

Simoneit, B.R.T., 1977. Diterpenoid compounds and other lipids in deep-sea sediments and their geochemical significance. *Geochim. Cosmochim. Acta,* 41:463–476.

———, 1978. The organic chemistry of marine sediments. *In* Riley, J.F., and Chester, R. (Eds.), *Chemical Oceanography* (2nd ed.)(Vol. 7): New York (Academic Press), 233–311.

Simoneit, B.R.T., Brenner, S., Peters, K.E., and Kaplan, I.R., 1981. Thermal alteration of Cretaceous black shale by basaltic intrusions in the eastern Atlantic. II: Effects on bitumen and kerogen. *Geochim. Cosmochim. Acta,* 45:1581–1602.

van Morkhoven, F.P.C.M., Berggren, W.A., and Edwards, A.S., 1986. Cenozoic cosmopolitan deep-water benthic foraminifera. *Bull. Cent. Rech. Explor.-Prod. Elf-Aquitaine,* 11:1–421.

Ms 141IR-110

NOTE: For all sites drilled, core-description forms ("barrel sheets") and core photographs have been reproduced on coated paper and can be found in Section 3, beginning on page 449. Forms containing smear-slide data can be found in Section 4, beginning on page 665.

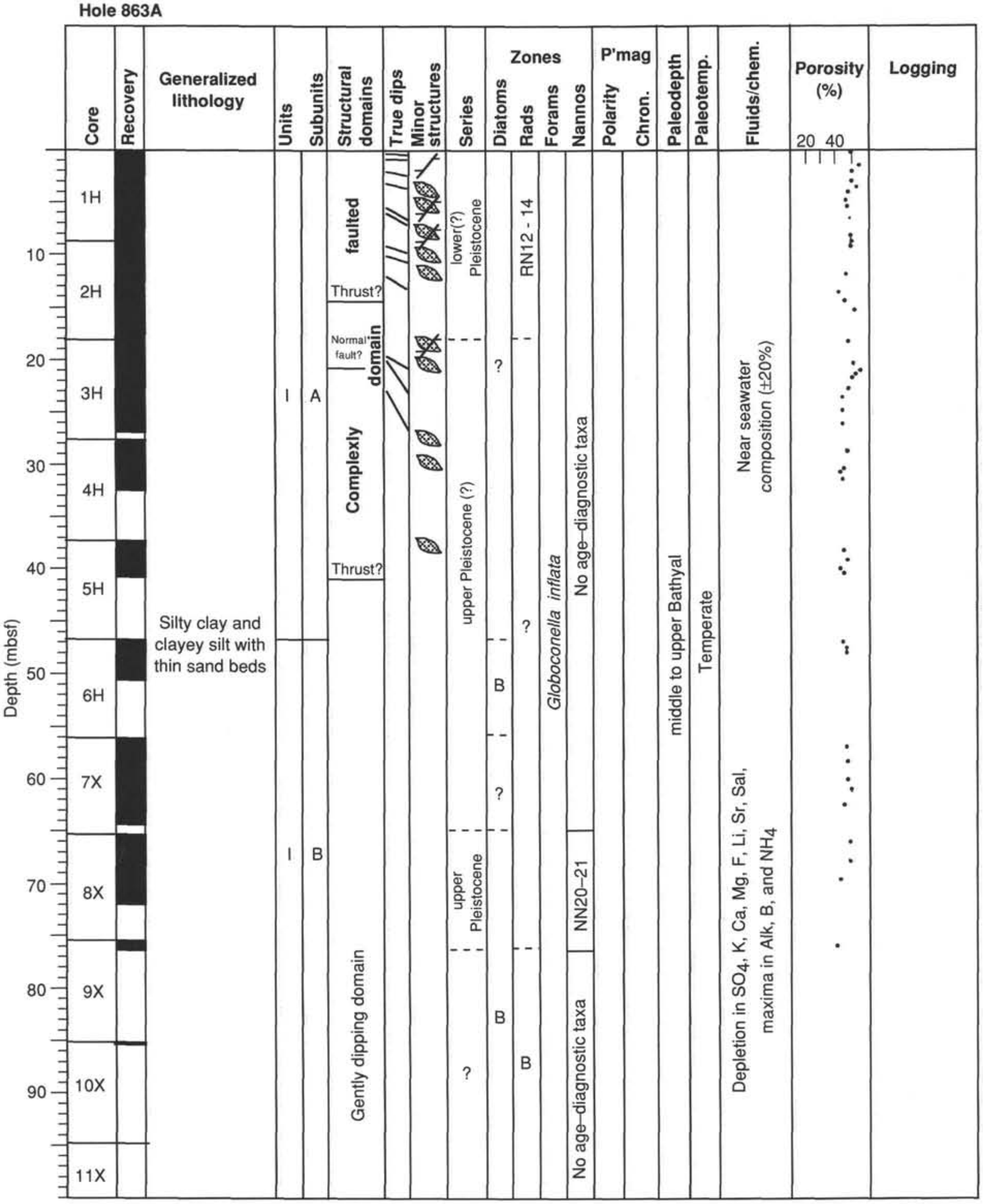

Figure 86. Master chart for Site 863.

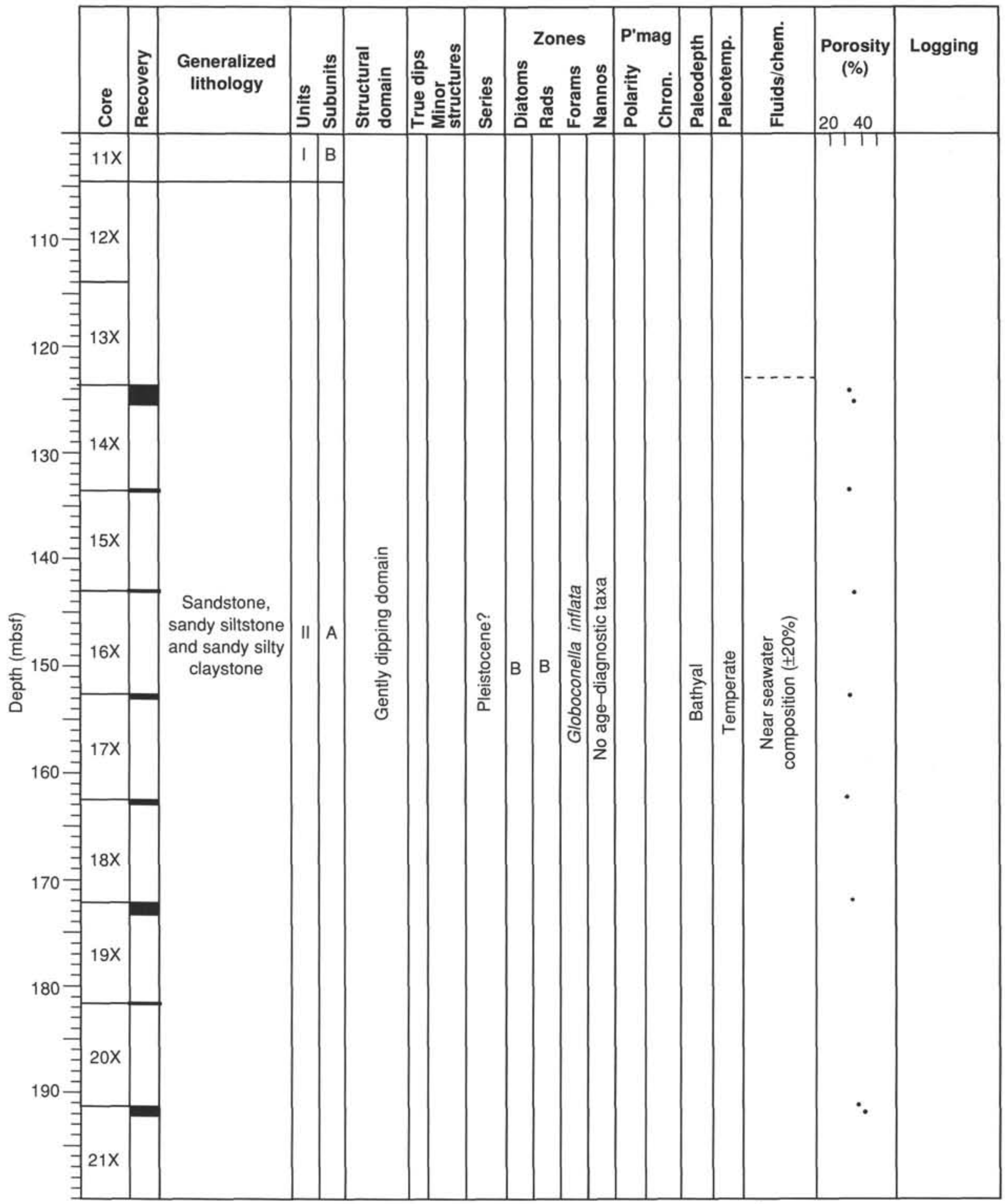

Figure 86 (continued).

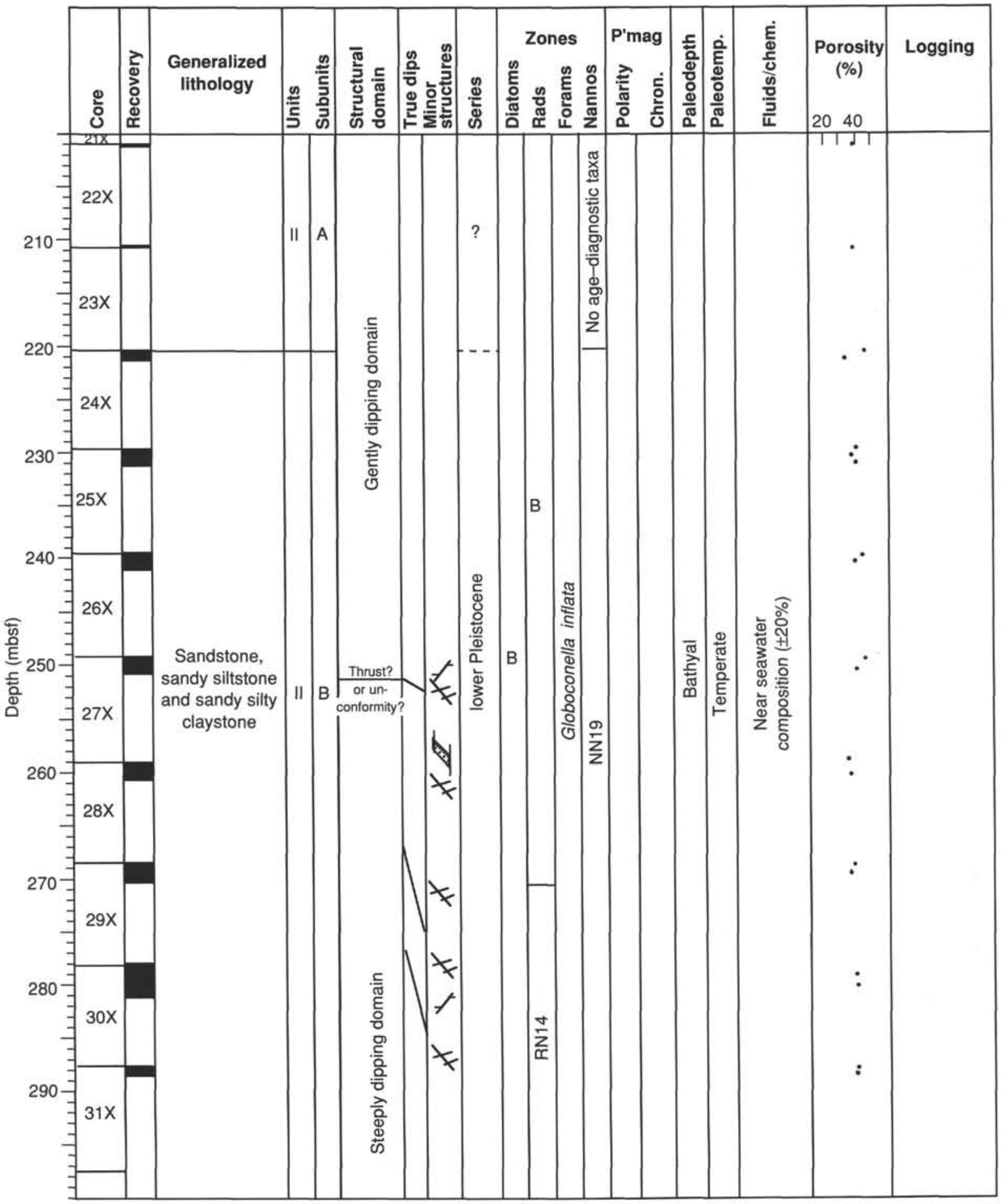

Figure 86 (continued).

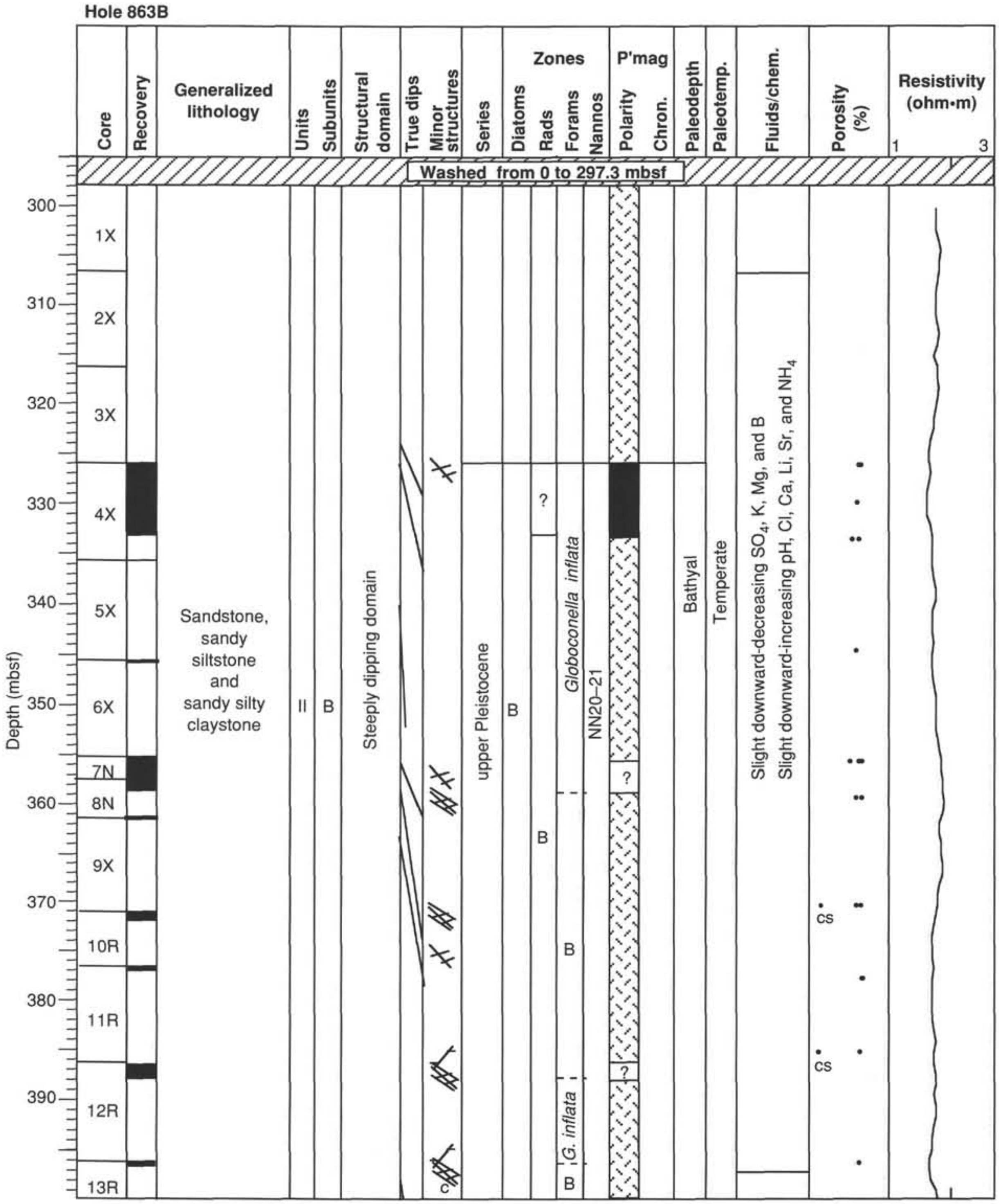

Figure 86 (continued).

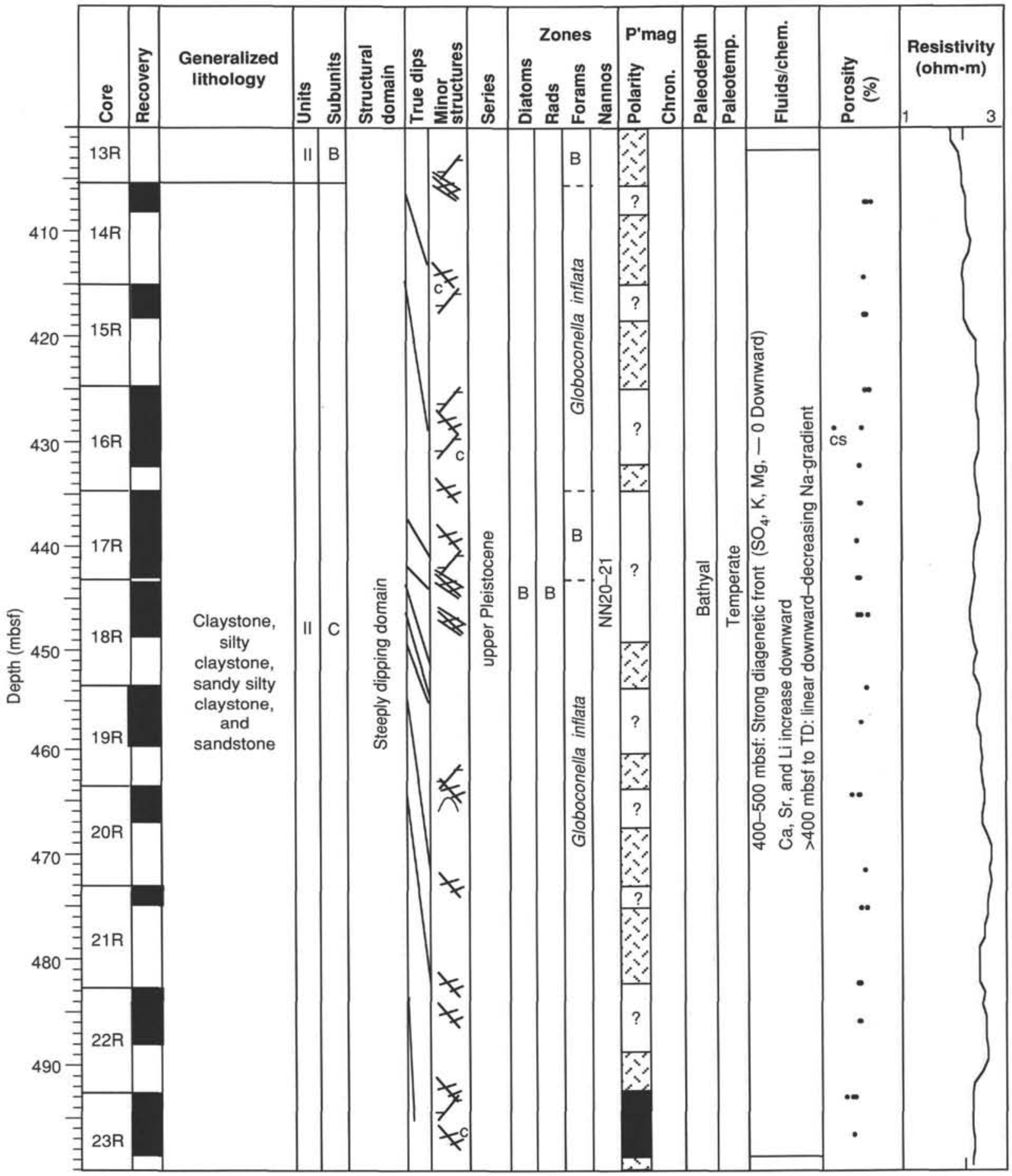

Figure 86 (continued).

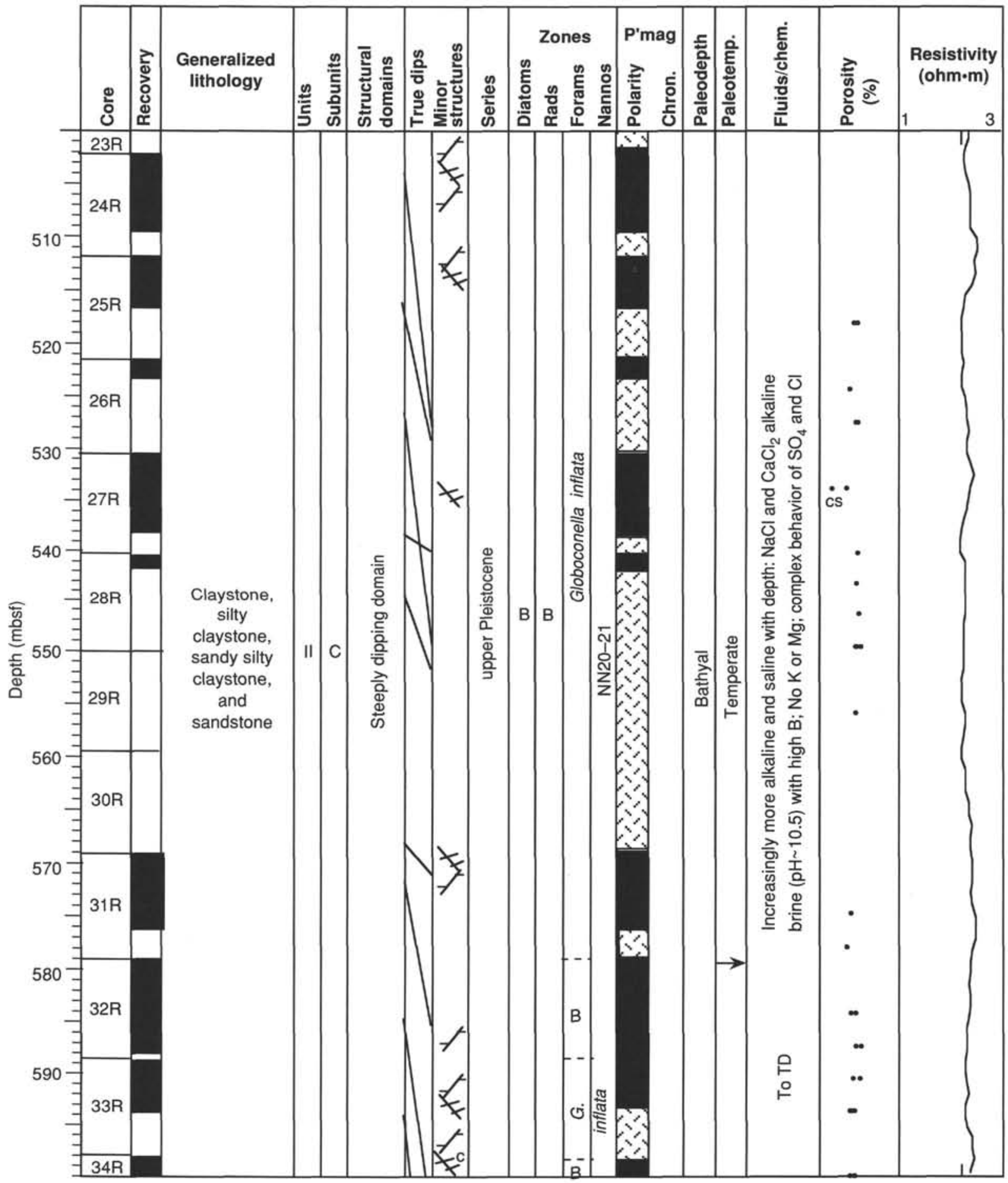

Figure 86 (continued).

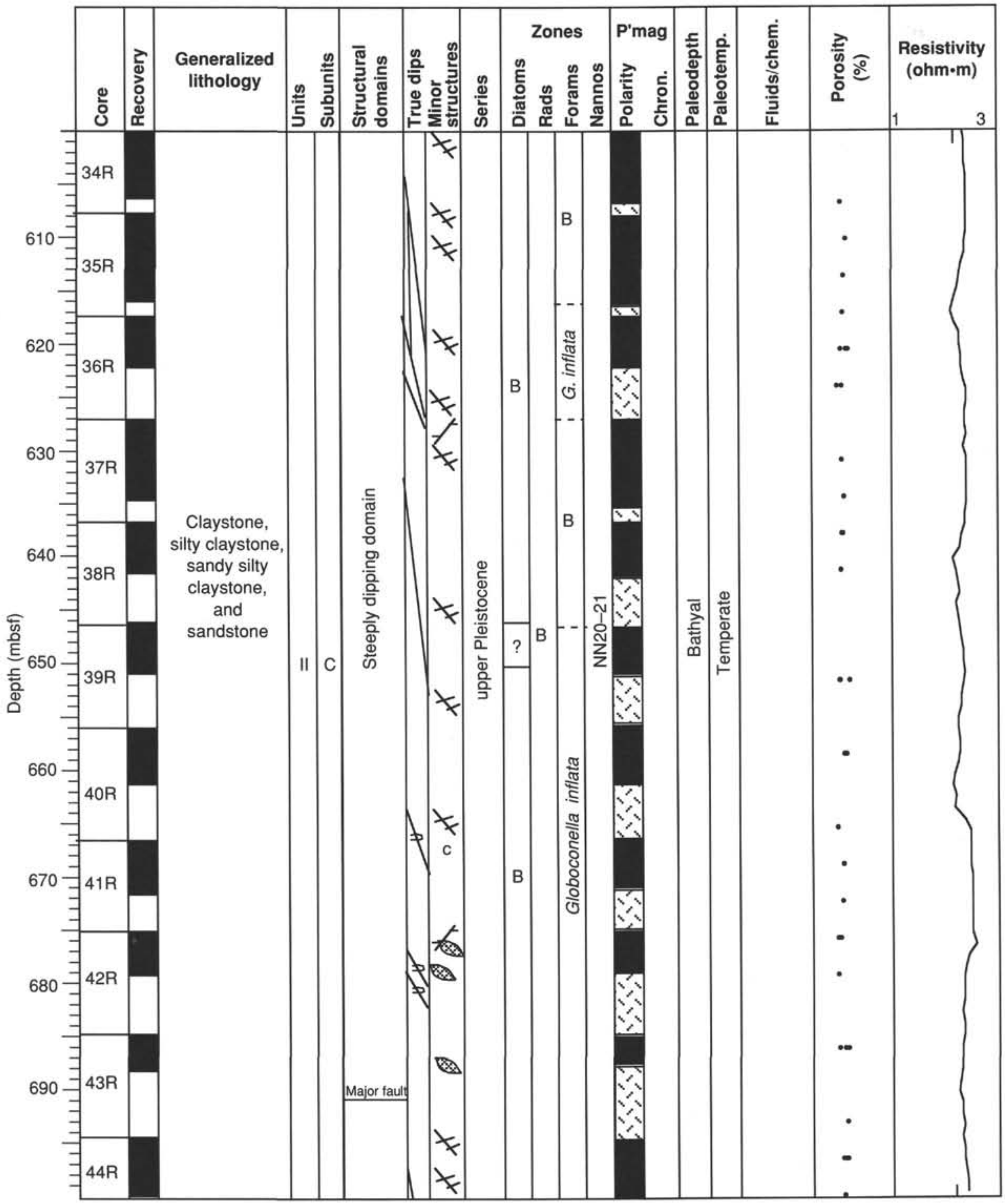

Figure 86 (continued).

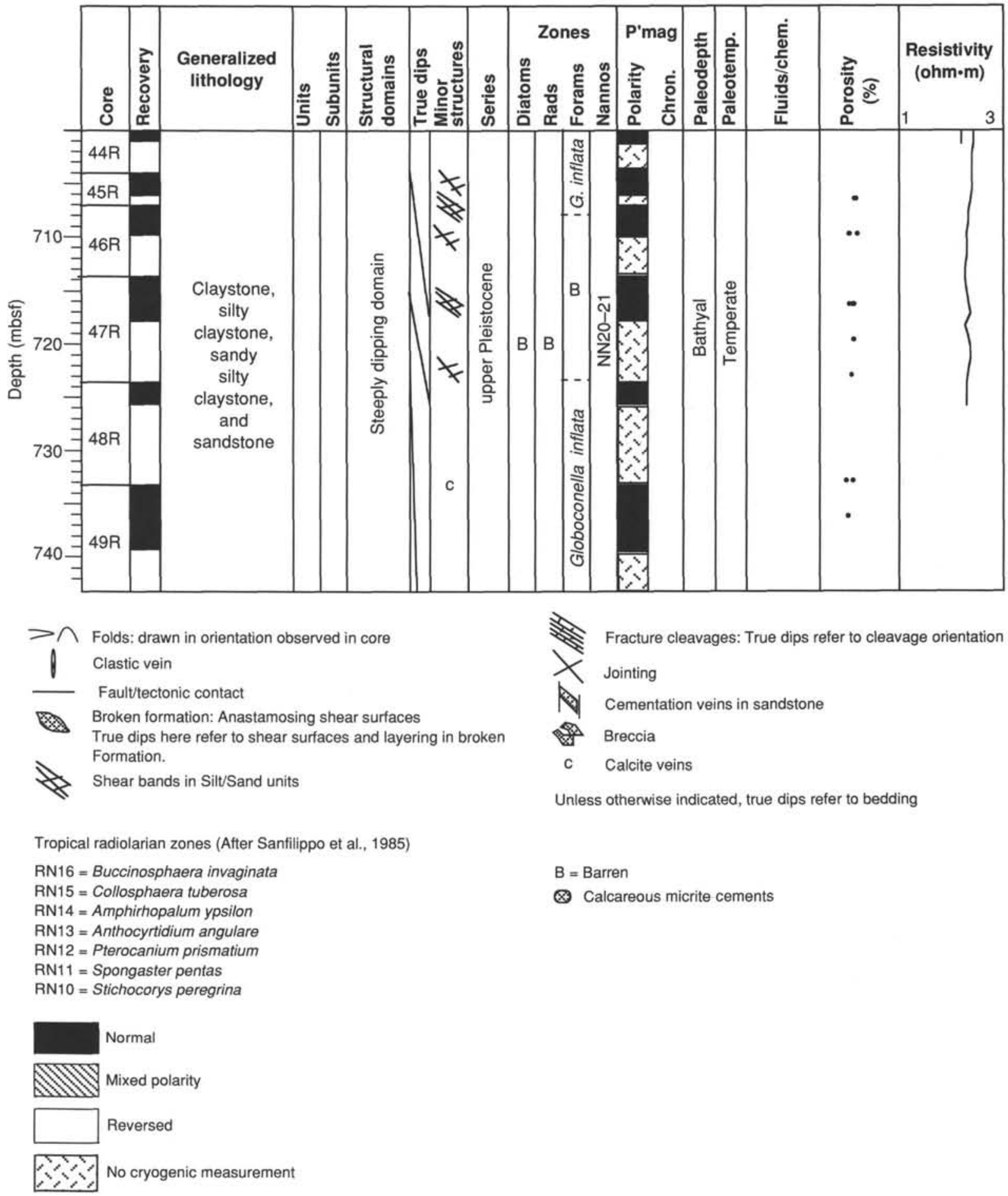

Figure 86 (continued).

Hole 863B: Resistivity-Velocity-Natural Gamma Ray Log Summary

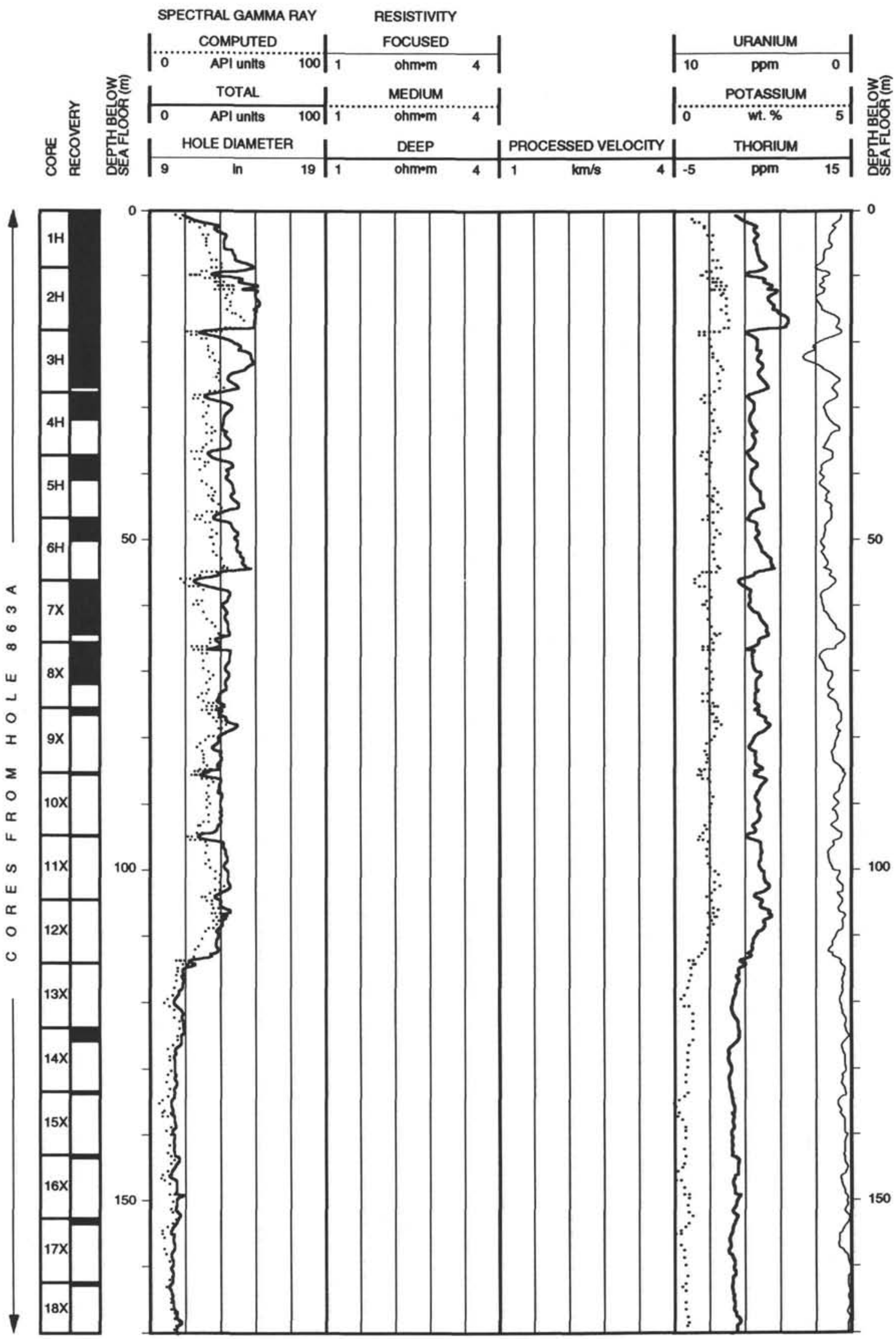

Hole 863B: Resistivity-Velocity-Natural Gamma Ray Log Summary (continued)

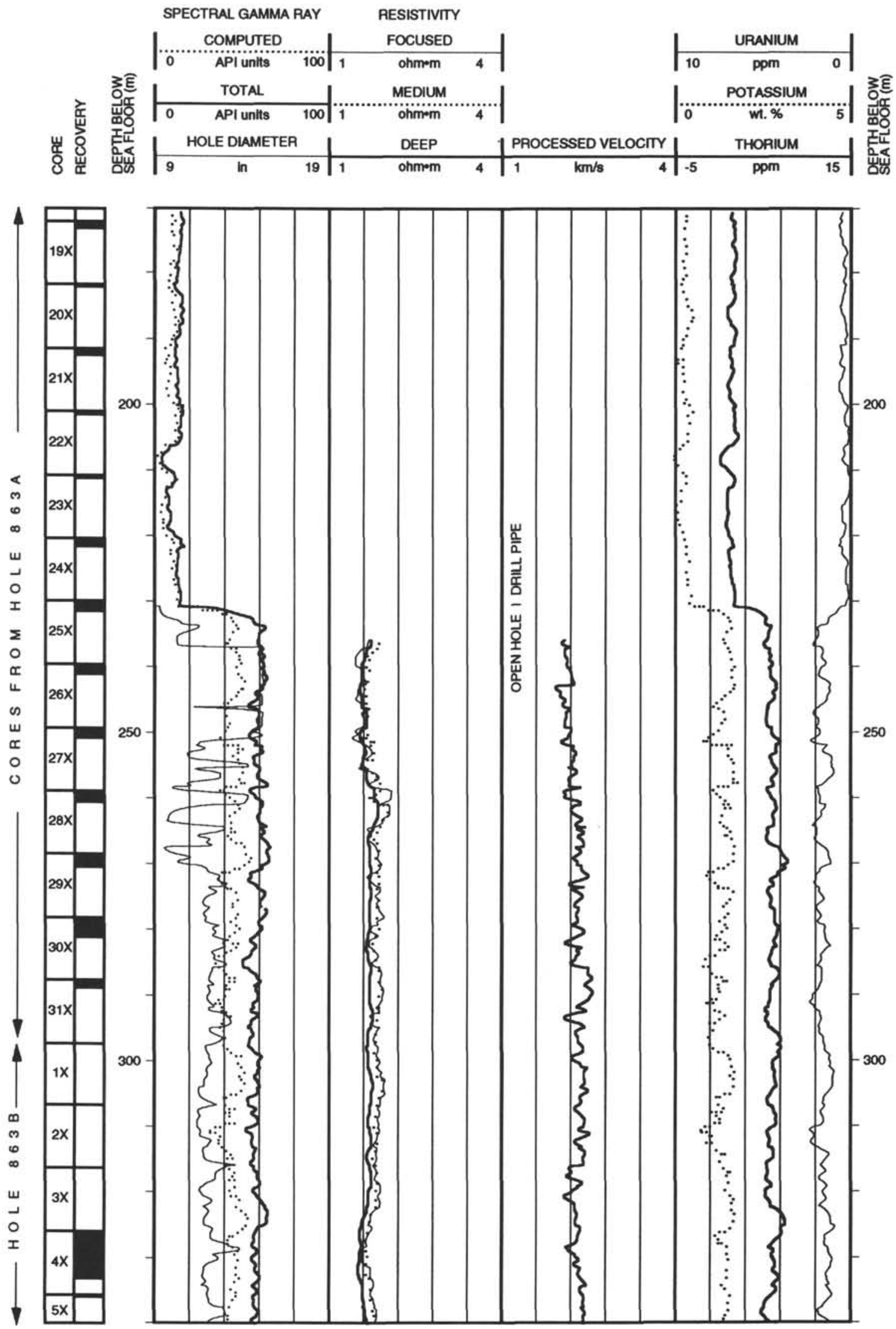

Hole 863B: Resistivity-Velocity-Natural Gamma Ray Log Summary (continued)

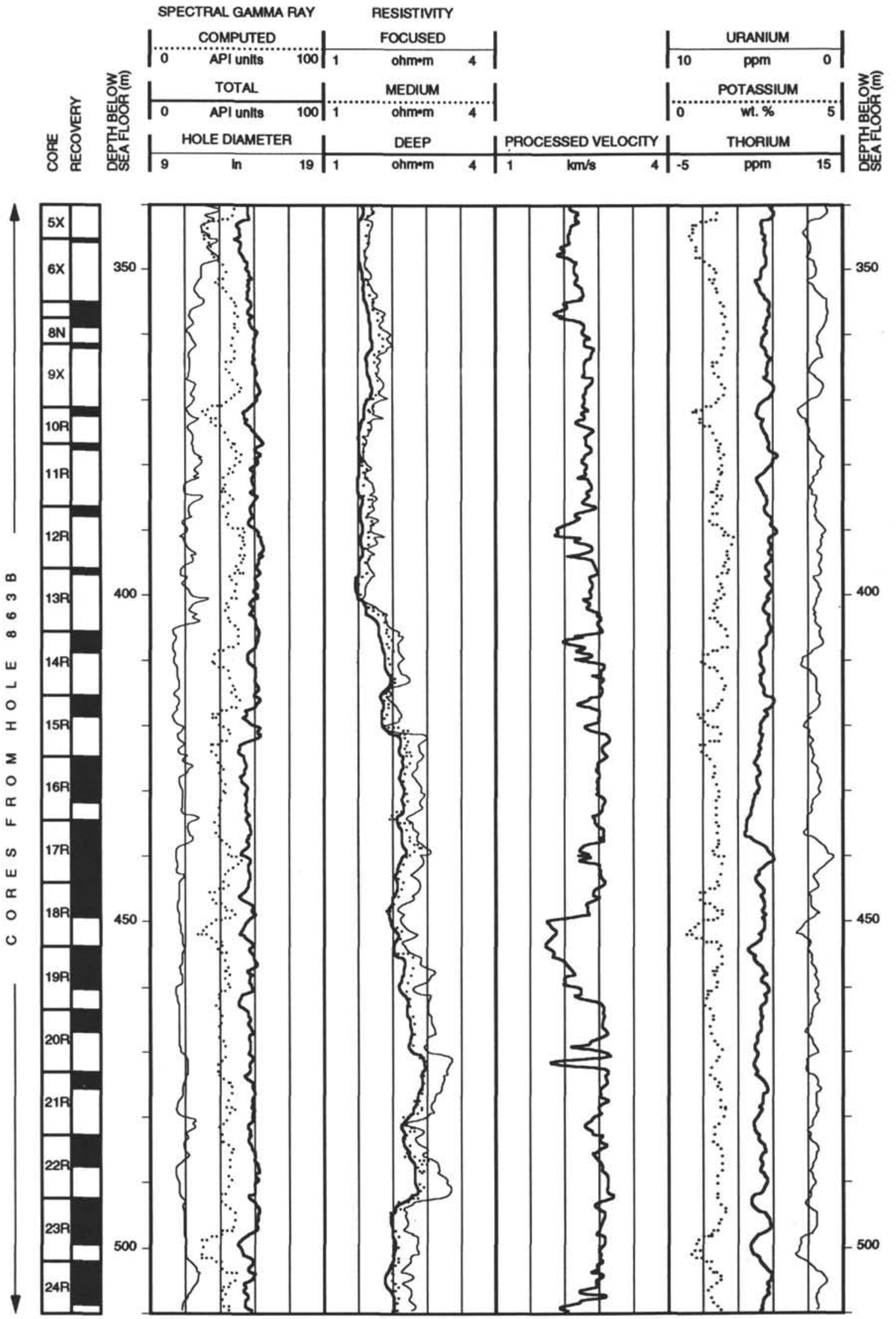

Hole 863B: Resistivity-Velocity-Natural Gamma Ray Log Summary (continued)

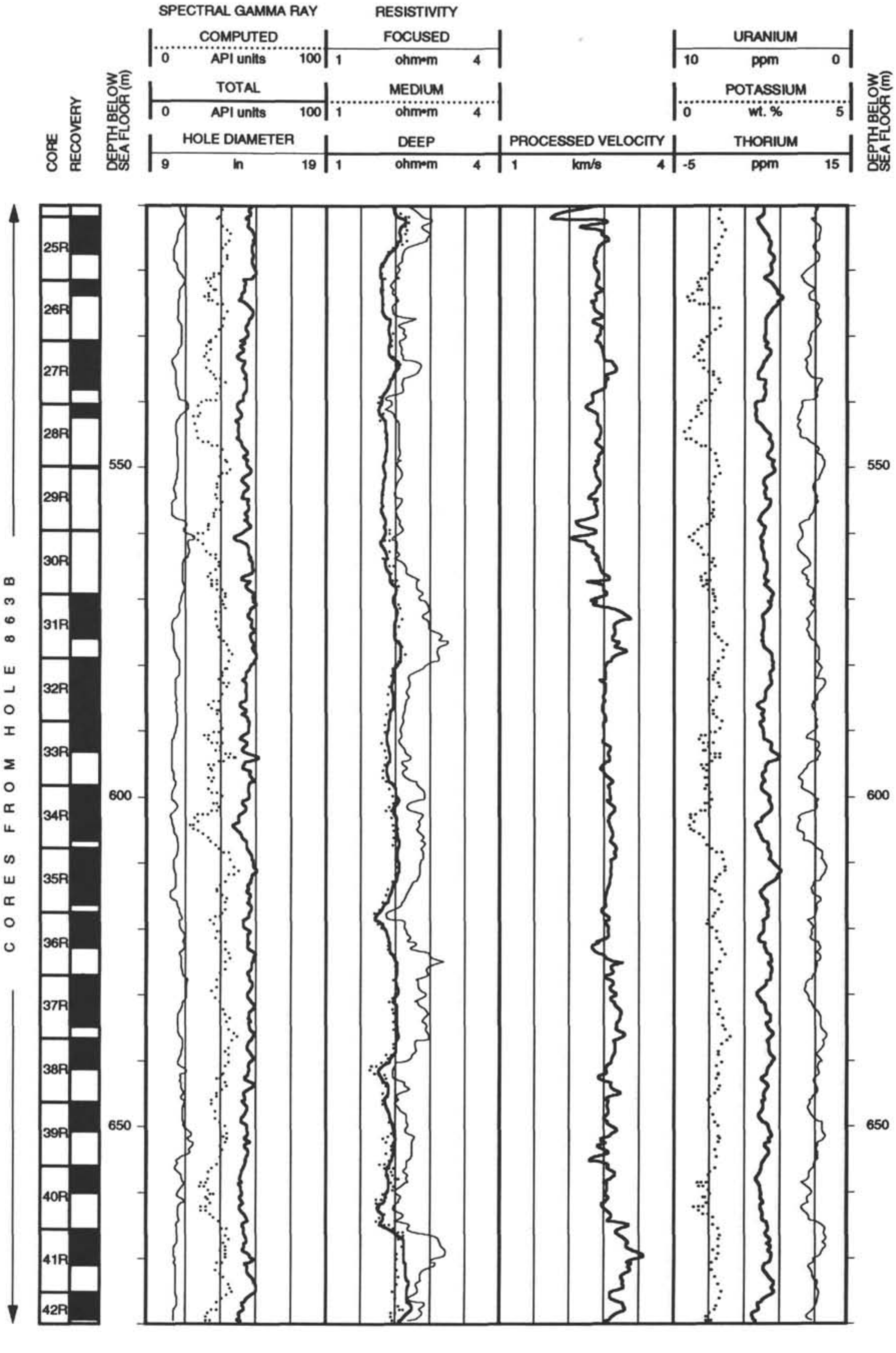

Hole 863B: Resistivity-Velocity-Natural Gamma Ray Log Summary (continued)

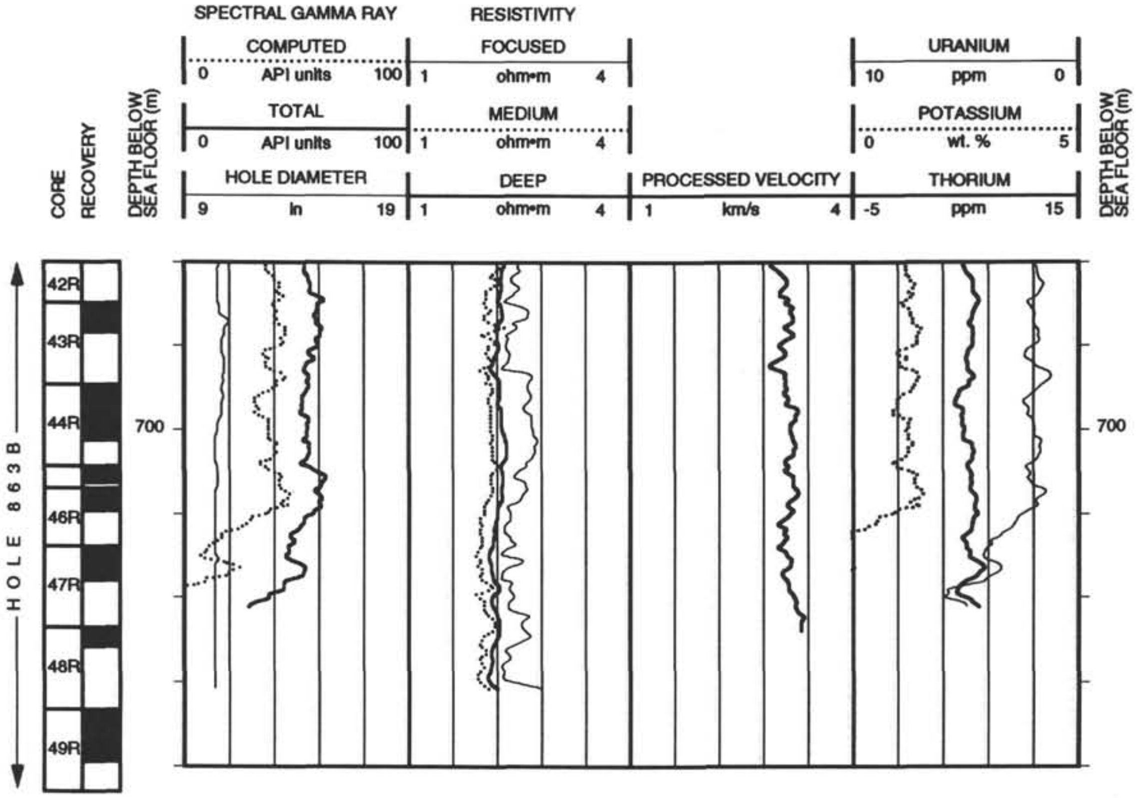

Hole 863B: Density-Natural Gamma Ray Log Summary

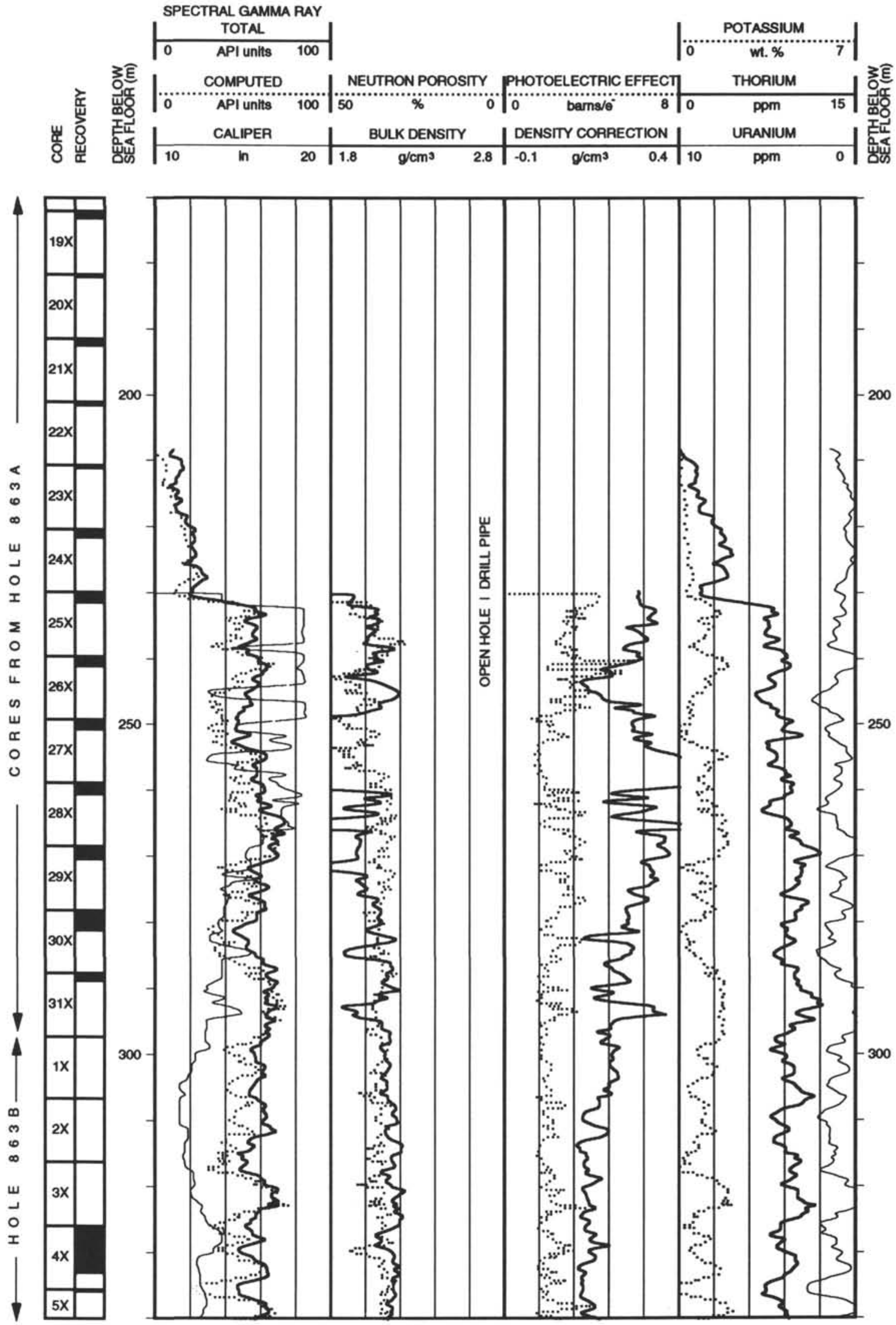

Hole 863B: Density-Natural Gamma Ray Log Summary (continued)

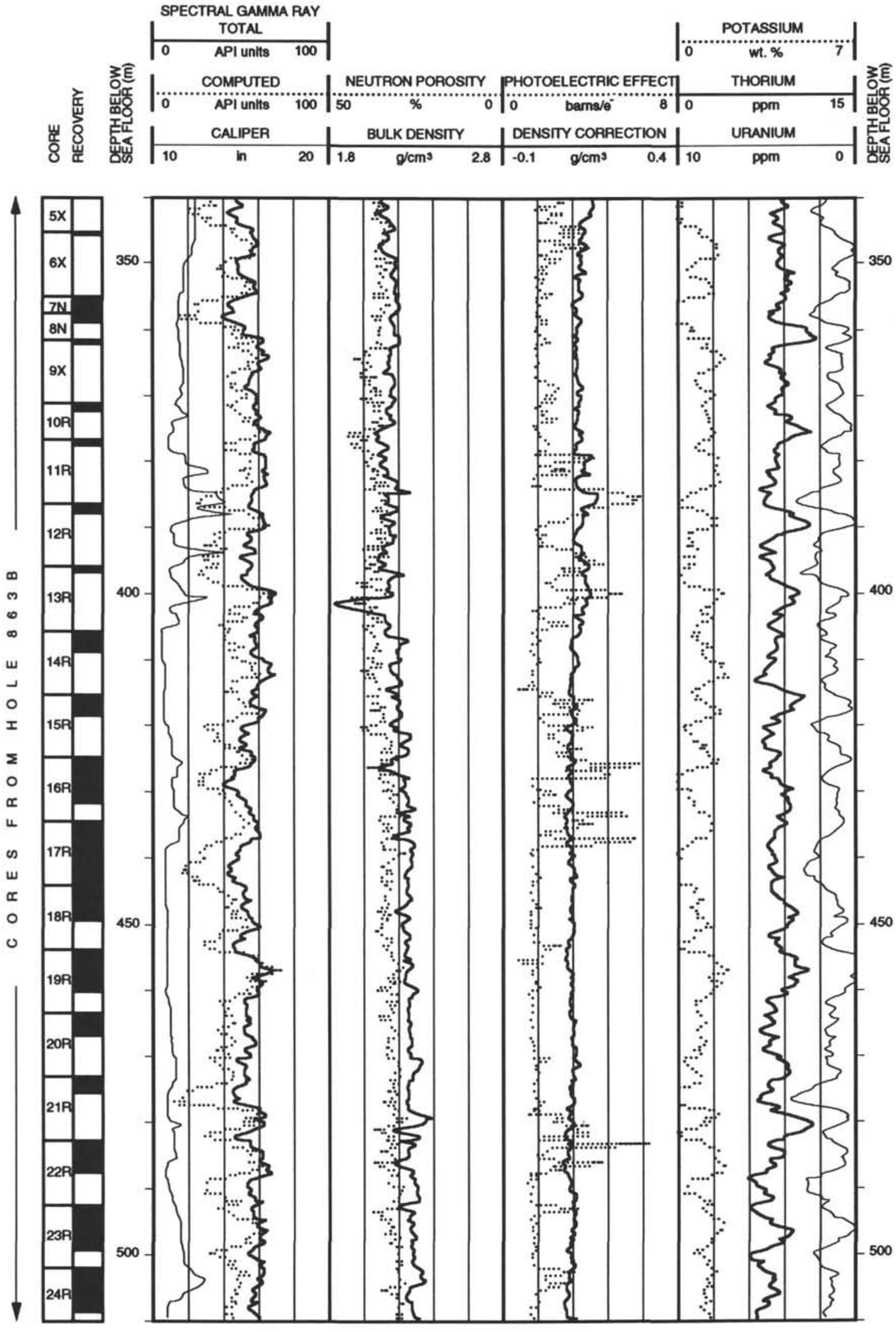

Hole 863B: Density-Natural Gamma Ray Log Summary (continued)

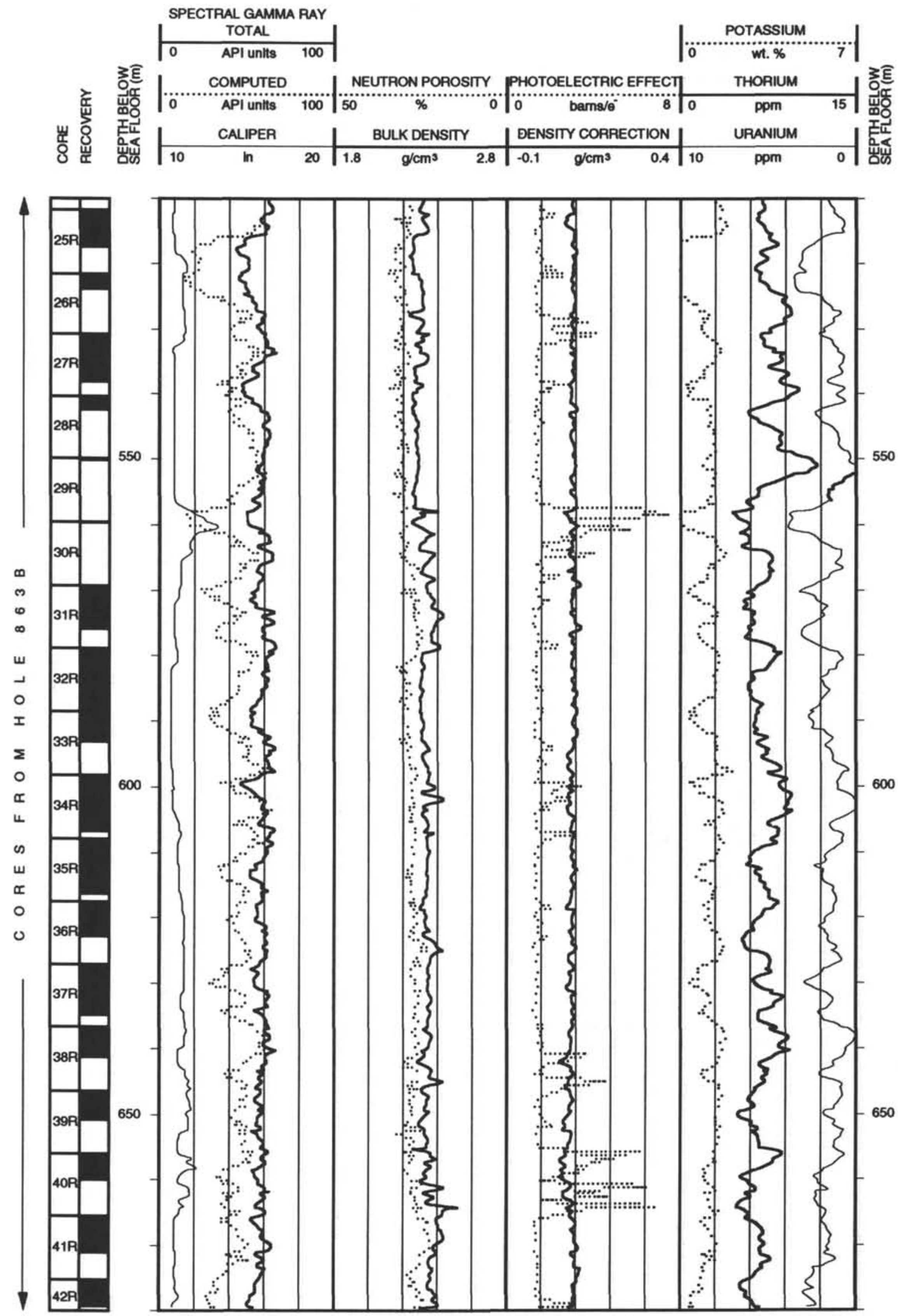

Hole 863B: Density-Natural Gamma Ray Log Summary (continued)

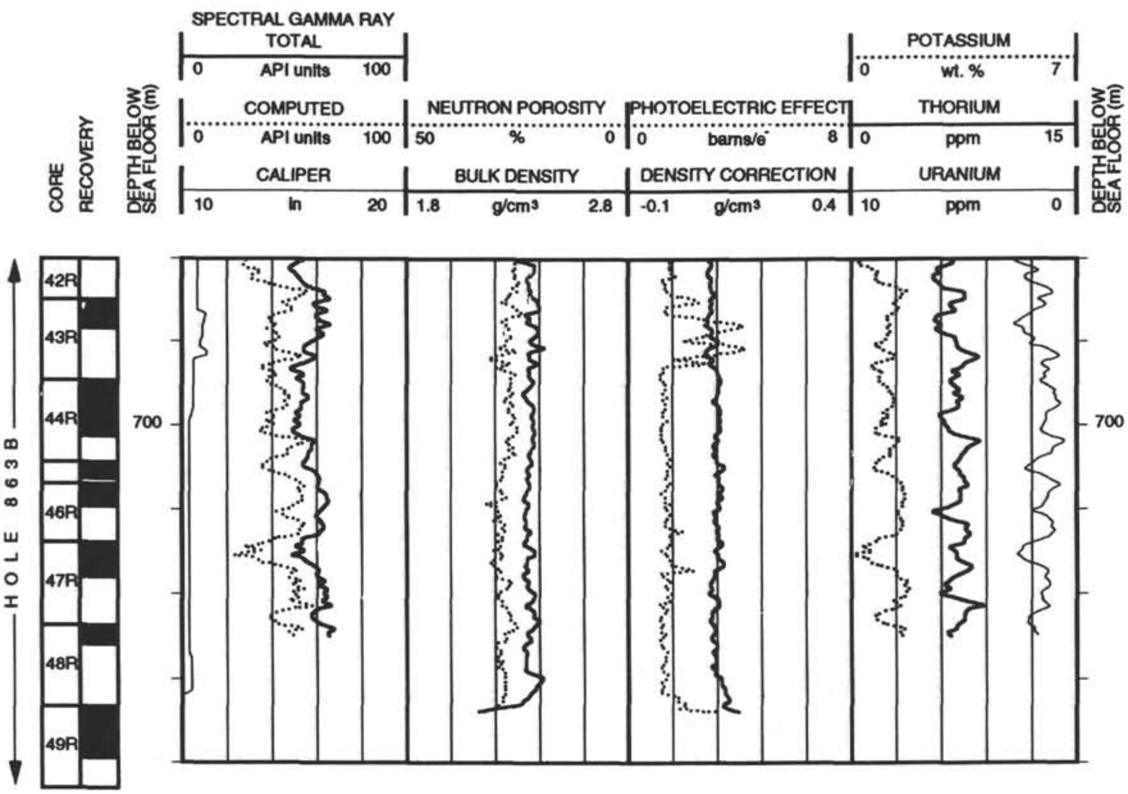

Hole 863B: Geochemical Log Summary

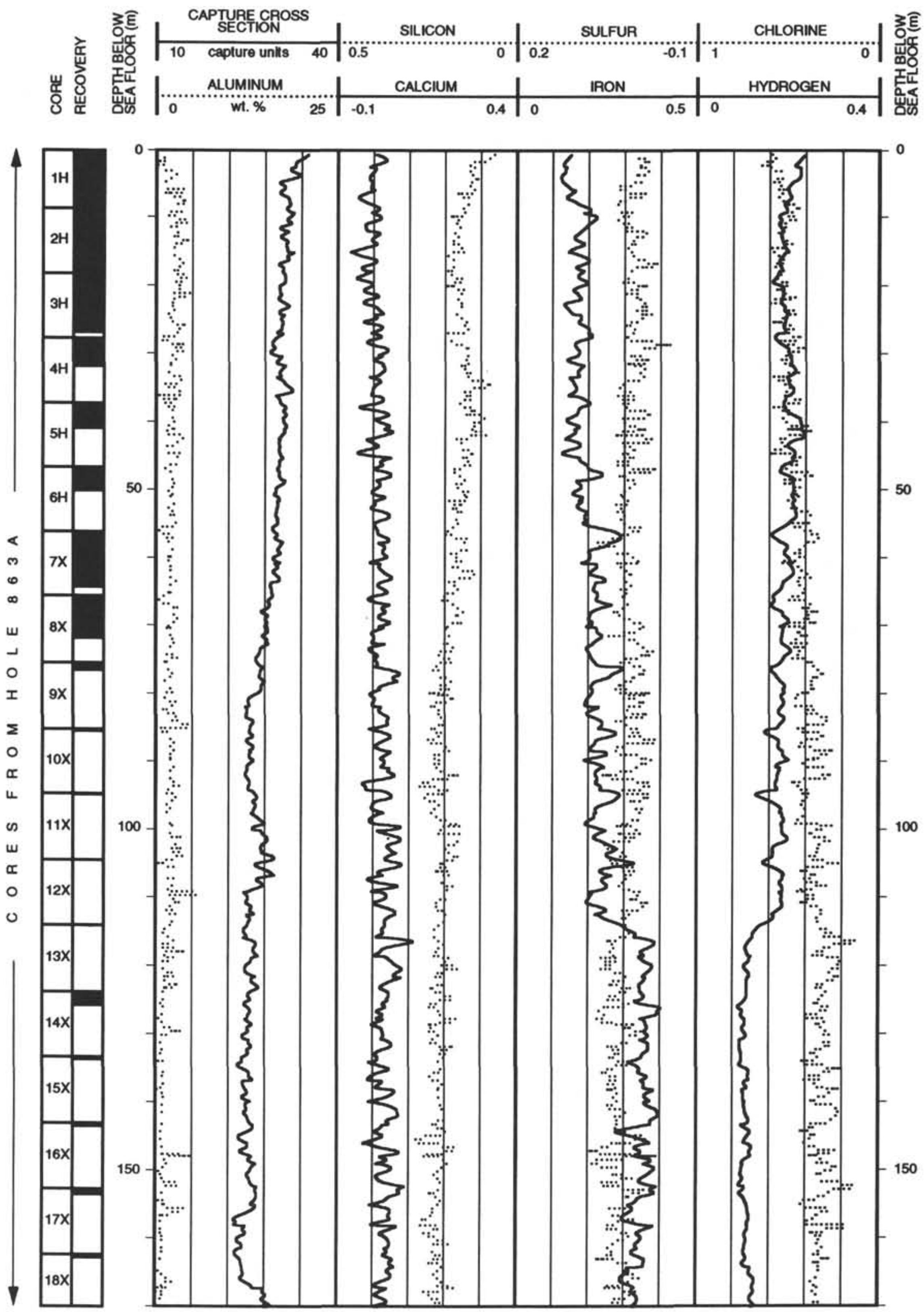

Hole 863B: Geochemical Log Summary (continued)

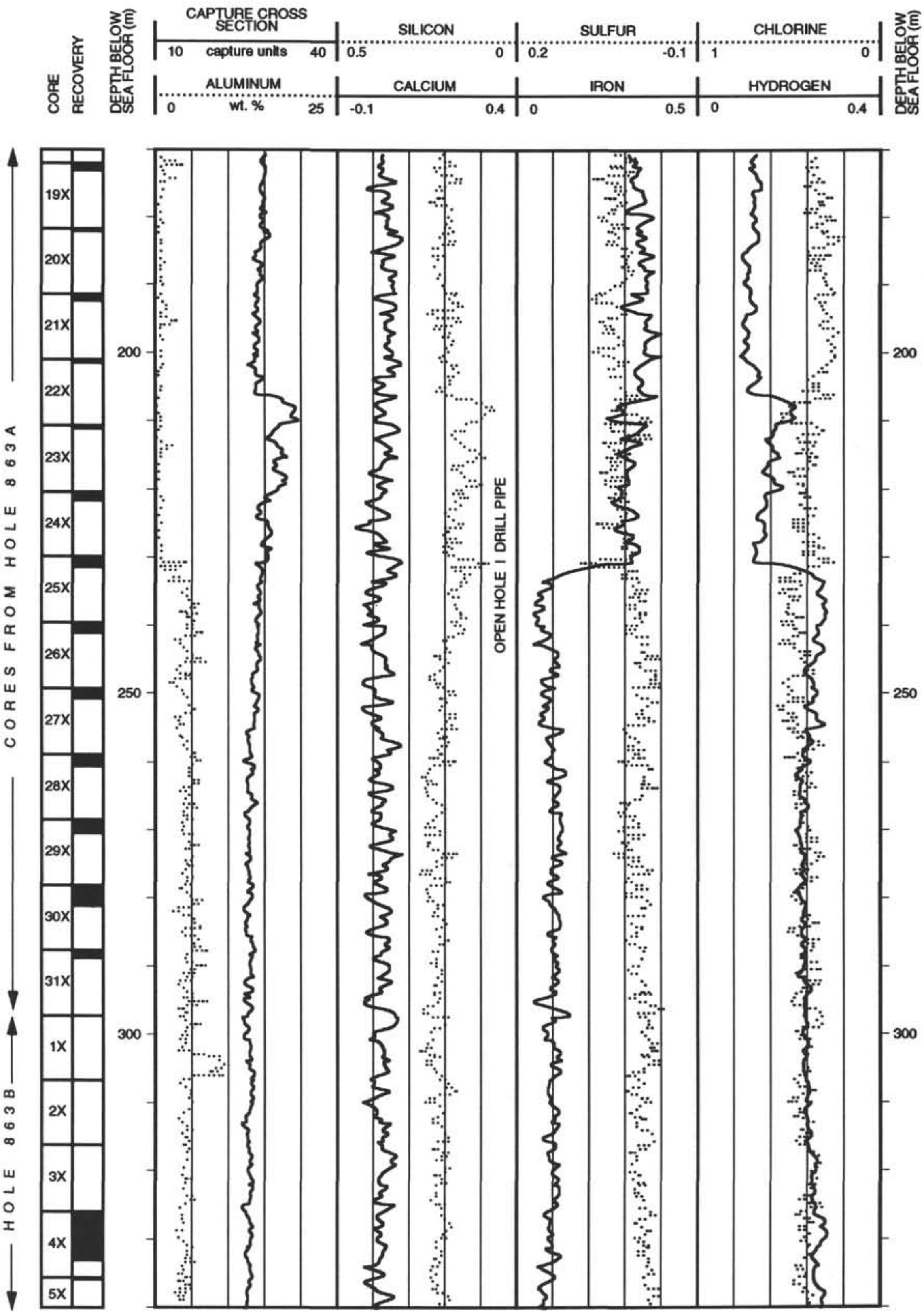

Hole 863B: Geochemical Log Summary (continued)

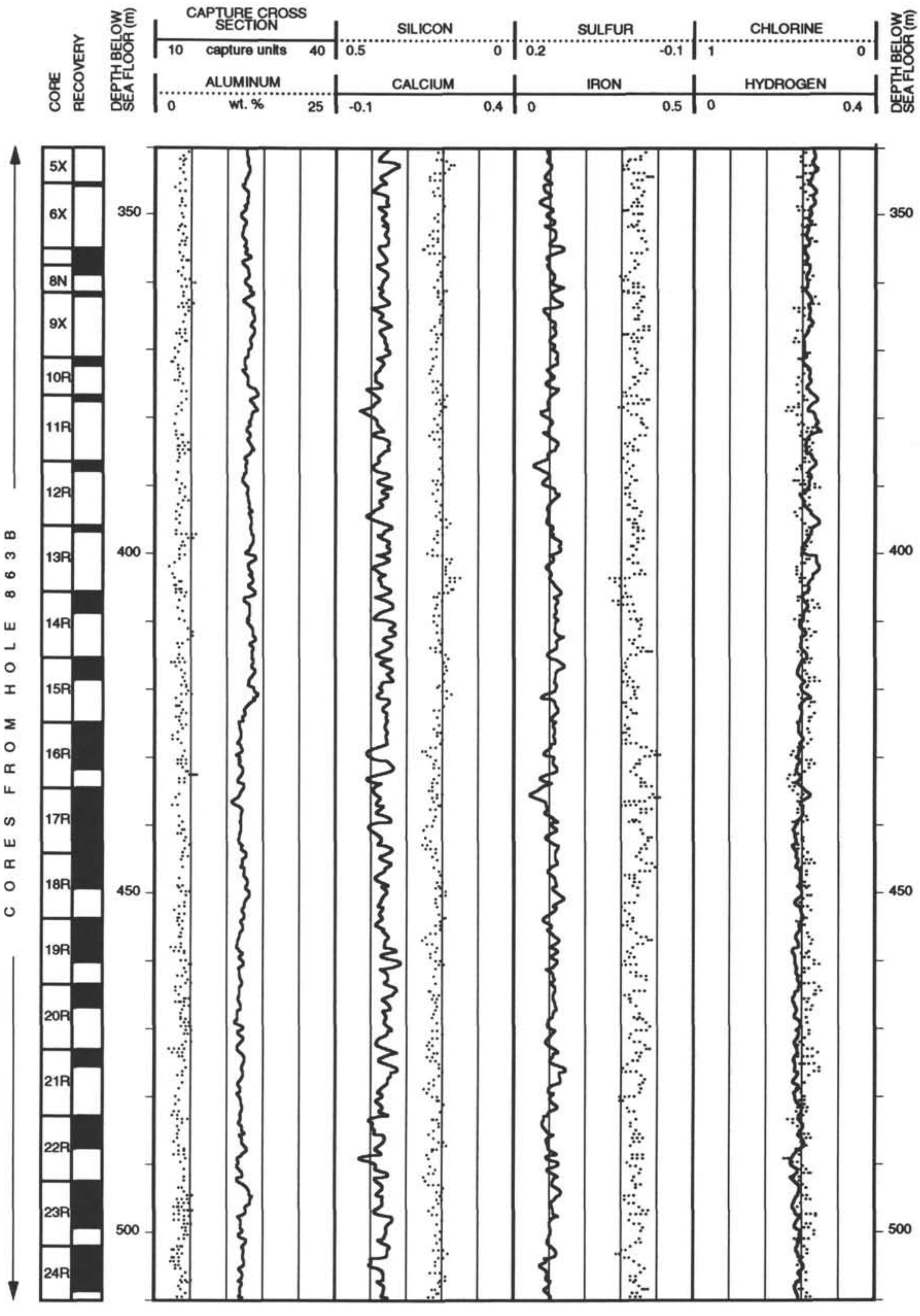

Hole 863B: Geochemical Log Summary (continued)

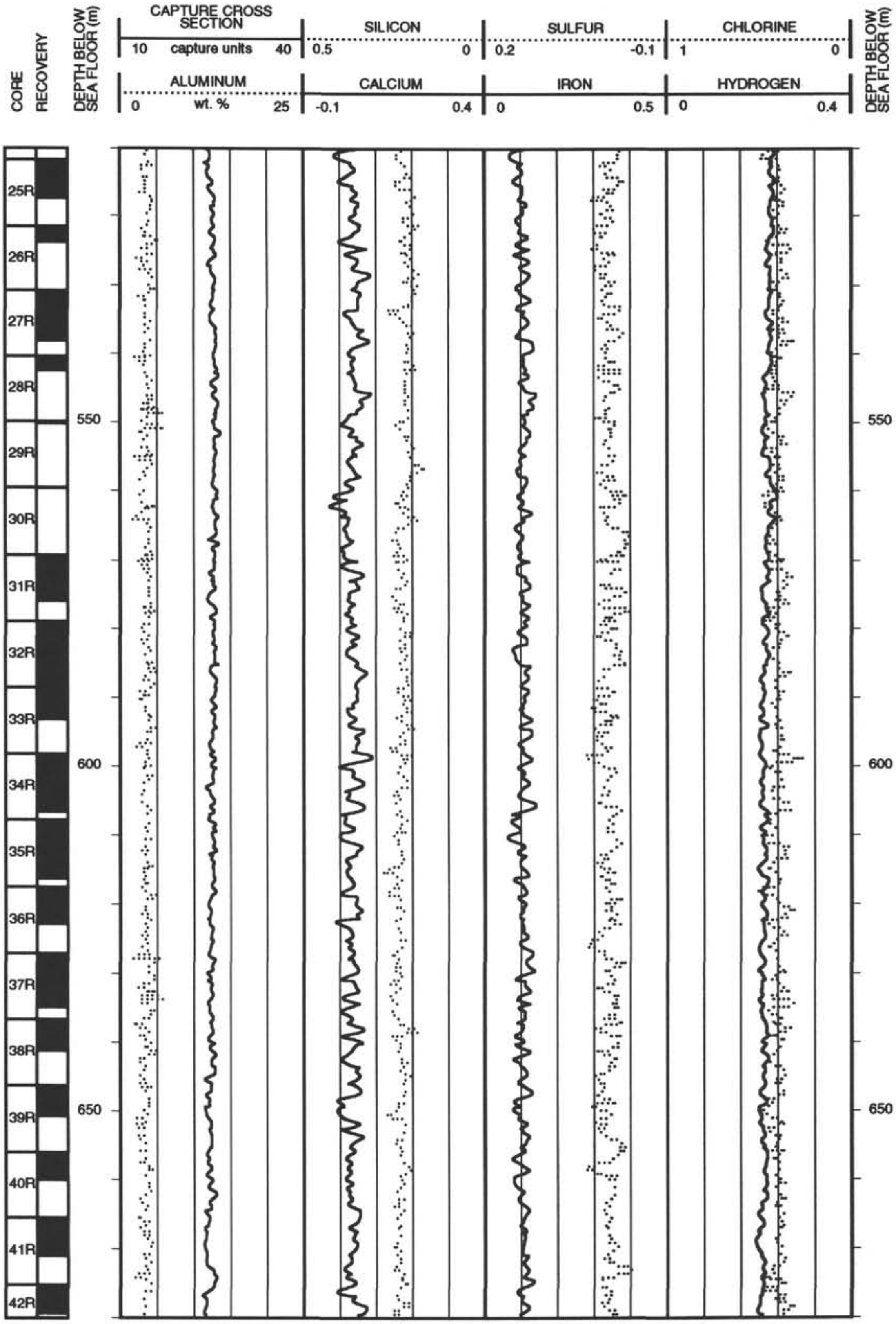

Hole 863B: Geochemical Log Summary (continued)